Lyubov Skopintseva

Exploring the potential of long offset reflections in AVO inversion and AVO analysis

Thesis for the degree of Philosophiae Doctor

Trondheim, October 2011

Norwegian University of Science and Technology
Faculty of Engineering Science and Technology
Department of Petroleum Engineering and Applied Geophysics

NTNU – Trondheim
Norwegian University of
Science and Technology

NTNU
Norwegian University of Science and Technology

Thesis for the degree of Philosophiae Doctor

Faculty of Engineering Science and Technology
Department of Petroleum Engineering and Applied Geophysics

ISBN 978-82-471-3105-3 (printed ver.)
ISBN 978-82-471-3106-0 (electronic ver.)
ISSN 1503-8181

Doctoral theses at NTNU, 2011:269

Printed by NTNU-trykk

Somewhere, something incredible
is waiting to be known

Dr. Carl Sagan

Research is what I'm doing
when I don't know what I'm doing

Werner von Braun

Abstract

Analysis of seismic reflection amplitudes versus offset (AVO) is one of common techniques widely exploited in the industry for reservoir characterization. For the last two decades a lot of approaches to analysis, inversion and interpretation of AVO data have been developed. Existing modifications valid for weak-contrast interfaces were successfully employed for conventional reservoirs. The growing interest of the industry to unconventional reservoirs, such as stiff-carbonate reservoirs, heavy oil traps and reservoirs close to salts domes - associated with strong-contrast interfaces and critical angles - implies the development of AVO techniques valid prior and beyond the critical angle. It has been reported in literature that near- and post-critical reflections have a potential to be employed as an additional source of information about the media. However, the use of these reflections is limited by the inability of well-known Zoeppritz equations to explain phenomena observed around and beyond the critical angle.

The aim of the thesis is to investigate phenomena observed at the reflected data around and beyond the critical angle, understand their potential from the AVO analysis and inversion point of view and develop a long-offset AVO inversion approach valid for strong-contrast interfaces. The theory of effective reflection coefficients is exploited as a mathematical apparatus providing an adequate description of phenomena observed at near- and post-critical reflections.

The thesis consists of five papers, where four major issues are addressed. The sensitivity of the reflection coefficient to isotropic and HTI media parameter changes prior to and beyond the critical angle is studied. The long-offset AVO inversion approach valid prior to and beyond the critical angle, strong-contrast and curved interfaces is developed and tested on synthetic data obtained for models with a single interface of various curvatures. Frequency effects in pre- near- and post-critical domains observed on the data of physical modeling are studied from the point of view of potential exploiting. Finally, the sensitivity of long-offset AVO inversion to errors related to overburden velocity misinterpretation is analyzed.

Acknowledgements

I am deeply indebted to many people, whose support allowed me to go through my Ph.D. study.

First of all, I thank my supervisor, Prof. Martin Landrø for his helpful guidance and support. His enthusiasm and valuable discussions brought me motivation and inspiration to look further for answers. He taught me to look at a problem from different angles due to his experience and independent point of view.

My deepest gratitude goes to my coauthors, Dr. Arkady Aizenberg, Milana Ayzenberg and Tatiana Nefedkina. Their endless discussions have brought a lot of ideas and made this work a reality. Special thanks goes to Prof. Alexey Stovas for his patience in discussing different scientific matters and sharing his knowledge and expertise. I also thank Amir Ghaderi for his effort to guide me during my laboratory experiment and provide unobvious hints in the experimental world.

I am grateful to the Seismic Wave Analysis Group at KAUST (Thuwal, Saudi Arabia) for a great opportunity to stay there and be part of the group in November-December 2010. This has been an amazing experience of integrating into a new country and seeing many impressive things. I was happy to collaborate with Prof. Tariq Alkhalifah, who introduced me to the word of anisotropy in a short time through numerous useful discussions. I also thank Sabrina Metzger, Hoby Razafindrakoto, Asim Iqbal and many others for making my stay in KAUST enjoyable.

I am grateful to my colleagues and friends from NTNU: Olena Tiapkina, Pamela Tempone, Pavel Golikov, Wiktor Weibull, Sandra Witsker, Lutz Muetschard, Hadi Balhareth, Laleh Farokhpoor, Mehran Namani, Mohammad Ashrafi and many others, not only for discussions on scientific matters and for resolving technical problems but also for bringing a lot of fun into our scientific world, which I will never forget. Especially, I would like to thank Kirill Glavatskiy for help in solving unexpected, unexplainable and sometimes unresolvable technical problems. I am also very thankful

to Sergii Chemerys for his invaluable help in explaining to me the logic of the MPI world, which allowed to saved me a lot of time in code parallelizing.

I thank the 4D group in Statoil ASA, Trondheim, Rotvoll for their discussions and for the opportunity to run modelling codes on their clusters. Additionally, I thank Statoil for providing financial support during the Ph.D. period.

My thanks goes to Prof. Boris Gurevich, Curtin University, and Mohammed Allhussain for providing experimental data, which contain post-critical reflections.

Next, I would like to express my gratitude to all my friends in Trondheim who were with me during these four years, supporting me and bringing a lot of fun and adventures into my boring life.

I would like to express my gratitude to my parents and brothers for their endless support and love, which always warms me and gives me power to grow and develop further. You are my best treasure.

Contents

List of Tables

List of Figures

Chapter 1

Introduction

This chapter contains a motivation for this thesis and involves the reader in the topic of reflections beyond the critical angle. It briefly summarises the basic ideas behind conventional AVO for elastic media and covers some aspects related to post-critical reflections: physics of phenomena, ideas of applications and challenges of implementations.

1.1 Conventional AVO inversion

The usefulness of analyzing amplitude versus offset behavior was discussed by Ostrander (1984). He linked AVO anomalies to changes in Poisson's ratio and revealed that such anomalies have a potential as direct hydrocarbon indicators.

To provide quantitative estimates of media parameters from AVO data, several AVO inversion techniques are developed. All these techniques exploit reflection coefficients for locally plane wavefronts and interfaces derived by Zoeppritz (1919), as a basis. However, due to their complexity, exact Zoeppritz equations do not provide straightforward insight of the influence of a particular model parameter on the reflection response. Therefore, most existing AVO inversion techniques exploit linear or quadratic approximations of plane-wave reflection coefficients, which are more convenient for interpretation. Although these approximations are based on different physical understandings and allow recovery of different characteristics of the media (Poisson's ratio, impedances, velocity contrasts across the interface, etc.), they are derived under the same basic assumptions:

- The relative changes in the P- and S-wave velocities and density across the interface are small.
- The incidence angle is sufficiently small.

A most convenient approximation of the reflection coefficient for elastic isotropic media, suitable for interpretation is given by Shuey (1985) as follows:

$$R_{PP}^{iso}(\theta) = A + B\sin^2\theta + C\sin^2\theta\tan^2\theta, \tag{1.1}$$

where θ is typically the incidence angle of the incoming wave.

Analysis of equation 1.1 as a function of $\sin^2\theta$ allows a straightforward interpretation of coefficients A, B and C. A is the reflection coefficient at zero offset (or intercept), B represents the initial slope of the reflection coefficient (or gradient) and is important for small or moderate incidence angles (up to 20^0) and C is the curvature term and is important for angles larger than 20^0.

The dependence of terms A, B and C on media parameters has several representations (Shuey, 1985; Wright, 1986). A practical relation is given by Wright (1986) and rewritten by Thomsen (1990) in the following form:

$$\begin{aligned} A &= \frac{1}{2}\left(\frac{\Delta V_P}{V_P} + \frac{\Delta\rho}{\rho}\right), \\ B &= \frac{1}{2}\left\{\frac{\Delta V_P}{V_P} - \left(\frac{2V_S}{V_P}\right)^2\frac{\Delta\mu}{\mu}\right\}, \\ C &= \frac{1}{2}\frac{\Delta V_P}{V_P}, \end{aligned} \tag{1.2}$$

where $\mathbf{m} = \frac{1}{2}(\mathbf{m}_1 + \mathbf{m}_2)$ is the vector of background media (or average) parameters; $\Delta\mathbf{m} = \mathbf{m}_1 - \mathbf{m}_2$ is the vector of contrast media parameters; $\mathbf{m}_i = (V_{P\,i},\ V_{S\,i},\ \rho_i, \mu_i)$ is a vector of media parameters above ($i = 1$) and below ($i = 2$) the interface; $V_{P\,i}$, $V_{S\,i}$ are P-and S-wave velocities, respectively; ρ_i is density (Figure 1.1); and $\mu_i = \rho_i V_{S\,i}^2$ is shear modulus.

According to equations 1.1-1.2, the intercept (A) represents the P-wave impedance. Reflections at small and moderate offsets (B) contain information about S-wave velocity, while reflections at larger offsets (C) are sensitive to P-wave velocity.

It is also obvious that AVO inversion, based on equations 1.1-1.2, can retrieve a maximum of three parameters. However, practically, the recovery of the third term in equation 1.1 is challenging, and therefore, often only a two-parameter AVO inversion is successful.

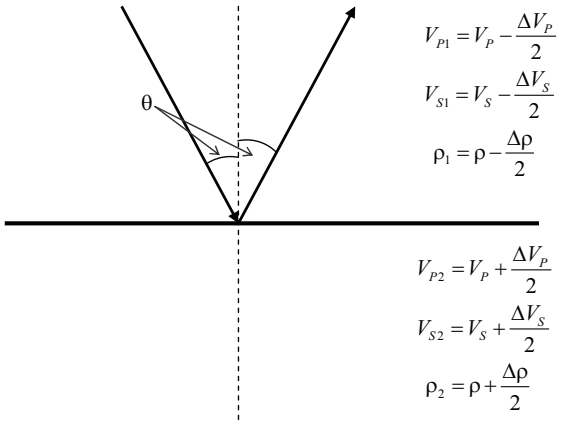

Figure 1.1: Explanation of terms used in equation 1.2

Rüger (2001) extended equations 1.1-1.2 for transversely isotropic media with a vertical symmetry axis (VTI media) and a horizontal symmetry axis (HTI media). In his approximations, the form of equation 1.1 is preserved, while terms A, B and C become functions of anisotropy parameters ϵ, δ and γ (Thomsen, 1986). For VTI media, equation 1.2 transforms to the following:

$$\begin{aligned} A &= \frac{1}{2}\left(\frac{\Delta V_P}{V_P} + \frac{\Delta\rho}{\rho}\right), \\ B &= \frac{1}{2}\left\{\frac{\Delta V_P}{V_P} - \left(\frac{2V_S}{V_P}\right)^2 \frac{\Delta\mu}{\mu} + \Delta\delta\right\}, \\ C &= \frac{1}{2}\left\{\frac{\Delta V_P}{V_P} + \Delta\epsilon\right\}, \end{aligned} \tag{1.3}$$

where vector of model parameters is $\mathbf{m}_i = (V_{P\,i},\ V_{S\,i},\ \rho_i,\ \mu_i,\ \epsilon_i,\ \delta_i)$, $V_{P\,i}$ and $V_{S\,i}$ are vertical P-and S-wave velocities.

Equation 1.3 shows that the PP-reflection coefficient contains information about anisotropy parameter δ at small incident angles, while larger offset amplitudes are more sensitive to the anisotropy parameter ϵ.

HTI media coefficients A, B and C become azimuthally dependent and have the

following form:

$$
\begin{aligned}
A &= \frac{1}{2}\left(\frac{\Delta V_P}{V_P} + \frac{\Delta\rho}{\rho}\right), \\
B &= \frac{1}{2}\left\{\frac{\Delta V_P}{V_P} - \left(\frac{2V_S}{V_P}\right)^2 \frac{\Delta\mu}{\mu} + \left[\Delta\delta^{(V)} + 2\left(\frac{2V_S}{V_P}\right)^2 \Delta\gamma\right]\cos^2\phi\right\}, \\
C &= \frac{1}{2}\left\{\frac{\Delta V_P}{V_P} + \Delta\epsilon^{(V)}\cos^4\phi + \Delta\delta^{(V)}\sin^2\phi\cos^2\phi\right\},
\end{aligned}
\tag{1.4}
$$

where $\mathbf{m}_i = \left(V_{P\,i},\ V_{S\,i},\ \rho_i,\ \mu_i,\ \epsilon_i^{(V)},\ \delta_i^{(V)},\ \gamma_i\right), i = 1, 2$; $V_{P\,i}$, $V_{S\,i}$ are P- and S-wave velocities in the isotropic plane; $\epsilon_i^{(V)}$, $\delta_i^{(V)}$ are anisotropy parameters in HTI notation (Rüger, 2001); γ_i is the shear wave Thompson anisotropy parameter; ϕ is the azimuth angle.

According to equations 1.4, reflection amplitudes at small and moderate offsets depend on anisotropy parameters $\delta^{(V)}$ and γ, while larger offsets contain information about $\delta^{(V)}$ and $\epsilon^{(V)}$ in addition to the P-wave velocity.

Despite equations 1.3 and 1.4 containing a larger number of model parameters, AVO inversion based on approximation 1.1 can still retrieve the maximum three parameters. To estimate more parameters, a priori information or additional data (for example, reflections of converted waves) are required.

Prior to AVO inversion, the data has to be pre-processed. This is a complex process, where the main challenge is to preserve the relative amplitude content. Normally, the pre-processing workflow includes removal of unwanted energy, relocation and compensation of energy and reflection coefficient restoring, defined as follows:

- Removal of unwanted energy implies the elimination or suppression of multiples and other systematic noise. One has to be careful to preserve amplitudes of the primary reflection as much as possible.
- Reallocation and compensation of energy aims to move the energy to its correct subsurface position, as it potentially can come from different reflection points. Additionally, this procedure corrects for energy loss that occurs during propagation, such as spherical divergence (or geometrical spreading), absorption, dissipation of energy, etc. This step is often handled by the AVO/AVA-oriented pre-stack migration algorithm.
- The reflection coefficient restoration implies offset-to-angle conversion and scaling of amplitudes. Offset-to-angle conversion can be handled by the migration

algorithm, if it generates output gathers directly into the reflection angle domain. Otherwise, ray tracing from the reflection point to the receiver is needed. Normally, a straight ray approach is employed. To obtain a true reflection coefficient suitable for the inversion, the amplitude scaling is performed by applying the global scaling factor. Usually, this factor is estimated with additional well log information.

1.2 Critical angle

Although the conventional methods in AVO inversion are proved to be successful in many case studies, their application is limited to weak contrast interfaces and small offsets. The growing interest of the industry to unconventional reservoirs (stiff-carbonates, heavy oil traps, salt domes) with large changes in media parameters across the interface and a continuous increase of length in modern acquisition setups causes problems in application of conventional AVO methods due to basic assumptions.

Unconventional reservoirs are characterized by the sufficient P-wave velocity increase. For example, the P-wave velocity increase for the top of a stiff-carbonate reservoir is around 700 m/s (Landrø, 2006), for the top of a shallow heavy oil reservoir, it is 1100 m/s (Hansteen et al., 2011); for the top of a salt body, it is 1400 m/s (Muerdter and Ratcliff, 2001). The velocity contrast across the interface, consequently, affects the critical angle (or critical offset), likely captured by modern acquisition. The larger the contrast is, the smaller the critical angle (or critical offset) is expected, as it is seen from Snell's law:

$$sin\left(\theta_{cr}\right) = \frac{V_{P1}}{V_{P2}}, \tag{1.5}$$

where θ_{cr} is the critical angle.

In the case of anisotropic media, the critical angle depends on the phase-velocities and is sensitive to the velocity anisotropy. Snell's law thus transforms into the following form (Landrø and Tsvankin, 2007):

$$sin\left(\theta_{cr}\right) = \frac{V_{P1}\left(\theta_{cr}\right)}{V_{P2,\,hor}}, \tag{1.6}$$

where θ_{cr} is the critical angle, $V_{P1}\left(\theta_{cr}\right)$ is the phase velocity in the upper layer, and $V_{P2,\,hor}$ is the horizontal phase velocity in the lower media. If phase velocities are azimuthally dependent, then the critical angle becomes sensitive to the azimuth.

The existence of the critical angle results in a non-zero complex component of the reflection coefficient and sufficient changes in the amplitude and phase of the reflection signal. These changes in reflection response might be an additional source of information about the media in AVO inversion. However, working with near- and post-critical reflections implies refusing existing linearizations of reflection coefficients and exploiting non-linear inversion methods.

Lavaud et al. (1999) investigated the potential of the near- and post-critical reflections in AVO inversion. His investigations are based on exact Zoeppritz equations and synthetic data generated by ray tracing. He confirmed that near- and post-critical reflections inherit more information about the media than only pre-critical reflections.

AVO inversion based on the exact Zoeppritz equation can retrieve a maximum of four parameters, as it contains four dimensionless parameters (Lavaud et al., 1999; Kurt, 2007). It is one parameter more than in the case of conventional AVO inversion. The result is consistent with the fundamental Buckingham Pi-theorem (Bluman and Kumei, 1989), which states that the number of independent parameters of the expression corresponds to the number of dimensionless parameters.

1.3 Seismic waves from the point source

Although the usefulness of post-critical reflections in AVO inversion is confirmed, the approach described by Lavaud et al. (1999) cannot be applied to seismic data. The reason is that Zoeptritz equations are not adequate around and beyond the critical angle (Downton and Ursenbach, 2006), as the assumption about a locally plane wavefront results in non-physical discontinuity of reflection coefficients at the critical angle. An experimental study performed by Alhussain (2007) showed that the reflection response does not have an abrupt amplitude increase at the critical angle. The amplitude gradually increases and reaches its maximum beyond the critical angle. This fact is also confirmed by the experiments done by Ortiz-Osornio and Schmitt (2011).

From a ray theory point of view, Zoeptritz equations can be interpreted as reflection/transmission of the wave at infinite frequency. Seismic waves, however, contain finite frequencies and are not plane, since they are normally generated by a point source. These wave characteristics result in a significant Fresnel zone effect at the interface, where the reflection at one point of the interface is influenced by reflections

from neighboring points. Consequently, this results in reflection amplitude dependency on frequency and wavefront curvature.

The critical ray is associated with a new wave appearance, called a head (or refracted) wave. Beyond the critical angle, part of the seismic energy starts propagating along the interface with the velocity of the underburden. According to the Huygens principle, excited points of interface act as secondary sources and produce a wave propagating towards the receiver. This wave illuminates the discontinuity between reflected and transmitted wavefronts beyond the critical angle. The head wave has a conical wavefront tangential to the reflected wavefront at the critical ray and coincident with the transmitted wavefront at the interface. Propagating towards the receiver with some phase shift relative to the reflected wave, the head wave creates interference with reflected wave. It affects the reflection amplitudes beyond the critical angle.

Červený (1961) was among the first who studied amplitude curves around and beyond the critical angle, considering spherical harmonic waves reflected from the plane interface. He theoretically showed that, indeed, the amplitude maximum does not coincide with the critical angle and appears beyond it and the amplitude function does not have a discontinuity at the critical angle. The position of this maximum depends on the wavefront curvature and frequency. These parameters enter the equation for reflection amplitude as a dimensionless quantity $k_{P1}r = \frac{\omega r}{V_{P1}}$, where k_{P1} is the wavenumber in the upper layer, ω is the angular frequency and r is the wavefront radius (reciprocal to the wavefront curvature). This quantity shows the linear trade-off between frequency and wavefront curvature. A frequency increase results in the same effect on the amplitude curves as a wavefront curvature increase. Červený (1961) also described the interference between reflected and head waves.

Later, Ursenbach et al. (2007) developed so-called spherical reflection coefficients for impulse reflections by involving the wavelet spectrum of the incident wave into the equations of the spherical wave, reflected from the plane interface (Aki and Richards, 2002). As a result, he obtained reflection coefficients that correctly describe the AVO response, containing a particular wavelet signature. In practical applications, the wavelet can contain an arbitrary frequency spectrum, which results in some limitations of the spherical coefficients application.

Ayzenberg et al. (2007) and Ayzenberg et al. (2009) developed so-called effective reflection coefficients for acoustic and elastic media. In contrast to spherical reflection coefficients, they are designed for harmonic waves. In contrast to the representation given by Červený (1961), effective reflection coefficients depend on the modified di-

mensionless parameter $k_{P1}r^*$, where r^* is a function of wavefront and the interface curvatures. Effective reflection coefficients thus are not restricted by the plane interfaces and wavelet spectrum. These equations are valid also for waves reflected from the interface between heterogeneous media.

1.4 Challenges and potential beyond the critical angle

Although phenomena created by the critical ray are fully understood, and theoretical apparatus describing amplitudes around and beyond the critical angle is developed, post-critical reflections have not been extensively used in AVO studies so far. One of the attempts is devoted to a 4D study of long offset data from the Valhall field (Mehdi Zadeh et al., 2011), where the authors exploited the maximum amplitude position shifts to estimate P-wave velocity changes, caused by production.

In the study of amplitudes beyond the critical angle, the crucial attention needs to be devoted to effects caused by the argument $k_{P1}r^*$. The dependency of the effective reflection coefficient on this additional dimensionless argument gives a potential for AVO inversion to retrieve five parameters instead of four, as it is in case of exact Zoeppritz equations (Lavaud et al., 1999). In addition, it might change the sensitivity of the reflection coefficient to the layer parameter changes. The dependency of the argument $k_{P1}r^*$ on the interface curvature is a nice tool to understand how the interface curvature affects the reflection amplitudes. The dependency of this argument on the frequency deserves an attention for fractured reservoirs, where the frequency content along and across the fractures differs (Chapman and Liu, 2003).

The dependence of the critical angle on the horizontal velocity in the underburden indicates that post-critical reflections might be useful for reservoirs with azimuthal anisotropy. Additionally, the strong dependence of post-critical offsets on anisotropy parameters, as it is shown by Ayzenberg et al. (2009) for the VTI case, might be useful in the estimation of anisotropy parameters.

Involving the post-critical offsets into AVO inversion is challenging from the AVO-oriented data pre-processing point of view. Seismic data at post-critical offsets are often distorted by the systematic noise, such as water column noise (Mehdi Zadeh, 2011). One has to be careful when removing this noise and seeking to achieve preservation of the reflection amplitude at the same time. This topic is omitted in this thesis.

Another challenge is related to migration algorithms for long offset data. Existing algorithms are not valid for reflections beyond the critical angle. A common assumption in migration is that there are only reflected waves. The post-critical domain, however, contains two types of waves. A possible way to overcome this problem is to correct for geometrical spreading and include a propagation term into the effective reflection coefficient. The latter step is necessary, as interference between reflected and head waves changes during propagation and cannot be compensated for by geometrical spreading. Obtaining the amplitudes from the data at post-critical offsets meets obstacles due to phase changes. There are two ways to overcome this problem: obtaining amplitudes in time or in frequency domains with an appropriate weighting of the effective reflection coefficients. The problem of accessing correct geometrical spreading and offset-to-angle conversion for the velocity-dependent overburden is actual, not only for post-critical but also for pre-critical offsets, and has to be taken into account.

The main objective of this thesis is to understand the potential of the post-critical reflections in AVO inversion and AVO analysis. This will enable us to assess perspectives of working with long offset data and allow us to think beyond the critical angle. The study is carried out for a simple model, where two homogeneous halfspaces are divided by one interface (plane or curved). Anisotropic study is done on the analysis of amplitudes reflected from HTI media and by using the experimental data obtained by Alhussain (2007).

1.5 Thesis content

The thesis consists of six chapters including this introduction and an additional Appendix. All chapters can be considered independent papers with their own abstract, motivation, introduction, conclusions and appendixes. Therefore, some introductory and background material presented in different chapters may coincide.

The potential of effective reflection coefficients in application to the long offset AVO inversion for single plane interface is explored in Chapter 2. The theoretical background of two different approaches to ERC-based AVO inversions is developed. Approaches differ by the method of extracting AVO data (time domain or frequency domain) and different frequency content. These versions of ERC-based AVO inversion are compared with the AVO inversion approach based on exact Zoeppritz equation and show their adequacy in application to the data generated by the point source,

especially in near- and post-critical domains. The results of this chapter have been presented at the ROSE Meeting, Trondheim, Norway, April 2008 and 2009; the 70th EAGE Conference & Exhibition, Rome, Italy, June 2008; and the 71th EAGE Conference & Exhibition, Amsterdam, Netherlands, June 2009. The paper was accepted in *Geophysics* in July 2011.

In Chapter 3, effects of the interface curvature on long-offset AVO inversion are investigated. Examples of synthetic modeling carried out for two homogeneous halfspaces divided by an anticlinal interface confirm a strong effect of the interface curvature on the amplitude strength and position of the amplitude maximum, associated with the head wave appearance. To explain the interface curvature effect on the amplitude strength, the theory of geometrical spreading for curved interfaces developed by Červený et al. (1974) is used. To explain the interface curvature effect on the position of the amplitude maximum, a semi-heuristic approach for correcting the effective reflection coefficient for the interface curvature dependent propagation term is developed. The quantitative estimates of the interface curvature effect on the AVO data are provided by the ERC-based AVO inversion. The work has been presented at the ROSE Meeting, Trondheim, Norway, April 2010 and the 72th EAGE Conference & Exhibition, Barcelona, Spain, June 2010. This paper is submitted to *Geophysics*.

The potential of the AVO inversion at post-critical offsets for HTI media is investigated in Chapter 4. The effective reflection coefficients are adopted for the solid isotropic/HTI interface. The paper demonstrates the benefits of post-critical reflections in the analysis of azimuthal anisotropy. The sensitivity study of reflection coefficient to anisotropy parameters $\epsilon^{(V)}$, $\gamma^{(V)}$, $\delta^{(V)}$, P- and S-wave velocities, density in underburden and azimuthal angle is performed for different offset ranges. The results show different sensitivity of the reflection coefficients to model parameters at different offset ranges. The analysis for optimal acquisition setup is also carried out and shows acquisition setup has blind zones, where AVO inversion for any offset range is expected to be poor. The results of this work are presented at the 73th EAGE Conference & Exhibition, Vienna, Austria, May 2011. The paper is submitted to *Geophysics*.

The frequency effects of the reflection amplitudes observed on the multi-azimuth experimental data (Alhussain, 2007) are studied in Chapter 5. The data show that the frequency dependency of the amplitude and phase at pre-, near- and post-critical offsets reveals azimuthal variation. The attempt to explain observed phenomena is carried out under HTI model assumption. The synthetic datasets generated by the

two independent modeling algorithms (reflectivity and ERC) capture frequency phenomena in near- and post-critical domains. The example of synthetic modeling shows that frequency dependence in a post-critical domain can be utilized for azimuthal anisotropy analysis. This study was presented at the ROSE Meeting, Trondheim, Norway, May 2011 and the 73th EAGE Conference & Exhibition, Vienna, Austria, May 2011. The work is submitted to *Geophysical Journal International*.

The influence of the traveltime analysis on the AVO inversion results is investigated in Chapter 6. The paper aims to show that the wrong interpretation of traveltime parameters affects the offset-to-angle conversion and geometrical spreading correction. The comparison between a two-parameter constant velocity model and a three-parameter, depth-dependent velocity models is provided. The effect of misinterpretation is quantified by the AVO inversion results provided for two different offset ranges. One offset range includes only pre-critical reflections, another contains pre-, near- and post-critical offsets. The study is carried out for a synthetic dataset generated by ray tracing. The work was presented at the ROSE Meeting, Trondheim, Norway, April 2008 and SEG 78th Annual Meeting, Las-Vegas, USA, November 2008. It was published in *Geophysics* in 2009.

The Appendix reviews the potential improvement in reservoir monitoring using permanent seismic receiver arrays. My part of this work is dedicated to the ultra-frequent acquisition setup, which is most likely to be applied in permanent installations. On the example of the synthetic modeling provided by the propagation matrix method the benefits of such a setup to minor 4D variations and random noise issues are shown. The results of my part of the work were presented at the 70th EAGE Conference & Exhibition, Rome, Italy, June 2008 and published in *The Leading Edge* in December 2008. The study is not related to post-critical reflection issues and is therefore placed in the Appendix.

Chapter 2

Long-offset AVO inversion of PP reflections from plane interfaces using effective reflection coefficients

Lyubov Skopintseva[1], Milana Ayzenberg[2],
Martin Landrø[1], Tatyana Nefedkina[3],
Arkady M. Aizenberg[3]

[1] Norwegian University of Science and Technology, Trondheim, Norway

[2] Statoil ASA

[3] Institute of Petroleum Geology and Geophysics SB RAS, Novosibirsk, Russia

Presented at the ROSE Meeting, Trondheim, Norway, April 2008, 2009; the 70th EAGE Conference & Exhibition, Rome, Italy, June 2008; the 71th EAGE Conference & Exhibition, Amsterdam, Netherlands, June 2009; Accepted for publication in Geophysics

2.1 Abstract

A conventional AVO inversion is based on geometrical seismics which exploits plane-wave reflection coefficients to describe the reflection phenomenon. Widely exploited linearizations of plane-wave coefficients are mostly valid at pre-critical offsets for media with almost flat and weak-contrast interfaces. Existing linearizations do not account for the seismic frequency range by ignoring the frequency content of the wavelet, which is a strong assumption. Plane-wave reflection coefficients do not fully describe the reflection of seismic waves at near-critical and post-critical offsets, because reflected seismic waves are typically generated by point sources. We propose an improved approach to AVO inversion, which is based on effective reflection coefficients. Effective reflection coefficients generalize plane-wave coefficients for seismic waves generated by point sources and therefore more accurately describe near-critical and post-critical reflections where head waves are generated. Moreover, they are frequency-dependent and incorporate the local curvatures of the wavefront and the reflecting interface. In our study, we neglect the effect of interface curvature and demonstrate the advantages of our approach on synthetic data for a simple model with a plane interface separating two isotropic halfspaces. A comparison of the inversion results obtained with our approach and the results from an AVO inversion method based on the exact plane-wave reflection coefficient suggests that our method is superior, in particular for long offset ranges which extend to and beyond the critical angle. We thus propose that long offsets can be successfully exploited in an AVO inversion under the correct assumption about the reflection coefficient. Such long-offset AVO inversion shows the potential of outperforming a conventional moderate-offset AVO inversion in the accuracy of estimated model parameters.

2.2 Introduction

AVO inversion converts the measured amplitude of a reflected event into physical medium parameters. The ultimate goal of a deterministic AVO inversion is to estimate the medium parameters through minimization of the misfit between the AVO data extracted from the target reflection and its theoretical description. A successful AVO inversion captures most of the phenomena contained in the observed wavefield.

A reflected event at the receiver can generally be described by the product of a propagation operator through the overburden and a reflectivity function at the target interface. The propagation operator includes the respective phenomena that occur during wave propagation, such as energy flux along ray tubes, focusing, attenuation, transmission losses, diffraction, etc. The propagation effects are usually compensated for through dedicated pre-processing of the AVO data.

The reflectivity function widely exploited in conventional AVO inversion is based on linearizations of the plane-wave reflection coefficient (PWRC) given by the Zoeppritz equations (Aki and Richards, 2002; Shuey, 1985). An underlying assumption is that the contrast in the seismic parameters across the reflecting interface is weak and the incidence angle is small. This limits the applicability of an AVO inversion to pre-critical offsets. The growing industry interest in reservoirs with strong-contrast interfaces (salt domes, heavy oil fields, basalts, etc.) and increased offset ranges in seismic acquisition lead to increased interest in near-critical and post-critical reflections in the data. These are associated with rapid amplitude variations and cannot be described by the linearized plane-wave reflection coefficients. Conventional approaches to AVO inversion cannot be applied in such circumstances. However, there is a potential for enhancing the accuracy of AVO inversion by incorporating and exploiting the near-critical and post-critical offsets.

Riedel and Theilen (2001) and Downton and Ursenbach (2006) were the among the first authors who have realized the power of long-offset AVO inversion. They exploited the exact Zoeppritz equations to describe the AVO data and showed that they are inadequate at long offsets. The main reason is that the respective equations honor the plane incident waves, when the original AVO data is caused by the non-plane waves and contains head waves. Van der Baan and Smit (2006) suggested to exploit the $\tau - p$ transform in order to reduce the original AVO data to the plane-wave domain, where the constituting plane waves can be correctly described by PWRCs for small incidence angles. Although this has proven to enhance the quality of AVO inversion,

the approach is limited to near-critical offsets and is prone to data sampling issues.

Because a typical seismic source emits a wave which is almost spherical and has finite frequency band, a qualitative and quantitative improvement in AVO inversion can be achieved by incorporating the Fresnel volume which surrounds the reflected ray (Favretto-Cristini et al., 2009). This will automatically include the seismic frequency range and capture the effect of transversal energy diffusion. It is also natural to expect that the Fresnel zone surrounding the reflection point has equally strong impact on the reflection strength as the reflection point itself. Červený (1961) and Brekhovskikh (1960) derived reflection coefficients that incorporate the Fresnel zone and are valid for point sources and finite frequencies. Later, Ursenbach et al. (2007) proposed the so-called spherical-wave reflection coefficients which depend on the wavelet form and are valid only for homogeneous media, plane reflectors and spherical waves.

To generally describe the reflection of arbitrary waves at curved reflectors in inhomogeneous media, De Santo (1983) and Kennett (1984) suggested the implicit local reflection and transmission operators as numerical solutions for acoustic and elastic media. Klem-Musatov et al. (2004) suggested a general rigorous reflection-transmission theory for scalar waves at curved interfaces between heterogeneous media. Later, Aizenberg et al. (2005) extended the theory for acoustic waves. Based on their results, Ayzenberg et al. (2007) and Ayzenberg et al. (2009) developed an explicit approximate description of the reflection at curved interfaces in the form of effective reflection coefficients (ERCs) for acoustic and elastic waves.

Similarly to the spherical-wave reflection coefficients, ERCs incorporate reflections from the interface points located inside the Fresnel zone. ERCs relax the assumptions of plane wavefront and locally plane reflecting interface implicit in PWRCs. ERCs thus generalize PWRCs and the spherical-wave reflection coefficients for curved reflectors and are adequate within the seismic frequency range. They capture the associated phenomena at the near-critical and post-critical offsets. Moreover, they do not depend on the wavelet form, unlike the spherical-wave reflection coefficients.

In this paper, we introduce the background theory for the new approach to long-offset AVO inversion based on ERCs. We test the approach on synthetic data for a simple model, where two homogeneous elastic halfspaces are separated by a horizontal plane interface. We propose to exploit two ways of extracting the amplitudes from the data, which we refer to as the single-frequency and the band-limited AVO data, and introduce their respective theoretical descriptions. We perform AVO inversion for different offset ranges and assess the performance of our approach at long offsets.

By comparing the results of our AVO inversion with the results obtained from AVO inversion based on exact PWRCs, we demonstrate the superiority of our inversion with increasing offset range.

The paper is divided in three parts. Part 1 introduces the statement of the AVO inversion problem for long-offset data. We review ERCs and discuss their properties in detail. Part 2 is devoted to the new approach to AVO inversion based on ERCs. We study the impact of the frequency content on AVO inversion. We then proceed to comparing the ERC-based and the PWRC-based AVO inversions. Part 3 demonstrates the advantages of performing a long-offset AVO inversion on a synthetic PP dataset for various offset ranges. In Discussion we cover some aspects connected with the possibility to exploit ERC-based AVO inversion in practice. In Appendix 2.9 we derive an approximation of the PP reflected wavefield at a receiver in terms of the effective reflection coefficient.

2.3 Deterministic AVO inversion

We consider a deterministic AVO inversion approach which consists in updating the model parameters through the minimization of the misfit function between the observed AVO data and its theoretical description:

$$F(\mathbf{v}) = \sqrt{\sum_{n=1}^{N} \left[AVO_{\text{obs}}(\mathrm{x}_n) - AVO_{\text{theo}}(\mathrm{x}_n)\right]^2} \rightarrow \min, \tag{1}$$

where $AVO_{\text{obs}}(\mathrm{x}_n)$ is the observed AVO data, $AVO_{\text{theo}}(\mathrm{x}_n)$ represents the theoretical description of the observed AVO data, $\mathbf{v}$ is the vector of required parameters, x_n ($n = 1,\ 2,\ \ldots,\ N$) are the receiver coordinates, N denotes the number of receivers. The dimension of vector $\mathbf{v}$ is equal to the number of unknown parameters.

Extraction of the AVO data by picking the amplitude maximum fails at long offsets because of the phase rotation which occurs at the near-critical and post-critical offsets (Riedel and Theilen, 2001). Lavaud et al. (1999) showed that taking the RMS value of the reflected event in the fixed time window along the moveout is appropriate to long-offset data, because it is insensitive to the phase changes.

Figure 2.1 shows the AVO data extracted from a 3D synthetic dataset computed using reflectivity modeling (Kennett, 1983). The theoretical plane-wave description of this

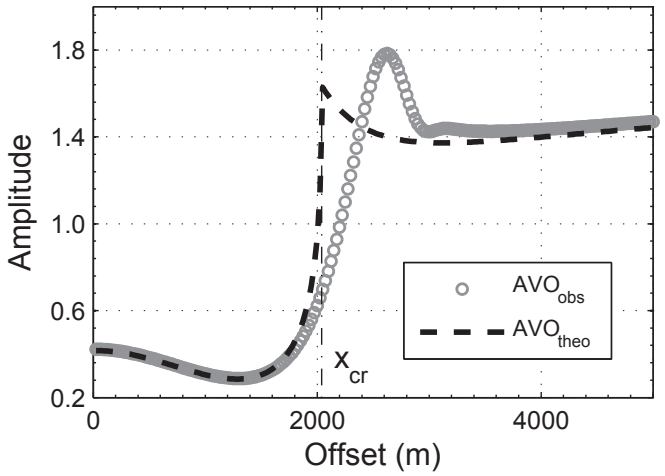

Figure 2.1: AVO data and its theoretical description based on the PWRC.

data is defined by:

$$AVO_{\text{theo}}\left(\mathrm{x}_n\right) = \frac{\left|R_{PP}\left(\theta\left(\mathrm{x}_n,\ \mathbf{m}\right)\right)\right|}{\frac{1}{N}\ \sum_{n=1}^{N}\left|R_{PP}\left(\theta\left(\mathrm{x}_n\right),\ \mathbf{m}\right)\right|}, \tag{2}$$

where $R_{PP}\left(\theta\left(\mathrm{x}_n\right),\ \mathbf{m}\right)$ is the exact PWRC, x_n is the receiver coordinate, $\theta\left(\mathrm{x}_n\right)$ is the reflection angle, $\mathbf{m} = \left(\frac{\rho_2}{\rho_1},\ \frac{V_{P2}}{V_{P1}},\ \frac{V_{S1}}{V_{P1}},\ \frac{V_{S2}}{V_{P2}}\right)$ is a dimensionless parameter vector, as introduced by Petrashen (1957), Lavaud et al. (1999) and Kurt (2007), ρ_1 and ρ_2 are the densities above and below the reflecting interface, V_{P1} and V_{P2} are the P-wave velocities, and V_{S1} and V_{S2} are the S-wave velocities. We observe a good match between the AVO data and the theoretical description only at the pre-critical offsets. The deviation of the plane-wave theoretical description from the AVO data becomes substantial at the near-critical and post-critical offsets. This is explained by the sphericity of the wavefront and the interference of the reflected and head waves near and beyond the critical incidence angle. The dependence of the theoretical plane-wave description in equation 2 on four dimensionless parameters allows unique recovery of a maximum of four parameters, as stated by the Buckingham pi-theorem (Bluman and Kumei, 1989).

A successful AVO inversion implies an adequate theoretical description of the phenomena contained in the AVO data. One way is to apply the $\tau - p$ transform to the data and exploit AVO inversion based on plane-wave reflection coefficients (PWRCs) (Van der Baan and Smit, 2006). Another way is to account for non-planar wave-

fronts by exploiting other reflection coefficients than PWRCs. Effective reflection coefficients (ERCs) represent an alternative to PWRCs for waves generated by point sources (Ayzenberg et al., 2007, 2009).

Although ERCs are valid for curved interfaces and inhomogeneous media, we leave the general ERCs outside the scope of this paper and consider only the particular case of plane interfaces. For a particular case of spherical incident waves, plane reflectors and homogeneous media, ERCs are similar to the spherical-wave reflection coefficients introduced by Ursenbach et al. (2007). The difference is that the former are defined at the interface and the latter are defined at the receiver point. Moreover, ERCs do not depend on the wavelet form unlike the spherical-wave reflection coefficients. Taking into account the potential of extending ERCs to curved interfaces and arbitrary shapes of wavefronts, we exploit them to introduce long-offset AVO inversion.

2.3.1 Effective reflection coefficients for PP-waves

The PP-wave ERC for a horizontal plane interface between two homogeneous elastic halfspaces is defined as (Ayzenberg et al., 2009)

$$\chi_{PP}\left[\theta\left(\mathrm{s}_n\right),\ k_P\, r^*_{PP}\left(\mathrm{s}_n\right),\ \mathbf{m}\right] = \frac{u^*_{PP\,\mathrm{norm}}\left(\mathrm{s}_n\right)\cos\theta\left(\mathrm{s}_n\right) + u^*_{PP\,\mathrm{tan}}\left(\mathrm{s}_n\right)\sin\theta\left(\mathrm{s}_n\right)}{\left[\frac{i}{k_P r^*_{PP}(\mathrm{s}_n)} - \frac{1}{k_P^2 r^{*2}_{PP}(\mathrm{s}_n)}\right] e^{ik_P r^*_{PP}(\mathrm{s}_n)}}, \quad (3)$$

where $\mathrm{s}_n = (s_{1n},\ s_{2n})$ is the reflection point, $k_P = \omega/V_{P1}$ is the wavenumber in the overburden, $r^*_{PP}\left(\mathrm{s}_n\right)$ is the apparent radius of the wavefront at the reflection point, $\theta\left(\mathrm{s}_n\right)$ is the incidence angle, $u^*_{PP\,\mathrm{norm}}\left(\mathrm{s}_n\right)$ and $u^*_{PP\,\mathrm{tan}}\left(\mathrm{s}_n\right)$ are the dimensionless normal and tangential components of the displacement vector. A general form of the radius $r^*_{PP}\left(\mathrm{s}_n\right)$ is introduced by Ayzenberg et al. (2007). For plane interfaces between homogeneous media, $r^*_{PP}\left(\mathrm{s}_n\right)$ reduces to the distance $l\left(\mathrm{s}_n\right)$ between the source and the reflection point. The components of the dimensionless displacement vector have the following form:

$$\begin{aligned} u^*_{PP\,\mathrm{norm}}\left(\mathrm{s}_n\right) &= -\int_0^{+\infty} R_{PP}\left(\zeta,\ \mathbf{m}\right) e^{i\,\alpha(\mathrm{s}_n)\sqrt{1-\zeta^2}} J_0\left[\beta\left(\mathrm{s}_n\right)\zeta\right]\zeta d\zeta, \\ u^*_{PP\,\mathrm{tan}}\left(\mathrm{s}_n\right) &= -\int_0^{+\infty} R_{PP}\left(\zeta,\ \mathbf{m}\right) \frac{i e^{i\,\alpha(\mathrm{s}_n)\sqrt{1-\zeta^2}}}{\sqrt{1-\zeta^2}} J_1\left[\beta\left(\mathrm{s}_n\right)\zeta\right]\zeta^2 d\zeta, \end{aligned} \quad (4)$$

where $R_{PP}\left(\zeta,\ \mathbf{m}\right)$ is the exact PWRC, $\alpha\left(\mathrm{s}_n\right) = k_P r^*_{PP}\left(\mathrm{s}_n\right)\cos\theta\left(\mathrm{s}_n\right)$, $\beta\left(\mathrm{s}_n\right) = k_P r^*_{PP}\left(\mathrm{s}_n\right)\sin\theta\left(\mathrm{s}_n\right)$, ζ is the horizontal component of the unit P-wave ray vector in the overburden, J_0 and J_1 are the Bessel functions of the zeroth and first orders.

We observe that because of the plane-wave decomposition in equations 3 and 4, the plane waves belonging to the Fresnel zone of the reflection point contribute to the ERC in formula 3 at this reflection point. ERCs thus represent a generalization of PWRCs for waves with the wavefronts other than plane.

In contrast to PWRC, equations 3 and 4 depend on an additional dimensionless argument $k_P\, r^*_{PP}(\mathrm{s}_n) = \frac{\omega_0 r^*_{PP}(0)}{V_{P1}}\, \frac{\omega}{\omega_0}\, \frac{r^*_{PP}(\mathrm{s}_n)}{r^*_{PP}(0)}$, where ω_0 is the dominant frequency. The argument is a hyperbolic function of offset and has a minimum at zero offset. It describes the frequency and wavefront curvature dependence of the ERC. Depending on the value of $k_P\ r^*_{PP}(0)$, we distinguish three domains: a near-field domain ($<$ 1), a transition zone (1-10), and a far-field domain ($>$ 10). Assuming a seismic frequency range of 8-60 Hz, an interface depth range of 1-4 km, P-wave velocity in the overburden of 2 km/s, we estimate that $k_P\, r^*_{PP}(0)$ at zero offset changes from 25 to 750. The values of $k_P\, r^*_{PP}(\mathrm{s}_n)$ increase with increasing offset.

Figure 2.2 shows the effect of $k_P\, r^*_{PP}(\mathrm{s}_n)$ on the amplitude and phase of the ERC. The P-wave velocities in upper and lower layers are 2.0 km/s and 2.8 km/s, the values of $k_P\ r^*_P(0)$ are 25 and 400, which are equivalent to interface depths of 1 km and frequencies of 8 Hz and 128 Hz or frequency of 32 Hz and interface depths of 240 m and 4 km. Comparison of the ERC with the corresponding PWRC shows that the frequency and wavefront curvature affects the amplitude and phase of the ERC mostly at the near-critical and post-critical offsets. Although $k_P\ r^*_{PP}(0)$ belongs to the far-field domain, we still observe its effect at the pre-critical offsets, where the phase deviates from zero. The difference between the ERC and the PWRC decreases for larger $k_P\ r^*_{PP}(0)$, which is equivalent to higher frequencies or smaller wavefront curvatures. However, the ERC will still oscillate in the post-critical domain even for unrealistically large values of $k_P\, r^*_{PP}(0)$. ERCs describe the interference between the reflected and head wave around the critical angle and are thus convenient for AVO inversion in the interference domain.

Argument $k_P\, r^*_{PP}(\mathrm{s}_n)$ depends on the velocity, frequency and wavefront curvature. It is therefore impossible to discriminate between the three parameters in the absence of additional information. To illustrate the sensitivity of ERCs and PWRCs to the model parameters, we compute their normalized partial derivatives for a model with the following parameters; $V_{P1} = 2000$ m/s, $V_{S1} = 1100$ m/s, $\rho_1 = 1800$ kg/m^3 in the overburden and $V_{P2} = 2800$ m/s, $V_{S2} = 1600$ m/s, $\rho_2 = 2100$ kg/m^3 in the underburden. The differences between the normalized derivatives of the ERC calculated for an interface at a depth of 1 km and frequencies of 8, 32 and 128 Hz and the

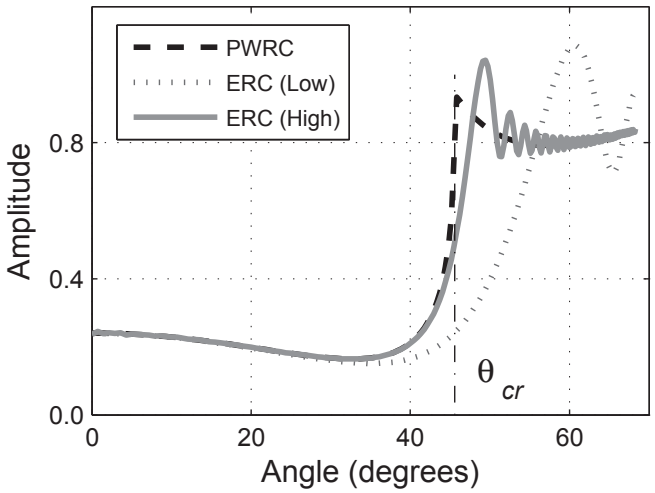

(a)

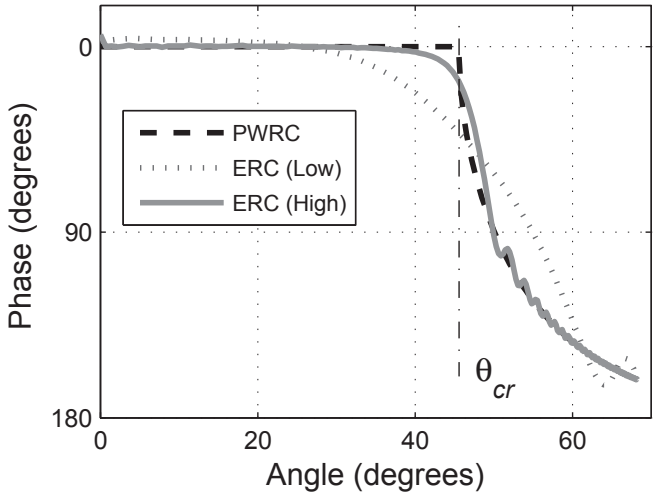

(b)

Figure 2.2: ERC as function on the incidence angle for $k_P\, r_P^*(0) = 402$ (High) and $k_P\, r_P^*(0) = 25$ (Low): (a) Amplitude; (b) Phase. PWRC is shown for comparison.

corresponding PWRC are plotted in Figure 2.3. Figure 2.3a predicts a high sensitivity at the near-critical and post-critical offsets. Each panel represents the change in one parameter while the other parameters are set to the true model parameters. A larger difference between the derivatives means a more accurate estimate of the

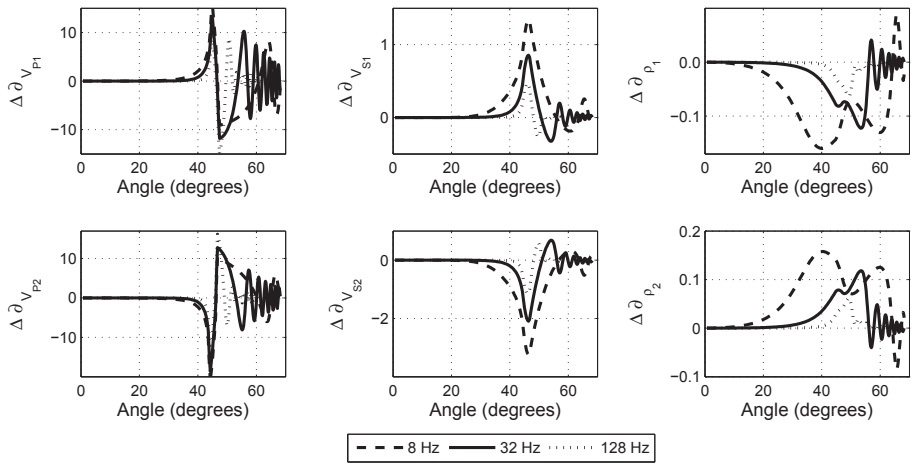

(a)

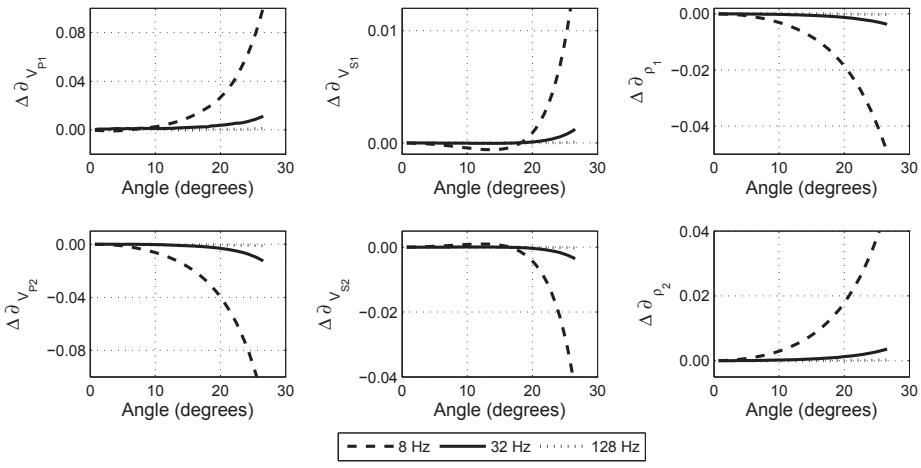

(b)

Figure 2.3: (a) Difference in sensitivity curves between the ERC and the PWRC; (b) Zoom of Figure (a) for an angle range of $0 - 30^0$. Each panel shows the sensitivity to one parameter while the rest of the parameters are set to the true model parameters. The ERC is calculated for frequencies 8, 32 and 128 Hz and an interface depth of 1 km.

respective parameter. The highest sensitivity is observed for the P-wave velocities. This confirms a common understanding that the P-wave velocity can be accurately inverted for. The least accuracy is expected for densities. We notice also that the

ERC is more sensitive to the P-wave and S-wave velocities in the lower layer than in the upper layer. The differences becomes smaller with increasing frequency. Figure 2.3b is the zoom of Figure 2.3a at the pre-critical offsets. We observe that the difference between the derivatives of the ERC and PWRC is not zero and increases with decreasing frequency, which indicates that the results of the ERC-based and the PWRC-based AVO inversion will be different even at the pre-critical offsets. We observe a generally higher sensitivity of the ERC to the P-wave velocities, while the sensitivity to the other parameters is somewhat lower.

According to the Buckingham pi-theorem (Bluman and Kumei, 1989), we can theoretically recover five parameters from an ERC-based AVO inversion, because ERC depends on five dimensionless parameters $\frac{\rho_2}{\rho_1}$, $\frac{V_{P2}}{V_{P1}}$, $\frac{V_{S1}}{V_{P1}}$, $\frac{V_{S2}}{V_{P2}}$, $\frac{\omega_0\, r^*_{PP}(0)}{V_{P1}}$. Assuming the dominant frequency and the $r^*_{PP}(0)$ in last parameter to be known, we can decouple and resolve all four velocities V_{P1}, V_{S1}, V_{P2}, V_{S2}. Densities can be decoupled only if one of them is available.

2.4 Long-offset AVO inversion

2.4.1 Approximate description of a single reflection at the receiver

Ayzenberg et al. (2009) have shown that the reflected seismic wavefield at a curved interface can be approximately described in terms of ERCs. Skopintseva et al. (2007) have numerically verified that the P-wave reflected at a plane interface can be described in terms of ERCs both at the interface and at the receiver. We derive a seismic-frequency approximation of the reflected P-wave at the receiver in terms of the ERC and show that it has a form convenient for AVO studies (Appendix 2.9):

$$\mathbf{u}_{PP}\left(\mathrm{x}_n,\,\omega\right) \cong \chi_{PP}\left[\mathrm{x}_n,\,\omega\right]\,\frac{i}{V_{P\,1}}\,S\left(\omega\right)\frac{e^{i\,k_P\,l(\mathrm{x}_n)}}{\sqrt{J_{PP}\left(\mathrm{x}_n\right)}}\,\mathbf{e}_{PP}\left(\mathrm{x}_n\right) \tag{5}$$

where $\chi_{PP}\left[\mathrm{x}_n,\,\omega\right] = \chi_{PP}\left[\theta\left(\mathrm{x}_n\right),\,k_P\,r^*_{PP}\left(\mathrm{x}_n\right),\,\mathbf{m}\right]$ is the ERC defined at the receiver, $l\left(\mathrm{x}_n\right) = l\left(\mathrm{x}_n,\,\mathrm{s}_n\right) + l\left(\mathrm{s}_n\right)$ is the distance between the source and receiver x_n along the ray, $l\left(\mathrm{x}_n,\,\mathrm{s}_n\right)$ is the distance between the reflection point and the receiver, $l\left(\mathrm{s}_n\right)$ is the distance between the source and the reflection point, $J_{PP}\left(\mathrm{x}_n\right) = \left[l\left(\mathrm{x}_n\right)\right]^2$ is the geometrical spreading of the reflected P-wave, $S\left(\omega\right)$ is the wavelet spectrum, $\mathbf{e}_{PP}\left(\mathrm{x}_n\right)$ is the polarization vector of the reflected P-wave. Equation 11 resembles the wavefield

representation from asymptotic ray theory, where the PWRC is substituted by the ERC at the receiver. Extrapolation of the ERC from the interface to the receiver is performed with help of the relation $r^*_{PP}(\mathrm{x}_n) = r^*_{PP}(\mathrm{s}_n)\,[1 + l(\mathrm{x}_n,\ \mathrm{s}_n)\,/l(\mathrm{s}_n)]$.

Equation 11 in the time domain has the following form:

$$\mathbf{U}_{PP}(\mathrm{x}_n, t) \cong \frac{i}{V_{P1}} \frac{\mathbf{e}_{PP}(\mathrm{x}_n)}{\sqrt{J_{PP}(\mathrm{x}_n)}} \int_{-\infty}^{+\infty} \chi_{PP}[\mathrm{x}_n,\ \omega]\, S(\omega)\ e^{i\{k_P l(\mathrm{x}_n) - \omega t\}} d\omega, \tag{6}$$

where $\mathbf{U}_{PP}(\mathrm{x}_n, t) = (U_{PPX}(\mathrm{x}_n, t),\ 0,\ U_{PPZ}(\mathrm{x}_n, t))$ is the displacement vector, and $\mathbf{e}_{PP}(\mathrm{x}_n) = (\sin\theta(\mathrm{x}_n),\ 0,\ \cos\theta(\mathrm{x}_n))$ is the polarization vector.

2.4.2 Band-limited AVO data and its theoretical description

We further consider the pre-processed AVO data, where the geometrical spreading is removed:

$$\begin{aligned} \tilde{\mathbf{U}}_{PP}(\mathrm{x}_n,\ t) &= \sqrt{J_{PP}(\mathrm{x}_n)}\ \mathbf{U}_{PP}(\mathrm{x}_n, t), \\ \tilde{\mathbf{u}}_{PP}(\mathrm{x}_n, \omega) &= \sqrt{J_{PP}(\mathrm{x}_n)}\ \mathbf{u}_{PP}(\mathrm{x}_n, \omega). \end{aligned} \tag{7}$$

Based on the property $\tilde{\mathbf{u}}_{PP}(\mathrm{x}_n, -\omega) = \bar{\tilde{\mathbf{u}}}_{PP}(\mathrm{x}_n, +\omega)$ of the spectrum of a real function, we write Parseval's theorem for the reflected wavefield $\tilde{\mathbf{U}}_{PP}(\mathrm{x}_n, t)$ and its spectrum $\tilde{\mathbf{u}}_{PP}(\mathrm{x}_n, \omega)$ (Korn and Korn, 1968):

$$\int_{-\infty}^{\infty} \left[\tilde{U}_{PP\,j}(\mathrm{x}_n, t)\right]^2 dt = 2\int_0^{\infty} \tilde{u}_{PP\,j}(\mathrm{x}_n, \omega)\, \bar{\tilde{u}}_{PP\,j}(\mathrm{x}_n, \omega)\, d\omega, \tag{8}$$

where the bar denotes a complex conjugation, $j = X, Z$ for the $X-$ and $Z-$components of the reflected wavefield $\tilde{\mathbf{U}}_{PP}(\mathrm{x}_n, t) = \left(\tilde{U}_{PPX}(\mathrm{x}_n, t),\ 0,\ \tilde{U}_{PPZ}(\mathrm{x}_n, t)\right)$. The left part of the equation represents the squared RMS value over an infinite time window. We define a finite time window $[t_1(\mathrm{x}_n),\ t_2(\mathrm{x}_n)]$ which follows the moveout of the reflected event. Substituting equation 11 and 7 to 8, we represent the RMS amplitudes for the $X-$ and $Z-$components of the reflected wavefield though the ERC:

$$\begin{aligned} &\left(\int_{t_1(\mathrm{x}_n)}^{t_2(\mathrm{x}_n)} \left[\tilde{U}_{PP\,j}(\mathrm{x}_n, t)\right]^2 dt\right)^{\frac{1}{2}} = \\ &\frac{\sqrt{2}}{V_{P1}} \left|e_{PP\,j}(\mathrm{x}_n)\right| \sqrt{\int_{\omega_{\min}}^{\omega_{\max}} |\,S(\omega)\,|^2\ |\,\chi_{PP}[\mathrm{x}_n,\ \omega]\,|^2\ d\omega}. \end{aligned} \tag{9}$$

Equation 9 incorporates all ERCs whose frequencies are within the frequency range $[\omega_{\min}, \omega_{\max}]$. Moreover, the ERCs are weighted with the amplitude spectrum of the

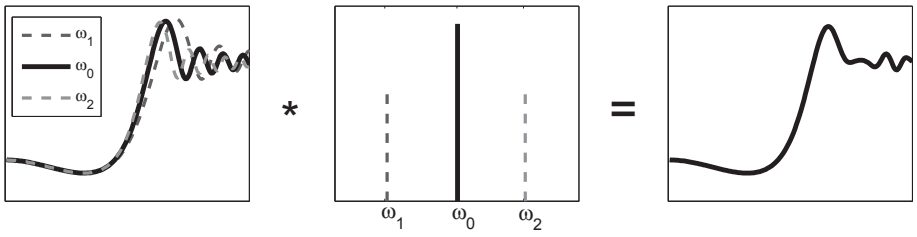

Figure 2.4: A scheme explaining the process of computing the theoretical description of the band-limited AVO data. From left to right: ERCs for three different frequencies, amplitude spectrum of the source wavelet, the result after weighting and averaging.

wavelet. Figure 2.4 shows the effect of weighting for three randomly chosen frequencies of the wavelet. We observe that the main contribution is obtained from the ERC calculated for the dominant frequency ω_0. The ERCs for the neighboring frequencies affect only the oscillations at the post-critical angles. The oscillations are suppressed when a wider frequency range is involved in the weighting.

The factor $\sqrt{2}/V_{P1}$ in equation 9 does not depend on the offset and can be eliminated through a normalizing procedure over the full offset range. Applying the normalizing procedure to the left and right parts of equation 9, we obtain the AVO data and its corresponding theoretical description:

$$
\begin{aligned}
AVO_{\mathrm{obs\,j}}\left(\mathrm{x}_n\right) &= \frac{\left(\int_{t_1(\mathrm{x}_n)}^{t_2(\mathrm{x}_n)} \left[\tilde{U}_{PP\,j}\left(\mathrm{x}_n, t\right)\right]^2 dt\right)^{\frac{1}{2}}}{\frac{1}{N}\ \sum_{n=1}^{N}\left(\int_{t_1(\mathrm{x}_n)}^{t_2(\mathrm{x}_n)} \left[\tilde{U}_{PP\,j}\left(\mathrm{x}_n, t\right)\right]^2 dt\right)^{\frac{1}{2}}} \\
AVO_{\mathrm{theo\,j}}\left(\mathrm{x}_n\right) &= \frac{\left|e_{PP\,j}\left(\mathrm{x}_n\right)\right| \sqrt{\int_{\omega_{\min}}^{\omega_{\max}} \left|\,S\left(\omega\right)\right|^2\ \left|\,\chi_{PP}\left[\mathrm{x}_n,\ \omega\right]\right|^2\ d\omega}}{\frac{1}{N}\ \sum_{n=1}^{N}\left(\left|e_{PP\,j}\left(\mathrm{x}_n\right)\right| \sqrt{\int_{\omega_{\min}}^{\omega_{\max}} \left|\,S\left(\omega\right)\right|^2\ \left|\,\chi_{PP}\left[\mathrm{x}_n,\ \omega\right]\right|^2\ d\omega}\right)},
\end{aligned}
\tag{10}
$$

where $j = X,\ Z$ for the $X-$ and $Z-$components of the reflected P-wave. Based on these equations, AVO inversion can be performed on either component of the reflected

P-wave data. If both components are available, equations 10 can be represented as

$$AVO_{\text{obs}}\left(\mathrm{x}_n\right) = \frac{\left(\int_{t_1(\mathrm{x}_n)}^{t_2(\mathrm{x}_n)} \left[\tilde{U}_{PP}\left(\mathrm{x}_n, t\right)\right]^2 dt\right)^{\frac{1}{2}}}{\frac{1}{N}\ \sum_{n=1}^{N}\left(\int_{t_1(\mathrm{x}_n)}^{t_2(\mathrm{x}_n)} \left[\tilde{U}_{PP}\left(\mathrm{x}_n, t\right)\right]^2 dt\right)^{\frac{1}{2}}}$$
$$AVO_{\text{theo}}\left(\mathrm{x}_n\right) = \frac{\sqrt{\int_{\omega_{\min}}^{\omega_{\max}} |\, S\left(\omega\right)|^2\ |\, \chi_{PP}\left[\mathrm{x}_n,\ \omega\right]|^2\ d\omega}}{\frac{1}{N}\ \sum_{n=1}^{N}\sqrt{\int_{\omega_{\min}}^{\omega_{\max}} |\, S\left(\omega\right)|^2\ |\, \chi_{PP}\left[\mathrm{x}_n,\ \omega\right]|^2\ d\omega}}, \tag{11}$$

where $\tilde{U}_{PP}\left(\mathrm{x}_n\right) = \sqrt{\tilde{U}^2_{PP\,X}\left(\mathrm{x}_n\right) + \tilde{U}^2_{PP\,Z}\left(\mathrm{x}_n\right)}$ is the magnitude of the displacement vector. $AVO_{\text{theo}}\left(\mathrm{x}_n\right)$ in this case does not require computation of the polarization vector.

We note that the theoretical description of the AVO data in equations 10 and 11 requires knowledge about the wavelet spectrum $S\left(\omega\right)$. We find the $X-$ and $Z-$components of the power spectrum of the reflected wavefield in terms of the wavelet spectrum from equations 11 and 7:

$$\left|S^D_j(\mathrm{x}_n, \omega)\right| = \sqrt{\tilde{u}_{PP\,j}\left(\mathrm{x}_n, \omega\right)\bar{\tilde{u}}_{PP\,j}\left(\mathrm{x}_n, \omega\right)} = \frac{\left|e_{PP\,j}\left(\mathrm{x}_n\right)\right|}{V_{P1}}\left|S(\omega)\right|\left|\chi_{PP}\left[\mathrm{x}_n,\ \omega\right]\right|, \tag{12}$$

where $j = X,\ Z$ and $\tilde{\mathbf{u}}_{PP}\left(\mathrm{x}_n, \omega\right) = \left(\tilde{u}_{PP\,X}\left(\mathrm{x}_n, \omega\right),\ 0,\ \tilde{u}_{PP\,Z}\left(\mathrm{x}_n, \omega\right)\right)$.

Figure 2.5 demonstrates the frequency dependence of the ERC magnitude for three chosen offsets corresponding to pre-critical, near-critical and post-critical domains. We observe that the ERC weakly depends on the frequency at the pre-critical offsets, while the frequency dependence becomes more prominent at the near-critical and post-critical offsets. We can therefore exploit the power spectrum $\left|S^D(\mathrm{x}_{pre}, \omega)\right|$ at any pre-critical offset in equations 10 and 12 instead of the wavelet spectrum $\left|S\left(\omega\right)\right|$. This does not affect the result, because of the following relationship:

$$\left|S^D_j(\mathrm{x}_{pre}, \omega)\right| = \frac{\left|e_{PP\,j}\left(\mathrm{x}_{pre}\right)\right|}{V_{P1}}\left|S(\omega)\right|\left|\chi_{PP}\left[\mathrm{x}_{pre},\ \omega\right]\right| \approx C\left|S(\omega)\right|, \tag{13}$$

where C is a constant which is eliminated through a normalization procedure. The power spectrum of the data can only serve as a proxy for the spectrum of the wavelet if there is no significant frequency dependence in the ERC at the pre-critical offsets. This may be not the case in attenuative media.

Because the considered AVO data includes all frequencies present in the reflected wavefield, we refer to $AVO_{\text{obs}}\left(\mathrm{x}_n\right)$ and $AVO_{\text{theo}}\left(\mathrm{x}_n\right)$ as the band-limited AVO data and its theoretical description, respectively.

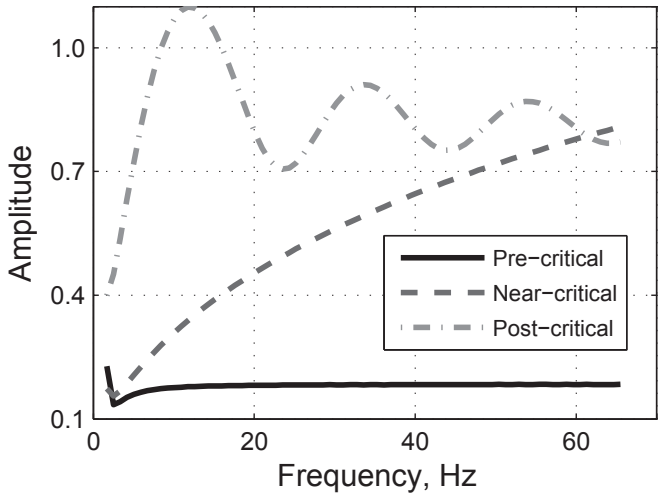

Figure 2.5: ERC as function of frequency for pre-critical, near-critical and post-critical offsets.

2.4.3 Single-frequency AVO data and its theoretical representation

An alternative way to obtain AVO data from the surface seismic data is based on equation 12. Applying the normalization procedure to the left and right parts of equation 12, we obtain the representation of the AVO data for each component of the reflected wavefield and their theoretical description in the frequency domain:

$$\begin{aligned} AVO_{\text{obs j}}\left(\mathrm{x}_n,\ \omega\right) &= \frac{\sqrt{\tilde{u}_{PP\,j}\left(\mathrm{x}_n,\omega\right)\bar{\tilde{u}}_{PP\,j}\left(\mathrm{x}_n,\omega\right)}}{\frac{1}{N}\ \sum_{n=1}^{N}\sqrt{\tilde{u}_{PP\,j}\left(\mathrm{x}_n,\omega\right)\bar{\tilde{u}}_{PP\,j}\left(\mathrm{x}_n,\omega\right)}} \\ AVO_{\text{theo j}}\left(\mathrm{x}_n,\ \omega\right) &= \frac{\left|e_{PP\,j}\left(\mathrm{x}_n\right)\right|\left|\chi_{PP}\left[\mathrm{x}_n,\ \omega\right]\right|}{\frac{1}{N}\ \sum_{n=1}^{N}\left|e_{PP\,j}\left(\mathrm{x}_n\right)\right|\left|\chi_{PP}\left[\mathrm{x}_n,\ \omega\right]\right|}. \end{aligned} \tag{14}$$

Similarly to equation 11, equation 14 can be rewritten in terms of displacements $\tilde{u}_{PP}\left(\mathrm{x}_n,\omega\right)=\sqrt{\tilde{u}^2_{PP\,X}\left(\mathrm{x}_n,\omega\right)+\tilde{u}^2_{PP\,Z}\left(\mathrm{x}_n,\omega\right)}$ in the frequency domain:

$$\begin{aligned} AVO_{\text{obs}}\left(\mathrm{x}_n,\ \omega\right) &= \frac{\sqrt{\tilde{u}_{PP}\left(\mathrm{x}_n,\omega\right)\bar{\tilde{u}}_{PP}\left(\mathrm{x}_n,\omega\right)}}{\frac{1}{N}\ \sum_{n=1}^{N}\sqrt{\tilde{u}_{PP}\left(\mathrm{x}_n,\omega\right)\bar{\tilde{u}}_{PP}\left(\mathrm{x}_n,\omega\right)}} \\ AVO_{\text{theo}}\left(\mathrm{x}_n,\ \omega\right) &= \frac{\left|\chi_{PP}\left[\mathrm{x}_n,\ \omega\right]\right|}{\frac{1}{N}\ \sum_{n=1}^{N}\left|\chi_{PP}\left[\mathrm{x}_n,\ \omega\right]\right|}. \end{aligned} \tag{15}$$

AVO data from equations 14 and 15 can be obtained for an arbitrary frequency within the range $[\omega_{\min},\omega_{\max}]$. This gives us the freedom to extract AVO data from

the reflected wavefield for particular frequencies. The theoretical description of AVO data is simpler, as it does not require any knowledge about the wavelet spectrum. It can be interpreted as a normalized ERC. The absence of integration allows to reduce the computational cost of the AVO inversion.

We refer to $AVO_{\text{obs}}(\mathrm{x}_n, \omega)$ and $AVO_{\text{theo}}(\mathrm{x}_n, \omega)$ as the single-frequency AVO data and its theoretical description.

2.5 AVO inversion of long-offset synthetic data

To test the described AVO inversion approach, we use a 3D long-offset synthetic PP data obtained from elastic reflectivity modeling. The tests are carried out for two models with a flat horizontal interface between two homogeneous isotropic halfspaces. We generate the seismograms for the X- and Z-components. For simplicity we consider common-shot gathers, which in the case of a plane interface are equivalent to CDP gathers with half the distance between the source and the receivers. The source and receiver array are located at the surface. The receiver sampling is 25 m.

We exploit an omni-directional source with the wavelet $S(t) = -\frac{\partial}{\partial t}\exp^{-((2\pi f t)/\pi)^2}\sin(2\pi f t)$, where t is time and $f = \omega/2\pi$ is the linear frequency. The wavelet has an amplitude spectrum $S(f)$ with a bell-like envelop, the frequencies ranging from $f_{\min} = 3$ Hz to $f_{\max} = 62$ Hz, and a dominant linear frequency of 39 Hz.

2.5.1 Model 1

The first test is performed for an interface located 1 km below the source. The upper half-space is described by the parameters $V_{P1} = 2000$ m/s, $V_{S1} = 1100$ m/s, $\rho_1 = 1800$ kg/m^3, and the lower half-space is described by the parameters $V_{P2} = 2800$ m/s, $V_{S2} = 1600$ m/s, $\rho_2 = 2100$ kg/m^3. The critical angle for this model is equal to 45.6^0, and the critical offset is $\mathrm{x}_{cr} = 2041$ m. The offsets vary from 0 m to 5000 m and cover pre-critical, near-critical and post-critical reflections.The value of argument $k_P\ r^*_{PP}(\mathrm{x}_n)$ at minimal frequency 3 Hz changes from 18 at zero offset to 60 at offset 5000 m, respectively. The value of this argument at maximal frequency 60 Hz changes from 584 at zero offset to 1246 at offset 5000 m, respectively. The argument $k_P\ r^*_{PP}(\mathrm{x}_n)$ at dominant frequency of 39 Hz changes from 245 to 784 at

zero and maximum offsets, respectively.

The seismogram of the Z-component obtained by reflectivity modelling is shown in Figure 2.6a. We observe a significant amplitude increase at the offsets above 2000 m. A weak head wave is present on the seismogram and separates from the reflected wave at long offsets. The amplitude of the wavelet spectrum is shown in Figure 2.6b.

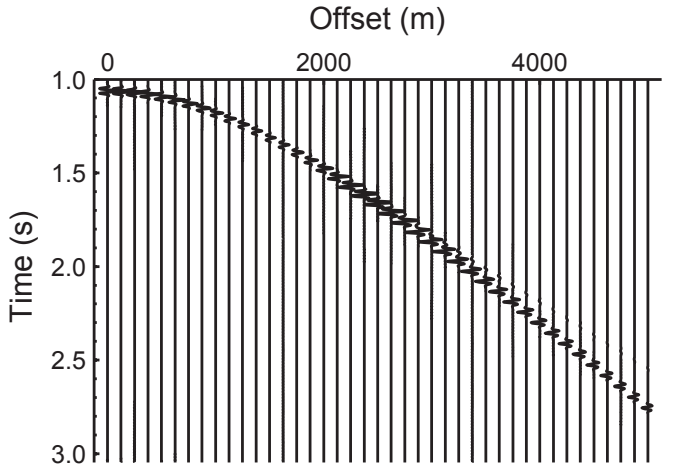

(a)

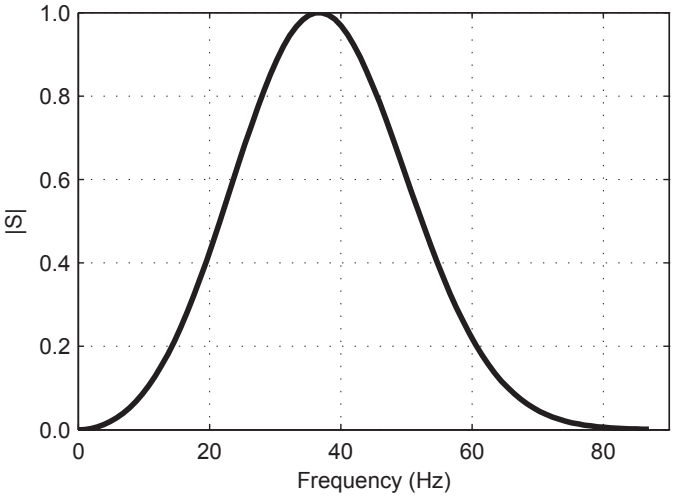

(b)

Figure 2.6: (a) Z-component of the reflected P-wave obtained from the reflectivity modeling; (b) Wavelet spectrum.

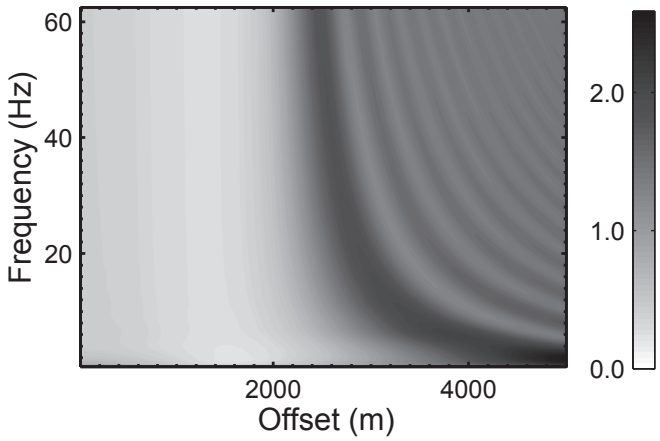

Figure 2.7: Single-frequency AVO data.

AVO data and its theoretical representation

To obtain the band-limited AVO data, we apply the first equation in 11 to the $X-$ and $Z-$components of the data compensated for the geometrical spreading.

To obtain the single-frequency AVO data, we apply the temporal Fourier transform to the X- and Z-components of the seismogram corrected for the geometrical spreading and use the first equation in 15. Figure 2.7 shows the single-frequency AVO data for all frequencies contained in the wavelet spectrum. The effect of the critical angle becomes prominent for the offsets above 2000 m. The rapid oscillations at the post-critical offsets are explained by the interference of the reflected and head waves. Moreover, we observe that the position of the amplitude maximum at the post-critical offsets depends on the frequency and tends to the critical offset with increasing frequency, while the amplitude at the pre-critical offsets is close to being frequency-independent.

Figure 2.8 shows the slice of the single-frequency AVO data for a frequency of 32 Hz, the band-limited AVO data and the corresponding theoretical descriptions calculated for the true model parameters. The ERC-based theoretical descriptions are obtained from the second equations in 15 and 11. In equation 15, we assume that the wavelet spectrum $|S(\omega)|$ is unknown and use the amplitude spectrum $\left|S^D(\mathrm{x}_{pre},\omega)\right|$ from the data at a pre-critical offset of 1500 m. We show also the PWRC-based theoretical description (equation 2) for comparison.

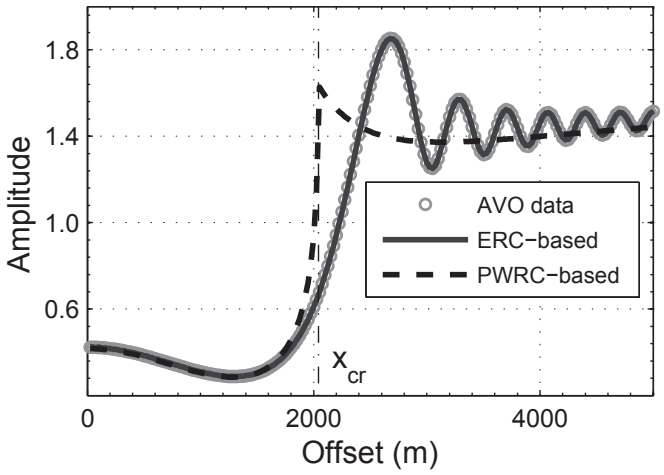

(a)

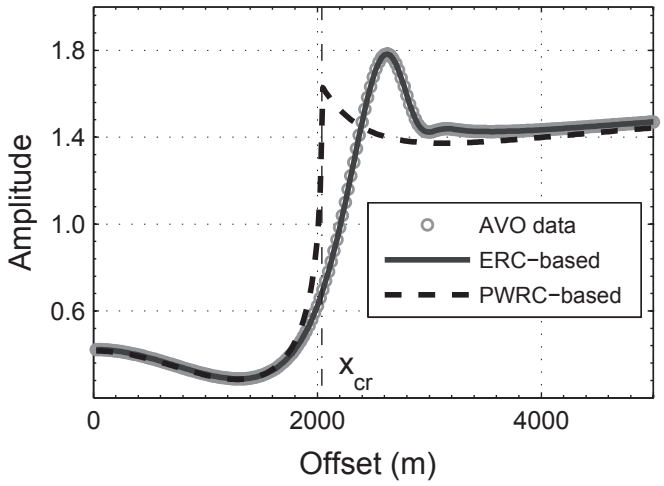

(b)

Figure 2.8: AVO data and their theoretical descriptions calculated for the true model parameters. (a) Single-frequency AVO data for 32 Hz (circles), ERC-based single-frequency theoretical description for 32 Hz (solid line) and PWRC-based theoretical description (dashed line); (b) Band-limited AVO data (circles), ERC-based band-limited theoretical description (solid line) and PWRC-based theoretical description (dashed line).

The single-frequency AVO data exhibits strong oscillations at the post-critical offsets, whereas such oscillations are absent in the band-limited AVO data because of the averaging over frequencies, as illustrated in Figure 2.4. The ERC-based theoretical description resembles the AVO data at all offsets, whereas the PWRC-based description coincides with the AVO data only at the pre-critical offsets and substantially deviates from it at the near-critical and post-critical offsets. Based on this observation, we may expect that the PWRC-based inversion will produce similar level of errors in parameter estimates to the ERC-based inversion at pre-critical offsets. At the same time, we expect a different behavior of errors with offset due to $k_P\ r^*_{PP}(\mathrm{x}_n)$, which enhances the sensitivity of the ERC to media parameters compared to the PWRC. We may expect that the ERC-based inversion will outperform the PWRC-based inversion at the near-critical and post-critical offsets.

Analysis of the objective functions

We examine the shape of the objective functions in order to understand the potential of the ERC-based and PWRC-based AVO inversions for parameter recovery at different offset ranges.

Figure 2.9 shows 2D cross-plots of the objective function $F(\mathbf{v})$ (equation 1), where we vary only two parameters while the rest are set to the true model parameters. The deviation of varying parameters from their true value is $\pm 20\%$. The first two columns represent maps of $F(V_{P1},\ \rho_1)$ and $F(V_{S2},\ \rho_1)$ computed from the ERC-based band-limited AVO data and the band-limited theoretical description. The last two columns show the same maps computed from the single-frequency AVO data and its ERC-based theoretical description (equation 15). The first row represents the maps computed for the pre-critical offset range $0-1500$ m $(0-36^0)$, whereas the second one shows the maps computed for the full offset range $0-5000$ m $(0-68^0)$. The circles denote the minimum of the objective function, while the squares indicate the true model parameters.

We observe that the behavior of the objective functions is different for the pre-critical and the full offset ranges. The objective function does not have well defined minima for the pre-critical offset range, whereas they become more isometric with increasing offset range. This is explained by the different sensitivity of the ERC to parameters at different offsets ranges. Stronger amplitudes at long offsets contribute more to the objective functions. We observe also that all the functions are most uncertain in the ρ_1-direction. This may result in higher uncertainties of the density estimates.

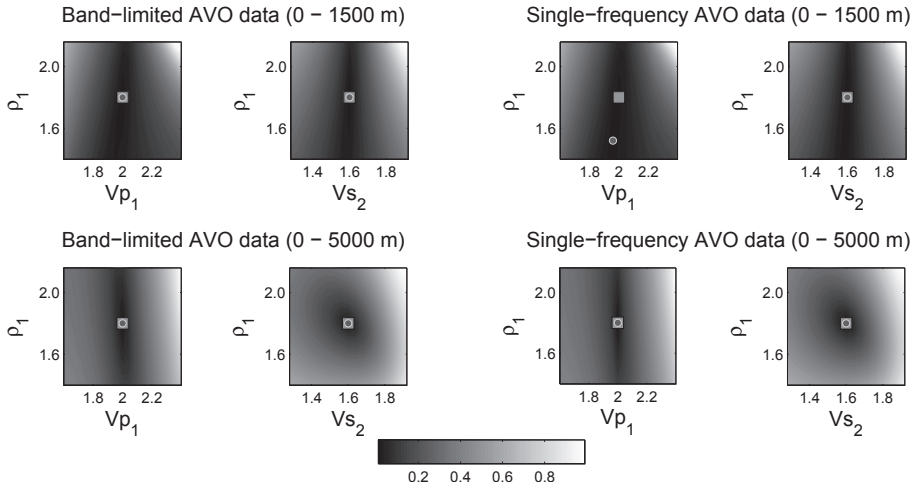

Figure 2.9: Cross-sections of the ERC-based objective functions. The band-limited and single-frequency theoretical descriptions are used for evaluation of the band-limited and single-frequency AVO data. Squares denote true model parameters and circles denote minima of the objective functions.

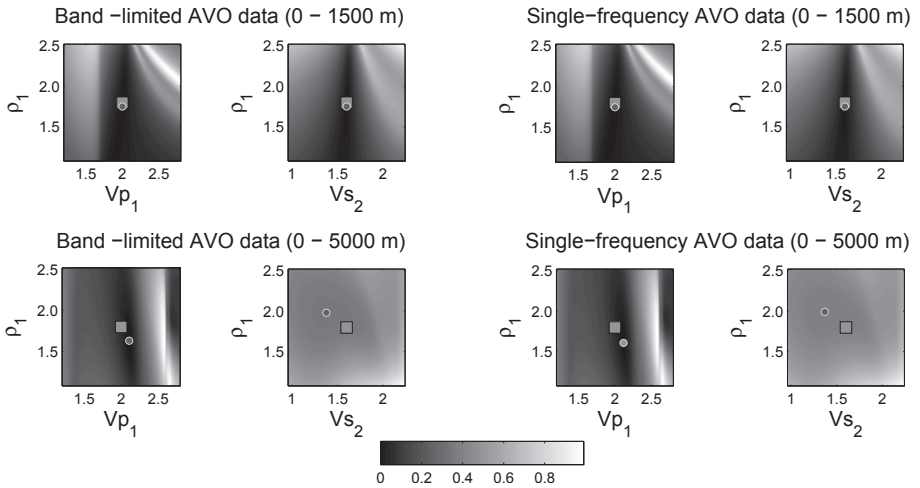

Figure 2.10: Cross-sections of the PWRC-based objective functions. The PWRC-based theoretical description is used for evaluation of the band-limited and single-frequency AVO data. Squares denote true model parameters and circles denote minima of the objective functions.

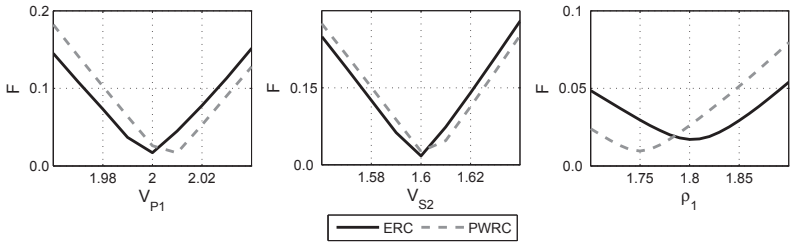

Figure 2.11: 1D cross-sections of the objective functions based on the ERC and the PWRC. The objective functions are calculated for the band-limited AVO data at pre-critical offset range (0-1500 m).

The objective functions are V-shaped and stretched in the ρ_1-direction for the pre-critical offsets. The minima of the objective functions coincide with the true model parameters on almost all the maps, except for the $F\left(V_{P1},\ \rho_1\right)$ for the single-frequency AVO data, where the deviation in the V_{P1}-direction is less than in the ρ_1-direction. This can probably be explained by the computational errors in the data at short offsets. We do not observe significant deviations for the band-limited case, because the band-limited theoretical data AVO_{theo} is more robust to the computational errors because of averaging over frequencies. Such behavior of the objective functions and the deviation of the minima may lead to unstable inversion results at the pre-critical offsets. We also expect more accurate results from the band-limited AVO inversion than from the single-frequency AVO inversion. The objective functions for the full offset range exhibit a good fit between the minima of the objective functions and the true model parameters. We therefore claim that the near-critical and post-critical offsets will increase the accuracy of parameter estimation.

We additionally analyze maps of the objective functions $F\left(V_{P1},\ \rho_1\right)$ and $F\left(V_{S2},\ \rho_1\right)$ evaluated using the PWRC-based theoretical description instead of the band-limited and single-frequency descriptions (Figure 2.10). The deviation of varying parameters from their true value is $\pm 40\%$. In this case, we observe a more complex behavior of the objective functions than those in Figure 2.9. The misfits between the minima of the objective functions and the true model parameters at the pre-critical offsets are explained by the wavefront curvature present in the data while it is not accounted for in the PWRC-based theoretical description. This will lead to less accurate parameter estimates. We observe also that incorporation of the near-critical and post-critical offsets does not improve the shapes of the objective functions. There are still significant deviations of the positions of the minima from the true model parameters.

Figure 2.11 compares the ERC-based and the PWRC-based one-dimensional objective functions for band-limited AVO data in the vicinity of their minimum. The computation is carried out for a pre-critical offset range of 0-1500 m. Despite the fact that the amplitudes of the ERC and the PWRC are almost equal, we observe that the PWRC-based objective function is asymmetric and its minimum is shifted from the true value. This confirms that the ERC-based and the PWRC-based AVO inversions will perform differently even at the pre-critical offsets.

AVO inversion results

To include post-critical offsets in the inversion, we use the exact reflection coefficients (ERCs or PWRCs), which imply nonlinear inversion methods. Among the existing optimization methods, we chose the nonlinear optimization method of Nelder-Mead for minimizing the objective function in equation 1 (Himmelblau, 1972). The method is computationally simple and effective, because it does not require calculation of partial derivatives. However, we need to provide an initial guess for the estimated parameters. A good starting model ensures fast convergence of the inversion to the final result. An initial guess is typically obtained from the low-frequency velocity trends and rock-physical relationships. In our case the objective function has only one minimum for the parameter deviation within 20%. The initial guess can therefore belong to this range.

We carried out AVO inversion for offset ranges varying from 0-250 m to 0-5000 m with an increment of 250 m. We allowed for a 20% variation in the estimated parameters. The initial guess deviates by 15% from the true model parameters. Figure 2.12 illustrates the results of the single-frequency ERC-based AVO inversion, where we invert for the five parameter vector $\mathbf{v} = (V_{P1},\ V_{S1},\ V_{P2},\ V_{S2},\ \rho_1)$ assuming the density ρ_2 in the underburden to be known. The inversion results are plotted as functions of the offset range. As expected, we see that increase in the offset range generally improves the inversion results. All the parameters are estimated more accurately when the post-critical offsets are involved in the inversion. The best accuracy is achieved for the P-wave velocities and the density ρ_1, while the S-wave velocities are less accurate. At pre-critical offset ranges (until 2000 m), the S-wave velocity and P-wave velocity in the underburden and density are estimated better than the other two parameters. The accuracy of V_{P2} is higher than the accuracy of V_{P1} at the pre-critical offsets, whereas the accuracy of their estimates is approximately the same at the post-critical offsets.

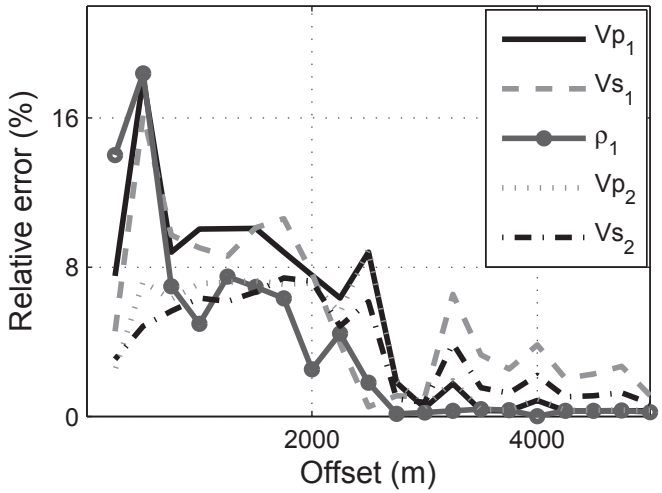

Figure 2.12: Relative errors in the five-parameter single-frequency (32 Hz) ERC-based AVO inversion for Model 1 as function of offset range.

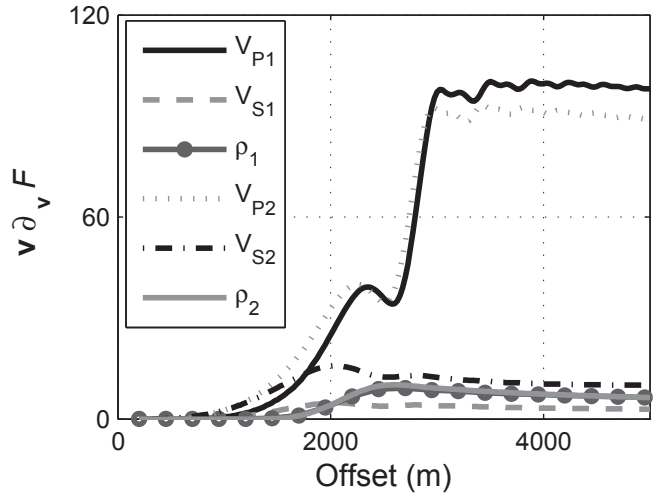

Figure 2.13: Normalized derivatives of the single-frequency ERC-based objective function with respect to the model parameters for different offset ranges. A higher value of the derivative with respect to a parameter corresponds to a higher sensitivity of the objective function to this parameter.

We illustrate the sensitivity of the objective function for the single-frequency AVO inversion to the model parameters by showing its normalized derivatives at different offset ranges (Figure 2.13). A larger derivative is associated with a better estimate of the inverted parameter. We observe that the derivatives with respect to V_{S2} and V_{P2} at short offset ranges forecast an accurate estimate of these parameters. The rapid increase of the derivative with respect to V_{P1} and V_{P2} at the near-critical and post-critical offsets confirms the ability of the inversion to resolve the P-wave velocities better than other parameters. The sensitivity to the densities becomes larger than the sensitivity to V_{S1} when the post-critical offsets are included in the computation. This indicates that the post-critical offsets contain additional information about the densities. These observations correlate well with the inversion results in Figure 2.12.

We additionally observe a zone between 2000 - 3000 m, where the relative behavior between the derivative curves changes and the objective function is almost equally sensitive to both P-wave velocities. This area corresponds to a local drop in the quality of estimated parameters (Figure 2.12). We observe that in this particular interval there is a strong correlation between the sensitivities to the two P-wave velocities. Although the Buckingham pi-theorem states that five parameters can be retrieved from the ERC-based inversion, the uniqueness of the five-parameter inversion for this particular interval is questionable and requires further study. Figure 2.13 explains some of the inversion results. However, it does not provide a full picture, because a nonlinear inversion is a nontrivial search for the minimum of a multidimensional objective function.

To demonstrate the improvement in the results obtained from the ERC-based AVO inversion, we compare it with the PWRC-based AVO inversion. We perform four-parameter inversions because the PWRC-based AVO inversion allows recovery of only four parameters (Lavaud et al., 1999). We assume V_{P2} and ρ_2 to be known and recover the parameter vector $\mathbf{v} = (V_{P1}, V_{S1}, \rho_1, V_{S2})$.

Figure 2.14 illustrates the results of the four-parameter ERC-based AVO inversion as a function of the offset range. Figures 2.14a and 2.14b correspond to the single-frequency and the band-limited AVO inversions. We observe that in both cases the accuracy of parameter estimation generally increases with increasing offset range. The results obtained at the pre-critical offset ranges are least accurate and least stable, in particular because of the short offsets and numerical errors. When proceeding from the pre-critical offsets to the near-critical offsets, the accuracy of all estimated parameters increases. We observe an increase in the error in the estimated S-wave

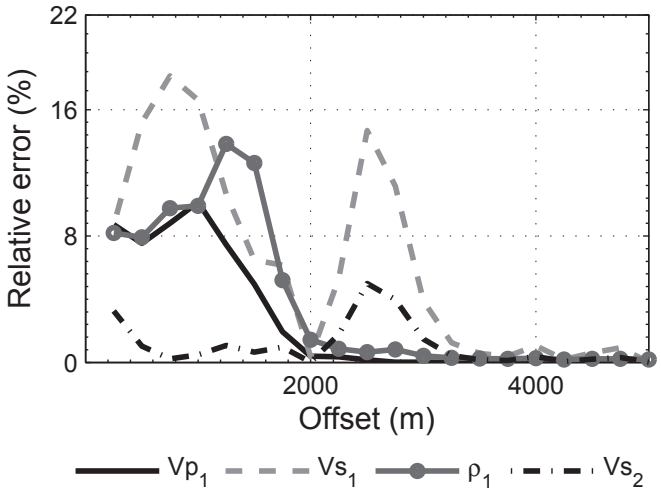

(a)

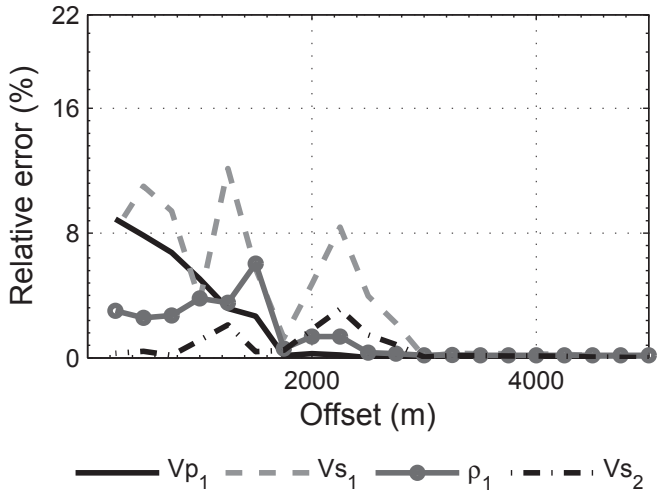

(b)

Figure 2.14: Relative errors in the four-parameter AVO inversion as function of the offset range for Model 1. (a) ERC-based single-frequency AVO inversion for 32 Hz; (b) ERC-based band-limited AVO inversion.

velocities an offset range of 2000-3000 m. The effect weakens outside this zone. This is well correlated with the local minima and maxima observed in Figure 2.13. The P-wave velocity estimate appears to be most accurate and robust at the near-critical

and post-critical offsets. The estimated S-wave velocities exhibit similar trends, but a somewhat lower accuracy. The lowest accuracy is achieved for the S-wave velocity V_{S1} in the overburden. The density estimates appear to be surprisingly good, in particular when the near-critical and post-critical offsets are included in the inversion.

Taking into account that the synthetic data contain numerical errors, we obtain an insight into the sensitivity of the ERC-based AVO inversion to the irregular noise. We observe from Figures 2.14a and 2.14b that the errors in the single-frequency AVO inversion at the pre-critical offsets are larger than those for the band-limited AVO inversion. It indicates that the latter inversion is more robust to irregular noise than the former. However, the band-limited AVO inversion implies an increase in the computational cost because of averaging over frequencies. The single-frequency AVO inversion, on the contrary, is faster and less accurate.

Figure 2.15 shows the inversion results obtained from the PWRC-based AVO inversion. Figures 2.15a and 2.15b correspond to the single-frequency and the band-limited AVO inversions. We observe that the PWRC-based AVO inversion generally produces less accurate results than the ERC-based AVO inversion. Despite the similarities between the ERC and the PWRC at the pre-critical offsets, we observe different behaviors of the relative errors in parameters estimates. The range of errors for both inversions varies between 2-12%. The differences are explained by the different sensitivities of the reflection coefficients to the parameters because of the additional argument $k_P r^*_{PP}(\mathrm{x}_n)$. This explanation is supported by the shapes of the objective functions and the sensitivity study. We observe an abrupt decrease in the accuracy of all estimated parameters at the near-critical offsets. This is explained by a strong inconsistency of the plane-wave description to the AVO data at the near-critical offsets. Whenever the post-critical offsets are involved in the inversion, the error curves become flat. This indicates that increase in the offset range will not improve the quality of estimated parameters. We note also that the S-wave velocity in the overburden is least accurately estimated regardless of the offset range. We suspect that S-wave velocities are more sensitive to errors at post-critical offsets than other parameters.

Although multi-component seismics continue to increase in popularity, single-component data is still widely acquired in the industry. We therefore provide the AVO inversion results obtained from only from the Z-component (Figure 2.16). We exploit equations 12 and perform the ERC-based band-limited AVO inversion. We observe that the accuracy of the parameter estimates decreases, especially at the near-critical and post-critical offsets.

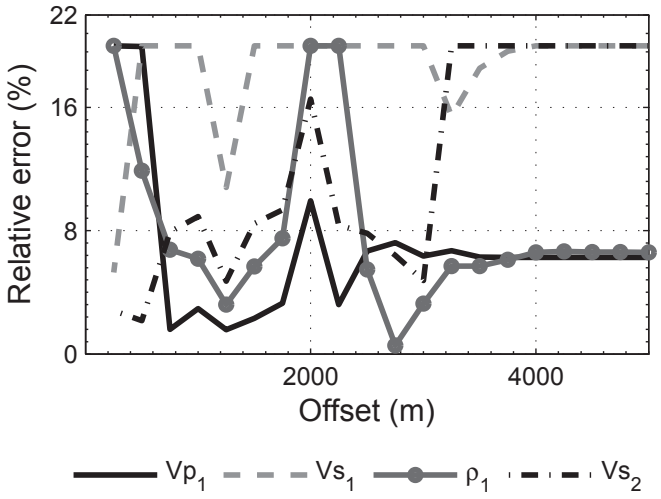

(a)

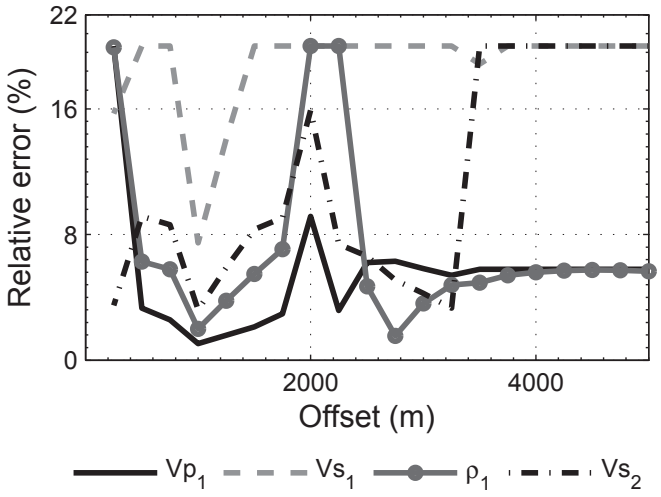

(b)

Figure 2.15: Relative error in the four-parameter AVO inversion as function of the offset range for Model 1. (a) PWRC-based single-frequency AVO inversion for 32 Hz; (b) PWRC-based band-limited AVO inversion.

The reason for a decreased accuracy is the approximation in the polarization vector of the reflected P-wave, which causes larger errors with increasing offset range. This consequently causes a shift in the minimum of the objective function. The error

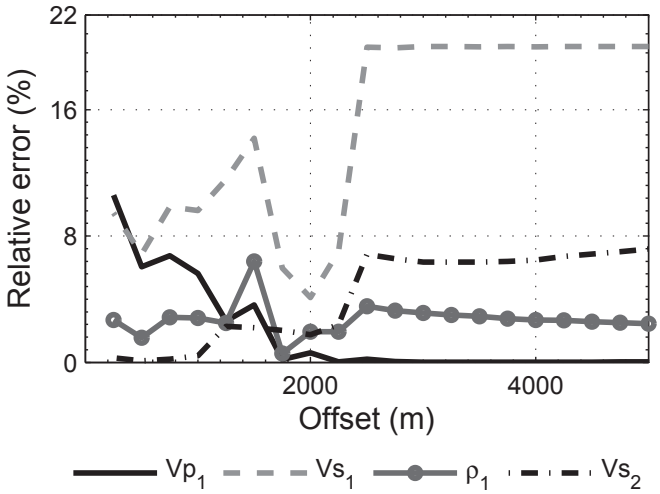

Figure 2.16: Relative error in the inversion results for the band-limited ERC-based AVO inversion of the $Z-$component AVO data.

curves at the pre-critical offsets resemble those for the two-component AVO inversion, however, they are nearly constant at the near-critical and post-critical offsets. Although the accuracy of the P-wave velocity estimation remains high, the errors in V_{S2} and ρ_1 increase to 8% and 3%, respectively. The S-wave velocity V_{S1} in the upper layer is not resolved, because the error exceeds the 20% limit used as a starting point for the inversion. The accuracy curves show qualitatively the same behavior as the accuracy curves in Figure 2.13. A comparison of the one-component ERC-based and PWRC-based AVO inversions shows that the former outperforms the latter.

2.5.2 Model 2

To illustrate the validity of the ERC-based AVO inversion, we perform an additional test on a model with two critical angles. An interface located 0.5 km below the source separates the two half-spaces with the parameters $V_{P1} = 1300$ m/s, $V_{S1} = 800$ m/s, $\rho_1 = 1800$ kg/m^3 in the overburden, and $V_{P2} = 2400$ m/s, $V_{S2} = 1700$ m/s, $\rho_2 = 2100$ kg/m^3 in the underburden. The first critical angle $\theta_{cr1} = 32.8^0$ (corresponding to a critical distance of $x_{cr1} = 644$ m) generates a PPP-type head wave. The second critical angle $\theta_{cr1} = 49.9^0$ (corresponding to a critical distance of $x_{cr2} = 1187$ m) creates a converted PSP-type head wave. The receiver offsets vary from 0 m to 2500

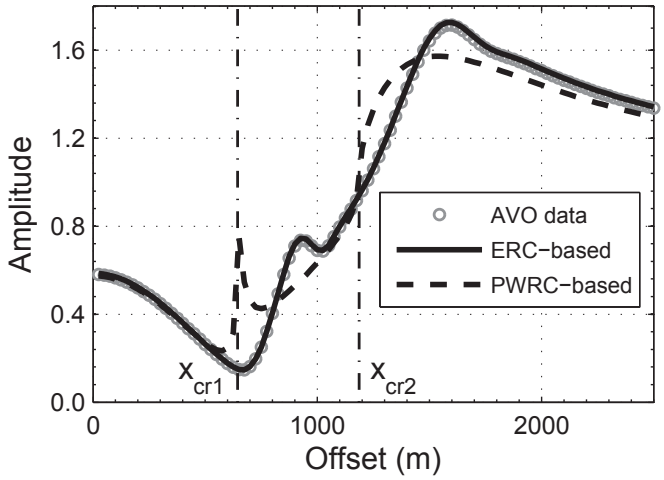

Figure 2.17: Band-limited AVO data for Model 2 and the corresponding theoretical descriptions calculated for the true model parameters.

m and cover the pre-critical, near-critical and post-critical reflections. The value of argument $k_P\, r^*_{PP}(\mathrm{x}_n)$ at minimal frequency 3 Hz varies from 14 at zero offset to 38 at offset 2500 m. The value of this argument at maximal frequency 60 Hz varies from 299 at zero offset to 779 at offset 2500 m. The value of this argument at dominant frequency of 39 Hz changes from 188 to 490 at zero and maximum offsets, respectively.

Figure 2.17 presents the band-limited AVO data and its ERC-based and PWRC-based theoretical descriptions. The behavior of the AVO data is more complex than that for Model 1. The first maximum in the AVO data is associated with the PPP-type head wave arrival, while the second maximum corresponds to the PSP-type head wave. Despite the complexity of the AVO data, the ERC-based theoretical description exhibits a good fit to the AVO data, while the PWRC-based description substantially deviates from it.

Figures 2.18a and 2.18b show the results of the four-parameter band-limited ERC-based and PWRC-based AVO inversions. The results generally resemble those obtained for Model 1 (Figure 2.14b), but the overall accuracy is almost twice as high. We suspect this is explained by the presence of an additional critical point which increases the sensitivity of the theoretical description to all the parameters. The PWRC-based AVO inversion produces relatively poor results for the offsets below the second critical point and almost constant errors behind the second critical point. V_{S1}

is still undefined, while the accuracy of the estimated V_{S2} increases considerably.

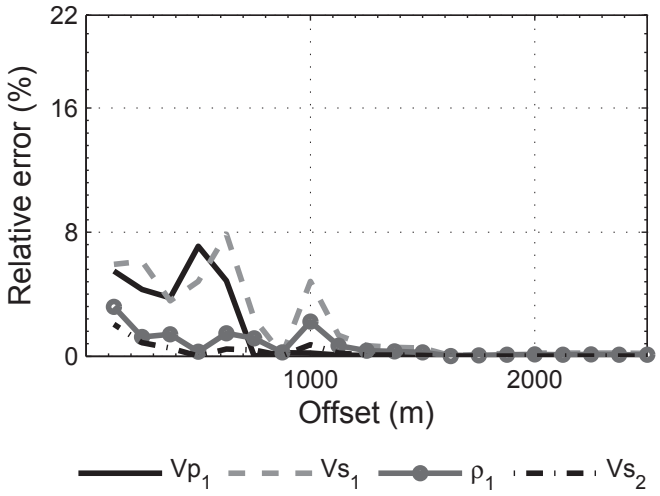

(a)

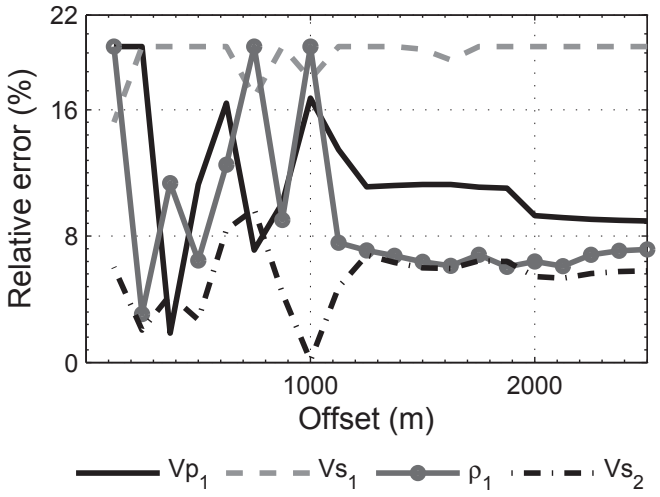

(b)

Figure 2.18: Relative error in the four-parameter AVO inversion as function of the offset range for Model 2. (a) ERC-based band-limited AVO inversion; (b) PWRC-based band-limited AVO inversion.

2.6 Discussion

We show that the ERC-based AVO inversion greatly improves the accuracy of estimated parameters as compared to the PWRC-based AVO inversion. The improvement is especially apparent when the near-critical and post-critical offsets come into play. This is explained by the wavefront curvature effect, which is captured by the ERC and ignored by the PWRC. We show also that incorporation of several frequencies rather than one enhances the accuracy of the ERC-based AVO inversion.

Although a significant improvement is observed when switching from the PWRC-based AVO inversion to the ERC-based AVO inversion, the computational effort is greater. The ERC-based AVO inversion, in particular the band-limited version of it, is CPU-demanding. The computational cost of band-limited AVO inversion is 15 times higher than single-frequency AVO inversion and it exhibits a non-linear dependency on the number of frequencies involved in the inversion. There is therefore a trade-off between the desired quality of the inversion and its computational cost.

The proposed approach and a conventional way of performing AVO inversion in the industry are essentially different. A typical setup for an inversion implies the application of a weak-contrast plane-wave reflection coefficient, which is written in terms of the contrasts in elastic parameters. Such an inversion will therefore estimate the contrasts in the parameters across the reflecting interface. We incorporate post-critical offsets and strong parameter contrasts across the interface. ERCs cannot be easily linearized in a similar way as PWRCs. Our inversion therefore performs a somewhat broader task of estimating the absolute values of seismic parameters. We show that ERCs provide the possibility of defining five absolute parameters while PWRCs are capable of estimating only four parameters.

In our tests, we recovered parameters both in the overburden and the underburden, by assuming two parameters in the underburden to be known. In principle, the ERC-based inversion allows retrieval of five parameters. However, one needs to carefully choose the estimated parameters because the objective function may not be equally sensitive to all the parameters, at least for some offset ranges. The inversion does not in general allow recovering of the densities independently. Nevertheless, we can recover the full set of seismic parameters in the underburden if the density in the overburden is known. It is also natural to perform a combination of a traveltime inversion and an AVO inversion to improve the quality of parameter estimation above and below the target interface. The only information we may miss is the density

estimate in the overburden.

We have shown examples of inverting multi-component as well as single-component synthetic data. We realize that multi-component data may not be available in the real-world tasks. However, we like to illustrate the difference in the performance of the inversion workflow for both cases. As we show in our examples, the quality of the inversion generally increases when we reconstruct the displacement along the ray. The comparison of one-component ERC-based AVO inversion with the multi-component PWRC-based inversion shows that the former is still better than the latter.

Given that in marine surveys we obtain scalar omni-directional pressure field, AVO data and its theoretical descriptions obey equations 11 and 15. We thus expect the inversion results to perform as good as in case of a multi-component inversion.

Our numerical tests are performed for one plane interface, although the theory of ERCs can be extended for curved reflectors and layered overburden. We concentrated on the simplest model of one plane interface between two homogeneous halfspaces in order to demonstrate that ERCs help to significantly enhance the inversion performance. The initial results provide motivation for further studies.

We have also avoided the topic of irregular noise in the data, although some noise is brought in because of the numerical errors of the modeling algorithm in the precritical domain. Systematic noise such as residual multiples, water-column noise and ground-roll, which might tune with the data at the post-critical offsets (Landrø and Tsvankin, 2007), deserve an additional study.

Last but not least important is the issue of quality of data processing prior to performing the inversion. There are particular requirements imposed on the processing sequence in order to condition the data for AVO inversion. One of the steps in such a sequence oftentimes is true amplitude imaging, which aims to remove the effects of wave propagation through the overburden in order to obtain the true reflection amplitudes at the target interfaces. The data after imaging become more regular with a better S/N ratio. However, the existing imaging algorithms assume that the interface is located in the far field and do not account for the reflections near and beyond the critical angle. In order to apply the ERC-based AVO inversion directly to imaged data, we need more advanced imaging techniques, which account for the wave phenomena associated with the critical angle. If the migration algorithm could properly account for post-critical reflections, we could directly exploit ERCs defined at the interface. At the current stage, we limit our work to non-imaged data. This issue needs a further investigation.

2.7 Conclusions

We show that long-offset data can significantly improve the performance of AVO inversion. It is however not enough to just increase the offset range. An adequate theoretical description of the observed AVO data is crucial for recovering the seismic parameters at long offsets. We propose to use the effective reflection coefficient (ERC) instead of the plane-wave reflection coefficient (PWRC). The ERC correctly describes the reflection of waves generated by point source at all offsets.

The synthetic tests show that including the near-critical and post-critical offsets in the AVO inversion based on PWRCs does not improve its quality and decreases the accuracy of S-wave velocity estimates in certain circumstances. Long-offset ranges increase the accuracy of parameter estimates in the AVO inversion based on ERCs. We achieve an error level of approximately 1% when including a wide range of offsets.

One of the advantages of our approach is the ability to recover five parameters, because of the presence of the additional dimensionless parameter $\frac{\omega_0\, r^{\star}_{PP}(0)}{V_{P1}}$. Although the quality of the five-parameter AVO inversion is somewhat lower than the quality of the four parameter inversion, it still recovers the desired parameters with a high accuracy at the post-critical offsets.

Among the considered versions of the AVO inversion based on ERCs, we found the band-limited inversion to perform the best. The single-frequency AVO inversion produces on average less accurate results.

2.8 Acknowledgments

Lyubov Skopintseva acknowledges Statoil ASA for financing her PhD study at NTNU. We acknowledge Statoil ASA and the Russian Foundation for Basic Research (grant 07-05-00671) for support of this work and the Norwegian Research Council for financial support of the ROSE project at NTNU. We are grateful to the reviewers for constructive suggestions which helped us to greatly improve the paper.

2.9 Appendix A: Reflected PP-wavefield at the receiver in terms of effective reflection coefficient

To theoretically describe the AVO data, we need to establish a link between the reflected wavefield and the ERC. There are three approaches to the description of the wavefields reflected from plane interfaces between two homogeneous media (Červený and Ravindra, 1971); a numerical representation, a local high-frequency asymptotic description and a rigorous plane-wave decomposition. The numerical representation is irrelevant for us, since we seek an analytical form of the solution. The high-frequency asymptotic solution represents the reflected wave and the head wave around the critical ray using the Weber-Hermite functions. This approximation does not describe the interference between the two waves at the near-critical and post-critical offsets and does not therefore fit our purpose. We use the rigorous plane-wave decomposition and exploit the results of Ayzenberg et al. (2009) to introduce the reflected wavefield at the receiver in terms of ERCs. We consider a model with two homogeneous halfspaces separated by a horizontal plane interface.

The interface given by equation $x_3\,(x_1,\ x_2) = -h$ in the global Cartesian system. We assume for simplicity that the source is located at the origin (0, 0, 0), the receiver is placed on the same side of the interface as the source and has coordinates $\mathrm{x} = (x_1,\ x_2,\ x_3)$.

The reflected P-wavefield at the receiver can be represented by the Kirchhoff propagation integral

$$\mathbf{u}_{PP}\,(\mathrm{x},\ \omega) = \iint\limits_{S} \mathbf{P}_P\,(\mathrm{x},\ \mathrm{s},\ \omega)\ \mathbf{u}_{PP}\,(\mathrm{s},\ \omega)\ d\mathrm{s} \tag{A-1}$$

where the reflected P-wavefield at the interface is represented by the convolutional reflection integral

$$\begin{aligned} \mathbf{u}_{PP}\,(\mathrm{s},\ \omega) &= \frac{1}{2\pi} \iint\limits_{S'} R_{PP}\,(\mathrm{s}-\mathrm{s}',\ \omega)\ \mathbf{u}^*_P\,(\mathrm{s}',\ \omega)\ d\mathrm{s}' = \\ &= \frac{1}{2\pi} \iint\limits_{S'} R_{PP}\,(\mathrm{s}',\ \omega)\ \mathbf{u}^*_P\,(\mathrm{s}-\mathrm{s}',\ \omega)\ d\mathrm{s}', \end{aligned} \tag{A-2}$$

$\mathbf{u}^*_P\,(\mathrm{s}',\ \omega) = \mathbf{H}_{PP}\,(\mathrm{s}',\ \tilde{\mathrm{s}},\ \omega)\,\mathbf{u}_P\,(\tilde{\mathrm{s}},\ \omega)$; $\mathbf{H}_{PP}\,(\mathrm{s}',\ \tilde{\mathrm{s}},\ \omega)$ is a matrix operator which transforms the polarization vector $\mathbf{e}_P\,(\tilde{\mathrm{s}})$ at point $\tilde{\mathrm{s}}$ to polarization vector $\mathbf{e}_{PP}\,(\mathrm{s}')$ at point

s'; $\mathbf{u}_P\,(\tilde{\mathrm{s}},\ \omega)$ is the incident P-wavefield at point $\tilde{\mathrm{s}}$ of the interface; s' is a point in the Fresnel zone; $\mathbf{P}_P\,(\mathrm{x},\ \mathrm{s},\ \omega)$ is the propagation operator, $R_{PP}\,(\mathrm{s}',\ \omega)$ is the reflection operator, $d\mathrm{s} = ds_1\,ds_2$, $d\mathrm{s}' = ds'_1\,ds'_2$. Wavefield $\mathbf{u}^*_P\,(\mathrm{s}',\ \omega)$ can be considered as the incident wave generated by the apparent source, which is a mirror image of the actual source with respect to the interface. The apparent source has coordinates $(0, 0, -2h)$. The wavefield generated by the apparent source differs from actual incident wavefield only by the polarization vector which coincides with the polarization vector of the reflected wave.

The wave propagation process described by equation A-1 is sketched in Figure 2.19a. There are two different mechanisms for energy propagation; the propagation along the ray tube, which has been discussed in detail in ray theory (Červený, 2001) and the energy diffusion across the ray tube (Klem-Musatov et al., 2008). Figure 2.19b illustrates reflection given by equation A-2. The operator decomposes the incident wavefield to plane waves at every point $\tilde{\mathrm{s}}$ of the interface, rotates the polarization vector with respect to the interface normal, multiplies each plane wave with the corresponding PWRC and then sums the obtained values at point s of the interface. The reflected field obtained at point s includes the contributions from all points $\tilde{\mathrm{s}}$.

Substituting equation A-1 to A-2, we obtain the four fold integral:

$$\mathbf{u}_{PP}\,(\mathrm{x},\ \omega) = \iint\limits_S \mathbf{P}_P\,(\mathrm{x},\ \mathrm{s},\ \omega)\ \left\{ \frac{1}{2\pi}\ \iint\limits_{S'} R_{PP}\,(\mathrm{s}',\ \omega)\ \mathbf{u}^*_P\,(\mathrm{s}-\mathrm{s}',\ \omega)\ d\mathrm{s}' \right\}\ d\mathrm{s} \tag{A-3}$$

The integral in A-3 can be evaluated in the seismic frequency range using ERCs (Ayzenberg et al., 2009). We rearrange the integrals in A-3 to show this. It is known that for plane interfaces the following is valid: $\mathbf{P}_P\,(\mathrm{x},\ \mathrm{s},\ \omega) = \mathbf{P}_P\,(\mathrm{x}-\mathrm{s}',\ \mathrm{s},\ \omega)$. We thus obtain:

$$\mathbf{u}_{PP}\,(\mathrm{x},\ \omega) = \frac{1}{2\pi}\ \iint\limits_{S'} R_{PP}\,(\mathrm{s}',\ \omega)\ \mathbf{u}^*_P\,(\mathrm{x}-\mathrm{s}',\ \omega)\ d\mathrm{s}' \tag{A-4}$$

where the vector integrand is represented by the propagation integral

$$\begin{aligned} \mathbf{u}^*_P\,(\mathrm{x}-\mathrm{s}',\ \omega) &= \iint\limits_S \mathbf{P}_P\,(\mathrm{x}-\mathrm{s}',\ \mathrm{s},\ \omega)\ \mathbf{u}^*_P\,(\mathrm{s},\ \omega)\ d\mathrm{s} \\ &= \iint\limits_S \mathbf{P}_P\,(\mathrm{x},\ \mathrm{s},\ \omega)\ \mathbf{u}^*_P\,(\mathrm{s}-\mathrm{s}',\ \omega)\ d\mathrm{s}. \end{aligned} \tag{A-5}$$

Exploiting the convolutional property for the reflection operator and defining the new variable $\mathrm{x}' = \mathrm{x} - \mathrm{s}'$, we obtain:

$$\mathbf{u}_{PP}(\mathrm{x},\ \omega) = \frac{1}{2\pi} \iint\limits_{\tilde{X}'} R_{PP}(\mathrm{x} - \mathrm{x}',\ \omega)\ \mathbf{u}_P^*(\mathrm{x}',\ \omega)\ d\mathrm{x}'\ , \tag{A-6}$$

where x' represents a point in the Fresnel zone located at the observation surface.

Equation A-6 says that the reflected wavefield at the receiver is the convolution of the wavefield originating at the apparent source and evaluated at the receiver and the reflection operator defined at the receiver.

Within the seismic frequency range, the spherical wave $\mathbf{u}_P^*(\mathrm{x}',\ \omega)$ can be represented by the approximation:

$$\mathbf{u}_P^*(\mathrm{x}',\ \omega) \cong \frac{i}{V_{P1}}\ S(\omega)\ \frac{e^{i\,k_P\ l(\mathrm{x}')}}{l(\mathrm{x}')}\ \mathbf{e}_{PP}(\mathrm{x}')\,, \tag{A-7}$$

where $l(\mathrm{x}')$ is the distance between the apparent source and point x', $S(\omega)$ is the wavelet spectrum, k_P is the wavenumber, V_{P1} is the P-wave velocity in the overburden, $\mathbf{e}_{PP}(\mathrm{x}')$ is the polarization vector at the receiver.

Substituting equation A-8 to equation A-6 and applying the approach proposed by Ayzenberg et al. (2009), we obtain the reflected PP-wavefield in terms of ERCs:

$$\mathbf{u}_{PP}(\mathrm{x},\ \omega) \cong \chi_{PP}[\mathrm{x},\ \omega]\ \frac{i}{V_{P1}}\ S(\omega)\ \frac{e^{i\,k_P\ l(\mathrm{x})}}{\sqrt{J_{PP}(\mathrm{x})}}\ \mathbf{e}_{PP}(\mathrm{x}) \tag{A-8}$$

where $\chi_{PP}[\mathrm{x},\ \omega] = \chi_{PP}[\theta(\mathrm{x}),\ k_P\ r_{PP}^*(\mathrm{x}),\ \mathbf{m}]$ is the ERC defined at the receiver, $r_{PP}^*(\mathrm{x})$ is the apparent wavefront radius at the receiver, $l(\mathrm{x})$ is the distance between the apparent source and the receiver, $J_{PP}(\mathrm{x}) = [l(\mathrm{x})]^2$ is the geometrical spreading of the reflected PP-wave. Equation A-9 was heuristically obtained and tested on synthetic data modelled by the finite-difference method by Skopintseva et al. (2008, 2009). It represents a seismic frequency approximation, which is similar to high-frequency approximation, when the ERC is replaced by the PWRC. However, the ERC takes into account the interference between the reflected and the head waves in the near-critical and the post-critical domains. For homogeneous media with plane interfaces, we obtain: $l(\mathrm{x}) = l(\mathrm{s}) + l(\mathrm{x},\ \mathrm{s})$, where $l(\mathrm{s})$ is the distance between the actual source and the reflection point, $l(\mathrm{x},\ \mathrm{s})$ is the distance between the reflection point and the receiver.

From the definition of ERCs in media with plane interfaces, we obtain that $r_{PP}^*(\mathrm{x}) = l(\mathrm{x})$. The ERC at the receiver is thus different from the one at the interface. The ERC

at the interface is defined for reflection angle $\theta\,(\mathrm{s})$ and apparent radius $r^*_{PP}\,(\mathrm{s})$. The ERC at the receiver depends on reflection angle $\theta\,(\mathrm{x})$ and apparent radius $r^*_{PP}\,(\mathrm{x})$. The position of amplitude maximum and the oscillations at the post-critical offsets are different for the two ERCs. Indeed, when the reflected wavefield propagates from the interface to the receiver, the interference between the reflected wave and the head wave changes because of the different nature of their propagation. This causes the energy diffusion across ray tube during propagation (Figure 2.19a). Quantity $r^*_{PP}\,(\mathrm{x})$ controls the diffusion. Representing the $r^*_{PP}\,(\mathrm{x})$ through $r^*_{PP}\,(\mathrm{s})$, we find the link between the two ERCs:

$$r^*_{PP}\,(\mathrm{x}) = \; r^*_P\,(\mathrm{s})\left(1 + \frac{l\,(\mathrm{x},\;\mathrm{s})}{l\,(\mathrm{s})}\right). \tag{A-9}$$

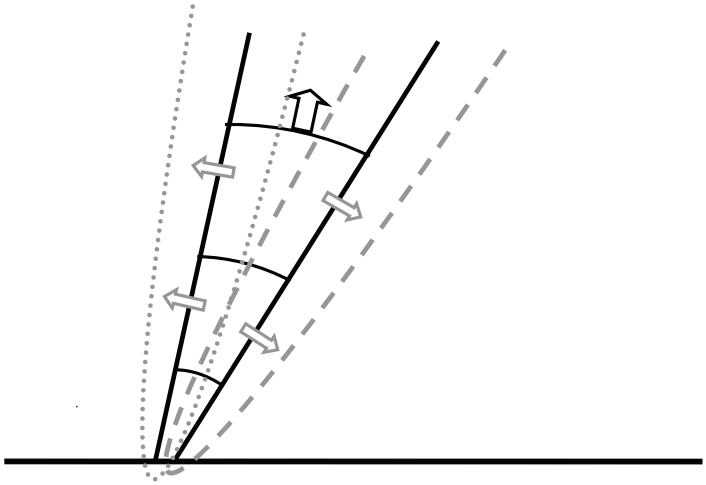

(a)

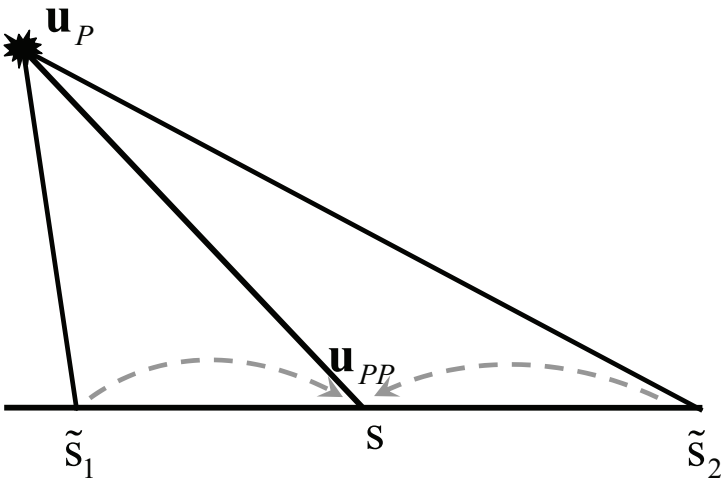

(b)

Figure 2.19: Scheme of (a) propagation and (b) reflection of the wave generated by a point source.

Chapter 3

Effect of the interface curvature on the reflections for long offset data

Lyubov Skopintseva[1], Arkady M. Aizenberg[2], Milana Ayzenberg[3], Martin Landrø[1], Tatyana Nefedkina[2],

[1] Norwegian University of Science and Technology, Trondheim, Norway

[2] Institute of Petroleum Geology and Geophysics SB RAS, Novosibirsk, Russia

[3] Statoil ASA

Presented at the ROSE Meeting, Trondheim, Norway, April 2010; the 72th EAGE Conference & Exhibition, Barcelona, Spain, June 2010; Submitted to Geophysics

3.1 Abstract

Widely exploited in the industry AVO inversion techniques are based on weak-contrast approximations of the plane-wave reflection coefficients. These approximations are valid for plane waves reflected at almost flat interfaces with weak contrasts in seismic parameters and for reflection angles below the critical angle. Regardless the underlying assumptions, linearized coefficients provide a simple and physically adequate tool to accurately invert AVO data for seismic parameters at pre-critical angles. However, the accuracy of linearized coefficients drastically decreases with increasing incidence angle. Limitations occur around and beyond the critical ray, where the effect of wavefront curvature becomes prominent and thus can no more be neglected. The effective reflection coefficients generalize the plane-wave reflection coefficients for waves generated by point sources and reflected at curved interfaces. They account for the wavefront curvature and are adequate at any incidence angle. Our previous studies have shown that including the reflections around and beyond the critical angle in the AVO inversion significantly improves the accuracy of estimated parameters. However, the interface curvature must also have its contribution to the long-offset AVO inversion. We find that the interface curvature affects the energy propagation along the ray tube and the energy diffusion across the ray tube. The energy propagation along the tube is characterized by the geometrical spreading which is strongly affected by interface curvature. The transverse diffusion is captured by the effective reflection coefficients which are less influenced by interface curvature. The long-offset AVO inversion is thus sensitive to interface curvature through a combination of several wave propagation factors.

3.2 Introduction

Conventional AVO inversion techniques exploit weak-contrast approximations of the plane-wave reflection coefficient (PWRC) described by the Zoeppritz equation (Aki and Richards, 2002). Such linearized reflection coefficients inherit the main underlying assumption of the Zoeppritz equation, which defines the ratio of the amplitudes of reflected and incident plane waves at a flat reflecting interface separating two homogeneous halfspaces. The assumption of a planar wavefront limits the applicability of the PWRC-based AVO inversion, because PWRCs do not account for wavefront curvature (Červený et al., 1964; Červený and Ravindra, 1971). The limitations of the assumption of plane interfaces for a seismic frequency range is studied and discussed by Ayzenberg et al. (2007).

Linearized reflection coefficients exhibit a remarkably good match to the observed reflection amplitudes for the media where the near-critical and post-critical reflections are not registered by the acquisition or muted during processing. In complex media containing interfaces with strong velocity contrasts, the critical incidence angle appears at relatively small offsets and the accompanying phenomena are observed in the data. In such circumstances, the effects associated with wavefront curvature and the interference between reflected and head waves play a vital role in the definition of the AVO behavior. This results in the inadequacy of PWRCs in the AVO inversion. Several authors address the effect of wavefront curvature on the reflections around and beyond the critical angle (Downton and Ursenbach, 2006; Alhussain et al., 2008; Haase, 2004). However, the local interface curvature has never been considered a factor affecting the AVO curve.

Ayzenberg et al. (2007, 2009) introduced effective reflection coefficients (ERCs) which generalize PWRCs for waves generated by point sources. The ERCs account for the wavefront curvature and the frequency range of the wavelet and thus naturally incorporate the Fresnel volume surrounding the specular ray. The ERCs also describe the interference between reflected and head waves beyond the critical ray and are adequate at any incidence ray. Skopintseva et al. (2011) developed an AVO inversion approach based on the ERCs and valid for plane interfaces. They showed that the a significant improvement in the accuracy of estimated parameters can be achieved through the incorporation of the data from near-critical and post-critical offsets. The ERCs also approximately account for local interface curvature, which relaxes the assumption of locally plane interfaces.

Interface curvature strongly affects the reflection response. Červený et al. (1974) and Hubral (1979) studied the impact of interface curvature on the energy propagation along the ray tube. They introduced the equations for the geometrical spreading dependent on interface curvature within the high-frequency approximation. Favretto-Cristini et al. (2009) showed that the interface curvature affects the size of the Fresnel zone and cannot be neglected. The ERCs are introduced in a way that naturally incorporates the Fresnel zone and, as a consequence, interface curvature (Ayzenberg et al., 2007, 2009).

The post-critical reflections additionally exhibit a more complex phase interference between the reflected and head waves. The phase interference characterizes the diffusion across the ray tube and, consequently, affects the post-critical amplitudes. Skopintseva et al. (2011) state the importance of accounting for the phase interference for long-offset AVO inversion at plane interfaces, where the phase interference is defined solely by wavefront curvature. Jin and Yin (2008) showed that interface curvature strongly affects the wavefront curvatures of reflected and head waves. This will result in phase interference affected by both wavefront and interface curvatures.

In this paper, we extend the ERC-based AVO inversion approach for curved interfaces and include a factor describing the transverse diffusion across the ray tube. We study the effect of interface curvature on the energy propagation along the ray tube and the transverse diffusion using synthetic modeled data. We show that the effect of interface curvature on the energy propagation can be accurately described by ray theory. The description of the transverse diffusion, however, requires an accurate approximation in the form of ERCs. We investigate the influence of interface curvature on the AVO inversion and show that including of interface curvature in the geometrical spreading significantly improves the accuracy of parameter estimates. Including of interface curvature in the transverse diffusion across the ray tube brings a minor improvement. We consider the interface curvature to be known a priori and leave the topic of accuracy of estimating interface curvature outside the scope of this paper.

The paper is divided in five parts. Part 1 describes our approach to the deterministic AVO inversion. In Part 2, we review the properties of ERCs at curved interfaces and introduce an approximate formula for the phase interference valid for curved interfaces. Part 3 is devoted to synthetic modelling, where we obtain data both at interface and at receiver for various interface shapes and azimuthal distributions of receiver arrays. In Part 4, we analyze the effect of interface curvature on the reflection response. In Part 5, we provide the results of the AVO inversion of synthetic data

and elaborate on the effect of interface curvature on geometrical spreading and ERCs. Finally, we discuss the aspects of applicability of the ERC-based AVO inversion for curved reflectors in practice. We derive a heuristic approximation of the P-wavefield reflected at curved interface in terms of ERCs in Appendix 3.11. Appendix 3.12 summarizes auxiliary equations used in the paper.

3.3 Deterministic ERC-based AVO inversion

We consider a curved interface between two isotropic elastic halfspaces. A point source in the upper halfspace generates an incident P-wavefield, which hits the interface and produces a reflected wavefield $\mathbf{U}_{PP}(\mathrm{x}_n, t) = (U_{PPX}(\mathrm{x}_n, t),\ 0,\ U_{PPZ}(\mathrm{x}_n, t))$ at receivers $\mathrm{x}_n = (x_{1\,n},\ x_{2\,n},\ x_{3\,n})$ located in the upper halfspace. The receivers are numbered by $n = 1,\ 2,\ \ldots,\ N$, and N is the number of receivers. The variable t denotes time. For simplicity, we consider only one horizontal component of the reflected wavefield.

A deterministic AVO inversion can be defined as the estimation of the sought-for model parameters through the minimization of misfit function between observed and modeled AVO data:

$$F(\mathbf{v}) = \sqrt{\sum_{n=1}^{N} \left[A_{\mathrm{obs}}(\mathrm{x}_n) - A_{\mathrm{mod}}(\mathrm{x}_n,\ \mathbf{v})\right]^2} \ \rightarrow\ \min, \tag{1}$$

where $\mathbf{v}$ is the vector of unknown model parameters. Vector $\mathbf{v}$ consists of the velocities and one of the densities (density ratio) and its length is defined by the number of unknown parameters.

According to Skopintseva et al. (2011), the observed AVO data can be represented as

$$A_{\mathrm{obs}}(\mathrm{x}_n) = \frac{\left(\int_{t_1(\mathrm{x}_n)}^{t_2(\mathrm{x}_n)} \left[\tilde{U}_{PP}(\mathrm{x}_n, t)\right]^2 dt\right)^{\frac{1}{2}}}{\frac{1}{N}\ \sum_{n=1}^{N} \left(\int_{t_1(\mathrm{x}_n)}^{t_2(\mathrm{x}_n)} \left[\tilde{U}_{PP}(\mathrm{x}_n, t)\right]^2 dt\right)^{\frac{1}{2}}}, \tag{2}$$

where $\tilde{U}_{PP}(\mathrm{x}_n) = \sqrt{\tilde{U}^2_{PP\,X}(\mathrm{x}_n) + \tilde{U}^2_{PP\,Z}(\mathrm{x}_n)}$ is the magnitude of displacement vector $\tilde{\mathbf{U}}_{PP}(\mathrm{x}_n, t) = \sqrt{J_{PP}(\mathrm{x}_n)}\ \mathbf{U}_{PP}(\mathrm{x}_n, t)$ corrected for geometrical spreading $\sqrt{J_{PP}(\mathrm{x}_n)}$, and $[t_1(\mathrm{x}_n),\ t_2(\mathrm{x}_n)]$ is a time window of constant length containing the reflected event.

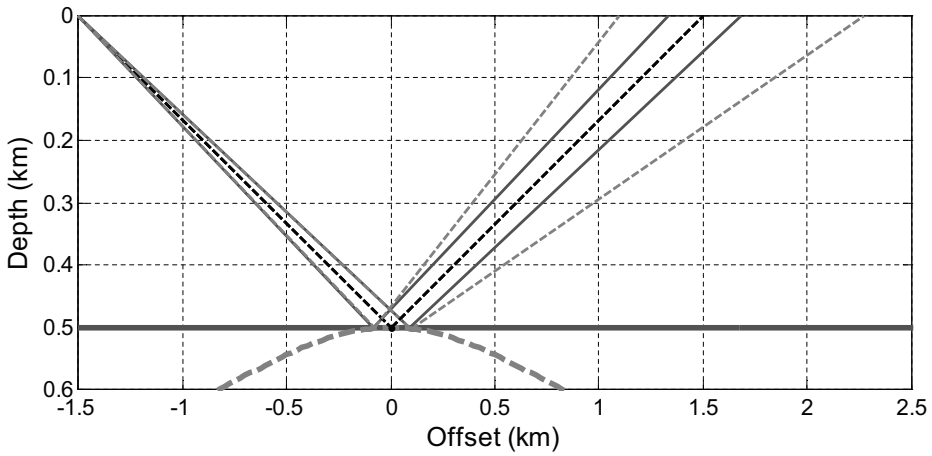

Figure 3.1: Spreading of the ray tube. Black dashed line indicates the specular ray. Gray solid lines show the ray tube in the case of reflection from a plane interface; gray dashed lines show the ray tube in the case of reflection from a curved interface.

We illustrate in Figure 3.1 the effect of interface curvature on the cross-section of the ray tube, which is proportional to the geometrical spreading. The cross-section of the ray tube at the receiver for reflection from a curved interface is considerably larger than the one from a plane interface. This indicates that the recorded reflection amplitude from interfaces of different local curvature will differ significantly. The effect of interface curvature in the geometrical spreading cannot thus be neglected.

Although Skopintseva et al. (2011) introduced equation 2 only for plane interfaces, it can be extended for curved interfaces by correcting the geometrical spreading for interface curvature, as shown in Appendix 3.12 (Červený et al., 1974; Hubral, 1979).

The modeled AVO data has the following form (Skopintseva et al., 2011):

$$A_{\mathrm{mod}}\left(\mathrm{x}_n,\ \mathbf{v}\right) = \frac{\sqrt{\int_{\omega_{\min}}^{\omega_{\max}} \left|\, S\left(\omega\right)\right|^2 \ \left|\, \chi_{PP}\left(\mathrm{x}_n,\ \omega\right)\right|^2 \ d\omega}}{\frac{1}{N}\ \sum_{n=1}^{N} \sqrt{\int_{\omega_{\min}}^{\omega_{\max}} \left|\, S\left(\omega\right)\right|^2 \ \left|\, \chi_{PP}\left(\mathrm{x}_n,\ \omega\right)\right|^2 \ d\omega}}, \tag{3}$$

where $|\, S\left(\omega\right)|$ is the wavelet spectrum amplitude for the displacement field, ω is the angular frequency, ω_{min} and ω_{max} are the lowest and highest frequencies contained in the reflection event, $\chi_{PP}\left(\mathrm{x}_n,\ \omega\right) = \chi_{PP}\left[\theta\left(\mathrm{x}_n\right),\ k_P\ r^*_{PP}\left(\mathrm{x}_n\right),\ \mathbf{m}\right]$ is the ERC defined at the receiver x_n, $\theta\left(\mathrm{x}_n\right)$ is the incidence angle, $\mathbf{m} = \left(V_{P1},\ V_{P2},\ V_{S1},\ V_{S2},\ \rho_1,\ \rho_2\right)$ is the vector of model parameters, V_{P1} and V_{P2} are the P-wave velocities, V_{S1} and V_{S2}

are the S-wave velocities, ρ_1 and ρ_2 are the densities above and below the reflecting interface. Vector $\mathbf{v}$ of the unknown parameters is a subset of vector $\mathbf{m}$. Skopintseva et al. (2011) showed that the maximum dimension of vector $\mathbf{v}$ is five, because ERCs contain only five independent parameters (the four velocities and one of the densities). Dimensionless argument $k_P\, r^*_{PP}(\mathrm{x}_n)$ controls the wavefront curvature and frequency dependencies in the ERCs, $k_P = \omega/V_{P1}$ is the wavenumber in the upper halfspace, $r^*_{PP}(\mathrm{x}_n)$ is the apparent wavefront curvature at the receiver (Ayzenberg et al., 2007). On the example of plane interface, Skopintseva et al. (2011) showed that parameter $r^*_{PP}(\mathrm{x}_n)$ contains a propagation term controlling a phase change caused by the interfering reflected and head waves, which is associated with the diffusion across the ray tube. Although equation 3 is derived for plane interfaces, it can be extended for curved interfaces by modifying parameter $r^*_{PP}(\mathrm{x}_n)$, as interface curvature affects the wavefront curvatures of the reflected and head waves (Jin and Yin, 2008).

To define parameter $r^*_{PP}(\mathrm{x}_n)$, we consider an auxiliary problem where the receivers are placed at reflection points $\mathrm{s}_n = (s_{1n},\ s_{2n})$ at the interface. By converging x_n to s_n in equations 1-3, the inversion reduces to:

$$F(\mathbf{v}) = \sqrt{\sum_{n=1}^{N} \left[A_{\mathrm{obs}}(\mathrm{s}_n) - A_{\mathrm{mod}}(\mathrm{s}_n,\ \mathbf{v})\right]^2} \ \rightarrow\ \min, \tag{4}$$

where

$$A_{\mathrm{obs}}(\mathrm{s}_n) = \frac{\left(\int_{t_1(\mathrm{s}_n)}^{t_2(\mathrm{s}_n)} \left[\tilde{U}_{PP}(\mathrm{s}_n, t)\right]^2 dt\right)^{\frac{1}{2}}}{\frac{1}{N}\ \sum_{n=1}^{N}\left(\int_{t_1(\mathrm{s}_n)}^{t_2(\mathrm{x}_n)} \left[\tilde{U}_{PP}(\mathrm{s}_n, t)\right]^2 dt\right)^{\frac{1}{2}}}, \tag{5}$$

$$A_{\mathrm{mod}}(\mathrm{s}_n,\ \mathbf{v}) = \frac{\sqrt{\int_{\omega_{\min}}^{\omega_{\max}} |\, S(\omega)\,|^2\ |\, \chi_{PP}(\mathrm{s}_n,\ \omega)\,|^2\ d\omega}}{\frac{1}{N}\ \sum_{n=1}^{N}\sqrt{\int_{\omega_{\min}}^{\omega_{\max}} |\, S(\omega)\,|^2\ |\, \chi_{PP}(\mathrm{s}_n,\ \omega)\,|^2\ d\omega}}, \tag{6}$$

$\tilde{U}_{PP}(\mathrm{s}_n, t)$ is the magnitude of displacement vector $\tilde{\mathbf{U}}_{PP}(\mathrm{s}_n, t) = \sqrt{J_{PP}(\mathrm{s}_n)}\ \mathbf{U}_{PP}(\mathrm{s}_n, t)$ at reflection point s_n, $\chi_{PP}(\mathrm{s}_n,\ \omega) = \chi_{PP}\left[\theta(\mathrm{s}_n),\ k_P\, r^*_{PP}(\mathrm{s}_n),\ \mathbf{m}\right]$ is the ERC defined at reflection point s_n of the interface, $\theta(\mathrm{s}_n) = \theta(\mathrm{x}_n)$, and $r^*_{PP}(\mathrm{s}_n)$ is the apparent wavefront radius at the interface (Ayzenberg et al., 2009).

Equations 4-6 do not contain propagation terms from the interface to the receiver. Geometrical spreading $J_{PP}(\mathrm{s}_n)$ does not depend on the interface curvature (Figure

3.1). The ERC is thus not affected by the diffusion phenomena across the ray tube of the reflected wave. However, the ERC depends on the wavefront and interface curvatures. We study this dependence in detail in the next chapter.

3.4 Effective reflection coefficients

3.4.1 PP-wave effective reflection coefficients at interface

Ayzenberg et al. (2009) defined the approximation for the PP-wave ERC at reflection point s_n at a curved interface separating two homogeneous elastic halfspaces as

$$\chi_{PP}\left(\mathrm{s}_n,\ \omega\right)=\frac{u^*_{PP\ \mathrm{norm}}\left(\mathrm{s}_n\right)\cos\theta\left(\mathrm{s}_n\right)+u^*_{PP\ \mathrm{tan}}\left(\mathrm{s}_n\right)\sin\theta\left(\mathrm{s}_n\right)}{\left[\frac{i}{k_P r^*_{PP}(\mathrm{s}_n)}-\frac{1}{k_P^2 r^{*2}_{PP}(\mathrm{s}_n)}\right]e^{ik_P r^*_{PP}(\mathrm{s}_n)}}, \tag{7}$$

where $u^*_{PP\ \mathrm{norm}}\left(\mathrm{s}_n\right)$ and $u^*_{PP\ \mathrm{tan}}\left(\mathrm{s}_n\right)$ are the dimensionless normal and tangential to the interface components of the displacement vector:

$$\begin{aligned} u^*_{PP\ \mathrm{norm}}\left(\mathrm{s}_n\right)&=-\int_0^{+\infty}R_{PP}\left(\zeta,\ \mathbf{m}\right)e^{i\,\alpha(\mathrm{s}_n)\sqrt{1-\zeta^2}}J_0\left[\beta\left(\mathrm{s}_n\right)\zeta\right]\zeta d\zeta,\\ u^*_{PP\ \mathrm{tan}}\left(\mathrm{s}_n\right)&=-\int_0^{+\infty}R_{PP}\left(\zeta,\ \mathbf{m}\right)\frac{ie^{i\,\alpha(\mathrm{s}_n)\sqrt{1-\zeta^2}}}{\sqrt{1-\zeta^2}}J_1\left[\beta\left(\mathrm{s}_n\right)\zeta\right]\zeta^2 d\zeta, \end{aligned} \tag{8}$$

where $R_{PP}\left(\zeta,\ \mathbf{m}\right)$ is the exact PWRC, $\alpha\left(\mathrm{s}_n\right)=k_P r^*_{PP}\left(\mathrm{s}_n\right)\cos\theta\left(\mathrm{s}_n\right)$ and $\beta\left(\mathrm{s}_n\right)=k_P r^*_{PP}\left(\mathrm{s}_n\right)\sin\theta\left(\mathrm{s}_n\right)$, ζ is the horizontal component of the P-wave ray vector in the overburden, J_0 and J_1 are the Bessel functions of the zeroth and first orders.

Ayzenberg et al. (2007) noticed that ERCs drastically differ from PWRCs, especially at the near-critical and post-critical offsets. The difference is controlled by argument $k_P r^*_{PP}\left(\mathrm{s}_n\right)$ and is more pronounced for smaller values of the argument. An essential constituent of this argument is the apparent wavefront radius $r^*_{PP}\left(\mathrm{s}_n\right)$, which we will study in more detail. Ayzenberg et al. (2007) derived an explicit approximation of parameter $r^*_{PP}\left(\mathrm{s}_n\right)$ for interfaces of arbitrary shape and spherical incident waves. We rewrite parameter $r^*_{PP}\left(\mathrm{s}_n\right)$ through the wavefront curvatures of reflected and head waves, which is more convenient for further analysis (see Appendix 3.11):

$$r^*_{PP}\left(\mathrm{s}_n\right)=\frac{1+\cos^2\theta\left(\mathrm{s}_n\right)}{\cos^2\theta\left(\mathrm{s}_n\right)\ \left[\tilde{K}_{11}\left(\mathrm{s}_n\right)-\delta\tilde{K}_{11}\left(\mathrm{s}_n\right)\right]+\tilde{K}_{22}\left(\mathrm{s}_n\right)}\ , \tag{9}$$

where

$$\begin{aligned}\tilde{K}_{11}(\mathrm{s}_n) =& \frac{1}{l(\mathrm{s}_n)} - 2\frac{D_{11}(\mathrm{s}_n)}{\cos\theta(\mathrm{s}_n)}\,,\\ \tilde{K}_{22}(\mathrm{s}_n) =& \frac{1}{l(\mathrm{s}_n)} - \cos\theta(\mathrm{s}_n)\, D_{22}(\mathrm{s}_n)\end{aligned} \tag{10}$$

are the main wavefront curvatures of the apparent reflected wavefield at the interface,

$$\delta\tilde{K}_{11}(\mathrm{s}_n) = -\frac{D_{11}(\mathrm{s}_n)}{\cos\theta(\mathrm{s}_n)} \tag{11}$$

is the wavefront curvature of the apparent head wave at reflection point s_n in the incidence plane, $l(\mathrm{s}_n)$ is the distance between the source and the reflection point, $\frac{1}{l(\mathrm{s}_n)}$ is the curvature of the spherical incident wave, $D_{11}(\mathrm{s}_n)$ and $D_{22}(\mathrm{s}_n)$ are the main local interface curvatures. For simplicity, we assume that $D_{11}(\mathrm{s}_n)$ and $D_{22}(\mathrm{s}_n)$ are defined in the incidence plane and out of incidence plane, respectively.

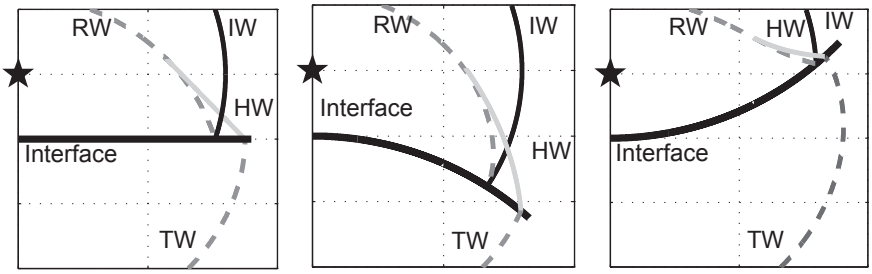

(a) (b) (c)

Figure 3.2: Propagation of the incidence (IW), reflected (RW), transmitted (TW) and head (HW) waves for various interface shapes. (a) Plane interface, (b) Anticlinal interface, (c) Synclinal interface. The point source is marked by a star.

The wavefront curvatures of the reflected and head waves entering equation 9 are affected by interface curvatures $D_{11}(\mathrm{s}_n)$ and $D_{22}(\mathrm{s}_n)$ (Figure 3.2). Although we exaggerate the influence of interface curvature on the wavefront curvatures in Figure 3.2 by showing wavefronts propagating away from the interface, the trend is also valid for the reflection point. For plane interfaces ($D_{11}(\mathrm{s}_n) = D_{22}(\mathrm{s}_n) = 0$), the wavefront of the reflected wave is spherical ($\tilde{K}_{11}(\mathrm{s}_n) = \tilde{K}_{22}(\mathrm{s}_n) = \frac{1}{l(\mathrm{s}_n)}$). The wavefront of the head wave is tangential to the spherical wavefront at the critical ray ($\delta\tilde{K}_{22}(\mathrm{s}_n) = \tilde{K}_{22}(\mathrm{s}_n)$) and has conical shape with zero curvature in the incidence plane ($\delta\tilde{K}_{11}(\mathrm{s}_n) =$

0). For curved interfaces, the reflected and head wavefronts are no longer spherical ($\tilde{K}_{11}(s_n) = \tilde{K}_{22}(s_n) \neq \frac{1}{l(s_n)}$) and conical ($\delta\tilde{K}_{11}(s_n) \neq 0$). Their phases interfere differently in the incidence plane, even at reflection point s_n. The phase interference is controlled by the term $\tilde{K}_{11}(s_n) - \delta\tilde{K}_{11}(s_n)$ in equation 9. The wavefront of the head wave remains tangential to the wavefront of the reflected wave at the critical ray ($\delta\tilde{K}_{22}(s_n) = \tilde{K}_{22}(s_n)$) and the phase interference out of incidence plane remains unchanged. The apparent wavefront radius $r^*_{PP}(s_n)$ can be interpreted as the distance

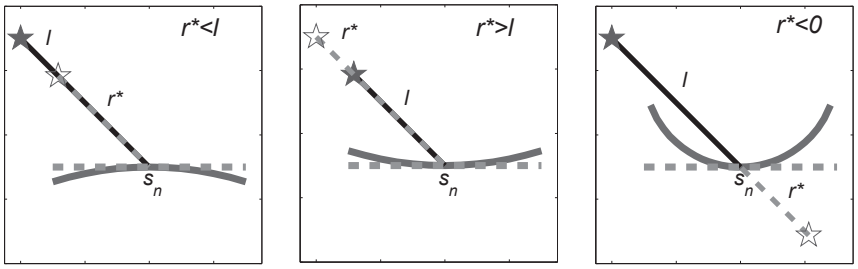

(a) (b) (c)

Figure 3.3: The apparent wavefront radius $r^*_P(s_n)$ (gray line) and the actual distance $l(s_n)$ between the source and the reflection point (black line) for various interface shapes. (a) Anticlinal interface, (b) Synclinal interface with the curvature radius larger than $l(s_n)$, (c) Synclinal interface with the curvature radius less than $l(s_n)$.

between reflection point s_n and an apparent source. The location of apparent source is chosen such that the wavefront curvature of the apparent spherical incident wave with respect to the tangential plane interface is equal to the wavefront curvature of the actual incident wave with respect to the actual curved interface (Ayzenberg et al., 2007). The ratio of the apparent wavefront radii to the distance between the source and the reflection point for different interface curvatures is shown in Figure 3.3. For anticline interfaces, the apparent distance is shorter than the actual one ($r^*_{PP}(s_n) < l(s_n)$). For syncline interfaces with curvature radius exceeding $l(s_n)$, it appears that the wave comes from a larger distance ($r^*_{PP}(s_n) > l(s_n)$). For syncline interfaces with the radius of curvature less than $l(s_n)$, the apparent wave comes from the opposite side of the interface ($r^*_{PP}(s_n) < 0$). When the radius of curvature of the interface coincides with the distance between the actual source and the reflection point, the apparent wave arrives from the infinity and is represented by a plane wave. In this degenerate case, the ERC coincides with the PWRC.

3.4.2 PP-wave effective reflection coefficients at receiver

To introduce $r^*_{PP}(\mathrm{x}_n)$ at receiver x_n, we need to include propagation from the interface to the receiver in the equation for $r^*_{PP}(\mathrm{s}_n)$. Figure 3.2 shows that propagation from the interface to the receiver changes the wavefront curvatures of the reflected and head waves. For plane interfaces, the propagation affects only the wavefront curvature of the reflected wave, while the wavefront curvature of the head wave in the incident plane remains unchanged. Skopintseva et al. (2011) showed that for plane interfaces equation for $r^*_{PP}(\mathrm{x}_n)$ has a simple form: $r^*_{PP}(\mathrm{x}_n) = r^*_{PP}(\mathrm{s}_n)\left(1+\frac{l(\mathrm{s}_n,\,\mathrm{x}_n)}{l(\mathrm{s}_n)}\right) = l(\mathrm{s}_n,\,\mathrm{x}_n) + l(\mathrm{s}_n)$, where $\frac{1}{l(\mathrm{s}_n,\,\mathrm{x}_n)+l(\mathrm{s}_n)}$ is the wavefront curvature of the reflected wave at the receiver, $l(\mathrm{s}_n,\,\mathrm{x}_n)$ is the distance between the reflection point and the receiver.

For curved interfaces, we modify the wavefront curvatures $\tilde{K}_{11}(\mathrm{s}_n)$, $\tilde{K}_{22}(\mathrm{s}_n)$ and $\delta\tilde{K}_{11}(\mathrm{s}_n)$ of the reflected and head waves by the propagation factor $l(\mathrm{s}_n,\,\mathrm{x}_n)$. After tedious derivations shown in Appendix 3.11, the equation for the apparent wavefront radius at receiver x_n has a form similar to equation 9:

$$r^*_{PP}(\mathrm{x}_n) = \frac{1+\cos^2\theta(\mathrm{x}_n)}{\cos^2\theta(\mathrm{x}_n)\,\left[\tilde{K}^*_{11}(\mathrm{x}_n) - \delta\tilde{K}_{11}(\mathrm{x}_n)\right] + \tilde{K}^*_{22}(\mathrm{x}_n)}\,. \tag{12}$$

where the main wavefront curvatures of the apparent reflected wave at the receiver are

$$\begin{aligned}
\tilde{K}^*_{11}(\mathrm{x}_n) &= \frac{\tilde{K}_{11}(\mathrm{s}_n)+G}{1+l(\mathrm{s}_n,\,\mathrm{x}_n)\left\{\tilde{K}_{11}(\mathrm{s}_n)+\tilde{K}_{22}(\mathrm{s}_n)+G\right\}},\\
\tilde{K}^*_{22}(\mathrm{x}_n) &= \frac{\tilde{K}_{22}(\mathrm{s}_n)+G}{1+l(\mathrm{s}_n,\,\mathrm{x}_n)\left\{\tilde{K}_{11}(\mathrm{s}_n)+\tilde{K}_{22}(\mathrm{s}_n)+G\right\}},\\
G &= \left[\tilde{K}_{11}(\mathrm{s}_n)\,\tilde{K}_{22}(\mathrm{s}_n) - \tilde{K}^2_{12}(\mathrm{s}_n)\right] l(\mathrm{s}_n,\,\mathrm{x}_n)
\end{aligned} \tag{13}$$

$\tilde{K}_{12}(\mathrm{s}_n) = -D_{12}(\mathrm{s}_n)$, $D_{12}(\mathrm{s}_n)$ is the mixed interface curvature, and the wavefront curvature of the head wave in the incidence plane at the receiver is

$$\delta\tilde{K}_{11}(\mathrm{x}_n) = \left[l(\mathrm{s}_n,\,\mathrm{x}_n) - \frac{D_{11}(\mathrm{s}_n)}{\cos\theta(\mathrm{s}_n)}\right]^{-1}. \tag{14}$$

The ERC at the receiver is obtained by substituting $r^*_{PP}(\mathrm{s}_n)$ by $r^*_{PP}(\mathrm{x}_n)$ in equations 7-8. The ERC at the receiver thus accounts for the phase interference between the reflected and head waves. The ERCs at the interface and at the receiver are compared with the PWRCs in Figure 3.4. The different reflection coefficients differ mainly at the

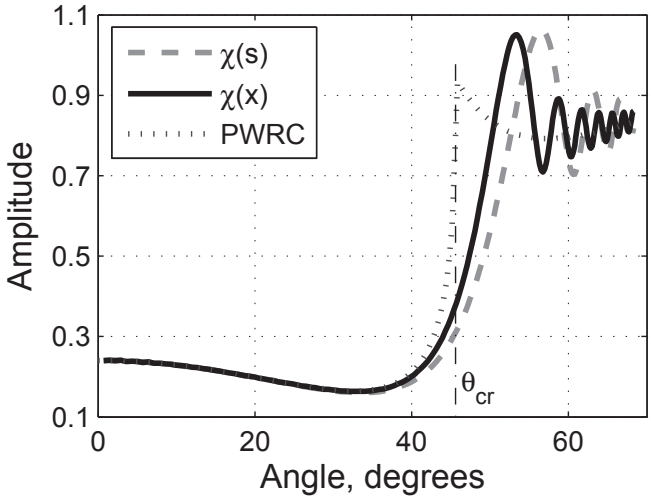

Figure 3.4: The ERC at the interface and the receiver calculated for a frequency of 32 Hz and a plane interface located at a depth of 1 km. The parameters of the upper half-space are $V_{P1} = 2$ km/s, $V_{S1} = 1.1$ km/s, $\rho_1 = 1.8$ g/cm^3, and the parameters of the lower half-space are $V_{P2} = 2.8$ km/s, $V_{S2} = 1.6$ km/s, $\rho_2 = 2.1$ g/cm^3. Plane-wave reflection coefficient (PWRC) is given for a comparison.

near-critical and post-critical offsets. The amplitude of the PWRC abruptly increases and reaches its maximum at the critical angle. The amplitudes of the ERCs increase smoothly in the vicinity of the critical angle and reach their maximum beyond it. Oscillations of the ERCs beyond the critical angle are induced by the interference of the reflected and head waves. The difference between the two ERCs at the near-critical and post-critical angles is associated with the transverse diffusion across the ray tube. The changing frequency of oscillations is explained by the changes in the interference between the reflected and head waves. Equations 12 and B-10 allow to generalize deterministic AVO inversion given by equations 1-3 for curved interfaces.

3.5 Synthetic modeling

The X and Z components of a 3D synthetic PP data are generated by the tip wave superposition method (TWSM) (Klem-Musatov et al., 2008; Ayzenberg et al., 2009). We use an omni-directional point source with the wavelet $S(t) = -\frac{\partial}{\partial t}\left[\exp^{-((2\pi ft)/\pi)^2}\sin(2\pi ft)\right]$. The wavelet has a bell-shaped amplitude spectrum

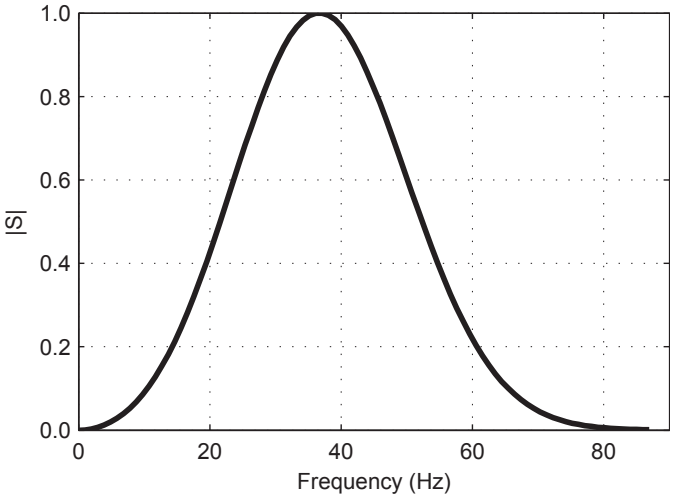

Figure 3.5: Wavelet spectrum for synthetic modeling.

$S(f)$ with a dominant linear frequency $f = \omega/2\pi$ of 39 Hz (Figure 3.5).

Simulations are performed for a model represented by two isotropic half-spaces separated by a curved interface. The medium parameters for the upper and lower half-spaces are $V_{P1} = 2$ km/s, $V_{S1} = 1.1$ km/s, $\rho_1 = 1.8$ g/cm^3, $V_{P2} = 2.8$ km/s, $V_{S2} = 1.6$ km/s, $\rho_2 = 2.1$ g/cm^3. The critical angle for the PP reflection is about 45^0.

The interface of a Gaussian shape has the following form in the global Cartesian coordinates $(x_1,\ x_2,\ x_3)$ (axis x_3 points upward):

$$x_3 = B + A\exp\left(-Cx_1^2 - Dx_2^2\right), \tag{15}$$

where B is chosen negative, C and D are the positive parameters controlling the interface steepness, and A is the maximal elevation or lowness of the interface. Anticlinal interfaces are characterized by positive values of A while synclinal interfaces are described by negative A.

To decrease the amount of computations dictated by the lateral extent of model, we consider only anticlinal interfaces as they generate relatively small Fresnel zones. We choose $B = -0.7$ km and $A = 0.2$ km in all tests. To avoid the smearing effect of reflection point within a CMP gather, we choose only one reflection point with the coordinates $x_1 = x_2 = 0,\ x_3 = -0.5$ km. The modeling is performed for two extreme types of interface; an isometric anticlinal interface with equal steepness parameters

($C = D = 1$ km^{-2}), and a linear anticlinal interface, where $C = 1$ km^{-2}and $D = 0$ km^{-2}. The interface geometries are shown in Figure 3.6.

The data is recorded at six different seismic lines; across the linear anticlinal interface, along the linear anticlinal interface and for the isometric anticlinal interface, as sketched in Figure 3.6. Lines 1, 2, 3 have common sources with lines 1a, 2a, 3a, respectively (lines with stars). Each source line consists of 53 point sources located at $x_3 = 0$ with a separation of 25 m. To monitor the influence of the propagation factor on the reflected wavefield, the data are recorded at two different depth levels. Receivers for lines 1, 2, 3 are located at $x_3 = 0$ km, receivers for lines 1a, 2a, 3a are buried at $x_3 = -0.4$ km (lines with triangles). Receiver lines consist of 53 receivers with a separation of 25 m (lines with $x_3 = 0$ km) and 5 m (lines with $x_3 = -0.4$ km). The different separations ensure same reflection angles for all lines. For all acquisition geometries, the minimum offset is zero. The synthetic data are obtained for a wide range of offset spread over the pre-critical, near-critical and post-critical domains.

Although the reflection angles are preserved for all the lines, the source-receiver offsets are different for the buried and non-buried receivers. This limits comparison of the data recorded at different depth levels. It is therefore convenient to analyze data versus source-zero offset h, as this distance is uniform for all the lines and proportional to the tangents of the reflection angles.

The main interface curvatures at the reflection point are $D_{11} = -0.4$ km^{-1} and $D_{22} = 0$ km^{-1} for lines 1 and 1a, $D_{11} = 0$ km^{-1} and $D_{22} = -0.4$ km^{-1} for lines 2 and 2a, $D_{11} = D_{22} = -0.4$ km^{-1} for lines 3 and 3a. D_{11} is an interface curvature along the shooting direction (in-line), while D_{22} is an interface curvature across the shooting direction (cross-line). The depth-interface curvature radius ratio for these models is 0.2, which is an indicator of a model with moderate interface curvatures.

Figure 3.7 shows fragments of the Z-component seismograms in the interference zone between the reflected and head waves for lines 1, 2 and 3. We observe that inline and crossline interface curvatures affect the amplitude strength and separation distance of the reflected and head waves. The weakest amplitude is registered when both the crossline and inline interface curvatures are non-zero (line 3). The strongest amplitude is observed for zero inline interface curvature (line 2). The shortest distance to the point of separation of reflected and head waves is observed when the crossline interface curvature is zero (line 1), whereas the longest distance to the separation point is noticed when the inline interface curvature is zero (line 2). The interface curvature also affects the angle between the moveouts of the reflected and head waves. This

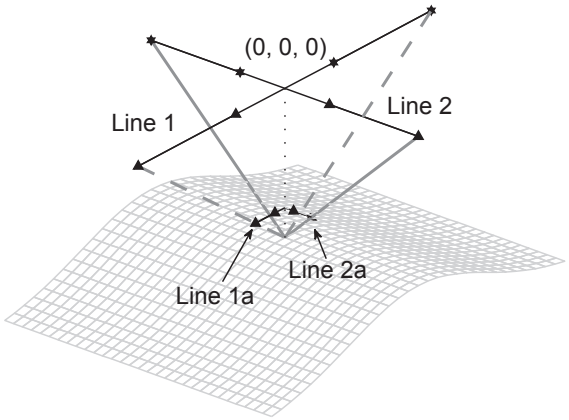

(a)

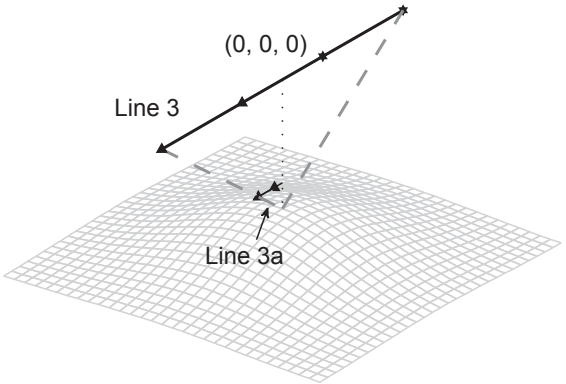

(b)

Figure 3.6: The anticlinal interfaces and acquisition geometry used for synthetic modeling. (a) A strongly asymmetric linear anticlinal interface, (b) An isometric anticlinal interface. Triangles denote receivers, stars denote sources.

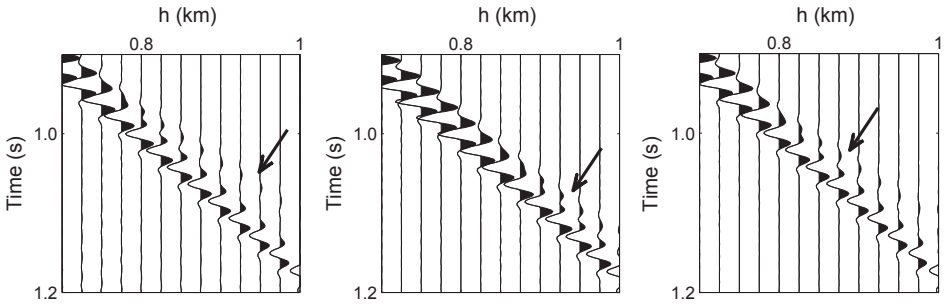

Figure 3.7: Fragments of seismograms for lines 1 (left), 2 (middle) and 3 (right) in the interference zone of the reflected and head waves. Arrows point to the head wave. h is source-zero offset distance.

results in different interferences between the two waves.

3.6 Data analysis

The RMS of the displacement vector magnitude $U_{PP}(\mathrm{x}_n) = \sqrt{U^2_{PP\,X}(\mathrm{x}_n) + U^2_{PP\,Z}(\mathrm{x}_n)}$ for lines 1, 2 and 3 calculated in a fixed time window are shown in Figure 3.8. The time window is chosen to be the same for all seismograms, which ensures comparable RMS amplitudes for all the lines. We observe that the strength of RMS amplitudes and position of RMS maximum differs.

Different RMS amplitudes for lines 1, 2 and 3 are explained by the energy loss along the ray tube associated with different interface curvatures. The strongest energy loss is observed for line 3, where both inline and crossline interface curvatures are non-zero. This effect is pronounced at any h. The energy loss is approximately the same for lines 2 and 3 at small offsets (0-0.5 km), while it is significantly less for line 2, where the inline interface curvature is zero.

The different positions of the maximum peak of the RMS curves are associated with the energy diffusion across the ray tube. The amplitude peak is related to the interference region of the reflected and head waves. The position of salient points behind the peak is correlated with the head wave separation in Figure 3.7. The width of the RMS amplitude peak is controlled by the separation angle between the reflected and head waves. A larger separation angle results in a narrower peak width. It is explained by the phase interference between the reflected and head waves. We observe

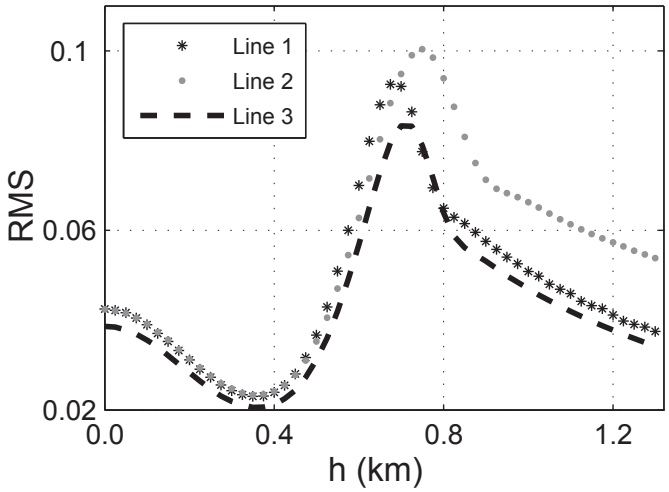

Figure 3.8: RMS amplitudes of the displacement vector for lines 1, 2 and 3

that the RMS amplitudes for the linear anticlines (lines 1 and 2) correspond to the two extreme cases in the maximum RMS positions and the width of their peak.

In the two following chapters, we analyze compensation of the contribution of interface curvature on the energy loss along the ray tube and the energy diffusion across the ray tube.

3.6.1 Energy propagation along the ray tube

Figure 3.9 illustrates the geometrical spreading for the six receiver lines compared to the geometrical spreading for the plane interface tangential to the actual interface at the reflection point computed at the receivers corresponding to depths of $x_3 = -0.4$ km and $x_3 = 0$ km. The geometrical spreading increases faster for the anticlinal interface than for the plane interface. The inline interface curvature affects the geometrical spreading more than the crossline interface curvature. This is especially pronounced at long offsets (above 0.5 km). Interface curvature has strongest impact on the geometrical spreading for the isometric anticlinal interface (lines 3a and 3). Geometrical spreadings for lines 1, 2 and 1a, 2a coincide at the pre-critical offsets (0-0.5 km). This confirms earlier observations in Figure 3.8. Figure 3.10 shows the extracted AVO data A_{obs} obtained by compensating the RMS amplitudes for the energy propagation along the ray tube using equation 2. The AVO data obtained at $x_3 = -0.4$ km and

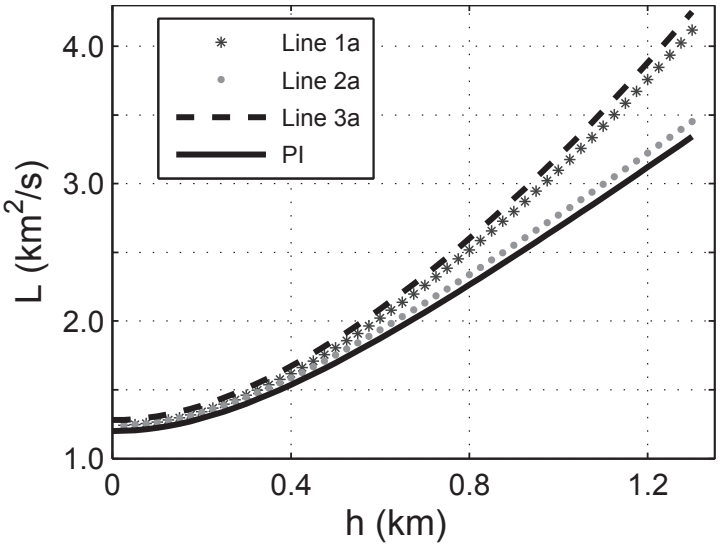

(a)

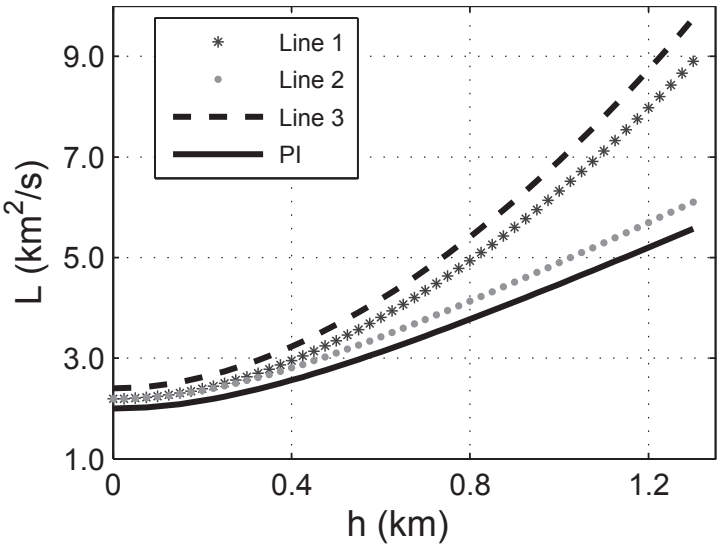

(b)

Figure 3.9: Geometrical spreading for the acquisition setup in Figure 3.6 for lines 1, 2 and 3 compared with geometrical spreading for the plane interface tangential to the actual curved interface at the reflection point (Pl). The geometrical spreading is calculated for receivers located at (a) $x_3 = -0.4$ km, (b) $x_3 = 0$ km.

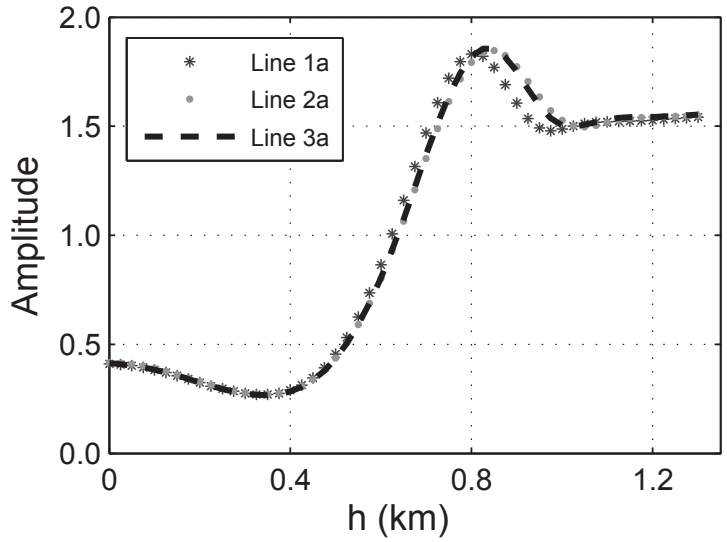

(a)

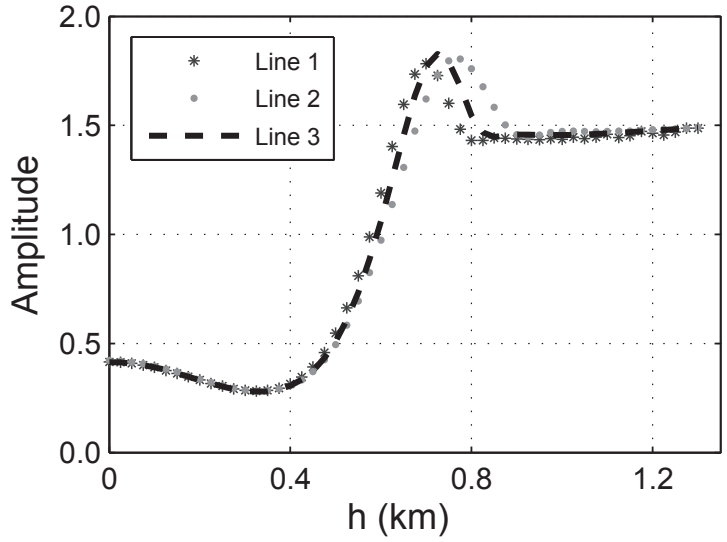

(b)

Figure 3.10: The observed AVO data A_{obs} obtained from the synthetic seismograms. (a) $x_3 = -0.4$ km, (b) $x_3 = 0$ km.

at $x_3 = 0$ km are shown in Figures 3.10a and 3.10b. The curvature dependence on the amplitude strength is successfully compensated and the AVO data coincide in the pre-critical domain (0-0.5 km) and in the post-critical domain (above 0.9 km).

3.6.2 Energy diffusion across the ray tube

The differences in the AVO data in Figure 3.10 result from the influence of the inline and crossline interface curvatures on the phase interference of the reflected and head wave. The differences are especially visible around the amplitude peak. A comparison of Figures 3.10a and 3.10b suggests that this influence is stronger at $x_3 = 0$ km than at $x_3 = -0.4$ km. This is explained by the contribution of the propagation factor $l\,(\mathrm{s}_n,\ \mathrm{x}_n)$ to the wavefront curvatures and, consequently, the interference of the reflected and head waves. The interference zone is smaller for larger values of the propagation factor. The amplitude peaks in Figures 3.10b are therefore narrower than the amplitude peaks in Figure 3.10a.

Figure 3.11 displays the apparent wavefront radii in equation 12 for the six lines. These are compared with the apparent wavefront radii for the plane interface calculated for $x_3 = -0.4$ km and $x_3 = 0$ km. We observe that the presence of inline and crossline interface curvatures reduces the apparent wavefront radii for $x_3 = -0.4$ km. This is consistent with Figure 3.3a. The strongest decrease in the apparent wavefront radius is observed for non-zero inline interface curvature (lines 2a and 3a). The smallest wavefront radius corresponds to non-zero inline and crossline interface curvatures (line 3a). A non-zero crossline interface curvature results in a decrease of the wavefront radius, while a non-zero inline interface curvature results in an increase of the wavefront radius relative to the one for the plane interface. The apparent wavefront radius for for the isometric anticlinal interface (line 3) lies between the radii for the linear anticlinal interface (lines 1 and 2). Figure 3.12 displays the modeled AVO data A_{mod} obtained from equation 3. The apparent wavefront radii in Figure 3.11 are used in the calculations. We observe that the relative shift in the position of amplitude peaks and the width of the amplitude peaks in Figure 3.12 are similar to those shown in Figure 3.10. We may therefore conclude that the approximations made in equations 3 and 12 qualitatively capture the main effects caused by inline and crossline interface curvatures and the propagation factor $l\,(\mathrm{s}_n,\ \mathrm{x}_n)$. However, the effect of the interface curvatures is quantitatively underestimated, since the shifts in the position of the amplitude peaks in the modeled AVO data are considerably smaller than the ones in the observed AVO data. This can be explained by the approximations in

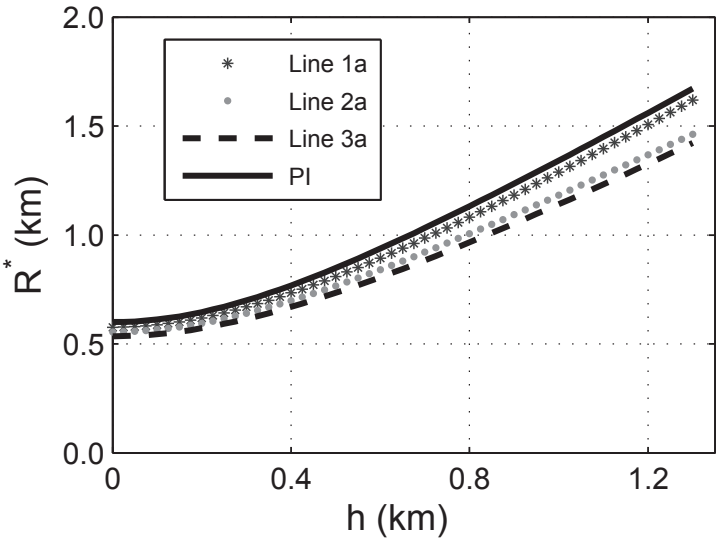

(a)

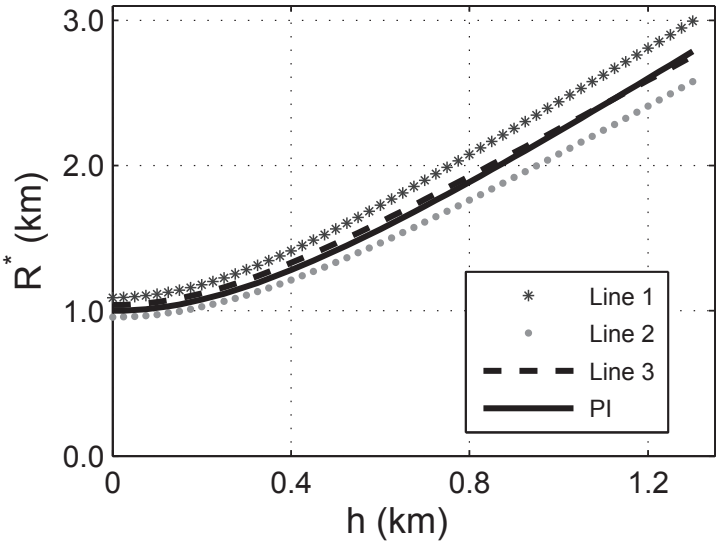

(b)

Figure 3.11: The apparent wavefront radius $r_P^*(\mathrm{x}_n)$ for the acquisition setup in Figure 3.6 compared with the wavefront radius for the plane interface tangential to the curved interface at the reflection point. (a) $x_3 = -0.4$ km, (b) $x_3 = 0$ km.

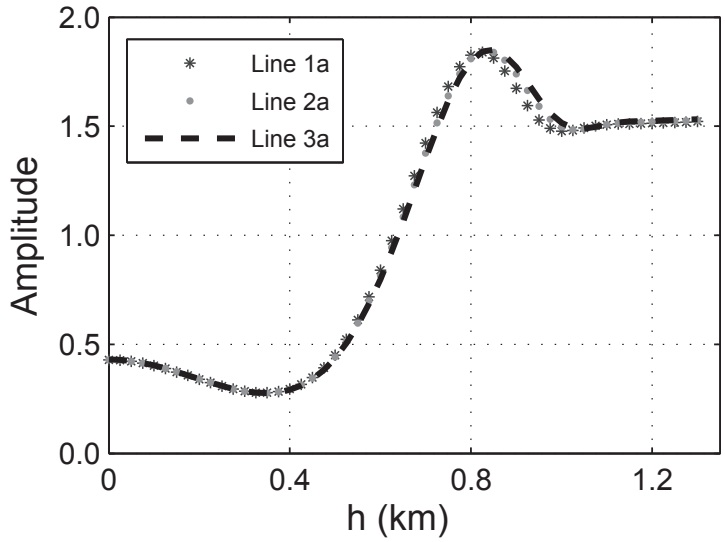

(a)

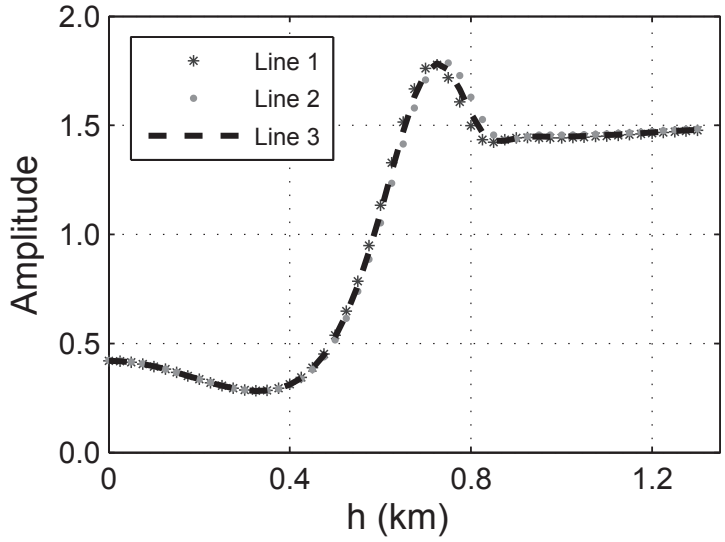

(b)

Figure 3.12: Modeled AVO data A_{teo} for the models in Figure 3.6 for receiver levels (a) $x_3 = -0.4$ km, (b) $x_3 = 0$ km.

equation 12.

The relative misfit between the extracted AVO data and the modeled AVO data is given by the formula

$$\Delta\left(\mathrm{x}_n\right) = \frac{AVO_{\mathrm{obs}}\left(\mathrm{x}_n\right) - AVO_{\mathrm{mod}}\left(\mathrm{x}_n\right)}{AVO_{\mathrm{obs}}\left(\mathrm{x}_n\right)}\,. \tag{16}$$

Here we assume that $AVO_{\mathrm{obs}}\left(\mathrm{x}_n\right) \neq 0$. The misfit is smaller for the data acquired at the $x_3 = -0.4$ km than at $x_3 = 0$ km (Figure 3.13). A 5% error at the pre-critical offsets (0-0.5 km) observed in Figure 3.13a can be explained by the numerical errors in the modeling algorithm for short distances between the interface and the receiver. We neglect such errors in our analysis and consider only the errors caused by mispositioning of the slopes of rapid amplitude changes and the amplitude peaks. Positive errors appear at the offsets where $A_{\mathrm{obs}} > A_{\mathrm{mod}}$, which indicates that the apparent radius is underestimated in our approximation. A comparison between different lines in Figure 3.13a shows that the values of $r^*_{PP}\left(\mathrm{x}_n\right)$ are underestimated for the non-zero inline interface curvature (lines 1a and 3a), and are overestimated for the zero inline interface curvatures and the non-zero crossline interface curvatures (line 2a). The relative misfit varies between 1.5% and 5%. At $x_3 = 0$ km (Figure 3.13b), the apparent wavefront radius is underestimated for line 1 and overestimated for the other two lines. The smallest relative misfit of 5% is observed for the isometric anticlinal interface (line 3). Since the best accuracy is achieved for the isometric anticlinal interface, we use this interface to monitor the behavior of the extracted AVO data A_{obs} for various curvatures (Figure 3.14a). We vary the steepness parameters $C = D = 1,\ 2,\ 4\ \mathrm{km}^{-2}$ and the main interface curvatures $D_{11} = D_{22} = -0.4,\ -0.8,\ -1.6\ \mathrm{km}^{-1}$. The depth to interface curvature radius ratio is 0.2, 0.4, 0.8. The data is recorded at $x_3 = 0$ km. For the three parameter values, the position of the amplitude peak in the observed AVO data shifts toward smaller h and the width of the amplitude peak becomes narrower with increasing curvature. This indicates that the apparent wavefront radius increases with curvature. Figure 3.14b shows that the relative misfit between the observed and the modeled AVO data in equation 16 increases with increasing interface curvature. This shows that the accuracy of our approximations in equations 3 and 12 decreases with increasing interface curvature.

Figures 3.13 and 3.14b illustrate that the ERCs corrected for the propagation term only partly account for interface curvature. There are two reasons for this. One source for systematic errors is related to the wavefront astigmatism, which is the half-difference between the main apparent wavefront curvatures. Ayzenberg et al.

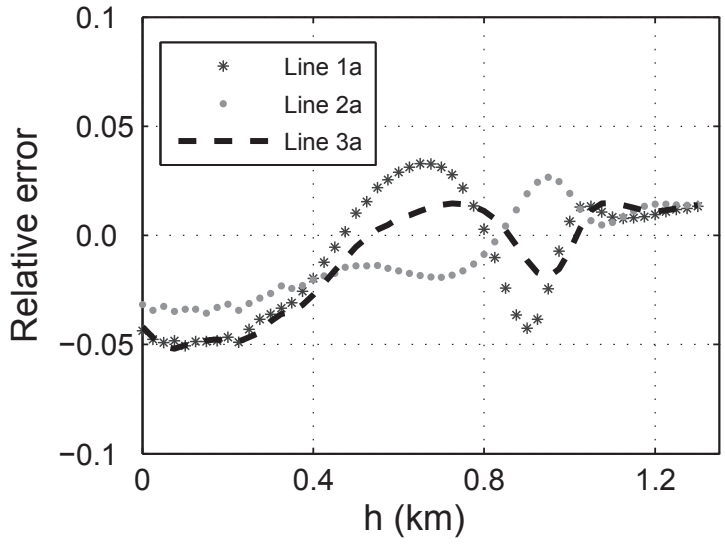

(a)

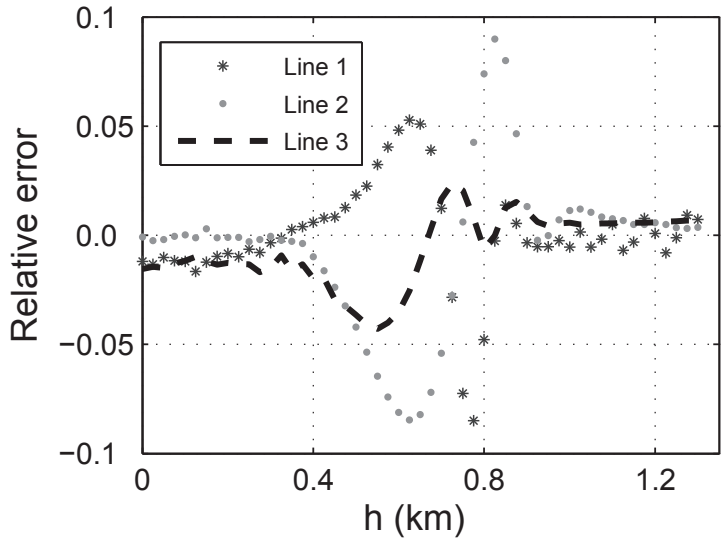

(b)

Figure 3.13: Relative misfit between the observed AVO data A_{obs} and the modeled AVO data A_{teo} at receiver levels (a) $x_3 = -0.4$ km, (b) $x_3 = 0$ km.

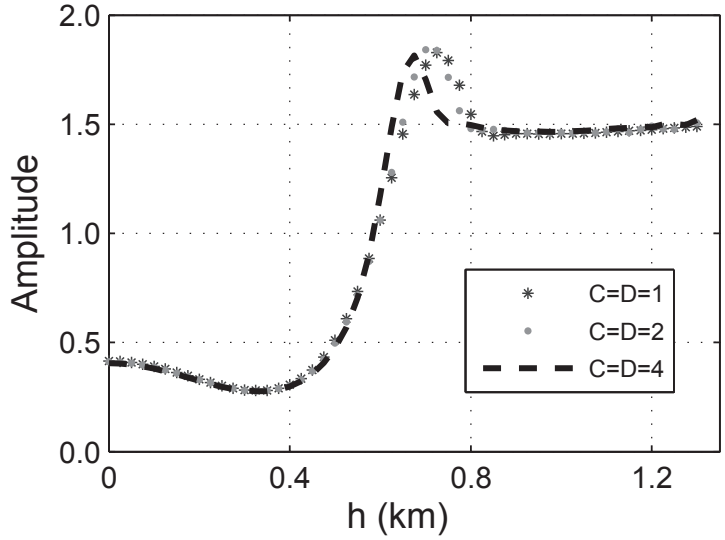

(a)

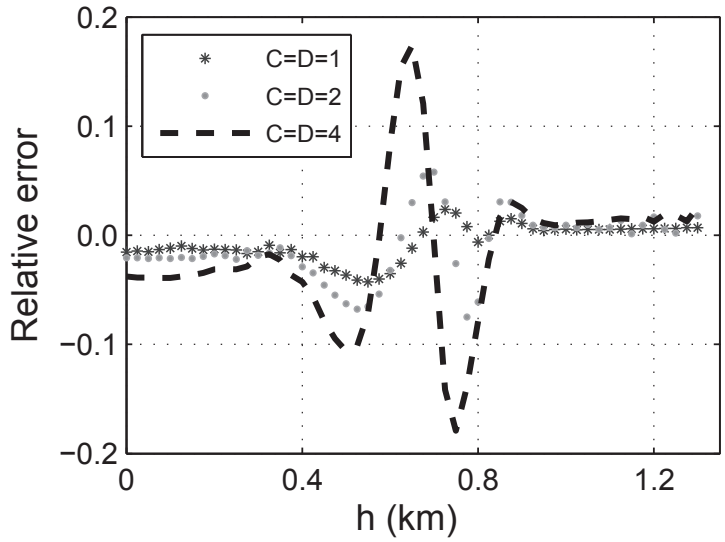

(b)

Figure 3.14: (a) Observed AVO data A_{obs} from the synthetic seismograms for the isometric anticlinal interface with different steepness parameters at receiver level $x_3 = 0$ km, (b) Relative misfit between the observed AVO data A_{obs} and the modeled AVO data A_{teo}.

(2007) neglected the astigmatic term in their derivations of the ERC. We also neglect the astigmatic term. The astigmatism is however incorporated in the synthetic data and its effect increases with increasing propagation term. The relative misfit between the observed and modeled AVO data is therefore larger at $x_3 = 0$ km than at $x_3 = -0.4$ km (Figure 3.13). The wavefront astigmatism is affected by the inline and crossline interface curvatures. Figure 3.13 illustrates a somewhat higher impact of the astigmatism for linear interface than for the isometric interface, as the misfit between the observed and the modeled AVO data is larger for the linear interface. Figure 3.14b indicates that the wavefont astigmatism increases with increasing interface curvature. All the examples thus show that astigmatism can not be neglected for strongly asymmetric interfaces and isometric interfaces, where the depth to interface curvature radius ratio is greater than 0.2.

Another source of errors is the approximate way of including the propagation term in the ERC. We assume that the apparent wavefront curvature matrices are frequency independent and assume ray theory (Appendix 3.11). In practice, the data is recorded within a finite seismic frequency band. Our approach to model the AVO data is thus a hybrid of ray theory used to include the propagation term and seismic wave theory used to describe the phenomena around the critical ray (Klem-Musatov et al., 2004). The combination provides a reasonably accurate approximation of the diffusion phenomena across the ray tube. The computational cost of the proposed method is relatively low.

3.7 AVO inversion of long-offset synthetic data

To assess the importance of compensation of interface curvature in the observed and the modeled AVO data (equations 2 and 32), we perform AVO inversion for three different scenarios. In scenario 1, we assume that no information about the interface curvature is available such that the geometrical spreading correction and the modeled AVO data are computed for zero inline and crossline interface curvatures. In scenario 2, we compute the geometrical spreading for the true interface curvatures, but the modeled AVO data are still computed for the plane interface. The purpose of this test is to assess the impact of incorrectly modeled AVO data, while the geometrical spreading is computed properly. In scenario 3, we compute the geometrical spreading and the modeled AVO data for true inline and crossline interface curvatures.

We exploit the nonlinear optimization method of Nelder-Mead to minimize the objec-

tive function in equation 1 (Himmelblau, 1972). An initial guess for estimated media parameters is chosen within ±20% of parameter deviations from true values, as the objective function is an unimodal function within this range (Skopintseva et al., 2011). In order to investigate the effect of interface curvature only, a noise-free inversion is performed and the seismic parameters in the overburden are assumed to be known. We estimate the remaining parameters V_{P2}, V_{S2} and ρ_2.

The available range of offsets is 0-1.3 km. We set the minimal offset to $h_{\min} = 0$ km and vary $h_{\max}$ between 0.1 km and 1.3 km with an increment of 0.075 km. The initial guess for each parameter deviates by 15% from the true model value. Figure 3.15 illustrates the relative errors in the AVO inversion results for the data in Figure 3.10b. The least stable estimates are obtained for the offset ranges with $h_{\max}$ varying between 0.1 km and 0.5 km. These offsets characterize pre-critical reflections. The use of near-critical and post-critical reflections decreases the relative errors and stabilize the parameter estimates. The error levels for scenarios 1 and 2 show that inaccurate geometrical spreading mostly affects the inversion results in the post-critical domain $0.6 < h_{\max} < 1.3$ km for the models with non-zero inline interface curvatures (lines 1 and 3). A significant improvement in the parameter estimates is achieved with accurate geometrical spreading correction. However, accurate geometrical spreading does not affect the inversion results for the non-zero crossline and zero inline curvatures (line 2). It is explained by the offset-independent ratio of the our geometrical spreading to the conventional geometrical spreading (Figure 3.9). Application of a more accurate or the conventional geometrical spreading results in the same AVO data for line 2, because all the offset-independent terms are removed during the normalization in equation 2.

The inversion can be further improved by including interface curvature in the modeled AVO data (scenario 3 in Figure 3.15). We observe that different lines provide different levels of errors in parameter estimates, which is explained by the approximations in equations 3 and 12. An overestimated apparent wavefront radius in the modeled AVO data results in an underestimated P-wave velocity in the underburden (lines 2 and 3), while an underestimated apparent wavefront radius results in an overestimated P-wave velocity. Figure 3.16 (left) displays the relative misfit between the observed and the modeled AVO data calculated for the true V_{P1}, V_{S1}, ρ_1, V_{S2}, ρ_2 and the estimated V_{P2}. The P-wave velocities are inverted for an offset range 0-1.3 km (Table 3.1). Comparison of Figures 3.16 (left) and 3.13b shows that the P-wave velocity mainly controls the AVO behavior in the zone of rapid amplitude increase ($0.6 < h < 0.9$ km). The increased relative misfits at moderate offset ranges ($0.2 < h < 0.6$ km) in

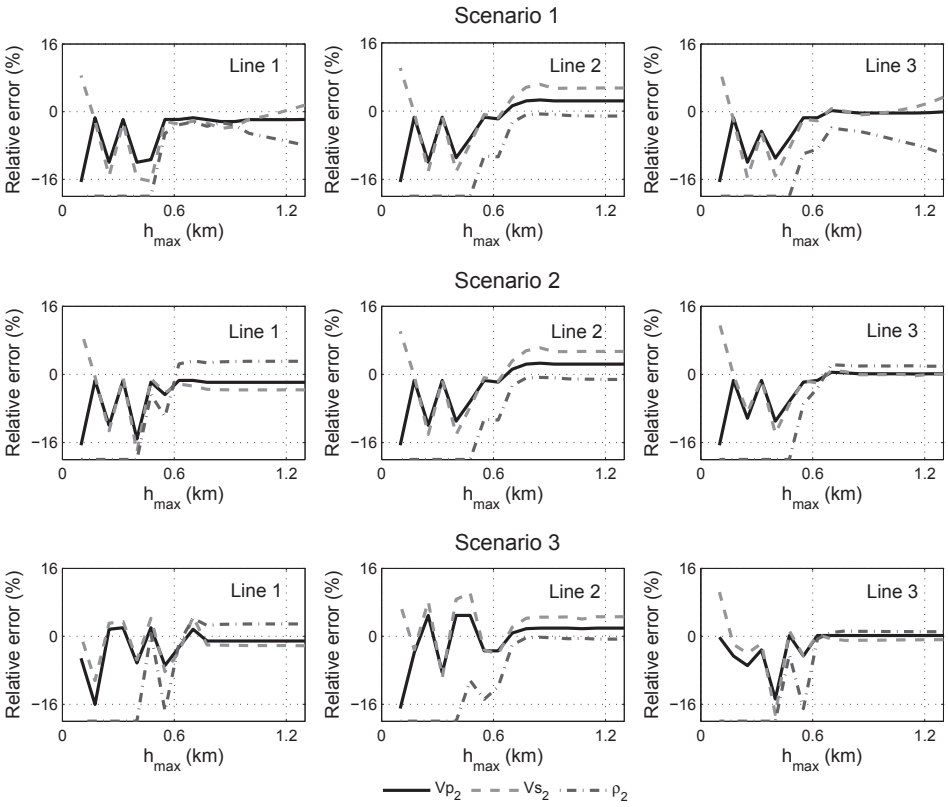

Figure 3.15: Relative error in the inversion results for scenarios 1, 2 and 3. The steepness parameters are $C = D = 1$ km^{-2} for line 3 and $C = 1$; $D = 0$ km^{-2} for line 1 and line 2. Negative errors correspond to larger values in parameter estimates compared with the true model parameters, while positive errors represent underestimated model parameters.

Figure 3.16 (left) and their absense in Figure 3.16 (middle) indicates that the zone of moderate offsets is mainly controlled by V_{S2}. In Figure 3.16 (middle), we keep the true values of V_{P1}, V_{S1}, ρ_1 and ρ_2, whereas the values for V_{P2} and V_{S2} are taken from Table 3.1. We conclude that the positive relative misfit between observed and modeled AVO data in Figure 3.16 (left) results in an underestimated V_{S2}, while the negative relative misfit overestimates V_{S2}. We find from Figures 3.16 (middle) and 3.16 (right) that the AVO data are sensitive to the density for $0 < h < 0.2$ km and $h > 0.9$ km. In Figure 3.16 (right), we keep the true values for V_{P1}, V_{S1}, ρ_1 and assign

the inverted values to V_{P2}, V_{S2}, ρ_2 (Table 3.1). The positive relative misfit between the observed and the modeled AVO data at $0 < h < 0.2$ km and the negative misfit at $h > 0.9$ km result in an overestimated density, and vice versa.

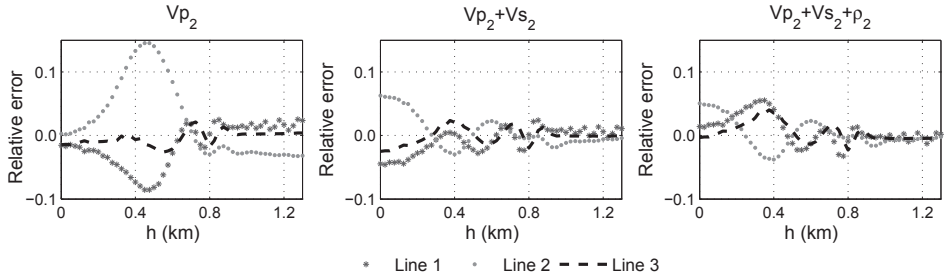

Figure 3.16: Relative misfit between the observed AVO data A_{obs} and the modeled AVO data A_{mod}. Left: AVO data calculated for the true values of V_{P1}, V_{S1}, ρ_1, V_{S2} and ρ_2 and the inverted value of V_{P2} in Table 3.1. Middle: AVO data calculated for the true values of V_{P1}, V_{S1}, ρ_1, ρ_2 and the inverted values of V_{P2} and V_{S2} in Table 3.1. Right: AVO data calculated for the true values of V_{P1}, V_{S1}, ρ_1 and the inverted values of V_{P2}, V_{S2} and ρ_2 in Table 3.1.

Table 3.1: Parameter estimates performed by AVO inversion for offset range $0 - 1.3$ km

	V_{P2}, km/sec	ΔV_{P2}, %	V_{S2}, km/sec	ΔV_{S2}, %	ρ_2, kg/m^3	$\Delta\rho_2$, %
line 1	2830	-1.1	2745	-2.2	2038	2.9
line 2	2745	1.9	1526	4.6	2114	-0.7
line 3	2795	0.14	1612	-0.01	2077	1.9

The errors in the AVO inversion results for the isometric anticlinal interface with various curvatures are displayed in Figure 3.17. We consider scenarios 2 and 3. Similarly to Figure 3.15, the accuracy of parameter estimates is unstable for offsets $0.1 < h_{\max} < 0.5$ km. The accuracy stabilizes when the near-critical and post-critical offsets are included in the inversion. The error in parameter estimates increases with increasing interface curvature. A negligible improvement of the in the inversion results is achieved for scenarios 2 and 3 when interface curvature is included in the diffusion across the ray tube.

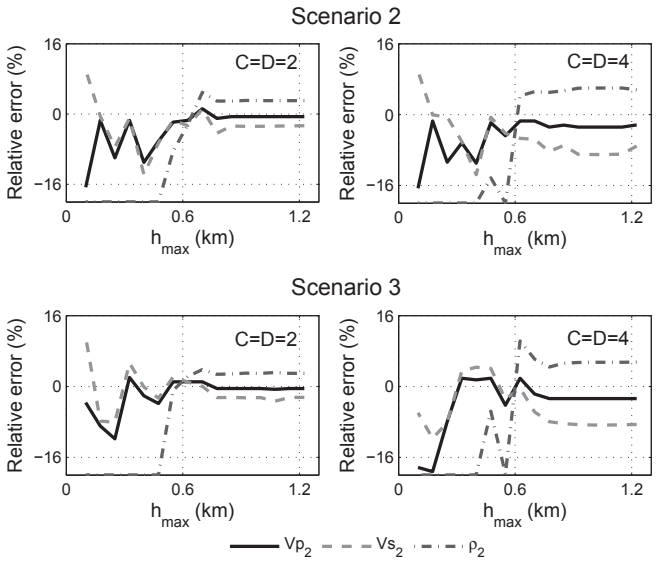

Figure 3.17: Relative errors in the inversion results for the isometric anticlinal interface with different interface curvatures for scenarios 2 and 3. Negative errors correspond to overestimated parameters and positive errors represent underestimated model parameters.

The relative behavior of the errors in estimated parameters in Figure 3.17 is similar to the ones for line 1 in Figure 3.15. The inversion of the post-critical offsets overestimates P-wave and S-wave velocities and underestimates the density in the underburden. This happens because of the underestimated apparent wavefront radii in the vicinity of amplitude peak (Figure 3.14b).

3.8 Discussion

Analysis of AVO data reflected at curved interfaces is not a straightforward task. Three facts need to be taken into consideration, namely the capabilities of the acquisition system to record sufficient aperture and spatial sampling of the data, the following processing which provide us with the data to invert, and the limitations of the theory describing the observed data which will contribute to the objective function in a deterministic inversion.

A potential pitfall for the majority of AVO inversion methods including our technique is the presence of shadow zones within the Fresnel zone of the specular ray. Shadow zones will result in cascade diffraction, which has a different physical nature than the specular reflections which we use as the basis for our AVO inversion approach. We avoided the topic of shadow zones in our tests by limiting the ratio of the interface depth to the interface curvature radius to a range of 0 to 0.8. We did not intend to study the effect of shadow zones on AVO response and thus avoided models where synthetic seismic modeling would produce unreliable that would be difficult to interpret.

The input data to AVO inversion is usually time-migrated. This partly compensates for the effects of wave propagation, in particular removes the geometrical spreading. A true-amplitude imaged data (see, for example, Arntsen et al. (2010)) can be directly inverted for seismic parameters based on equations 4-6. However, conventional true-amplitude migration algorithms are not valid for the near-critical and post-critical angles as they are designed for the reflected waves only, and do not treat the amplitudes of the head waves correctly. The data at large offsets are often muted because of the interference between the reflected and head waves and low signal-to-noise ratio. Prior to being used in a long-offset AVO inversion, the data has to be exposed to a dedicated pre-processing.

Another important issue is related to the availability of information about interface curvatures. Interface curvatures can theoretically be obtained from structural image of the subsurface. Today we are able to estimate local interface slopes with sufficient accuracy, while estimation of local interface curvatures is a tedious and highly uncertain problem. We, however, believe that the current challenges of data processing should not stop the development of advanced methods for AVO inversion of long-offset data.

The method we develop captures the major effects of wave propagation in the modeled AVO data, such as the geometrical spreading of the ray tube as function of interface curvature. We show that these are strongly dependent on the local reflector geometry and should not be neglected. However, in our approximations we neglect some of the effects which may also contribute to the AVO behavior. One of them is the asymmetry of the wavefront which consider as a second-order effect and it was therefore disregarded for the sake of simplicity of the formulas and reduced computational time. This motivates us for further search for improved approximations of the ERC. We believe that a more comprehensive study of the diffusion phenomena affecting the

phase interference of the reflected and head waves and, as a consequence, the ERC should be conducted.

3.9 Conclusions

Interface curvature is encoded in AVO data and affects both the amplitude and the phase of reflected wave. We show that these effects become prominent for ratios of depth to interface curvature radius greater than 0.2 and are observable at both short, moderate and long offsets. Interface curvature shall not be neglected, as this significantly reduces the accuracy of the AVO inversion.

We found that interface curvature is manifested both in the energy loss along the ray tube and in the transverse energy diffusion across the ray tube. The energy loss along the direction of propagation is described with sufficient accuracy by ray theory an the dynamic ray tracing equations. Geometrical spreading plays a vital role in the recovery of true amplitudes and its accuracy is therefore of high importance. The AVO inversion tests clearly show that an incorrect geometrical spreading results in lower accuracy of the inversion results.

The transverse energy diffusion across the ray tube is contained in the phase interference of the reflected and head waves and is to a large extent captured by the ERC (effective reflection coefficient). Based on a detailed study of the ERC, we conclude that interface curvature mostly affects the near-critical and post-critical offsets, i.e. the zone of interference of the reflected and head waves. The ERC qualitatively describes the position of the amplitude peak as function of interface curvature. The actual approximation neglects the wavefront astigmatism and is reasonably accurate for moderate interface curvatures. It should therefore be used with care.

Our numerical tests show that despite all the approximations, the ERC-based AVO inversion provides stable estimates of the model parameters when the near-critical and post-critical offsets are incorporated. Although the relative error in the inversion results varies within a few percent limit for various acquisition directions and offset ranges, the figures show obvious benefits of using the ERC and offsets beyond the critical angle in the AVO inversion. This motivates us for further search for improved approximations of the ERC. We believe that a more comprehensive study of the diffusion phenomena affecting the phase interference of the reflected and head waves and, as a consequence, the ERC should be conducted.

3.10 Acknowledgments

Lyubov Skopintseva acknowledges Statoil ASA for financing her PhD study at NTNU. The authors are grateful to Statoil ASA and the Russian Foundation for Basic Research (grant 07-05-00671) for support of this work and the Norwegian Research Council for financial support of the ROSE project at NTNU. We thank Alexey Stovas for constructive suggestions which helped us to improve the paper.

3.11 Appendix A: Reflected PP-wavefield in terms of ERC

Here we derive an approximate description for the P-wave reflected at a curved interface between two homogeneous isotropic half-spaces. Our aim is to find a form which resembles the ray-theoretical formula, includes the ERC and is valid for a finite frequency bandwidth (Ayzenberg et al., 2007, 2009).

The reflected PP-wavefield at receiver can be represented by the Kirchhoff propagation integral

$$\mathbf{u}_{PP}\,(\mathrm{x}) = \iint\limits_{S} \mathbf{P}_P\,(\mathrm{x}\,;\,\mathrm{s})\;\mathbf{u}_{PP}\,(\mathrm{s})\;\,d\mathrm{s}\;, \tag{A-1}$$

where $\mathbf{P}_P\,(\mathrm{x}\,;\,\mathrm{s})$ is the kernel of operator based on the Green function, s and x are the coordinates of the reflection point and receiver in the global Cartesian system of coordinates $(x_1,\ x_2,\ x_3)$, and $d\mathrm{s} = ds_1\,ds_2$. The reflected PP-wavefield at interface is given by the reflection integral of convolutional type

$$\mathbf{u}_{PP}\,(\mathrm{s}) = \frac{1}{2\pi}\iint\limits_{S'} \mathrm{R}_{\mathrm{PP}}\,(\mathrm{s}')\;\mathbf{u}^*_P\,(\mathrm{s}-\mathrm{s}')\;\,d\mathrm{s}', \tag{A-2}$$

where $\mathbf{u}^*_P\,(\mathrm{s}-\mathrm{s}',\ \omega)$ is the incident wavefield generated by the apparent source, which is located below the interface such that its polarization coincides with the polarization of the actual reflected wavefield, $\mathrm{R}_{\mathrm{PP}}\,(\mathrm{s}')$ is the reflection operator for PP-waves, s' is a point at the interface, $d\mathrm{s}' = ds'_1\,ds'_2$. More details about equations A-1 and A-2 can be found in Skopintseva et al. (2011).

There are two different mechanisms for energy propagation described in equation A-1; the propagation along the ray tube (Červený, 2001) and the energy diffusion

across the ray tube (Klem-Musatov et al., 2008). These mechanisms are sketched in Figure 3.18a. Figure 3.18b illustrates the action of operator $\mathrm{R_{PP}}\,(\mathrm{s}')$ in equation A-2. Operator $\mathrm{R_{PP}}\,(\mathrm{s}')$ acts as the summation of the plane waves constituting the incident wavefield and weighted by the corresponding PWRC. Reflected field $\mathbf{u}_{PP}\,(\mathrm{s})$ contains contributions from all points s′.

Equation A-2 can be approximately rewritten as (Ayzenberg et al., 2009)

$$\mathbf{u}_{PP}\,(\mathrm{s}) \cong \chi_{PP}\,[\mathrm{s},\ \omega]\ \frac{i}{V_{P1}}\ S\,(\omega)\ \frac{e^{i\,k_P\,l(\mathrm{s})}}{\sqrt{J_{PP}\,(\mathrm{s})}}\ \mathbf{e}_{PP}\,(\mathrm{s})\ , \tag{A-3}$$

where $S\,(\omega)$ is the wavelet spectrum for the displacement wavefield, V_{P1} is the P-wave velocity in the underburden, $J_{PP}\,(\mathrm{s})$ is the geometrical spreading at the reflection point, $\mathbf{e}_{PP}\,(\mathrm{s})$ is the polarization vector of the reflected field, $l\,(\mathrm{s})$ is the distance between the actual source and the reflection point, $\chi_{PP}\,[\mathrm{s},\ \omega] = \chi_{PP}\,[\theta\,(\mathrm{s})\,,\ k_P\ r^*_{PP}\,(\mathrm{s}),\ \mathbf{m}]$ is PP-wave ERC at the interface, $\theta\,(\mathrm{s})$ is the incidence angle. The apparent wavefront curvature radius $r^*_{PP}\,(\mathrm{s})$ has the following form (Ayzenberg et al., 2007):

$$r^*_{PP}\,(\mathrm{s}) = \frac{1+\cos^2\theta\,(\mathrm{s})}{\cos^2\theta\,(\mathrm{s})\left[\frac{1}{l(\mathrm{s})} - \frac{D_{11}(\mathrm{s})}{\cos\theta(\mathrm{s})}\right] + \left[\frac{1}{l(\mathrm{s})} - \cos\theta\,(\mathrm{s})\,D_{22}\,(\mathrm{s})\right]}, \tag{A-4}$$

where $D_{11}\,(\mathrm{s})$ and $D_{22}\,(\mathrm{s})$ are the main interface curvatures in and out of the incidence plane defined in the local Cartesian coordinates (z_1, z_2, z_3) (Appendix 3.12). For plane interfaces, $r^*_{PP}\,(\mathrm{s}) = l\,(\mathrm{s})$.

Skopintseva et al. (2011) obtained an approximate formula the reflected wavefield A-1 at the receiver for plane interfaces:

$$\mathbf{u}_{PP}\,(\mathrm{x}) \cong \chi_{PP}\,[\mathrm{x},\ \omega]\ \frac{i}{V_{P1}}\ S\,(\omega)\ \frac{e^{i\,k_P\ (l(\mathrm{s})+l(\mathrm{x},\,\mathrm{s}))}}{\sqrt{J_{PP}\,(\mathrm{x})}}\ \mathbf{e}_{PP}\,(\mathrm{s})\ . \tag{A-5}$$

where $\chi_{PP}\,[\mathrm{x},\ \omega] = \chi_{PP}\,[\theta\,(\mathrm{x})\,,\ k_P\ r^*_{PP}\,(\mathrm{x}),\ \mathbf{m}]$ is the PP-wave ERC at the receiver, $l\,(\mathrm{x}\,,\mathrm{s})$ is the distance between the reflection point and the receiver, $J_{PP}\,(\mathrm{x})$ is the geometrical spreading at the receiver, $r^*_{PP}\,(\mathrm{x}) = l\,(\mathrm{s}) + l\,(\mathrm{x},\ \mathrm{s})$ is the apparent wavefront radius at the receiver. Equation A-5 resembles the well-known equation from asymptotic ray theory. The difference is the reflection coefficient, where the PWRC is replaced with the ERC. We also observe that the structure of equation A-5 is similar to that of equation A-3.

Equation A-5 follows from the analytical evaluation of integral A-1 with the boundary conditions A-3. For plane interfaces, equation A-1 is given by a convolutional integral.

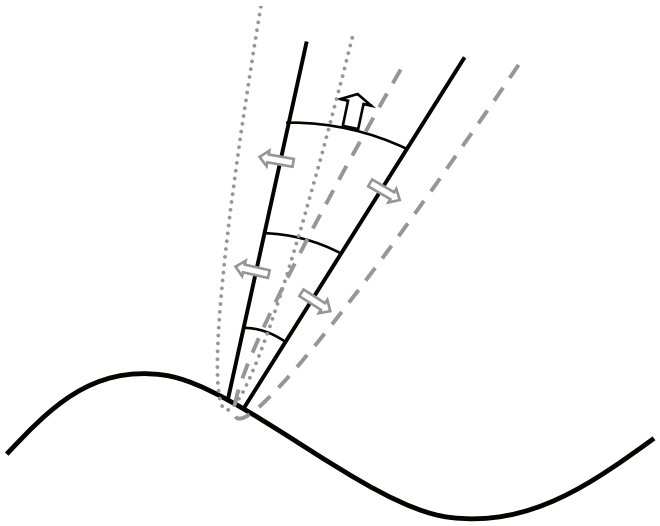

(a)

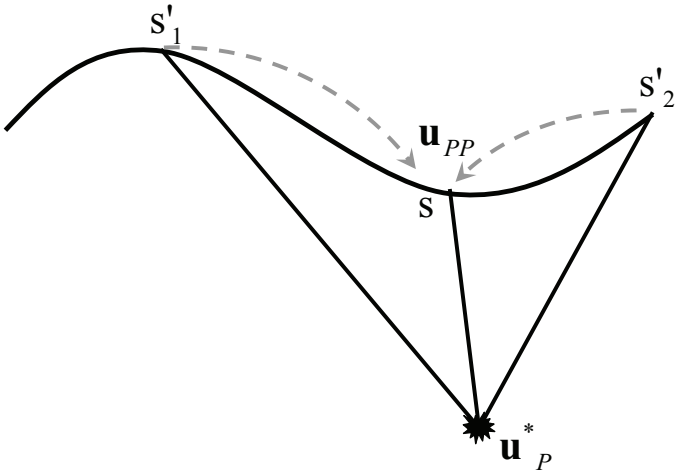

(b)

Figure 3.18: Scheme of (a) propagation and (b) reflection of the wave generated by a point source.

We are thus able to evaluate this integral analytically by permutation of integrals A-1 and A-2. For curved interfaces, integral A-1 is no longer a convolutional integral. Its exact analytical evaluation with the boundary values A-3 is yet unknown. To obtain analytical representation of the reflected PP-wavefield through the ERC, we cannot apply numerical or high-frequency asymptotic methods. We use instead a heuristic approach based on the similarity between the structures of reflected and head waves in the vicinity of the reflection point and the receiver. We also notice that the forms of equations A-3 and A-5 are similar and the number of independent parameters in these equations is the same. These similarities allow us to assume that the form of equation A-5 is valid for curved interfaces, according to Buckingam pi-theorem (Bluman and Kumei, 1989).

According to equations A-3 and A-4 and Červený (2001), interface curvatures affect $\chi_{PP}\left[\mathrm{x},\ \omega\right]$ and $J_{PP}\left(\mathrm{x}\right)$ in equation A-5. The equation for the geometrical spreading for curved interfaces is derived by Červený (2001) and summarized in Appendix 3.12. The form of $\chi_{PP}\left[\mathrm{x},\ \omega\right]$ is controlled by parameter $r^{*}_{PP}\left(\mathrm{x}\right)$, which is to be defined.

We recall that the incident wavefield is a spherical P-wave, while the reflected wavefield is an interference of the reflected PP-wave and the PPP-head wave. For plane interfaces, the wavefronts of the reflected and head waves are spherical and conical. The phase interference of the two waves is defined by the difference of their wavefront curvatures only in incidence plane, as it is zero in the plane orthogonal to the incidence plane. On one hand, curvature $\frac{1}{r^{*}_{PP}(\mathrm{s})}$ of the reflected wavefront is equal to the curvature of the incident wavefront. On the other hand, curvature $\frac{1}{r^{*}_{PP}(\mathrm{s})}$ of the reflected wavefront represents the difference between the wavefront curvatures of the reflected and head waves within the incidence plane, where the wavefront curvature of the head wave is equal to zero. Similarly, the wavefront curvature $\frac{1}{r^{*}_{PP}(\mathrm{x})}$ of the apparent reflected wave at the receiver can be considered as the difference between the wavefront curvatures of the reflected and head waves at the receiver.

We assume that the properties of the wavefronts of the reflected and head waves are known for plane interfaces and are valid for curved interfaces. The wavefronts are tangent in the vicinity of the critical ray, and have different phases in the interference zone. The interface curvature at the reflection point results in a deviation of the wavefronts of the reflected and head waves from spherical and conical shapes. We thus need to compensate for these deviations in quantities $r^{*}_{PP}\left(\mathrm{s}\right)$ and $r^{*}_{PP}\left(\mathrm{x}\right)$.

We introduce a matrix describing the distortion of the wavefront of the head wave at

the reflection point by representing matrix $\mathbf{D}\,(\mathrm{s})$ of interface curvatures in the form

$$\mathbf{D}\,(\mathrm{s}) = \mathbf{D}_1\,(\mathrm{s}) + \mathbf{D}_2\,(\mathrm{s})\,, \tag{A-6}$$

where

$$\mathbf{D}_1\,(\mathrm{s}) = \begin{bmatrix} D_{11}\,(\mathrm{s}) & 0 \\ 0 & 0 \end{bmatrix},\ \mathbf{D}_2\,(\mathrm{s}) = \begin{bmatrix} 0 & D_{12}\,(\mathrm{s}) \\ D_{12}\,(\mathrm{s}) & D_{22}\,(\mathrm{s}) \end{bmatrix}.$$

Equation A-6 is defined in the local Cartesian coordinates (Appendix 3.12). The incidence plane coincides with the plane of the maximum phase difference between the wavefronts of the reflected and head waves. We therefore consider

$$\delta\tilde{\mathbf{F}}\,(\mathrm{s}) = -\cos\theta\,(\mathrm{s})\ \mathbf{D}_1\,(\mathrm{s}) \tag{A-7}$$

as the matrix representing the deviation of wavefront of the head wave from conical.

For simplicity of derivations, we consider the curvature matrices in the ray-centered coordinates. We rotate matrix A-7 by angle $\theta\,(\mathrm{s})$:

$$\begin{aligned} \delta\tilde{\mathbf{K}}\,(\mathrm{s}) &= \mathbf{G}\,[\theta\,(\mathrm{s})]^{-1}\,\delta\tilde{\mathbf{F}}\,(\mathrm{s})\,\mathbf{G}\,[\theta\,(\mathrm{s})]^{-1} = \\ &= \begin{bmatrix} -\frac{D_{11}(\mathrm{s})}{\cos\theta(\mathrm{s})} & 0 \\ 0 & 0 \end{bmatrix}, \end{aligned} \tag{A-8}$$

where $\mathbf{G}\,[\theta\,(\mathrm{s})]$ is the rotation matrix (Appendix 3.12). In the special case of cylindrical interface with non-zero curvature in the incident plane, it is easy to see that A-8 describes bending of the conical wavefront of the head wave along the interface. By rewriting equation A-4 using equations A-8 and B-5, we obtain

$$r_P^*\,(\mathrm{s}) = \frac{1 + \cos^2\theta\,(\mathrm{s})}{\cos^2\theta\,(\mathrm{s})\ \left[\tilde{K}_{11}\,(\mathrm{s}) - \delta\tilde{K}_{11}\,(\mathrm{s})\right] + \tilde{K}_{22}\,(\mathrm{s})}\,, \tag{A-9}$$

where term $\tilde{K}_{11}\,(\mathrm{s}) - \delta\tilde{K}_{11}\,(\mathrm{s})$ is the phase difference between the reflected and head waves in the incidence plane. This explains the choice of the matrix form in equation A-7.

By separating the reflected wavefield B-4 at the reflection point from the part related to head wave, we find the matrix of relative curvatures for the reflected P-wave at the reflection point:

$$\begin{aligned} \tilde{\mathbf{F}}^*\,(\mathrm{s}) &= \mathbf{G}\,[\theta\,(\mathrm{s})]\ \tilde{\mathbf{K}}\,(\mathrm{s})\ \mathbf{G}\,[\theta\,(\mathrm{s})] + \cos\theta\,(\mathrm{s})\ \mathbf{D}_2\,(\mathrm{s}) = \\ &= \begin{bmatrix} \frac{\cos^2\theta(\mathrm{s})}{l(\mathrm{s})} - 2\ \cos\theta\,(\mathrm{s})\ D_{11}\,(\mathrm{s}) & -\cos\theta\,(\mathrm{s})\ D_{12}\,(\mathrm{s}) \\ -\cos\theta\,(\mathrm{s})\ D_{12}\,(\mathrm{s}) & \frac{1}{l(\mathrm{s})} - \cos\theta\,(\mathrm{s})\ D_{22}\,(\mathrm{s}) \end{bmatrix}, \end{aligned} \tag{A-10}$$

which has the following form in the ray-centered coordinates:

$$\begin{aligned}\tilde{\mathbf{K}}^{*}(\mathrm{s}) &= \mathbf{G}\left[\theta(\mathrm{s})\right]^{-1}\ \tilde{\mathbf{F}}^{*}(\mathrm{s})\ \mathbf{G}\left[\theta(\mathrm{s})\right]^{-1} = \\ &= \begin{bmatrix} \frac{1}{l(\mathrm{s})} - 2\,\frac{D_{11}(\mathrm{s})}{\cos\theta(\mathrm{s})} & -D_{12}(\mathrm{s}) \\ -D_{12}(\mathrm{s}) & \frac{1}{l(\mathrm{s})} - \cos\theta(\mathrm{s})\ D_{22}(\mathrm{s}) \end{bmatrix}. \end{aligned} \tag{A-11}$$

To obtain $r^{*}_{PP}(\mathrm{x})$ at the receiver, we need to separately propagate the curvature matrices A-8 and A-11 along the ray. We find from equations B-6:

$$\delta\tilde{\mathbf{K}}(\mathrm{x}) = \begin{bmatrix} \frac{1}{l(\mathrm{s},\,\mathrm{x}) - \frac{\cos\theta(\mathrm{s})}{D_{11}(\mathrm{s})}} & 0 \\ 0 & 0 \end{bmatrix}, \tag{A-12}$$

$$\tilde{\mathbf{K}}^{*}(\mathrm{x}) = \left\{\mathbf{R}^{*}(\mathrm{x})\right\}^{-1} = \left\{\mathbf{R}^{*}(\mathrm{s}) + l(\mathrm{s},\ \mathrm{x})\ \mathbf{I}\right\}^{-1} = \left\{\left[\tilde{\mathbf{K}}^{*}(\mathrm{s})\right]^{-1} + l(\mathrm{s},\ \mathrm{x})\ \mathbf{I}\right\}^{-1}. \tag{A-13}$$

Since the receiver position is usually defined in the global Cartesian coordinate system, we rotate matrices A-12 and A-13 by angle $\theta(\mathrm{x})$ and obtain:

$$\begin{aligned}\delta\tilde{\mathbf{F}}(\mathrm{x}) &= \mathbf{G}\left[\theta(\mathrm{x})\right]\ \delta\tilde{\mathbf{K}}(\mathrm{x})\ \left[\theta(\mathrm{x})\right] \\ &= \begin{bmatrix} \cos^{2}\theta(\mathrm{x})\ \delta\tilde{K}_{11}(\mathrm{x}) & 0 \\ 0 & 0 \end{bmatrix} = \\ &= \begin{bmatrix} \frac{\cos^{2}\theta(\mathrm{x})}{l(\mathrm{s},\,\mathrm{x}) - \frac{\cos\theta(\mathrm{s})}{D_{11}(\mathrm{s})}} & 0 \\ 0 & 0 \end{bmatrix}, \end{aligned} \tag{A-14}$$

$$\begin{aligned}\tilde{\mathbf{F}}^{*}(\mathrm{x}) &= \mathbf{G}\left[\theta(\mathrm{x})\right]\ \tilde{\mathbf{K}}^{*}(\mathrm{x})\ \mathbf{G}\left[\theta(\mathrm{x})\right] = \\ &= \begin{bmatrix} \cos^{2}\theta(\mathrm{x})\ \tilde{K}^{*}_{11}(\mathrm{x}) & \cos\theta(\mathrm{x})\ \tilde{K}^{*}_{12}(\mathrm{x}) \\ \cos\theta(\mathrm{x})\ \tilde{K}^{*}_{12}(\mathrm{x}) & \tilde{K}^{*}_{22}(\mathrm{x}) \end{bmatrix}. \end{aligned} \tag{A-15}$$

The mean curvature of the wavefront projection of the reflected wavefield on the receiver surface is:

$$h(\mathrm{x}) = \mathrm{tr}\left[\tilde{\mathbf{F}}^{*}(\mathrm{x}) - \delta\tilde{\mathbf{F}}(\mathrm{x})\right] = \cos^{2}\theta(\mathrm{x})\ \left[\tilde{K}^{*}_{11}(\mathrm{x}) - \delta\tilde{K}_{11}(\mathrm{x})\right] + \tilde{K}^{*}_{22}(\mathrm{x}). \tag{A-16}$$

The mean curvature of the wavefront projection of the apparent spherical PP-wave has the following form:

$$h^{*}(\mathrm{x}) = \frac{1 + \cos^{2}\theta(\mathrm{x})}{r^{*}_{PP}(\mathrm{x})}, \tag{A-17}$$

where $r^*_{PP}(\mathrm{x})$ is the required quantity. By assuming that $h^*(\mathrm{x}) = h(\mathrm{x})$, we obtain the radius of curvature of the apparent reflected wavefield at the receiver:

$$r^*_{PP}(\mathrm{x}) = \frac{1+\cos^2\theta(\mathrm{x})}{\cos^2\theta(\mathrm{x})\,\left[\tilde{K}^*_{11}(\mathrm{x}) - \delta\tilde{K}_{11}(\mathrm{x})\right] + \tilde{K}^*_{22}(\mathrm{x})}\,. \tag{A-18}$$

We observe that $\lim\limits_{\mathrm{x}\to\mathrm{s}} r^*_{PP}(\mathrm{x}) = r^*_{PP}(\mathrm{s})$.

3.12 Appendix B: Equations of dynamic ray tracing for reflected wave

Here we recall the known formulas of dynamic ray tracing which are used in our derivations. The formulas are related to wave propagation in homogeneous media with curved reflectors (Červený, 2001; Hubral, 2002).

A curved interface can be described by equation $z_3 = \frac{1}{2}\ D_{ij}(\mathrm{s})\ \ z_i\ \ z_j$, where $\mathbf{D}(\mathrm{s}) = \begin{bmatrix} D_{11}(\mathrm{s}) & D_{12}(\mathrm{s}) \\ D_{12}(\mathrm{s}) & D_{22}(\mathrm{s}) \end{bmatrix}$ is the matrix of interface curvatures relative to the plane Z tangential to the interface at point s and described by the local Cartesian coordinates $(z_1,\ z_2,\ z_3)$. Coordinates $(z_1,\ z_2)$ parameterize plane Z, while the normal coordinate z_3 is orthogonal to this plane.

Wavefront propagation in dynamic ray tracing is traditionally considered in the ray-centered coordinates tied to the ray. Coordinates q_1 and q_2 of this system are orthogonal to the ray, while coordinate q_3 is tangential to it. Without restricting the generality, we can assume that the directions of the projections of q_1 and q_2 coincide with directions of coordinates z_1 and z_2. The curvature of spherical wavefront in homogeneous media is controlled by the distance $l(\mathrm{s})$ traveled by the ray:

$$\mathbf{K}(\mathrm{s}) = \begin{bmatrix} \frac{1}{l(\mathrm{s})} & 0 \\ 0 & \frac{1}{l(\mathrm{s})} \end{bmatrix}. \tag{B-1}$$

When the incident wave hits a smooth curved interface, its wavefront deforms in accordance with the interface curvature. We rotate the matrix $\mathbf{K}(\mathrm{s})$ of wavefront curvatures by the rotation matrix

$$\mathbf{G}[\theta(\mathrm{s})] = \begin{bmatrix} \cos\theta(\mathrm{s}) & 0 \\ 0 & 1 \end{bmatrix}, \tag{B-2}$$

and find the incident wavefront curvature at point s in the local Cartesian coordinates is

$$\begin{aligned}\mathbf{F}\,(\mathrm{s}) &= \mathbf{G}\,[\theta\,(\mathrm{s})]\ \mathbf{K}\,(\mathrm{s})\ \mathbf{G}\,[\theta\,(\mathrm{s})] - \cos\theta\,(\mathrm{s})\ \mathbf{D}\,(\mathrm{s}) = \\ &= \begin{bmatrix} \frac{\cos^2\theta(\mathrm{s})}{l(\mathrm{s})} - \cos\theta\,(\mathrm{s})\ D_{11}\,(\mathrm{s}) & -\ \cos\theta\,(\mathrm{s})\ D_{12}\,(\mathrm{s}) \\ -\ \cos\theta\,(\mathrm{s})\ D_{12}\,(\mathrm{s}) & \frac{1}{l(\mathrm{s})} - \cos\theta\,(\mathrm{s})\ D_{22}\,(\mathrm{s}) \end{bmatrix}. \end{aligned} \tag{B-3}$$

The wavefront curvature of the reflected wave at point s also depends on the interface curvature but with the opposite sign. Assuming that incident and reflected angles are the same, we write equation for the wavefront curvature of the reflected wave:

$$\tilde{\mathbf{F}}\,(\mathrm{s}) = \mathbf{G}\,[\theta\,(\mathrm{s})]\ \tilde{\mathbf{K}}\,(\mathrm{s})\ \mathbf{G}\,[\theta\,(\mathrm{s})] + \cos\theta\,(\mathrm{s})\ \mathbf{D}\,(\mathrm{s})\,, \tag{B-4}$$

where $\tilde{\mathbf{K}}\,(\mathrm{s})$ is the wavefront curvature of the reflected wave in the ray-centered coordinates with the origin at point s. The matrices of wavefront curvatures at the interface are continuous, i.e. $\mathbf{F}\,(\mathrm{s}) = \tilde{\mathbf{F}}\,(\mathrm{s})$. We find the elements of matrix $\tilde{\mathbf{K}}\,(\mathrm{s})$:

$$\tilde{\mathbf{K}}\,(\mathrm{s}) = \begin{bmatrix} \frac{1}{l(\mathrm{s})} - 2\ \frac{D_{11}(\mathrm{s})}{\cos\theta(\mathrm{s})} & -\ 2\ D_{12}\,(\mathrm{s}) \\ -\ 2\ D_{12}\,(\mathrm{s}) & \frac{1}{l(\mathrm{s})} - 2\ D_{22}\,(\mathrm{s})\ \cos\theta\,(\mathrm{s}) \end{bmatrix} \tag{B-5}$$

To propagate the matrix of curvatures from the reflection point to the receiver, we exploit the known equations:

$$\begin{aligned} \mathbf{K}\,(\mathrm{s}) &= \{\mathbf{R}\,(\mathrm{s})\}^{-1}, \\ \mathbf{R}\,(\mathrm{x}) &= \mathbf{R}\,(\mathrm{s}) + l\,(\mathrm{s},\ \mathrm{x})\ \mathbf{I}, \end{aligned} \tag{B-6}$$

where $\mathbf{R}\,(\mathrm{s})$ and $\mathbf{R}\,(\mathrm{x})$ are the matrices of wavefront radii at the reflection point and at the receiver in the ray-centered coordinates, $l_2\,(\mathrm{s},\ \mathrm{x})$ is the distance between the reflection point and the receiver, $\mathbf{I}$ is the unit matrix. Matrix $\tilde{\mathbf{K}}\,(\mathrm{x})$ at the receiver thus has the following form:

$$\tilde{\mathbf{K}}\,(\mathrm{x}) = \{\mathbf{R}\,(\mathrm{x})\}^{-1} = \{\mathbf{R}\,(\mathrm{s}) + l\,(\mathrm{s},\ \mathrm{x})\ \mathbf{I}\}^{-1} = \left\{\left[\tilde{\mathbf{K}}\,(\mathrm{s})\right]^{-1} + l\,(\mathrm{s},\ \mathrm{x})\ \mathbf{I}\right\}^{-1}. \tag{B-7}$$

It is convenient to use the global Cartesian system (x_1, x_2, x_3) at the observation plane. In this coordinate system, the matrix $\tilde{\mathbf{F}}\,(\mathrm{x})$ of wavefront curvatures of the reflected wave at the receiver is obtained by rotating matrix $\tilde{\mathbf{K}}\,(\mathrm{x})$ by emergence angle $\theta\,(\mathrm{x})$:

$$\begin{aligned}\tilde{\mathbf{F}}\,(\mathrm{x}) &= \mathbf{G}\,([\theta\,(\mathrm{x})])\ \tilde{\mathbf{K}}\,(\mathrm{x})\ \mathbf{G}\,([\theta\,(\mathrm{x})]) = \\ &= \begin{bmatrix} \cos^2\theta\,(\mathrm{x})\ \tilde{K}_{11}\,(\mathrm{x}) & \cos\theta\,(\mathrm{x})\ \tilde{K}_{12}\,(\mathrm{x}) \\ \cos\theta\,(\mathrm{x})\ \tilde{K}_{12}\,(\mathrm{x}) & \tilde{K}_{22}\,(\mathrm{x}) \end{bmatrix}. \end{aligned} \tag{B-8}$$

The relative geometrical spreading of the PP-wave for a single reflection has the following form:

$$\frac{J_P\left(\mathrm{s}\right)}{J_{PP}\left(\mathrm{x}\right)} = \frac{\Delta S\left(\mathrm{s}\right)}{\Delta S\left(\mathrm{x}\right)}, \tag{B-9}$$

where $\Delta S\left(\mathrm{x}\right)$ and $\Delta S\left(\mathrm{s}\right)$ are the cross-sections of the ray tube at the receiver and at the reflection point, respectively. Taking into account that $\frac{\Delta S(\mathrm{s})}{\Delta S(\mathrm{x})} = \frac{\det \mathbf{R}(\mathrm{s})}{\det \mathbf{R}(\mathrm{x})}$, we obtain the geometrical spreading in terms of wavefront curvatures:

$$\begin{aligned}
\frac{J_P\left(\mathrm{s}\right)}{J_{PP}\left(\mathrm{x}\right)} &= \frac{\det \mathbf{R}\left(\mathrm{s}\right)}{\det \mathbf{R}\left(\mathrm{s}\right) + \operatorname{tr} \mathbf{R}\left(\mathrm{s}\right)\ l\left(\mathrm{s},\ \mathrm{x}\right) + \left[l\left(\mathrm{s},\ \mathrm{x}\right)\right]^2} = \\
&= \left\{1 + \frac{\operatorname{tr} \mathbf{R}\left(\mathrm{s}\right)}{\det \mathbf{R}\left(\mathrm{s}\right)}\ l\left(\mathrm{s},\ \mathrm{x}\right) + \frac{\left[l\left(\mathrm{s},\ \mathrm{x}\right)\right]^2}{\det \mathbf{R}\left(\mathrm{s}\right)}\right\}^{-1} = \\
&= \left\{1 + \operatorname{tr} \tilde{\mathbf{K}}\left(\mathrm{s}\right)\ l\left(\mathrm{s},\ \mathrm{x}\right) + \det \tilde{\mathbf{K}}\left(\mathrm{s}\right)\ \left[l\left(\mathrm{s},\ \mathrm{x}\right)\right]^2\right\}^{-1},
\end{aligned} \tag{B-10}$$

where

$$\begin{aligned}
\operatorname{tr} \tilde{\mathbf{K}}\left(\mathrm{s}\right) &= 2\ \left[\frac{1}{l\left(\mathrm{s}\right)} - H'\left(\mathrm{s}\right)\right]\ , \\
\det \tilde{\mathbf{K}}\left(\mathrm{s}\right) &= \left[\frac{1}{l\left(\mathrm{s}\right)}\right]^2 - \frac{2}{l\left(\mathrm{s}\right)}\ H'\left(\mathrm{s}\right) + 4\ \det \mathbf{D}\left(\mathrm{s}\right)\ , \\
H'\left(\mathrm{s}\right) &= \frac{D_{11}\left(\mathrm{s}\right)}{\cos\theta\left(\mathrm{s}\right)} + \cos\theta\left(\mathrm{s}\right)\ D_{22}\left(\mathrm{s}\right).
\end{aligned} \tag{B-11}$$

Chapter 4

An analysis of AVO inversion for post-critical offsets in HTI media

Lyubov Skopintseva[1], Tariq Alkhalifah[2],

[1] Norwegian University of Science and Technology, Trondheim, Norway

[2] King Abdullah University of Science and Technology, Thuwal, Saudi Arabia

Presented at the 73th EAGE Conference & Exhibition, Vienna, Austria, May 2011; Submitted to Geophysics

4.1 Abstract

Azimuthal variations of the wavefield characteristics, such as traveltime or reflection amplitude, play an important role in the identification of fractured media. Transversely isotropic media with a horizontal symmetry axis (HTI media) is the simplest azimuthally anisotropic model typically used to describe one set of vertical fractures. There exist many techniques in the industry to recover anisotropic parameters based on moveout equations and linearized reflection coefficients using such a model. However, most of the methods have limitations in defining properties of the fractures due to linearizations and physical approximations used in their development. Thus, azimuthal analysis of traveltimes based on normal moveout (NMO) ellipses recovers a maximum of three media parameters instead of the required five. Linearizations made in plane-wave reflection coefficients limit amplitude-versus-offset (AVO) analysis to small incident angles and weak-contrast interfaces. Azimuthal AVO inversion at small offsets has challenges in estimating anisotropy parameters due to nonuniqueness problems. Extending the AVO analysis and inversion to and beyond the critical angle increases the amount of information recovered from the medium. However, well accepted plane-wave reflection coefficients are not valid in the vicinity of the critical angle and beyond it, due to frequency and spherical wave effects. Recently derived spherical and effective reflection coefficients methods overcome this problem. We extend the effective reflection coefficients approach to HTI media to analyze the potential of near- and post-critical reflections in azimuthal AVO analysis. From the sensitivity analysis, we show that effective reflection coefficients are sensitive to different sets of parameters prior and beyond the critical angle, which might be a nice feature for joint inversion. Additionally, the resolution of the parameters depends on a healthy azimuthal coverage in the acquisition setup, with the most stable AVO results achieved with a separation in angle that exceeds 45 degrees.

4.2 Introduction

The role of anisotropy has dramatically increased over the past two decades due to advances in acquisition setups, data quality, data processing and parameter estimation. It has been demonstrated countless times that including anisotropy in the data analysis considerably reduces uncertainty in interpretation. Fracture identification and fracture direction and fracture density estimation became possible with the use of multi-azimuth acquisition setup and multi-azimuth data analysis. Although, often we see that fractured reservoirs often adhere to the orthorhombic symmetry (Grechka et al., 2006) representation, the azimuthal analysis based on HTI symmetry is widely exploited for a vertical set of fractures detection, as HTI is a the simplest azimuthally anisotropic model (Rüger, 2001).

One of the most widely exploited approaches in fracture identification is the azimuthal analysis of reflection traveltimes based on the concept of NMO ellipse (Grechka et al., 1999). Although P-wave azimuthal moveout analysis is practically effective in predicting the fracture direction (Lynn et al., 1999; Tod et al., 2007), the NMO ellipse constrains only three combinations of the medium parameters, which results in a three-parameter inversion (Al-Dajani and Alkhalifah, 2000). Azimuthally dependent P-wave traveltime inversion recovers vertical P-wave velocity, anisotropy parameter $\delta^{(V)}$ (or anellipticity parameter η (Alkhalifah and Tsvankin, 1995)) and the symmetry axis direction. It is, however, not enough for defining the physical properties of the fractures, as five parameters are required to fully characterize the HTI model. Additional sources of information are required.

Reflection coefficients contain valuable information about the local medium properties on both sides of an interface. Therefore, analysis of amplitude variations with incidence angle or offset is often used in reservoir characterization (Avseth et al., 2001). Generally, AVO analysis has higher vertical resolution than traveltime methods. Existing in industry AVO inversion techniques are based on the linearizations of plane-wave reflection coefficients, made under the assumption of weak contrast interfaces (Ostrander, 1984). As a consequence application of these linearizations is limited to small offsets, where a reasonably good match with real data is achieved. Application of azimuthally-dependent approximations (Rüger, 2001) in azimuthal AVO inversion, however, is hindered by nonuniqueness in parameter estimation. Practically, azimuthal variations of AVO response are exploited in the recovery of fracture azimuth with a 90^0 uncertainty (Hall and Kendall, 2003). Despite this ambiguity, azimuthal AVO analysis has been successful in many cases (Gray et al., 2002; Hall

and Kendall, 2003; Xu and Tsvankin, 2007).

Because azimuthal AVO inversion works for small offsets associated with pre-critical reflections, there are some attempts to extend AVO analysis to longer offsets, where post-critical reflections appear. Such AVO analysis can, thus, be applied to the reservoirs with high contrast in media parameters across the interface, such as stiff carbonate reservoirs, heavy oil traps or salt domes. The drawback of the long-offset approach is that the existing linearizations of reflection coefficients have to be disregarded as they are not valid for long offsets. The analysis of the exact plane-wave reflection coefficients for different azimuths (Hall and Kendall, 2003) showed strong sensitivity of the critical angle to the azimuth and fracture content. Using the weak-anisotropy approximation for azimuthal horizontal phase velocities in orthorhombic media, Landrø and Tsvankin (2007) confirmed the sensitivity of the critical angle to the azimuth and showed the potential of exploiting the critical angle in anisotropy parameter estimations.

Despite that the critical angle is well defined from the exact plane-wave reflection coefficient, its identification on the data generated by a point source is not obvious, as in this case the critical angle position is not marked by the special reflection amplitude features. These amplitude features appear beyond the critical angle and depend on the wavefront radius and frequency (Červený, 1961). The physical and reflectivity modeling made by Alhussain (2007) confirms these observations, which implies the invalidity of the exact plane-wave reflection coefficients near- and beyond the critical angle. To overcome this problem spherical and effective reflection coefficients are developed (Ursenbach et al., 2007; Ayzenberg et al., 2007, 2009). These coefficients adequately describe amplitude behavior beyond the critical angle and thus can be exploited for long offset amplitude analysis. The benefits of the post-critical reflections in AVO inversion are shown on the example of a reflection from isotropic/isotropic interface (Skopintseva et al., 2011). Effective reflection coefficients developed for a horizontal isotropic/VTI interface show their sufficient sensitivity to anisotropy parameters in the post-critical domain (Ayzenberg et al., 2009). It motivates us to study azimuthal effects of post-critical reflections.

In this paper, we investigate the potential of using post-critical reflections in azimuthal AVO analysis and inversion. For this purpose, we extend effective reflection coefficient technique to work for an isotropic/HTI interface and compare their azimuthal dependence prior and beyond the critical angle. We show that the amplitude maximum observed beyond the critical angle can be utilized in anisotropy parameters

estimation. We provide the sensitivity analysis of the underburden parameters to the reflection coefficient changes prior and beyond the critical angle for the multi-azimuth acquisition coverage with minimal number of survey lines (three). Obtained results indicate that pre- and post-critical domains are sensitive to different sets of parameters. In addition, we provide analysis for optimal acquisition setup which results in better stability of the inversion.

4.3 Phase velocity surface vs critical angle surface

Consider a two-layer model with a plane interface, where the upper halfspace is isotropic, and lower halfspace represents HTI media. The velocity of the isotropic halfspace is lower than the phase velocity of the HTI medium for any azimuthal direction. Assume that the P-wave generated in the upper halfspace hits the isotropic/HTI interface at the critical angle. When incidence angle is critical, part of the energy reflects from the interface and part of the energy starts propagating along the interface with velocity of the lower medium (Figure 4.1), and generates head waves. Noticing that the velocity in the lower halfspace depends on the angle between incidence plane and symmetry axis of HTI media φ and transmitted angle θ_t, the critical angle obeys the modified Snell's law (Landrø and Tsvankin, 2007):

$$\sin\theta_{cr}(\varphi) = \frac{V_{P1}}{V^h_{P2}(\varphi)}, \tag{1}$$

where φ is the azimuthal angle between symmetry axis and survey line, $\theta_{cr}(\varphi)$ is the critical reflection angle along the vertical plane defined by φ, $V^h_{P2}(\varphi)$ is the horizontal phase P-wave velocity for the HTI medium as a function of azimuth, $V^h_{P2}(0)$ is the phase velocity along the symmetry axis, $V^h_{P2}(90) = V_{P2}$ is the phase P-wave velocity in isotropic plane. The plot in Figure 4.1 defines the angles involved for two orthogonal incidence planes. Plane II is located along the symmetry axis of HTI media, and plane $\perp$ coincides with the isotropic plane of HTI media. The horizontal velocity in plane II is less than one for plane $\perp$. It, consequently, results in a larger critical angle in the plane along the symmetry axis than that for the isotropic plane. The reciprocal proportionality of the sinus of the critical angle to the horizontal phase velocity (equation 4) shows that the azimuthal dependence of the critical angle is the source of additional information about the underburden media.

Azimuthal dependency of the horizontal P-wave phase velocity surface for HTI media is equivalent to the P-wave phase velocity surface for VTI media in vertical plane, as

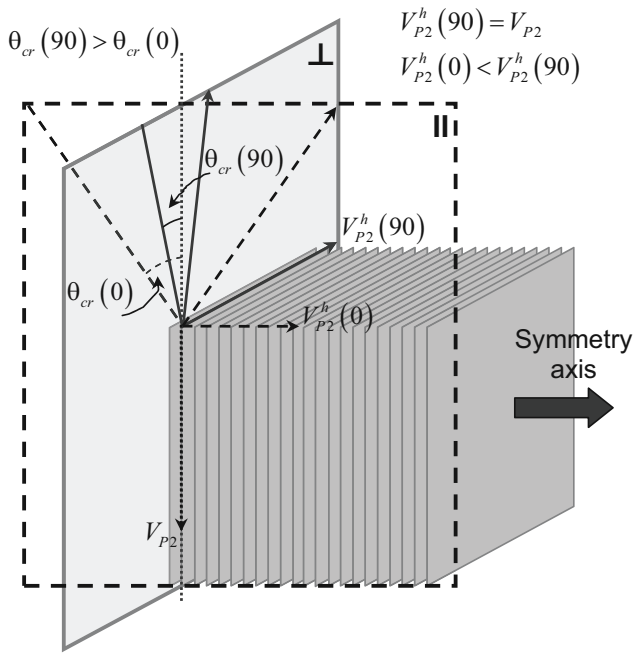

Figure 4.1: A schematic plot depicting the model setting considering here. The ray curves corresponds to a reflection at the critical angle from the horizontal isotropic/HTI interface.

HTI media is equivalent to VTI media rotated by 90 degrees in the vertical plane. According to well-known acoustic approximations for the phase velocity in VTI media, the azimuthally dependent horizontal phase velocity for HTI media has the following form:

$$V^{h\,2}_{P2}(\varphi) = V^2_{P2}\left[\frac{1}{2} + \epsilon^{(V)}\cos^2\varphi + \right. \\ \left. + \frac{1}{2}\sqrt{1 + 4\cos^2\varphi\left[\epsilon^{(V)}\cos 2\varphi + 2\delta^{(V)}\sin^2\varphi\right] + 4\epsilon^{(V)\,2}\cos^4\varphi}\right], \tag{2}$$

where $\epsilon^{(V)}$ and $\delta^{(V)}$ are anisotropy parameters in HTI notation (Rüger, 2001).

Substituting equation 4 into 5 and exploiting the three azimuthal directions corresponding to $\varphi = 0^0$, 45^0 and 90^0 yields equations for anisotropy parameters in terms

of their critical angles:

$$\epsilon^{(V)} = \frac{\sin^2\theta_{cr}\,(90) - \sin^2\theta_{cr}\,(0)}{2\sin^2\theta_{cr}\,(0)}$$
$$\delta^{(V)} = \frac{\sin^2\theta_{cr}\,(90)\left[\sin^2\theta_{cr}\,(45) - 2\sin^2\theta_{cr}\,(0)\right]\left[\sin^2\theta_{cr}\,(45) - 2\sin^2\theta_{cr}\,(90)\right]}{2\sin^2\theta_{cr}\,(0)\sin^4\theta_{cr}\,(45)} - \frac{1}{2}. \tag{3}$$

To obtain anisotropy parameter $\epsilon^{(V)}$, we need information about the critical angles in the incidence planes along and across the symmetry axis of HTI media. Anisotropy parameter $\delta^{(V)}$ requires additional knowledge about the critical angle for an azimuth of 45 degrees. Equation 7 implies that the symmetry axis direction is known.

4.4 Effective reflection coefficient for isotropic/HTI interface

Here, we extend the effective reflection coefficients for the isotropic/HTI case. We choose the incidence plane coinciding with the $(x_1,\ x_3)$ plane of the global coordinate system $(x_1,\ x_2,\ x_3)$ and forming an angle φ with symmetry axis of HTI media. A point source exciting a spherical P-wave is located in the upper halfspace. The effective reflection coefficient for the isotropic/HTI interface at the point of a receiver has the following form:

$$\chi_{PP}\left[\mathrm{x},\ \omega,\ \mathbf{g}\right] = \frac{u^*_{PP\,\mathrm{norm}}\left(\mathrm{x},\ \mathbf{g}\right)\cos\theta\left(\mathrm{x}\right) + u^*_{PP\,\tan}\left(\mathrm{x},\ \mathbf{g}\right)\sin\theta\left(\mathrm{x}\right)}{\left[\frac{i}{k_P r^*_{PP}(\mathrm{x})} - \frac{1}{k_P^2 r^{*2}_{PP}(\mathrm{x})}\right] e^{ik_P r^*_{PP}(\mathrm{x})}}, \tag{4}$$

where matrix $\mathbf{x} = (\mathrm{x}_1,\ \mathrm{x}_2,\ ...,\ \mathrm{x}_\mathrm{N})$ consists of N receivers with coordinates $\mathrm{x}_\mathrm{N} = (x_{1\,N},\ x_{2\,N},\ x_{3\,N})$, ω is angular frequency, $\mathbf{g} = \left(V_{P1},\ V_{S1},\ \rho_1,\ V_{P2},\ V_{S2},\ \epsilon^{(V)},\ \gamma^{(V)},\ \delta^{(V)},\ \varphi,\ \rho_2\right)$ is the vector of model parameters; V_{P1}, V_{S1} are P- and S-wave velocities of the isotropic halfspace; V_{P2} and V_{S2} are P- and S-wave velocities of the HTI model in the isotropic plane; ρ_1, ρ_2 are densities of the upper and lower halfspaces, respectively; $\epsilon^{(V)}$, $\gamma^{(V)}$, $\delta^{(V)}$ are anisotropy parameters in HTI notation (Rüger, 2001); $k_P = \frac{\omega}{V_{P1}}$ is the wavenumber in the overburden, $\theta\left(\mathrm{x}\right)$ is the incidence/reflection angle, $r^*_{PP}\left(\mathrm{x}\right)$ is the apparent radius of the wavefront at the receiver. A general form of the radius $r^*_{PP}\left(\mathrm{x}\right)$ is introduced by Skopintseva et al. (2010). For a plane interface, $r^*_{PP}\left(\mathrm{x}\right)$ is the distance between the source and the receiver along the ray (Skopintseva et al., 2011). $u^*_{PP\,\mathrm{norm}}\left(\mathrm{x}\right)$

and $u^*_{PP\,\tan}(\mathrm{x})$ are the dimensionless normal and tangential components of the displacement vector, which have the following form:

$$\begin{aligned} u^*_{PP\,\mathrm{norm}}(\mathrm{x},\ \mathbf{g}) &= -\int_0^{+\infty} R_{PP}(\zeta,\ \mathbf{g})\, e^{i\,\alpha(\mathrm{x})\sqrt{1-\zeta^2}} J_0\left[\beta(\mathrm{x})\,\zeta\right]\zeta d\zeta, \\ u^*_{PP\,\tan}(\mathrm{x},\ \mathbf{g}) &= -\int_0^{+\infty} R_{PP}(\zeta,\ \mathbf{g})\, \frac{i e^{i\,\alpha(\mathrm{x})\sqrt{1-\zeta^2}}}{\sqrt{1-\zeta^2}} J_1\left[\beta(\mathrm{x})\,\zeta\right]\zeta^2 d\zeta, \end{aligned} \tag{5}$$

where $R_{PP}(\zeta,\ \mathbf{g})$ is an exact plane-wave reflection coefficient for the isotropic/HTI interface derived by Schoenberg and Protazio (1992) (Appendix 4.11), $\alpha(\mathrm{x}) = k_P r^*_{PP}(\mathrm{x})\cos\theta(\mathrm{x})$, $\beta(\mathrm{x}) = k_P r^*_{PP}(\mathrm{x})\sin\theta(\mathrm{x})$, ζ is the horizontal component of the unit P-wave ray vector in the overburden, J_0 and J_1 are the Bessel functions of the zeroth and first order.

Figure 4.2 shows the amplitude of the normalized effective reflection coefficient (ERC) $A(\mathbf{x},\ \varphi) = \chi(\mathbf{x},\ \varphi)/\chi(\mathrm{x}_1,\ \varphi)$ in comparison with amplitudes of the normalized plane-wave reflection coefficient (PWRC) $A_R(\mathbf{x},\ \varphi) = R_{PP}(\mathbf{x},\ \varphi)/R_{PP}(\mathrm{x}_1,\ \varphi)$ and one obtained from reflectivity modeling using technique described by Skopintseva et al. (2011). Reflection coefficients are calculated for the model where $V_{P1} = 1.484$ km/s, $V_{S1} = 0$ km/s, $\rho_1 = 1$ g/cm^3, $V_{P2} = 2.709$ km/s, $V_{S2} = 1.382$ km/s $\rho_2 = 1.2$ g/cm^3, $\epsilon^{(V)} = -0.0019$, $\delta^{(V)} = -0.0069$, $\gamma^{(V)} = -0.0439$, $\varphi = 30^0$, the frequency is 218 Hz, and the interface depth is 240 m. ERC and PWRC curves coincide at pre-critical angles, while they are different around and beyond the critical angle. The ERC has a gradual amplitude increase with angle and reaches its maximum beyond the critical angle, whereas the PWRC has an abrupt amplitude increase at the critical angle. Additionally, the ERC has oscillations in the post-critical domain, while these are absent for PWRC. Effects observed at the ERC around and beyond the critical angle occur due to the influence of the dimensionless argument $k_P r^*_{PP}(\mathrm{x})$ in equations 2-3. This argument represents the wavefront curvature and frequency effects on the reflection process. The perfect match of the ERC with the reflection coefficient extracted from the synthetic data shown by Skopintseva et al. (2011) confirms the soundness of the observed phenomena described by the effective reflection coefficients. The synthetic data are obtained by reflectivity modeling.

The wavefront curvature and frequency have a linear tradeoff with each other as they are coupled in equations 2-3 by the argument $k_P r^*_{PP}(\mathrm{x})$. A frequency increase has the same effect as a wavefront curvature decrease (the reciprocal of $r^*_{PP}(\mathrm{x})$). The value of the argument $k_P r^*_{PP}(\mathrm{x})$ controls the amplitude maximum shift and oscillation frequency in the post-critical domain (Figure 4.3). The larger the argument

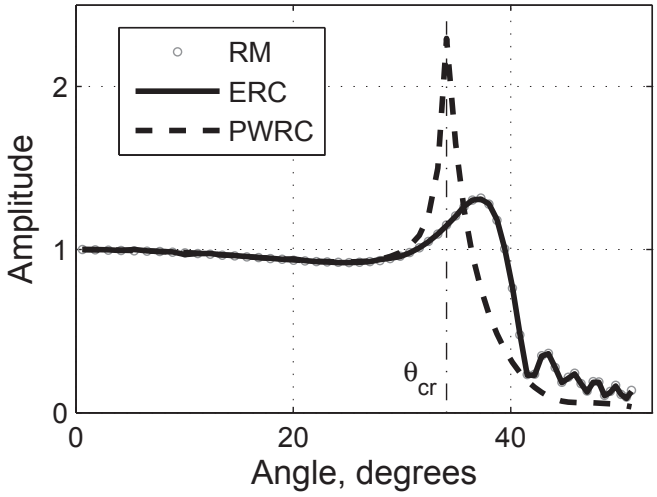

Figure 4.2: Comparison between normalized effective reflection coefficient (ERC), plane-wave reflection coefficient (ERC) and reflection response obtained from the reflectivity modeling (RM).

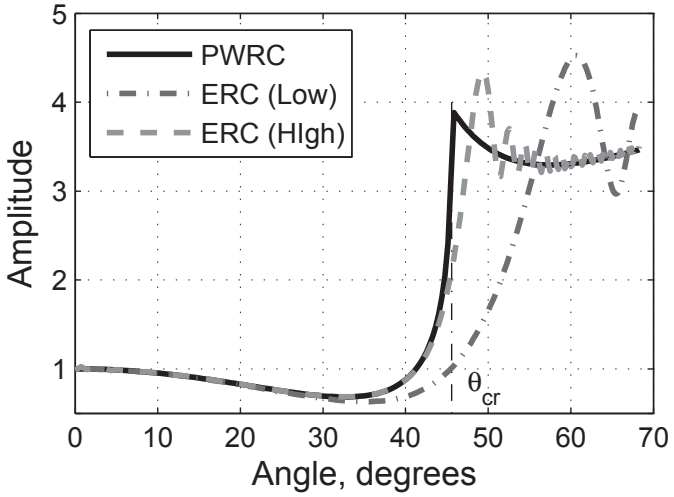

Figure 4.3: Amplitude of normalized effective reflection coefficients in the isotropic plane $\varphi = 90^0$ for $k_P\, r_P^*(0) = 402$ (High) and $k_P\, r_P^*(0) = 25$ (Low). The normalized plane wave reflection coefficient (PWRC) is given for comparison. Model parameters are: $V_{P1} = 2$ km/s, $V_{S1} = 1.1$ km/s, $\rho_1 = 1.8$ g/cm^3, $V_{P2} = 2.8$ km/s, $V_{S2} = 1.6$ km/s $\rho_2 = 2.1$ g/cm^3, $\epsilon^{(V)} = -0.1$ $\delta^{(V)} = -0.05$, $\gamma^{(V)} = -0.1$.

$k_P r^*_{PP}$ (x) is, the closer the amplitude maximum is to the critical angle, and the faster the oscillations beyond the critical angle. These oscillations are associated with the interference between reflected and head waves, which appears at the critical angle.

Figures 4.4 and 4.5 show maps of azimuthal distributions of the normalized reflection coefficients for different anisotropy parameters $\epsilon^{(V)}$, $\delta^{(V)}$, $\gamma^{(V)}$. The model parameters are $V_{P1} = 2$ km/s, $V_{S1} = 1.1$ km/s, $\rho_1 = 1.8$ g/cm^3, $V_{P2} = 2.8$ km/s, $V_{S2} = 1.6$ km/s $\rho_2 = 2.1$ g/cm^3, an interface depth of 1 km, and a frequency of 32 Hz. For each row we change only one anisotropy parameter, while others are set to zero. Left column represents the weak anisotropy effect, while the right column corresponds to strong anisotropy. Color indicates the amplitude strength. The offset increases in the radial direction from the center. The circle of 1 km corresponds to the incident/reflection angle of 30 degrees (if anisotropy parameters are zeros), which is normally a limit for conventional AVO studies. The circle of 2 km corresponds to the critical angle, if anisotropy parameters are zeros. Azimuthal angle φ changes from 0^0 to 360^0. Offset range in Figure 4.4 corresponds to pre-critical domain, while it captures pre-, near- and post-critical domains in Figure 4.5.

In the isotropic media case, we expect a uniform amplitude response with azimuth for any offset range. The influence of anisotropy results in the deviation from this azimuthal dependence of amplitude. Figure 4.4 shows that the parameter $\epsilon^{(V)}$ does not cause much azimuthal changes in amplitude within the circle of 1 km. Its effect appears at larger offsets, specifically when incident angle reaches the critical angles. The influence of the parameter $\delta^{(V)}$ is stronger within the circle of 1 km, but larger offsets are more influenced by this parameter. The largest effect on the azimuthal distribution of amplitudes in Figure 4.4 is caused by the anisotropy parameter $\gamma^{(V)}$. The amplitude strength deviates from the circle at all offset within the range 0-2 km.

Despite that the position of the amplitude maximum does not coincide with the critical angle, Figure 4.5 indicates that post-critical reflections contain additional information about the media below the interface. The post-critical domain is clearly defined by the amplitude maximum contour. The sensitivity of post-critical domain to the anisotropy parameters $\epsilon^{(V)}$ and $\delta^{(V)}$ is clearly observed, while its sensitivity to parameter $\gamma^{(V)}$ is not obvious. Changes in anisotropy parameter $\epsilon^{(V)}$ controls the amplitude maximum deviation from the isotropic circle in the symmetry axis direction ($\varphi = 0^0$). Parameter $\delta^{(V)}$ influences the amplitude maximum deviations in the oblique direction ($\varphi = 45^0$), as well amplitude strength for $\varphi = 0^0$ and $\varphi = 90^0$. These observations are consistent with the equations 7, where $\epsilon^{(V)}$ is a function of the

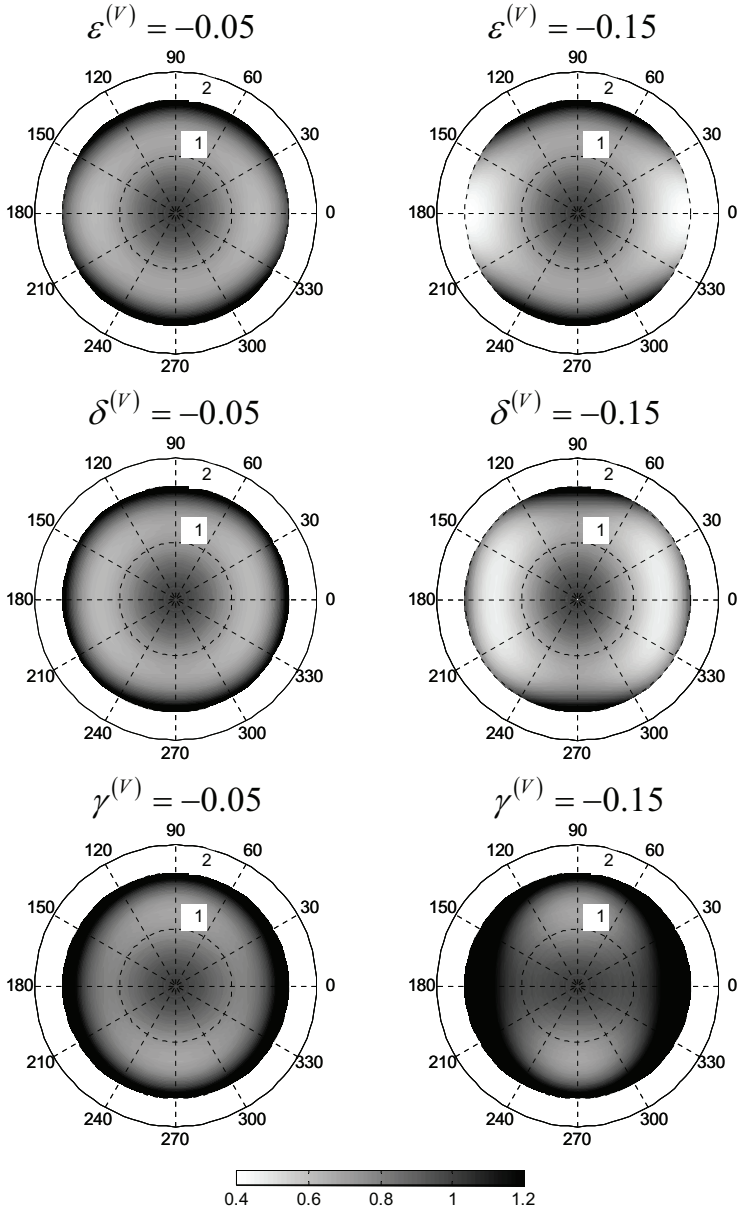

Figure 4.4: Maps of the normalized azimuthal effective reflection coefficients prior to the critical offset (2km in the isotropic plane $\varphi = 90^0$) for different anisotropy parameters. Radial direction corresponds to the source-receiver offset, angular direction corresponds to the angle between the survey line and the symmetry axis direction. Each row represents changes in one of the anisotropy parameters, while the others are set to zero.

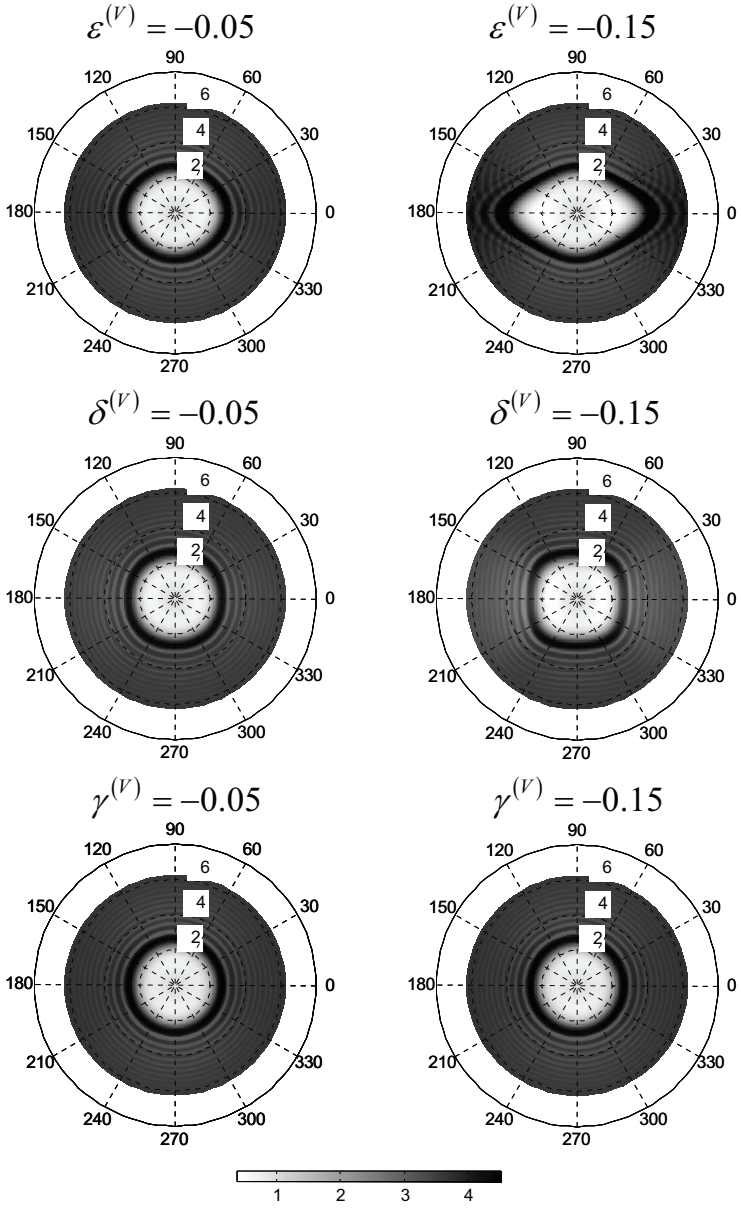

Figure 4.5: Maps of the normalized azimuthal effective reflection coefficients prior and beyond the critical offset for different anisotropy parameters. Radial direction corresponds to the source-receiver offset, angular direction corresponds to the angle between the survey line and symmetry axis direction. Each row represents changes in one of the anisotropy parameters, while the others are set to zero.

critical angles along and across the symmetry axis and $\delta^{(V)}$ is a function of critical angles for three azimuths ($\varphi = 0^0,\ 45^0,\ 90^0$), and $\gamma^{(V)}$ is independent of the critical angle.

4.5 Critical offset vs amplitude maximum offset

From Figure 4.2, it is seen that the critical angle (offset) cannot be clearly defined, as it is not associated with special amplitude features of the reflection coefficient. However, azimuthal dependence on offset, where the maximum amplitude is observed, can be exploited for anisotropy parameters detection. Assume that the deviations of the amplitude maximum position from the critical offset are controlled only by parameter $k_P r^*_{PP}(\mathrm{x})$ and are weakly dependent on the anisotropy parameters. Then the azimuthal dependence of the critical offset is proportional to the azimuthal dependence of the amplitude maximum offset:

$$\mathrm{x}_{cr}(\varphi) = n\mathrm{x}_m(\varphi), \tag{6}$$

where n is azimuthally independent proportionality coefficient $\mathrm{x}_{cr}(\varphi)$ is the azimuthally-dependent critical offset, and $\mathrm{x}_m(\varphi)$ is the azimuthally-dependent amplitude maximum offset.

Exploiting equation 6 and relation $\sin\theta^2_{cr} = \frac{\mathrm{x}^2_{cr}}{h^2+\mathrm{x}^2_{cr}}$, where h is the interface depth, we rewrite equations 7 in terms of the amplitude maximum offset x_m:

$$\begin{aligned}
\epsilon^{(V)} &= \cos^2\theta_{cr}(90)\left[\frac{\mathrm{x}^2_m(90) - \mathrm{x}^2_m(0)}{2\mathrm{x}^2_m(0)}\right] \\
\delta^{(V)} &= -M_1\cos^2\theta_{cr}(90) + M_2\cos^2\theta_{cr}(90)\cos 2\theta_{cr}(90),
\end{aligned} \tag{7}$$

where

$$\begin{aligned}
M_1 =& 1 - \frac{\mathrm{x}^2_m(90)}{2\mathrm{x}^2_m(45)} - \frac{\mathrm{x}^4_m(90)}{\mathrm{x}^4_m(45)} + \frac{\mathrm{x}^4_m(90)}{2\mathrm{x}_m(0)^2\,\mathrm{x}^2_m(45)} \\
M_2 =& \frac{1}{2} - \frac{3\mathrm{x}^2_m(90)}{2\mathrm{x}^2_m(45)} + \frac{\mathrm{x}^4_m(90)}{\mathrm{x}^4_m(45)} + \frac{\mathrm{x}^2_m(90)}{2\mathrm{x}_m(0)^2} - \frac{\mathrm{x}^4_m(90)}{2\mathrm{x}_m(0)^2\,\mathrm{x}^2_m(45)},
\end{aligned} \tag{8}$$

Despite that equations 11-12 are functions of the maximum offsets, the information about critical angle in the isotropic plane is still needed. This information can be retrieved from the AVO inversion in the isotropic plane (Skopintseva et al., 2011).

Relative errors in anisotropy parameter estimates obtained from the different types of data are shown in Figure 4.6. The three datasets are exploited for estimations:

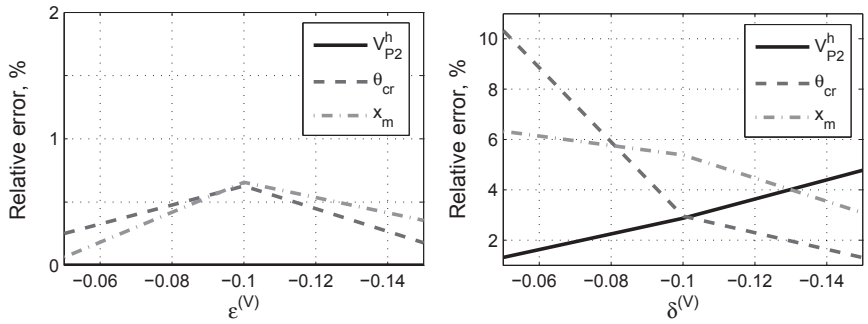

(a) (b)

Figure 4.6: Relative errors in the anisotropy parameter $\epsilon^{(V)}$ (a) and $\delta^{(V)}$ (b) estimates obtained from velocity, critical angle and offsets corresponding to the maximum amplitudes.

azimuthal dependency of the horizontal phase velocity $V^h_{P2}(\varphi)$, azimuthal dependency of the critical angle $\theta_{cr}(\varphi)$, and azimuthal dependency of the maximum amplitude offset $\mathrm{x}_m(\varphi)$. The most accurate estimates are obtained for the anisotropy parameter $\epsilon^{(V)}$. The error level is within 1% for any type of data. The error level in $\delta^{(V)}$ estimates increases up to 10%. The reason for such inaccuracies is the acoustic approximation of phase velocity used in anisotropy parameter estimates. This approximation is least accurate at azimuth of $\varphi = 45^0$. This consequently results in errors for all types of data. In general, the amplitude maximum offset provides simular level of errors as the critical angle and thus has a potential to be utilized for anisotropy analysis.

4.6 Sensitivity analysis and parameter dependency

Observations made in the previous section have the potential for anisotropy parameter analysis only in the case of a full azimuthal coverage. In this situation the direction of the symmetry axis is easily defined from the azimuthal dependence of amplitude maximum position as seen in Figure 4.5. However, it is quite often, when there is a lack of full azimuth coverage, data are available only for several azimuth directions. Then, the symmetry axis direction identification becomes not obvious.

To understand the potential for using post-critical reflections in this situation, we

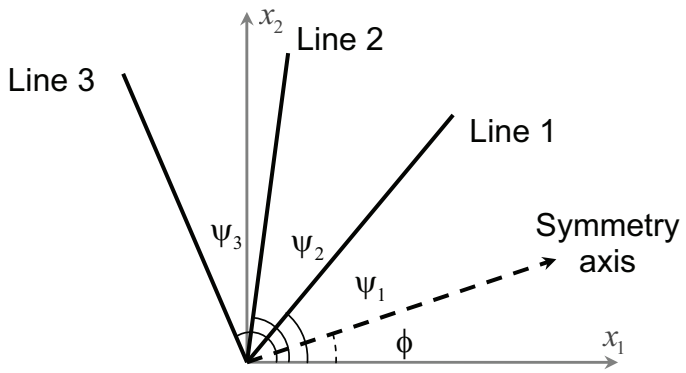

Figure 4.7: A plan view of three 2D survey lines over a horizontal HTI layer with the arbitrary symmetry axis direction from the chosen global coordinate system.

provide a sensitivity analysis for the multi-azimutal acquisition coverage with minimal number of lines, which create angles ψ_1, ψ_2 and ψ_3 with a chosen global coordinate system (Figure 4.7). The symmetry axis direction forms the angle ϕ with axis x_1. For simplicity, we assume that the azimuthal separation between the survey lines $\Delta\psi$ is equal and, thus, satisfies $\Delta\psi = \psi_3 - \psi_2 = \psi_2 - \psi_1$. Assuming that the parameters of the isotropic overburden are known, we investigate the sensitivity of the normalized reflection coefficients for isotropic/HTI interface to the changes in the medium parameters related to the HTI halfspace only. To conduct the sensitivity analysis, we exploit techniques described by Al-Dajani and Alkhalifah (2000) and build up the following Jacobian matrix:

$$\mathbf{J}^T = \left(\mathbf{d}\left(\psi_1,\ \mathbf{x}\right)\ \mathbf{d}\left(\psi_2,\ \mathbf{x}\right)\ \mathbf{d}\left(\psi_3,\ \mathbf{x}\right)\right), \tag{9}$$

where

$$\mathbf{d} = \left(\frac{V_{P2}\partial_{V_{P2}}A}{A},\ \frac{V_{S2}\partial_{V_{S2}}A}{A},\ \frac{\rho_2\partial_{\rho_2}A}{A},\ \frac{\partial_{\epsilon^{(V)}}A}{A},\ \frac{\partial_{\delta^{(V)}}A}{A},\ \frac{\partial_{\gamma^{(V)}}A}{A},\ \frac{2\pi\partial_{\phi}A}{A}\right) \tag{10}$$

are submatrices of derivatives of the normalized reflection coefficient $A\left(\mathbf{x},\ \theta - \phi\right)$ with respect to the medium parameters for a particular survey line; T indicates the transpose of a matrix. The derivatives with respect to velocity and density are normalized to allow for direct comparison with the dimensionless anisotropic parameters.

As a result, the resolution matrix $\mathbf{M} = \mathbf{J}^T\mathbf{J}$ provides information on the linear dependency of the parameters and the strength of their resolution. A perfect resolution

matrix is the identity matrix, which indicates that all parameters are resolvable within the linear limit and do not have tradeoffs between each other. However, the resolution matrix only allows for a linearized analysis of the sensitivities valid at a point in the model space and depending on the level of nonlinearity can be representative of the general behavior.

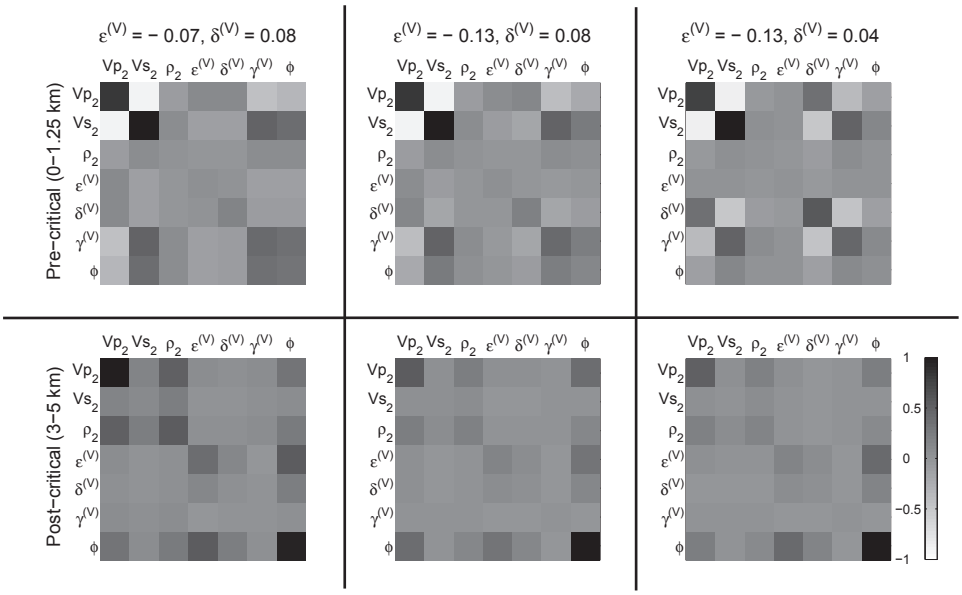

Figure 4.8: Resolution matrices of parameters for the HTI layer for different values of $\epsilon^{(V)}$ and $\delta^{(V)}$. Other parameters remain constant: $V_{P2} = 2.8$ m/s, $V_{S2} = 2.8$ km/s, $\rho_2 = 2.8$ kg/m^3, $\gamma^{(V)}$, $\phi = 0^0$. Acquisition parameters are: $\psi_2 = 30^0$, $\Delta\psi = 60^0$. Parameters of the upper isotropic halfspace are: $V_{P1} = 2.0$ km/s, $V_{S1} = 1.1$ km/s, and $\rho_1 = 1.8$ g/cm^3.

Figure 4.8 represents the resolution matrix $\mathbf{M}$ for all underburden model parameters for pre-critical (top row) and post-critical (bottom row) offsets for the following acquisition setups: $\psi_2 = 30^0$ and $\Delta\psi = 60^0$. Medium parameters in the isotropic upper layer are $V_{P1} = 2.0$ km/s, $V_{S1} = 1.1$ km/s, and $\rho_1 = 1.8$ g/cm^3. The parameters of the underburden are chosen to be $V_{P2} = 2.8$ km/s, $V_{S2} = 1.6$ km/s, $\rho_2 = 2.1$ g/cm^3, $\gamma^{(V)} = -0.1$, and $\phi = 0^0$. Each column corresponds to different combinations of anisotropy parameters $\epsilon^{(V)}$ and $\delta^{(V)}$. Higher diagonal values indicate higher sensitivity of the normalized reflection coefficients to the particular parameter, which consequently results in higher resolution of this parameter in the inversion. Non-zero

off-diagonal element reveal the tradeoff between parameters related to this element.

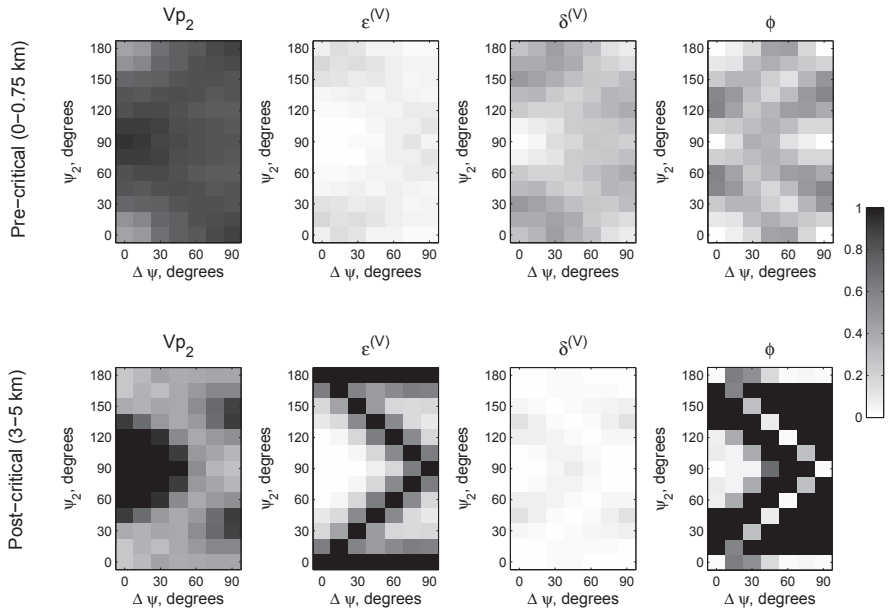

Figure 4.9: Dependence of some diagonal values of the resolution matrix on the acquisition parameters ψ_2 and $\Delta\psi_2$. The HTI medium is given by the following parameters $V_{P2} = 2.8$ m/s, $V_{S2} = 2.8$ km/s, $\rho_2 = 2.8$ g/cm^3, $\epsilon^{(V)} = -0.13$, $\delta^{(V)} = -0.08$, $\gamma^{(V)} = -0.1$, $\phi = 0^0$.

Generally, we observe that the sensitivity of medium parameters is model dependent, but there are common trends for different combinations of $\epsilon^{(V)}$ and $\delta^{(V)}$. Normalized effective reflection coefficients are sensitive to different sets of parameters at pre- and post-critical offsets. Exploiting only pre-critical domain results in resolving P- and S-wave velocities with reasonable tradeoff, and anisotropy parameters $\delta^{(V)}$ and $\gamma^{(V)}$ with some tradeoff between them, as well. The sensitivity of the reflection coefficients to the symmetry axis direction in the pre-critical domain is highly dependent on the strength of anisotropy. In the post-critical domain, the vertical P-wave velocity remains highly resolved with less tradeoff with the shear wave velocity, whereas the resolution of $\delta^{(V)}$ and $\gamma^{(V)}$ decreases. Instead, the resolution of density, anisotropy parameter $\epsilon^{(V)}$ and the symmetry axis direction increases considerably. We observe tradeoffs between V_{P2} and ρ_2; ϕ , $\epsilon^{(V)}$ and V_{P2}. However, it is important to note that the symmetry axis resolution is high with minor tradeoff with other parameters, which implies the importance of the post-critical reflection coefficients in resolving

the symmetry axis direction.

Figure 4.9 gives an idea of how azimuth ψ_2 and separation angle between the survey lines $\Delta\psi$ affect the resolution of some parameters in the pre-critical (top row) and the post-critical (bottom row) domains. Only diagonal values of the matrix $\mathbf{M} = \mathbf{J}^T\mathbf{J}$ corresponding to V_{P2}, $\epsilon^{(V)}$, $\delta^{(V)}$ and ϕ are exploited for this purpose. The calculations are made for the model, where parameters of the isotropic halfspace are the same as in Figure 4.8 and parameters of the HTI halfspace are given in the caption of Figure 4.9. The largest effect of the azimuth ψ_2 and angle separation $\Delta\psi$ on the resolution of media parameters is achieved in the post-critical domain than in the pre-critical domain. Moreover, different combinations of acquisition parameters affect the resolution of different sets of parameters. Thus, $45^0 < \psi_2 < 135^0$ and $\Delta\psi < 45^0$ results in the best resolution of V_{P2} in the post-critical domain, as this acquisition setup provides the best coverage of the isotropic plane. The best resolution of the anisotropy parameter $\epsilon^{(V)}$ is achieved, when one of the survey lines is close to the symmetry axis direction ($\psi_2 \approx \Delta\psi$). Although the normalized effective reflection coefficient in the post-critical domain is less sensitive to the anisotropy parameter $\delta^{(V)}$, its best resolution is observed, when one or more acquisition lines are close to the direction of 45^0 from the symmetry axis ($|\psi_2 - \Delta\psi| \approx 45^0$). The highest resolution of the symmetry axis direction is achieved, when survey lines deviate from the symmetry axis and isotropy plane. It is interesting that the direction of the symmetry axis ϕ has less blind regions than other parameters, and therefore has more chances to be resolved with acquisition setup, where $\Delta\psi > 45^0$.

4.7 Stability of the inversion

To gain insights on the feasibility of applying an inversion for all or some of the parameters, we exploit the reciprocal of the condition number (Al-Dajani and Alkhalifah, 2000) $\kappa^{-1} = \sqrt{\frac{|\lambda_{min}|}{|\lambda_{max}|}}$, where λ_{min} and λ_{max} are the minimum and maximum eigenvalues of the matrix $\mathbf{M} = \mathbf{J}^T\mathbf{J}$, respectively. Larger κ^{-1} values indicate better stability in the inversion. The value of κ^{-1} depends on the number of unknown parameters used in the inversion. To increase κ^{-1}, we have to assume some of the parameters known.

Here we focus on the assessment of the inversion stability for the most useful HTI parameters in practice: V_{P2}, $\epsilon^{(V)}$, and ϕ. It implies that the matrix $\mathbf{M} = \mathbf{J}^T\mathbf{J}$ consists of derivatives of the normalized effective reflection coefficients with respect

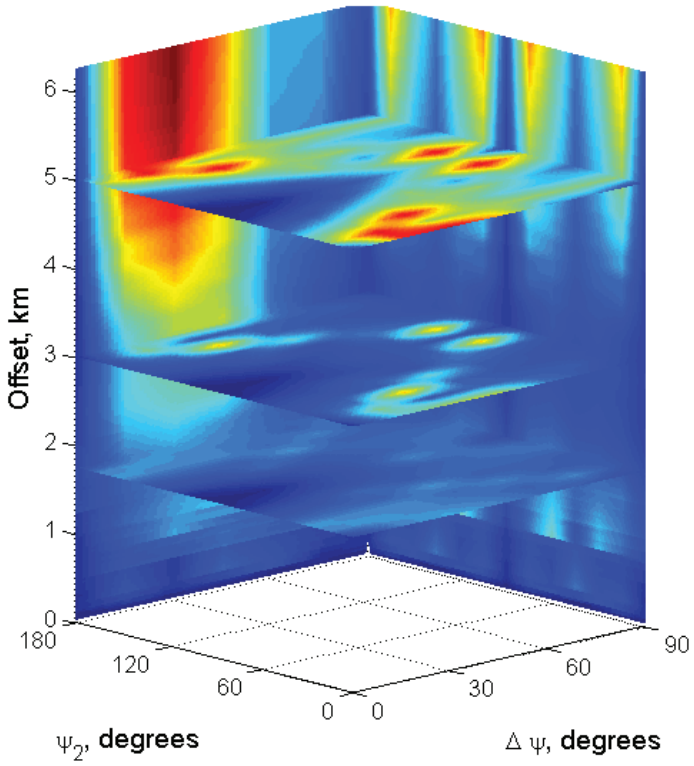

Figure 4.10: The reciprocal of the condition number (κ^{-1}) as a function of offset, ψ_2 and $\Delta\psi$. Model parameters are given in Figure 4.9.

to these three parameters only and therefore represents a 3×3 matrix. Figure 4.10 shows κ^{-1} as a function of offset, azimuth ψ_2 and separation angle $\Delta\psi$. Cold color is associated with poor parameter resolution and represents blind zone, while the warm color indicates good resolution. Horizontal slices, corresponding to pre-, near- and post-critical offsets, show the best resolution of all three parameters when post-critical offsets are involved in the matrix $\mathbf{M}$ evaluation. However, the influence of the azimuth angle and the separation angle in parameter resolution cannot be disregarded and one has to be careful with acquisition setup. The location of the survey line around the isotropic plane ($45^0 < \psi_2 < 135^0$, $\Delta\psi < 45^0$) results in blind zones. For optimal acquisition setup separation angles of larger than 45 degrees ($\Delta\psi > 45^0$) are preferable. This observation is consistent with Figure 4.9.

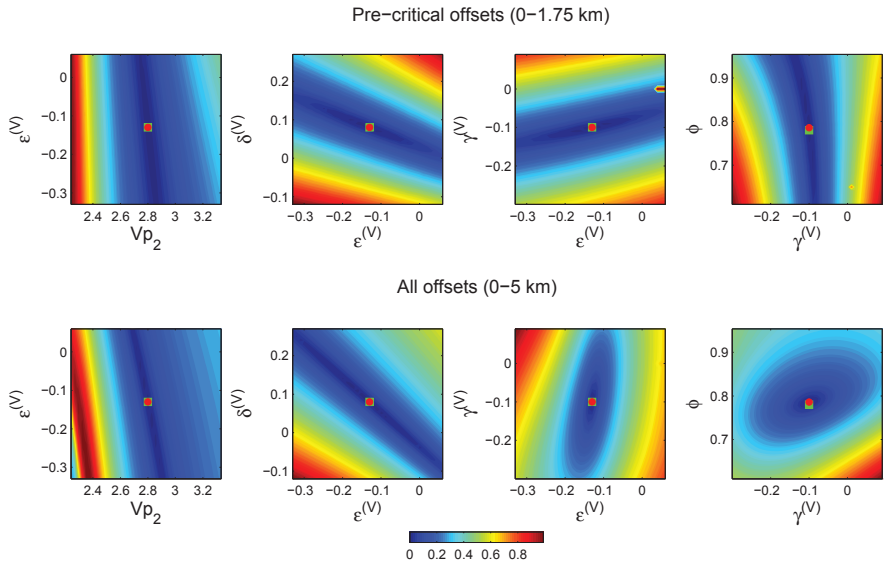

Figure 4.11: 2D cross-plots of the objective function for different offset ranges for model parameters given in Figure 4.9. Squares denote true model values; circles indicate a minima in the objective function.

To confirm the previous observations and obtain some insights into the changes in the accuracy of parameter recovery process beyond the linear limit, we monitor changes of the shape of the objective function using post-critical reflections. For this purpose, we exploit objective functions for a single azimuth, given by equation:

$$\mathbf{F} = \sqrt{\sum_{n=1}^{N} \left[A^D\left(\mathrm{x}_n\right) - A\left(\mathrm{x}_n\right)\right]^2} \tag{11}$$

where $A^D\left(\mathrm{x}_n\right)$ is the normalized reflection coefficient obtained from the data (Skopintseva et al., 2011) for a chosen azimuth, $A\left(\mathrm{x}_n\right)$ is the normalized effective reflection coefficient.

Figure 4.11 shows 2D cross-plots of the objective function for an azimuth of 45 degrees. For calculations, we exploited the model with parameters given in Figure 4.9. For each plot we vary only two parameters by 20%, while the rest of the parameters remain constant corresponding to their true values (the minima of the objective function). Top row represents the objective function for only pre-critical offsets, whereas the bottom row represents the objective function with information from near- and

post-critical offsets included. Although Figure 4.11 does not represent the whole set of possible 2D cross-sections, the effect of post-critical offsets on the shape of the objective function is obvious. We note that the shape of the objective function is generally smooth, which implies that our linearized observations in Figures 4.8-4.10 can be generalized. Figure 4.11 (top row) show strong tradesoffs between the anisotropy parameters. Specifically, the shape of the objective function along the ϕ and $\epsilon^{(V)}$ directions is stretched indicating their larger uncertainty compared with parameters V_{P2}, $\delta^{(V)}$, $\gamma^{(V)}$. This observation is consistent with the resolution matrix. When the post-critical offsets are involved into the objective function, its shape significantly changes, indicating better resolution of ϕ and $\epsilon^{(V)}$.

4.8 Discussion

Analysis of the reflection coefficients for an isotropic/HTI interface shows that post-critical reflections contain additional information about the underburden compared to pre-critical reflections. Pre-critical reflections have higher sensitivity to P- and S-wave velocities and anisotropy parameters $\gamma^{(V)}$ and $\delta^{(V)}$. Sensitivity analysis of post-critical reflections shows that they can potentially recover the P-wave velocity, the symmetry axis direction, the anisotropy parameter $\epsilon^{(V)}$ with small uncertainties, and the anisotropy parameter $\delta^{(V)}$ with a larger uncertainty. Despite that the pre-critical reflections are sensitive to the direction of symmetry axis, which is observed in some cases, the sensitivity of the post-critical reflections to this parameter is much higher. This is explained by the proportionality of the critical angle to the horizontal velocity of the underburden. Inversion of azimuthal traveltimes (Al-Dajani and Alkhalifah, 2000) also allows the retrieval of a set of parameters, similar to post-critical reflection. The difference between these two approaches is that inversion of azimuthal traveltimes provides information about the overburden, while azimuthal post-critical reflections answers questions of local properties of underburden.

Some insights about the anisotropy strength can be gained in the azimuthal analysis of the amplitude maximum observed beyond the critical angle. Our investigations show the proportionality between the the critical offset (not angle!) and the position of the amplitude maximum. Although, it is obvious that the difference between the critical offset and position of the amplitude maximum is controlled by the argument $k_P r^*_{PP}(\mathrm{x})$, explicit link between these two characteristics is not fully understood.

Despite that the sensitivity analysis and assessment of the inversion stability is per-

formed for the multi-azimuth coverage with only three survey lines for simplicity, we gain some insights on the effect of the acquisition setup on parameter estimation. The azimuthal distribution of the survey lines in the vicinity of the isotropic plane results in a reduced stability in the inversion. An increase in the number of survey lines, distributed azimuthally well, might improve stability of the inversion. However, stability of the inversion, where post-critical reflections are involved, is expected to be better than when only pre-critical reflections are used.

An analysis of the objective function for a potential inversion of parameters reveals the post-critical reflections influence on its shape. Noticing that the reflection coefficient has varying sensitivities to the inverted parameters prior and beyond the critical angle, the joint azimuthal inversion of pre- and post-critical reflections looks promising. Involving the azimuthal traveltime information into the inversion has a potential to reduce uncertainty in parameter estimates. It implies a requirement of further more detailed investigations of the objective functions.

Our analysis demonstrates the potential of post-critical reflections in exploiting the azimuthal analysis. However, their practical application might be befogged by noise in the data. This topic is not covered in this paper, but definitely deserves special attention.

4.9 Conclusions

Azimuthal analysis of the effective reflection coefficients for horizontal isotropic/HTI interface shows that the reflections beyond the critical angle are highly affected by the azimuthal variations in the horizontal velocity and therefore contain additional information about the anisotropy of underburden. The simple link between the azimuthally-dependent critical angle and the azimuthally-dependent horizontal velocities provides an opportunity to use post-critical reflections in the recovery of anisotropy parameters, however it is not practically applicable, as it is difficult to retrieve the critical angle from the data. The position of the amplitude maximum beyond the critical angle can be utilized instead.

Sensitivity analysis of the effective reflection coefficients for isotropic/HTI interface shows that the resolution of media parameters is highly dependent on the on the critical angle. Reflections prior the critical angle are more sensitive to anisotropy parameters $\delta^{(V)}$ and $\gamma^{(V)}$, while reflections beyond the critical angle provide better

resolution of the anisotropy parameter $\epsilon^{(V)}$ and the symmetry axis direction.

The acquisition setup plays an important role in parameter resolution especially in the post-critical domain. Our investigation performed for an acquisition with minimal multi-azimuthal coverage (three survey lines with constant angle of separation) show that poor resolution is obtained when all survey lines are located close to the isotropic plane. The optimal acquisition setup, which implies better resolution of media parameters, should have a separation angle between survey lines more than 45 degrees or alternatively larger number of survey lines.

4.10 Acknowledgments

We acknowledge Statoil for funding the PhD study of Lyubov Skopintseva and KAUST for its financial support.

4.11 Appendix A: Plane-wave reflection coefficients for horizontal isotropic/HTI interface

Here, we present the derivation of the exact plane-wave reflection coefficients for a horizontal interface between an isotropic medium in the upper halfspace and an HTI medium in lower halfspace. We associate the (x, y) - plane with the interface and let the z-axis be positive with depth. Consider (x, z)-plane as a wave propagation plane. Down-going P-wave propagating in upper halfspace, hits interface and generates three up-going waves in the isotropic half-space (P, SV, SH) and three down-going wave in the HTI halfspace (qP, qSV, qSH).

In the isotropic halfspace, P-wave polarization coincides with the propagation direction, SV-wave polarization is perpendicular to the propagation vector and is in the incidence plane, while SH-wave polarization is perpendicular both to the propagation vector and the incidence plane. Defining P-wave velocity as V_{P1}, SV- and SH-wave velocities as V_{S1} and the horizontal slowness as p, the vertical P- and S-wave slownesses

are given by

$$\begin{aligned} q_P^{(1)} &= \frac{1}{V_{P1}}\sqrt{1 - V_{P1}^2 p^2}, \\ q_S^{(1)} &= \frac{1}{V_{S1}}\sqrt{1 - V_{S1}^2 p^2}. \end{aligned} \tag{B-1}$$

The propagation directions of the down-going and up-going P-waves and up-going SV and SH waves are:

$$\begin{aligned} \mathbf{n}_P^{d\,(1)} &= \left(pV_{P1}, 0, q_P^{(1)} V_{P1}\right), \\ \mathbf{n}_P^{u\,(1)} &= \left(pV_{P1}, 0, -q_P^{(1)} V_{P1}\right), \\ \mathbf{n}_{SV}^{u\,(1)} &= \left(pV_{S1}, 0, -q_S^{(1)} V_{S1}\right), \\ \mathbf{n}_{SV}^{u\,(1)} &= \mathbf{n}_{SH}^{u\,(1)}, \end{aligned} \tag{B-2}$$

where d denotes down-going waves, u denotes up-going waves, (1) corresponds to the upper halfspace. The polarization vectors of down-going and up-going P-waves and up-going SV and SH waves are:

$$\begin{aligned} \mathbf{l}_P^{d\,(1)} &= \mathbf{n}_P^{d\,(1)}, \\ \mathbf{l}_P^{u\,(1)} &= \mathbf{n}_P^{u\,(1)}, \\ \mathbf{l}_{SV}^{u\,(1)} &= \left(-q_S^{(1)} V_{S1}, 0, -pV_{S1}\right), \\ \mathbf{l}_{SH}^{u\,(1)} &= (0,\ -1,\ 0), \end{aligned} \tag{B-3}$$

where the signs of the components of the polarization vectors are chosen according to Schoenberg and Protazio (1992). The stress vectors at the element of the interface in the isotropic halfspace have the following form:

$$\mathbf{t}_m^{k\,(1)} = \begin{pmatrix} V_{S1}^2 \rho_1 \left[l_{m\,3}^{k\,(1)} p + l_{m\,1}^{k\,(1)} q_m^{(1)} \right] \\ V_{S1}^2 \rho_1 l_{m\,2}^{k\,(1)} q_m^{(1)} \\ V_{P1}^2 \rho_1 \left[l_{m\,1}^{k\,(1)} p + l_{m\,3}^{k\,(1)} q_m^{(1)} \right] - 2V_{S1}^2 \rho_1 l_{m\,1}^{k\,(1)} p \end{pmatrix}, \tag{B-4}$$

where $m = P,\ SV,\ SH$ and $k = d,\ u$.

In the HTI halfspace, velocities qP-, qSV- and qSH-wave propagation is azimuthally dependent, and the polarization vectors deviate from the propagation direction (for qP-wave) and the plane perpendicular to the propagation direction (for qSV and qSH waves).

When the horizontal symmetry axis of the HTI medium is in the propagation plane and coincides with x-axis the stiffness tensor in Voigt notation has the following form

(Musgrave, 1970):

$$\mathbf{C} = \begin{pmatrix} c_{11} & c_{13} & c_{13} & 0 & 0 & 0 \\ c_{13} & c_{33} & c_{33}-2c_{44} & 0 & 0 & 0 \\ c_{13} & c_{33}-2c_{44} & c_{33} & 0 & 0 & 0 \\ 0 & 0 & 0 & c_{44} & 0 & 0 \\ 0 & 0 & 0 & 0 & c_{66} & 0 \\ 0 & 0 & 0 & 0 & 0 & c_{66} \end{pmatrix}. \tag{B-5}$$

When the horizontal symmetry axis has an angle φ with the incidence plane, the stiffness matrix can be written as:

$$\mathbf{C}' = \begin{pmatrix} c'_{11} & c'_{12} & c'_{13} & 0 & 0 & c'_{16} \\ c'_{12} & c'_{22} & c'_{23} & 0 & 0 & c'_{26} \\ c'_{13} & c'_{23} & c'_{33} & 0 & 0 & c'_{36} \\ 0 & 0 & 0 & c'_{44} & c'_{45} & 0 \\ 0 & 0 & 0 & c'_{45} & c'_{55} & 0 \\ c'_{16} & c'_{26} & c'_{36} & 0 & 0 & c'_{66} \end{pmatrix}, \tag{B-6}$$

where matrix components are functions of azimuth and stiffness components in old coordinates from equation B-2:

$$\begin{aligned}
c'_{11} =& c_{11}\cos^4\varphi + 2(c_{13}+2c_{66})\cos^2\varphi\sin^2\varphi + c_{33}\sin^4\varphi, \\
c'_{22} =& c_{33}\cos^4\varphi + 2(c_{13}+2c_{66})\cos^2\varphi\sin^2\varphi + c_{11}\sin^4\varphi, \\
c'_{33} =& c_{33}, \\
c'_{44} =& c_{44}\cos^2\varphi + c_{66}\sin^2\varphi, \\
c'_{55} =& c_{66}\cos^2\varphi + c_{44}\sin^2\varphi, \\
c'_{66} =& \frac{1}{8}(c_{11}-2c_{13}+4c_{66}+c_{33}-(c_{11}-2c_{13}-4c_{66}+c_{33})\cos 4\varphi), \\
c'_{16} =& \frac{1}{4}(c_{11}-c_{33}+(c_{11}-2c_{13}-4c_{66}+c_{33})\cos 2\varphi)\sin 2\varphi, \\
c'_{26} =& -\frac{1}{4}(-c_{11}+c_{33}+(c_{11}-2c_{13}-4c_{66}+c_{33})\cos 2\varphi)\sin 2\varphi, \\
c'_{36} =& (-c_{11}+c_{13}+2c_{66})\cos\varphi\sin\varphi, \\
c'_{12} =& \frac{1}{8}(c_{11}+6c_{13}-4c_{66}+c_{33}-(c_{11}-2c_{13}-4c_{66}+c_{33})\cos 4\varphi), \\
c'_{13} =& c_{13}\cos^2\varphi + (c_{11}-2c_{66})\sin^2\varphi, \\
c'_{23} =& (c_{11}-2c_{66})\cos^2\varphi + c_{13}\sin^2\varphi.
\end{aligned} \tag{B-7}$$

The vertical slowness components $q^{(2)}$ ((2) denotes lower half-space) are obtained

from the eigenvalues of the Christophel equation:

$$\det \begin{vmatrix} c'_{11}p^2 + c'_{55}\left(q^{(2)}\right)^2 - \rho_2 & c'_{16}p^2 + c'_{45}\left(q^{(2)}\right)^2 & \left(c'_{13} + c'_{55}\right)p^2 \\ c'_{16}p^2 + c'_{45}\left(q^{(2)}\right)^2 & c'_{66}p^2 + c'_{44}\left(q^{(2)}\right)^2 - \rho_2 & \left(c'_{36} + c'_{45}\right)pq^{(2)} \\ \left(c'_{13} + c'_{55}\right)p^2 & \left(c'_{36} + c'_{45}\right)pq^{(2)} & c'_{55}p^2 + c'_{33}\left(q^{(2)}\right)^2 - \rho_2 \end{vmatrix} = 0 \tag{B-8}$$

and have the following form:

$$\begin{aligned} q_P^{(2)} =& \frac{1}{2}\sqrt{K_1 - \sqrt{K_1^2 - K_2}} \\ q_{SV}^{(2)} =& \frac{1}{2}\sqrt{K_1 + \sqrt{K_1^2 - K_2}} \\ q_{SH}^{(2)} =& \sqrt{\frac{\rho_2 - \left[c_{66}\cos^2\varphi + c_{44}\sin^2\varphi\right]p^2}{c_{44}}}, \end{aligned} \tag{B-9}$$

where

$$\begin{aligned} K_1 =& \frac{1}{c_{66}c_{33}}\Big[2\left(c_{33} + c_{66}\right)\rho_1 \\ &+ 2\left(c_{13}^2 cos^2\varphi - c_{11}c_{33}cos^2\varphi\right)p^2 \\ &+ 4c_{66}\left(c_{13}cos^2\varphi - c_{33}\sin^2\varphi\right)p^2\Big], \\ K_2 =& \frac{4}{c_{66}c_{33}}\Big[4\rho_2^2 \\ &- 4p^2\left(\rho_2 - c_{66}p^2 cos^2\varphi\right)\left(c_{33} + c_{11}cos^2\varphi\right) \\ &- 4p^2 c_{66}\left(\rho_2 - c_{33}p^2\sin^2\varphi\right) \\ &+ p^4\sin^2 2\varphi\left(-c_{13}\left(c_{13} + c_{66}\right) + c_{33}\left(c_{11} - 2c_{66}\right)\right)\Big]. \end{aligned} \tag{B-10}$$

The phase velocities are obtained from equations:

$$V_{j\,2} = \frac{1}{\sqrt{\left(q_j^{(2)}\right)^2 + p^2}}, \tag{B-11}$$

where $j = qP,\ qSV,\ qSH$. It yields vectors of wave propagation $\mathbf{n}_j^{d\,(2)} = \left(pV_{j\,2}, 0, q_j^{(2)}V_{j\,2}\right)$.

The eigenvectors of the Christophel equation B-5 yield the polarization vectors. The analytical solution is very cumbersome and we thus do not obtain its actual form here.

Generally, polarization vectors do not coincide with the direction of wave propagation or plane perpendicular to the wave propagation and deviate from the incident plane: $\mathbf{l}_j^{d\,(2)} = \left(l_{j\,1}^{d\,(2)},\ l_{j\,2}^{d\,(2)},\ l_{j\,3}^{d\,(2)}\right)$, $j = qP,\ qSV,\ qSH$. To choose signs of the components for polarization vectors, sign convention extended for the three-dimensional case, given by Schoenberg and Protazio (1992), is used here.

Stress vectors at the element of interface in HTI media have the following form:

$$\mathbf{t}_j^{d\,(2)} = \begin{pmatrix} c'_{55} l_{j\,3}^{d\,(2)} p + c'_{55} l_{j\,1}^{d\,(2)} q_j^{(2)} + c'_{54} l_{j\,2}^{d\,(2)} q_j^{(2)} \\ c'_{54} l_{j\,3}^{d\,(2)} p + c'_{54} l_{j\,1}^{d\,(2)} q_j^{(2)} + c'_{44} l_{j\,2}^{d\,(2)} q_j^{(2)} \\ c'_{13} l_{j\,1}^{d\,(2)} p + c'_{63} l_{j\,2}^{d\,(2)} p + c'_{33} l_{j\,3}^{d\,(2)} q_j^{(2)} \end{pmatrix}. \tag{B-12}$$

Using boundary conditions at the isotropic/HTI interface $z = 0$, which states that the normal and tangential components of the displacement and stress traction components are continuous, we obtain the following system of equations:

$$\mathbf{b} = \mathbf{A}\mathbf{X}, \tag{B-13}$$

where

$$\mathbf{b} = \left(\mathbf{l}_P^{d\,(1)}, \mathbf{t}_P^{d\,(1)}\right)^T,$$

$$\mathbf{A} = \begin{pmatrix} -\mathbf{l}_P^{u\,(1)} & -\mathbf{l}_{SV}^{u\,(1)} & -\mathbf{l}_{SH}^{u\,(1)} & \mathbf{l}_{qP}^{d\,(2)} & \mathbf{l}_{qSV}^{d\,(2)} & \mathbf{l}_{qSH}^{d\,(2)} \\ -\mathbf{t}_P^{u\,(1)} & -\mathbf{t}_{SV}^{u\,(1)} & -\mathbf{t}_{SH}^{u\,(1)} & \mathbf{t}_{qP}^{d\,(2)} & \mathbf{t}_{qSV}^{d\,(2)} & \mathbf{t}_{qSH}^{d\,(2)} \end{pmatrix}, \tag{B-14}$$

$$\mathbf{X} = \left(R_{P\,P},\ R_{P\,SV},\ R_{P\,SH},\ T_{P\,qP},\ T_{P\,qSV},\ T_{P\,qSH}\right)^T,$$

$R_{P\,P}$, $R_{P\,SV}$, $R_{P\,SH}$ are reflection coefficients, $T_{P\,qP}$, $T_{P\,qSV}$, $T_{P\,qSH}$ are transmission coefficients, T is the transpose sign.

Solving the system of equations B-10, we obtain plane-wave reflection and transmission coefficients for an isotropic/HTI interface. For our purpose we focus on reflection coefficients for PP-reflections.

Chapter 5

Frequency effects at pre-, near- and post-critical offsets observed on water-plexiglas interface

Lyubov Skopintseva[1], Tariq Alkhalifah[2], Martin Landrø[1],

[1] Norwegian University of Science and Technology, Trondheim, Norway

[2] King Abdullah University of Science and Technology, Thuwal, Saudi Arabia

Presented at the ROSE Meeting, Trondheim, Norway, May 2011; the 73th EAGE Conference & Exhibition, Vienna, Austria, May 2011; Submitted to Geophysical Journal International

5.1 Abstract

The frequency dependence of the reflection coefficients can be an important interpretational tool in detecting and analyzing seismic anisotropy. We perform such analysis on experimental data containing multi-azimuth reflections from a simple water-plexiglas interface, where the underburden is designed to represent a medium with vertical fractures. We show that the frequency dependency of the amplitude and phase at pre-, near- and post-critical offsets reveals azimuthal variation. We attempt to explain the observed frequency phenomena within a transversely isotropic model with a horizontal symmetry axis (HTI). For this purpose we introduce effective reflection coefficients valid for horizontal water/HTI interface. These coefficients account for wavefront curvature and frequencies and thus provide adequate description of phenomena generated at the critical angle. We show that our approach explains some of the frequency dependence of the experimental data. Furthermore, we show that the post-critical domain is useful for the analysis of the anisotropy properties of HTI media, as it is sensitive to the anisotropy parameters and the symmetry axis direction.

5.2 Introduction

Detecting fractures and their azimuth direction is one of the useful but still challenging tasks in the industry. It provides information crucial to drilling and injection strategies. We should, therefore, seek all potential sources of information to improve our ability to predict fracture density and fracture direction.

One source of information is the frequency dependency of seismic data, which could provide some insights into the physics of wave propagation in such media. There is significant amount of work dedicated to the frequency dependence of attenuation and the dispersion phenomena. Carcione (2007), for example, derived plane-wave reflection coefficients for an elastic anisotropic media. Chapman and Liu (2003) showed that fracture density and fluid saturation have an influence on frequency characteristics of the seismic wavefield and developed plane-wave frequency-dependent reflection coefficients describing these phenomena. Nevertheless, plane-wave reflection coefficients are not capable of describing reflection phenomena accurately at near- or post-critical domains, where the critical angle comes into play and produces head waves, resulting in the associated interference between head waves and the reflected wave.

Clearly, the analysis of near- and post-critical offsets has the potential to bring additional information about the medium. Landrø and Tsvankin (2007) analyzed azimuthal dependence of the critical angle and showed that long-offset reflections have the potential to improve the quality of our interpretation of anisotropic data. Downton and Ursenbach (2006) and Ayzenberg et al. (2009) derived reflection coefficients for isotropic and VTI media, which are valid prior and beyond the critical angle. They showed that the frequency dependence of these coefficients is associated with non-planar wavefronts. Skopintseva et al. (2011) showed that exploiting near- and post-critical reflections improves the quality of AVO inversion for isotropic media.

In this paper, we analyze frequency dependence of the reflected wavefield from an experiment performed by Alhussain (2007), which includes reflections from pre-, near- and post-critical offsets. He acquired data for a horizontal planar water-plexiglas interface, where the underburden is set once to imitate isotropic media (Alhussain et al., 2008) and second time to imitate media with vertical fractures. The latter medium was covered by multi-azimuth survey lines with 15 degrees of separation angle. We divide the wavefield into amplitude and phase components and show that they have similar features.

To explain the observed frequency effects, we extend the theory of effective reflection

coefficients (Ayzenberg et al., 2009) for an HTI model and show that this approach can explain a big part of the observed phenomena. However, results of the independent synthetic modeling confirm the presence of phenomena not related to the HTI model. We associate these phenomena with diffraction from the edge of the model. Additionally, we provide an analysis of the special features of the reflected data in post-critical domain and show their dependence on azimuth and anisotropy parameters.

5.3 Theory

We consider a two-layer model with a horizontal plane interface, where the underburden is represented by HTI or isotropic media, and the overburden is a water layer. For non-attenuative media, the reflected wavefield from a point source in the frequency approximation has the following form (Skopintseva et al., 2011):

$$\mathbf{u}_{PP}\left(\mathrm{x},\ \omega\right) \cong \chi_{PP}\left[\mathrm{x},\ \omega,\ \mathbf{g}\right]\ \frac{i}{V_{P1}}\ S\left(\omega\right) \frac{e^{i\,k_P\ l(\mathrm{x})}}{\sqrt{J_{PP}\left(\mathrm{x}\right)}}\ \mathbf{e}_{PP}\left(\mathrm{x}\right) \tag{1}$$

where $\chi_{PP}\left[\mathrm{x},\ \omega,\ \mathbf{g}\right]$ is the effective reflection coefficient (ERC) defined at the receiver, ω is angular frequency, $\mathbf{g} = \left(V_{P1}, \rho_1, V_{P2},\ V_{S2},\ \epsilon^{(V)},\ \gamma^{(V)},\ \delta^{(V)}, \varphi, \rho_2\right)$ is the model parameter vector, V_{P1} is the overburden P-wave velocity, ρ_1 and ρ_2 are densities in overburden and underburden, respectively; V_{P2} and V_{S2} are P- and S-wave velocities of underburden in isotropic plane; $\epsilon^{(V)},\ \gamma^{(V)},\ \delta^{(V)}$ are anisotropy parameters in HTI notation (Rüger, 2001), φ is the azimuth angle between the survey line and the symmetry axis, $l\left(\mathrm{x}\right)$ is the distance between the source and receiver along the ray, $J_{PP}\left(\mathrm{x}\right) = \left[l\left(\mathrm{x}\right)\right]^2$ is the geometrical spreading of the reflected PP-wave, $k_P = \frac{\omega}{V_{P1}}$ is the wavenumber in the overburden, $\mathbf{e}_{PP}\left(\mathrm{x}\right)$ is the polarization vector and $S\left(\omega\right)$ is the source wavelet. The vector $\mathrm{x} = (x_1, x_2, ..., x_N)$ contains the receiver coordinates. The coordinate system is chosen in such a way that x-axis coincides with the survey line.

Originally, ERC at the interface is derived by Ayzenberg et al. (2007) for acoustic media and Ayzenberg et al. (2009) for VTI media. Skopintseva et al. (2011) extrapolated ERC to the receiver surface for the case of plane interface. Here, we adopt ERC at the receiver for a model consisting of a water layer overlying an HTI media. It has the following form:

$$\chi_{PP}\left[\mathrm{x},\ \omega,\ \mathbf{g}\right] = \frac{u^*_{PP\ \mathrm{norm}}\left(\mathrm{x},\ \mathbf{g}\right)\cos\theta\left(\mathrm{x}\right) + u^*_{PP\ \tan}\left(\mathrm{x},\ \mathbf{g}\right)\sin\theta\left(\mathrm{x}\right)}{\left[\frac{i}{k_P r^*_{PP}(\mathrm{x})} - \frac{1}{k_P^2 r^{*2}_{PP}(\mathrm{x})}\right] e^{ik_P r^*_{PP}(\mathrm{x})}}, \tag{2}$$

where $\theta(\mathrm{x})$ is the reflection angle, $u^*_{PP\,\mathrm{norm}}(\mathrm{x})$ and $u^*_{PP\,\tan}(\mathrm{x})$ are the dimensionless normal and tangential components of the displacement vector, which have the following form:

$$\begin{aligned} u^*_{PP\,\mathrm{norm}}(\mathrm{x},\ \mathbf{g}) &= -\int_0^{+\infty} R_{PP}(\zeta,\ \mathbf{g})\, e^{i\,\alpha(\mathrm{x})\sqrt{1-\zeta^2}} J_0\left[\beta(\mathrm{x})\,\zeta\right]\zeta d\zeta, \\ u^*_{PP\,\tan}(\mathrm{x},\ \mathbf{g}) &= -\int_0^{+\infty} R_{PP}(\zeta,\ \mathbf{g})\, \frac{i e^{i\,\alpha(\mathrm{x})\sqrt{1-\zeta^2}}}{\sqrt{1-\zeta^2}} J_1\left[\beta(\mathrm{x})\,\zeta\right]\zeta^2 d\zeta, \end{aligned} \tag{3}$$

and $R_{PP}(\zeta,\ \mathbf{g})$ is the exact plane-wave reflection coefficient for the water/HTI interface (Appendix 5.11), $\alpha(\mathrm{x}) = k_P r^*_{PP}(\mathrm{x})\cos\theta(\mathrm{x})$, $\beta(\mathrm{x}) = k_P r^*_{PP}(\mathrm{x})\sin\theta(\mathrm{x})$, $r^*_{PP}(\mathrm{x})$ is the apparent radius of the wavefront at the receiver, ζ is the horizontal component of the unit P-wave ray vector in the overburden, J_0 and J_1 are the Bessel functions of the zeroth and first order. A general form of the radius $r^*_{PP}(\mathrm{x})$ is introduced by Skopintseva et al. (2011). For plane interfaces, $r^*_{PP}(\mathrm{x})$ reduces to the distance $l(\mathrm{x})$ between the source and the receiver along the ray. Equations 2 and 3 can be easily adopted for water-isotropic solid interface though substituting the appropriate reflection coefficient $R_{PP}(\zeta,\ \mathbf{g})$ in equation 3, where $\mathbf{g} = (V_{P1}, \rho_1, V_{P2},\ V_{S2}, \rho_2)$(Appendix 5.10).

In addition to the dependence on media parameters $\mathbf{g}$, the reflection coefficient is a function of an additional argument $k_P r^*_{PP}(\mathrm{x})$, which describes the wavefront curvature and the frequency effects on the reflection amplitudes. Ayzenberg et al. (2007) showed that these effects are mostly pronounced in near- and post-critical domains, where head waves appear and interfere with the reflected wave. The value of the argument $k_P r^*_{PP}(\mathrm{x})$ affects the slope of rapid amplitude increase in the near-critical domain, the position of amplitude maximum and the frequency of oscillations in the post-critical domain. The larger the argument $k_P r^*_{PP}(\mathrm{x})$ is, the steeper the slope of amplitude increase, the smaller the offset of amplitude maximum, and the higher the frequency of the observed oscillations.

Rewriting equation 1 in terms of amplitude and phase components, we obtain:

$$\mathbf{u}_{PP}(\mathrm{x},\ \omega) \cong \frac{\left|\chi_{PP}[\mathrm{x},\ \omega,\ \mathbf{g}]\right|\left|S(\omega)\right|}{V_{P1}\sqrt{J_{PP}(\mathrm{x})}}\, e^{i\left[\omega t(\mathrm{x}) + \varphi(\mathrm{x},\,\omega,\,\mathbf{g}) + \Phi(\omega) + \frac{\pi}{2}\right]}\mathbf{e}_{PP}(\mathrm{x}) \tag{4}$$

where $|\chi_{PP}(\mathrm{x},\omega,\ \mathbf{g})|$ and $\varphi(\mathrm{x},\omega,\ \mathbf{g})$ are the magnitude and phase of the effective reflection coefficient, respectively, $|S(\omega)|$ and $\Phi(\omega)$ are the magnitude and phase of the incidence wavelet, $t(\mathrm{x})$ is the traveltime.

The magnitude of the reflected wavefield, compensated for geometrical spreading

$J_{PP}\,(\mathrm{x})$ is:

$$|u_{PP}\,(\mathrm{x},\ \omega)| \cong \frac{|\chi_{PP}\,[\mathrm{x},\ \omega,\ \mathbf{g}]|\,|S\,(\omega)|}{V_{P1}}\ . \tag{5}$$

Normalizing equation 5 by the magnitude of the reflected wavefield at minimum offset, we remove the effect of the incidence wavelet and obtain a normalized magnitude of the reflected wavefield coefficient:

$$|u_{PP}\,(x_n,\ \omega)|_{norm} = \frac{|u_{PP}\,(x_n,\ \omega)|}{|u_{PP}\,(x_1,\ \omega)|} = \frac{|\chi_{PP}\,[x_n,\ \omega,\ \mathbf{g}]|}{|\chi_{PP}\,[x_1,\ \omega,\ \mathbf{g}]|}\ , \tag{6}$$

$n = 1,\ 2,\ \ldots,\ N$. This equation indicates that $|u_{PP}\,(\mathrm{x},\ \omega)|_{norm}$ is equivalent to the normalized magnitude of the reflection coefficient. We thus define $|u_{PP}\,(\mathrm{x},\ \omega)|_{norm}$ as AVO data.

Taking the imaginary part of the normalized derivative of the wavefield in equation 4, we obtain the following equation:

$$\mathrm{Im}\left[\frac{1}{\mathbf{u}_{PP}\,(\mathrm{x},\ \omega)}\frac{\partial \mathbf{u}_{PP}\,(\mathrm{x},\ \omega)}{\partial \omega}\right] = t\,(\mathrm{x}) + \frac{\partial \varphi\,(\mathrm{x},\omega,\ \mathbf{g})}{\partial \omega} + \frac{\partial \Phi\,(\omega)}{\partial \omega} \tag{7}$$

Assuming that the water layer representing the overburden is homogeneous, the frequency independent traveltime $t\,(\mathrm{x})$ obtained from ray theory can be easily removed from equation 7. Noticing that the phase of the wavelet is offset independent, it can be removed through subtracting data at minimum offset:

$$T\,(x_n,\ \omega)_{norm} = \frac{\partial \varphi\,(x_n,\omega,\ \mathbf{g})}{\partial \omega} - \frac{\partial \varphi\,(x_1,\omega,\ \mathbf{g})}{\partial \omega} \tag{8}$$

The obtained function in equation 8 represents an extra traveltime caused by the phase rotation of the effective reflection coefficient between two offsets.

Equations 6 and 8, thus, allow us to focus on the frequency effects of the reflected wavefield. As water is incompressible and considered to be homogeneous, the associated frequency effects will only occur in the underburden.

5.4 The experiment

We analyze data from the physical modeling provided by Alhussain (2007), where he acquired pre-, near- and post-critical reflections from a horizontal plane interface between water in the overburden and plexiglas in the underburden.

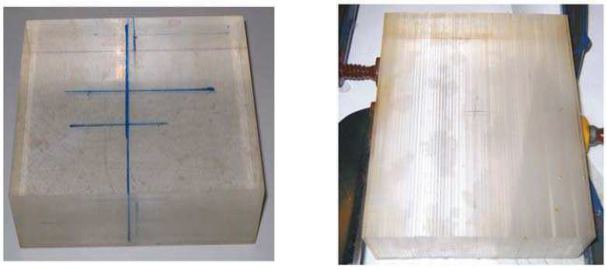

Figure 5.1: Isotropic (left) and fractured (right) samples of plexiglas used in the Experiment. (Figure courtesy of Alhussain (2007)).

He exploited two types of plexiglas media: solid, imitating an isotropic medium, and a stack of 2 mm thick plates, imitating media with vertical fractures (Figure 5.1). The medium parameters are obtained from transmission measurements of P- and S-wave velocities, where omni-directional P-wave and S-wave transducers with dominant frequencies of 220 and 500 kHz, respectively, are used. Parameters measured for the isotropic plexiglas are $V_{P2} = 2.724$ km/sec, $V_{S2} = 1.384$ km/sec, and $\rho_2 = 1.2$ g/cm^3. Parameters measured for the fractured plexiglas are $V_{P2} = 2.709$ km/sec, $V_{S2} = 1.382$ km/sec, $\rho_2 = 1.2$ g/cm^3, $\varepsilon^{(V)} = -0.0019$, $\delta^{(V)} = -0.069$, $\gamma^{(V)} = -0.0439$ (Alhussain, 2007).

The scheme of the reflection experiment is shown in Figure 5.2. The plexiglas is submerged into water with parameters $V_{P1} = 1.484$ km/sec, $\rho_1 = 1$ g/cm^3. Omni-directional P-wave transducers with a dominant frequency of 220 kHz are placed in the water 24 cm above the water-plexiglas interface. The dominant wavelength of the P-wave in the water layer is 6.7 mm, which is approximately 3.5 times larger than the thickness of the plexiglas plates. To carry out the AVO study, one CMP gather is acquired for the model with isotropic plexiglas. To provide an AVO azimuth study, seven CMP gathers, corresponding to different azimuth angles, are acquired for the model with fractured plexiglas. The azimuth separation between these survey lines is 15 degrees and angle φ corresponds to 0, 15, 30, 45, 60, 75, 90 degrees. The minimum offset is 2 cm and the source and receiver were moved apart from each other with an increment of 2 mm. The maximum offset is 54 cm. Each CMP gather consists of 270 traces. The critical angle (offset) is approximately the same for both types of interfaces, when survey lines are located in isotropic plane, and is 33^0 (31 cm). It is equivalent to offset-to-depth ratio $x/h = 1.29$.

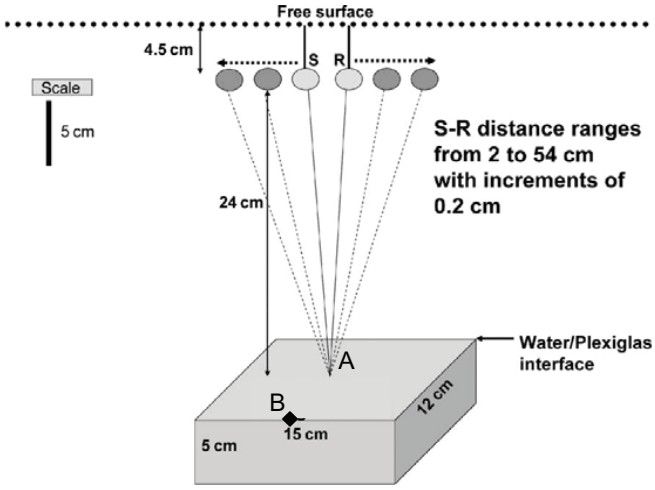

Figure 5.2: Scheme of the acquisition setup used in the Experiment (Figure courtesy of Alhussain (2007)). A is the reflection point, B is the edge point of the plexiglas.

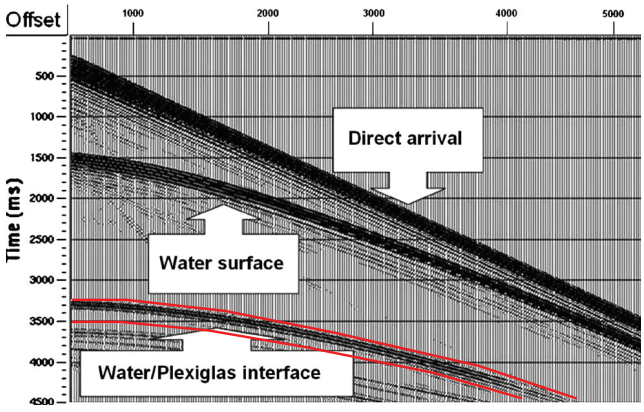

Figure 5.3: Example of seismogram obtained from experiment (Figure courtesy of Alhussain (2007)).

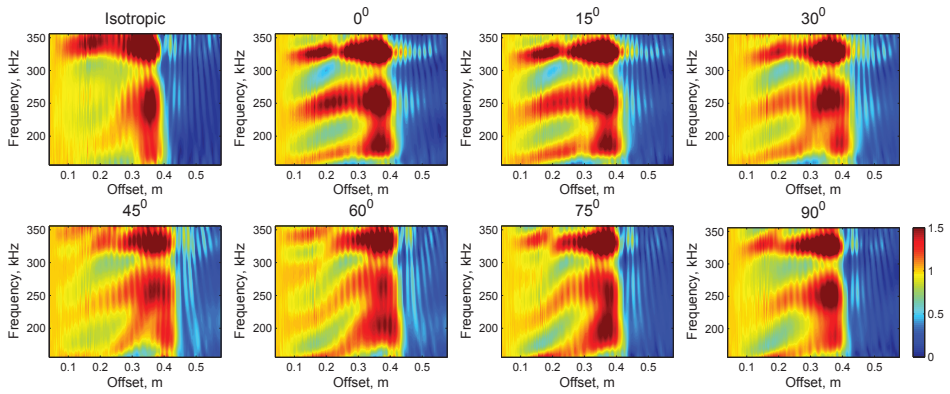

Figure 5.4: Normalized to the minimum offset amplitude spectra of the target reflection (AVO data) for isotropic and fractured media for various azimuthal angles ($\varphi = 0,\ 15,\ 30,\ 45,\ 60,\ 75,\ 90^0$), obtained by the physical modeling.

An example of the acquired CMP gather is shown in Figure 5.3. We observe a clear reflection from the water-plexiglas interface at traveltime 3.2×10^{-4} sec. The length of the wavelet impuls is around 2×10^{-5} sec. The next weak event related to the reflection from the bottom of plexiglas piece has a traveltime 3.6×10^{-4} sec at the nearest offset. The target water/plexiglas reflection is thus well separated from the bottom reflection and is considered in the analysis.

5.4.1 Experimental AVO data

Figure 5.4 shows AVO signatures for the isotropic and fractured media, extracted from the experimental data according to equation 6. The computations are made for the target water/plexiglas reflection registered with traveltime 3.2×10^{-4} at nearest offset within the 2×10^{-5} sec time window. In general, we observe strong amplitudes at near-critical offsets ($0.3 - 0.4$ m), and oscillating weak amplitudes at post-critical offsets ($>$ 0.4 m). These oscillations are interpreted as interference between the reflected and the head waves (Skopintseva et al., 2011). Amplitude at near-critical offsets periodically changes and tends to increase with frequency and depends on azimuth. The position of amplitude maximum in near-critical domain shifts towards smaller offsets with the frequency increase. The amplitude at pre-critical offsets ($<$ 0.3 m) has a complex behavior both for the fractured and the isotropic cases. There are relatively strong offset-dependent periodical variations with frequency. The strength

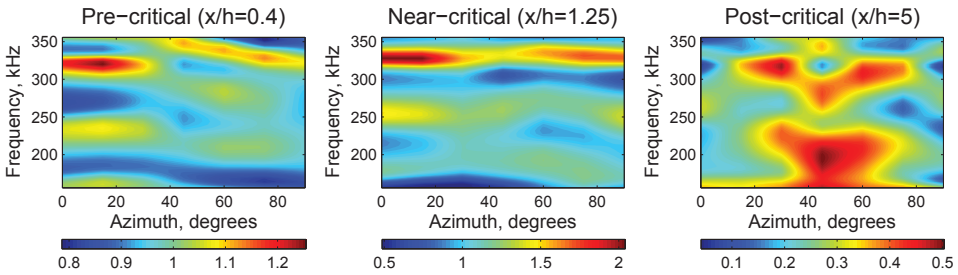

Figure 5.5: The slices of AVO data for different azimuths of fractured media (Figure 5.4) taken at pre-, near- and post-critical offsets with offset-to-depth ratios of 0.4, 1.25 and 5, respectively.

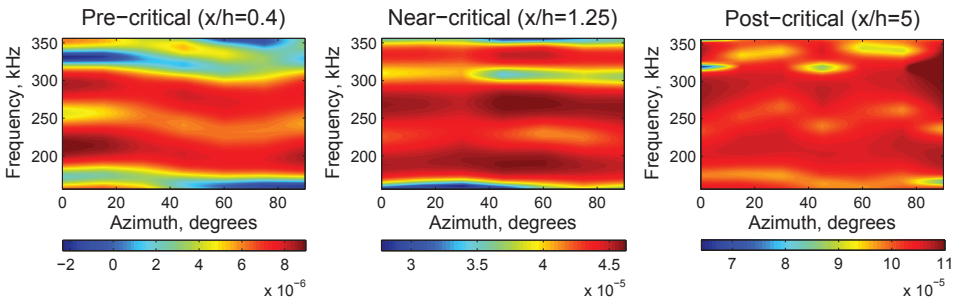

Figure 5.6: Maps of phase related traveltimes $T\left(x_n,\ \omega\right)_{norm}$ (equation 8) for different azimuths of fractured media at pre-, near- and post-critical offsets with offset-to-depth ratios of 0.4, 1.25 and 5, respectively. The units of color scale are given in seconds.

of the finger shaped phenomena depends on the azimuth and the weakest dependence is observed for an azimuth of 45 degrees. A minor fingering phenomenon is also observed for the isotropic case.

Figure 5.5 shows slices of the amplitude as a function of azimuth for certain offsets corresponding to pre-, near- and post-critical offsets, where offset-to-depth ratios are 0.4, 1.25, 5, respectively. Despite the noise, we observe systematic periodical behavior of the amplitude with azimuth with a full cycle as the azimuth varies from 0 to 90 degrees. The amplitude is influenced mainly by the fracturing as it approaches the azimuth of 45 degrees. This phenomenon is most pronounced at post-critical offsets.

Figure 5.6 represents the quantity $T\left(\mathrm{x},\ \omega\right)_{norm}$ obtained from the experimental data according to equation 8. Slices, corresponding to offset-to-depth ratios of 0.4, 1.25

and 5, reflect fracture effect on the phases of the reflections. The features in Figure 5.6 are similar to the ones in Figure 5.5. Isochrones of $T\,(\mathrm{x},\,\omega)_{norm}$ periodically vary with azimuth and frequency. These variations describe a full cycle as a function of azimuth with maximum frequencies across (0^0) and along (90^0) the fracture directions for pre- and near-critical domains and with minimum frequencies at 0^0 and 90^0 for post-critical domain. $T\,(\mathrm{x},\,\omega)_{norm}$ for a fixed azimuth, has two or more cycles of the strength changes.

5.5 Forward modeling of AVO data

To explain the frequency dependence of the experimental AVO data, we compare these data with AVO data obtained from modeling. For this purpose, the values for the media parameters described in the previous section are used to describe the fractured plexiglas in an HTI model. Despite the dominant wavelength of the incident wave is just 3.5 times larger than the distance between fractures, we investigate frequency effects which HTI model is able to describe.

The modeling is performed by two independent methods. The first approach is based on equation 6, where we calculate effective reflection coefficients, given by equations 2 and 3 for different frequencies. The second method is based on 3D reflectivity modeling. The reflectivity modeling is used to verify the ERC-based modeling and to confirm effects related to HTI model.

5.5.1 ERC-based modeling

Figure 5.7 shows effective reflection coefficients calculated for the setup of the physical modeling. According to equation 6, all coefficients are normalized by the amplitude at nearest offset. Color scale is preserved as in Figure 5.4. Generally, similar amplitude behavior in near- and post-critical domains are observed. Large amplitudes in near-critical domain gradually increase with frequency, position of the amplitude maximum shifts towards smaller offsets with frequency increase and weak amplitudes in the post-critical domain contain frequency-dependent oscillations. However, the pre-critical domain does not contain strong finger shaped phenomena and is associated with frequency-independent amplitudes. The maximum amplitude and variations of its position with azimuth are generally weaker than those observed in the experimental data.

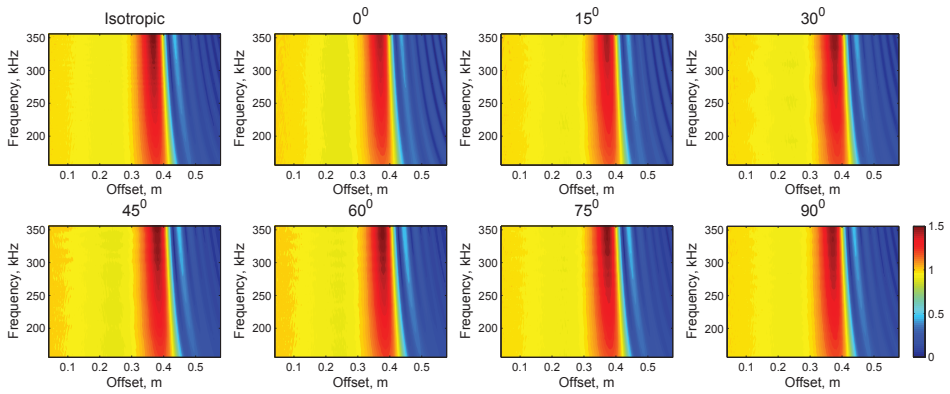

Figure 5.7: Normalized to the minimum offset magnitude of effective reflection coefficients calculated for isotropic and HTI model parameters estimated from the physical modeling.

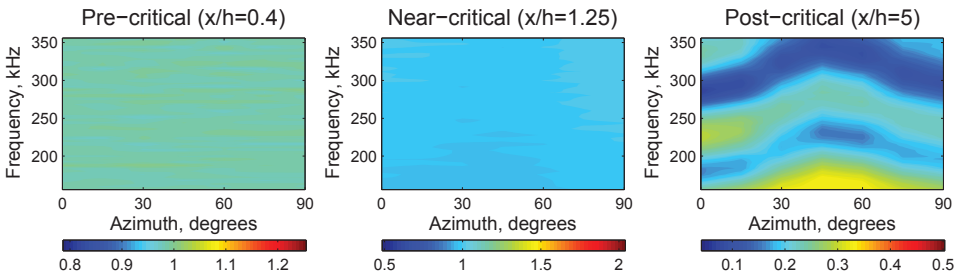

Figure 5.8: The slices of normalized to the minimum offset magnitudes of effective reflection coefficients for different azimuths of HTI model (Figure 5.7) taken at pre-, near- and post-critical offsets with offset-to-depth ratios of 0.4, 1.25 and 5, respectively.

Figure 5.8 shows 2D offset slices of the normalized effective reflection coefficients as a function of frequency and azimuth for offset-to-depth ratios of 0.4, 1.25, and 5. The color scale is preserved as in Figure 5.5 for comparison. The normalized effective reflection coefficients do not depend on the azimuth and frequency in pre- and near-critical domains, while this dependence is obvious in the post-critical domain. However, the behavior of the isochrones of the normalized effective reflection coefficients with azimuth does not fully coincide with Figure 5.5 as it has a maximum frequency for azimuth of 45^0 and minimum frequencies for azimuths 0^0 and 90^0, while

experimental data have minimum frequencies for all three azimuths.

The azimuthal frequency dependency of amplitudes in post-critical domain shows that long-offset reflections are useful in detecting fracture directions, as the frequency content of the reflection coefficient reaches a minimum at the symmetry and normal to the symmetry axis directions.

5.5.2 Reflectivity modeling

The reflectivity modeling is carried out for an acquisition setup scaled by a factor of 1000, where the interface depth is 240 m and the dominant frequency of the Ricker wavelet is 220 Hz. The source-receiver distance varies from 5 to 600 m with increment of 10 m. Modeled seismograms contain 60 traces. Despite that the model size and the frequency content are changed, it does not affect the reflection coefficient, because the vector of model parameters $\mathbf{g}$ and the argument $k_P r^*_{PP}(0)$ in equations 2 and 3 remain unchanged. The modeling, thus, provides an appropriate comparison between AVO data from reflectivity modeling and AVO data based on effective reflection coefficient.

Figure 5.9 shows AVO data obtained from synthetic seismograms using equation 6. Generally, there is a good match between the reflectivity modeling and the normalized ERCs shown in Figure 5.7. Azimuthal frequency dependence of the synthetic AVO data in pre-, near- and post-critical domains shown in Figure 5.10 represents similar features as in Figure 5.8: zero, minor and significant frequency effects, respectively. Minor deviations of synthetic AVO data in the post-critical domain from normalized ERCs are explained by the spatial aliasing due to less dense acquisition setup used in the reflectivity modeling.

The consistency between AVO data obtained from reflectivity modeling and normalized effective reflection coefficients derived for water/HTI interface indicates that the frequency dependence of the experimental AVO data in the pre-critical domain is not related to the HTI model.

5.5.3 The edge diffraction effect

The experimental model was performed in a finite space that includes edges. With the wavelengths considered in the experiment, the diffractions from these edges induces frequency dependent tuning effects. So to explain the offset-dependent frequency

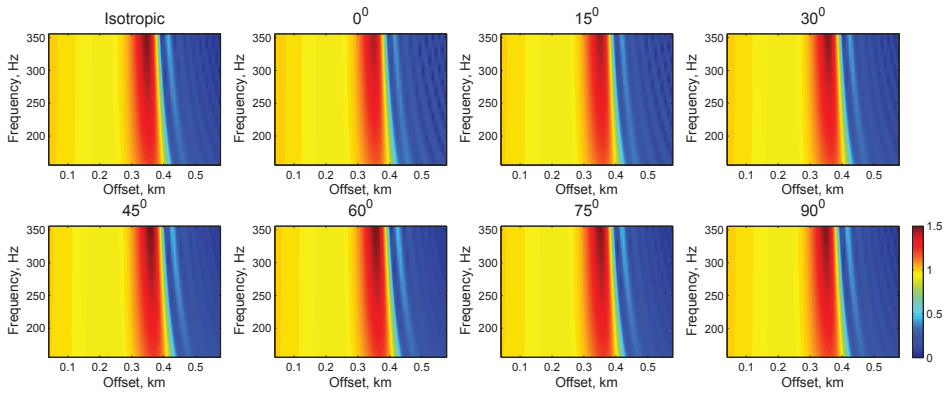

Figure 5.9: Synthetic AVO data for isotropic and HTI model for various azimuthal angles ($\varphi = 0,\ 15,\ 30,\ 45,\ 60,\ 75,\ 90^0$) provided by the reflectivity modeling. The model parameters estimated in the experiment are used in the reflectivity modeling.

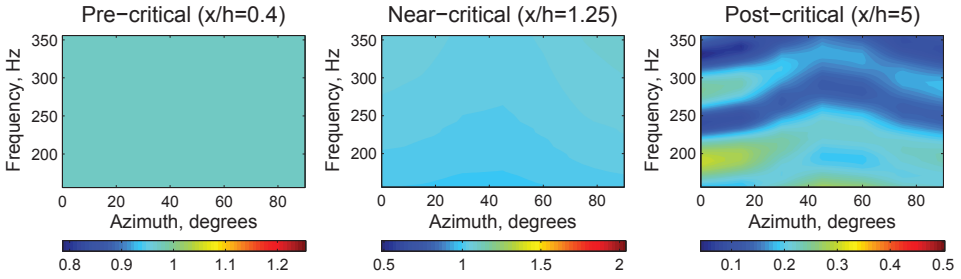

Figure 5.10: Frequency and azimuth dependence of the synthetic AVO data at pre-, near- and post-critical offsets

variation in the pre-critical domain, we first examine the traveltime differences between the desired reflection and those resulting from an additional edge. Figure 5.11 shows traveltimes calculated for a main reflected wave and wave diffracted from the edge point of the model (point B in Figure 5.2). The edge diffraction comes to the receiver 1×10^{-5} sec later than the target reflected event. Since the wavelet impulse is about 2×10^{-5} sec, the target event interferes with the edge diffraction waves. The interference between the two waves is offset-dependent as the difference between the two moveouts decreases with offset.

To model the effect of the edge diffracted wave on the AVO data, a simple convolutional modeling procedure is used, where the traveltimes for the two cases are

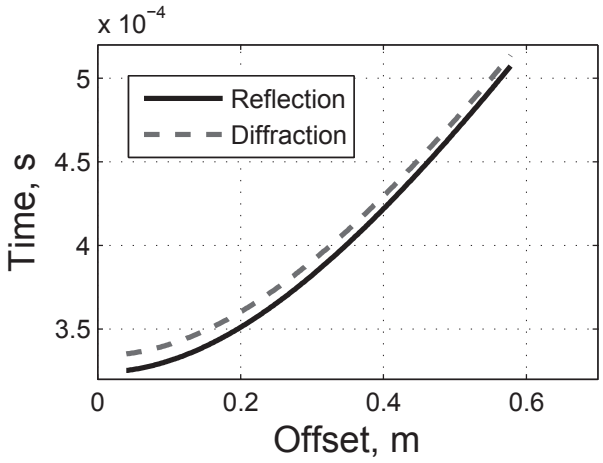

Figure 5.11: Traveltimes of the wave reflected from the point A and wave diffracted from edge point B shown in Figure 5.2.

convolved with a Ricker wavelet with frequency of 220 kHz. For simplicity, we disregard the offset-dependent amplitude effect by omitting reflection coefficients. The amplitude of the edge reflection event is assumed to be 5 times weaker than the amplitude of the reflected event.

Figure 5.12(a) illustrates AVO data obtained from the convolution modeling by the recipe given in equation 6. The frequency and offset dependent amplitudes are clearly observed for the whole offset range. Comparison of the frequency oscillating amplitudes with the finger-shaped features on experimental AVO data in 5.12(c) and Figure 5.12(d) shows a similarity in offset dependent periodical changes.

Figure 5.12 (b) illustrates the effect of the edge diffraction event when added together with the on reflection amplitudes. The diffraction event modeled by the convolution of the Ricker wavelet with the dominant frequency of 220 Hz and corresponding traveltime of the wave diffracted from the edge point B (Figure 5.2) is added to the synthetic seismogram obtained for isotropic model by reflectivity method. Figure 5.12 (b) shows amplitude behavior similar to the one observed in Figures 5.12(c) and Figure 5.12(d). It indicates that the finger-shaped features are caused by the edge diffractions. However, slopes of modeled and observed finger-shaped phenomena slightly differ. It might be due to disregarding the effect of neighboring edge diffraction points with suitable traveltime and correct diffraction amplitudes, affecting the phase and, consequently, the slope of finger-shaped phenomena.

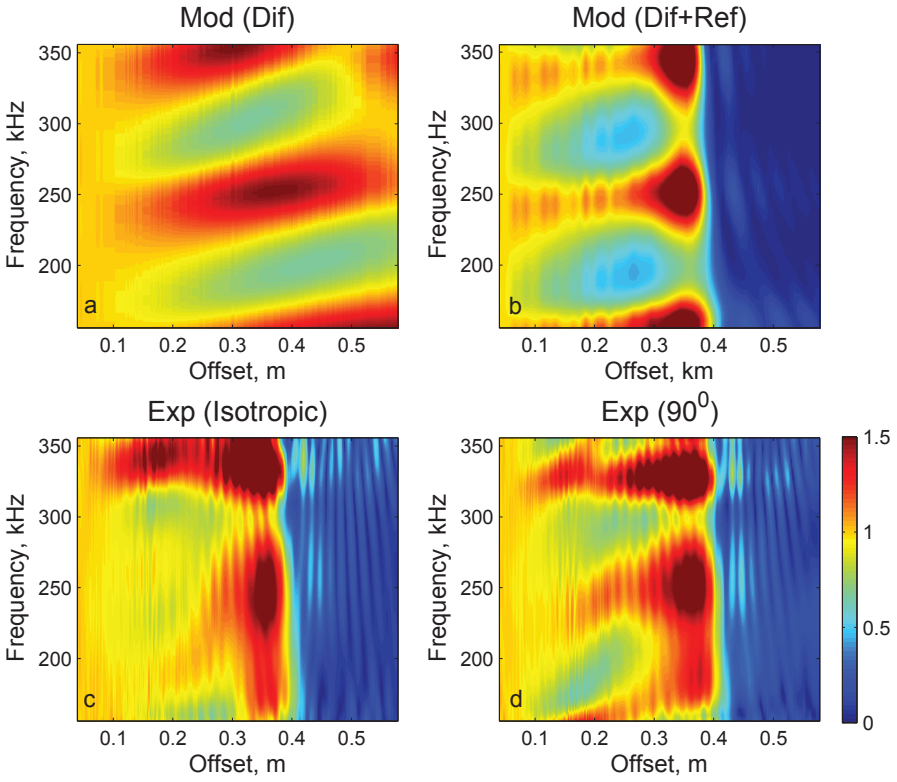

Figure 5.12: Comparison of normalized to the minimum offset amplitude spectra for modeled and experimental data. (a) diffraction effect from the edge point on the target reflection with uniform amplitude. Modeling is performed by simple convolution. (b) diffraction effect from the edge point on the target event with correct amplitudes. Diffraction event is modeled by convolution method, target event is modeled by reflectivity modeling. Model is scaled by factor of 1000. (c) Data of physical modeling obtained for water/isotropic plexiglas. (d) Data of physical modeling obtained for water/fractured plexiglas for azimuthal direction coinciding with symmetry plane.

Although the survey lines for the data observed in 5.12(c) and Figure 5.12(d) are located in isotropy planes, a strength and behavior of finger-shaped phenomena differ. This likely can be explained by the effect of the Fresnel zone related reflection points, as reflections fractured interface are expected to be different than reflections from isotropic interface.

5.6 RMS data Analysis

We also analyze RMS curves for the experimental and synthetic data in order to compare azimuthal dependences of the amplitude data in post-critical domain. We calculate RMS values in a time window containing the target event for each offset. The time window remains constant along the reflection moveout. The extracted RMS curves are normalized by their values at the nearest offset. Amplitudes obtained in this fashion contain information about the whole frequency spectrum of the wavelet, which may affect the amplitude shape in near- and post-critical domain (Skopintseva et al., 2007, 2011).

Figure 5.13 illustrates the normalized RMS data obtained from the experiment and the reflectivity modeling. Despite that the wavelet spectra of these two datasets are different, it does not affect the relative azimuthal behavior. Comparison between Figures 5.13a and 5.13b shows that the azimuthal dependence of the experimental data is stronger than that of the synthetic data and is well observed in azimuthal variations of maximum amplitude values and slopes of rapid amplitude changes. Moreover, azimuthal dependence of the experimental RMS data is well defined for incidence angles between 20 and 30 degrees, while it is not seen on synthetic RMS data.

The azimuthal dependence of the special characteristics of the RMS curves is shown in Figure 5.14. Figure 5.14a indicates an average shift in the slope of rapid amplitude changes with respect to the reference RMS curve $\Delta\theta$. The reference RMS curve has the slope of rapid amplitude changes at the smallest angles. The comparison between $\Delta\theta$ for the experimental and synthetic datasets show that the HTI model underestimates $\Delta\theta$ for an azimuth of 45 degrees by 50 percent, despite that the curves have similar shapes. Figure 5.14b represents shifts of maximum amplitudes relative to the reference RMS curve ΔA. The reference RMS curve has the smallest value of maximum amplitude. Analysis of Figure 5.14b shows that the HTI model does not explain azimuthal dependence of ΔA obtained from the experimental data, as they provide the smallest maximum amplitude for an azimuth of 45 degrees, while the smallest maximum amplitude for synthetic data is observed for an azimuth of 0 degrees.

To assure that the difference between experimental and synthetic $\Delta\theta$ and ΔA are not related to the choice of HTI model, we investigate how these two quantities are affected by different values of the anisotropy parameters $\epsilon^{(V)}$, $\delta^{(V)}$ and $\gamma^{(V)}$. For this purpose, ERC-based modeling is exploited, where RMS data are imitated by weighting

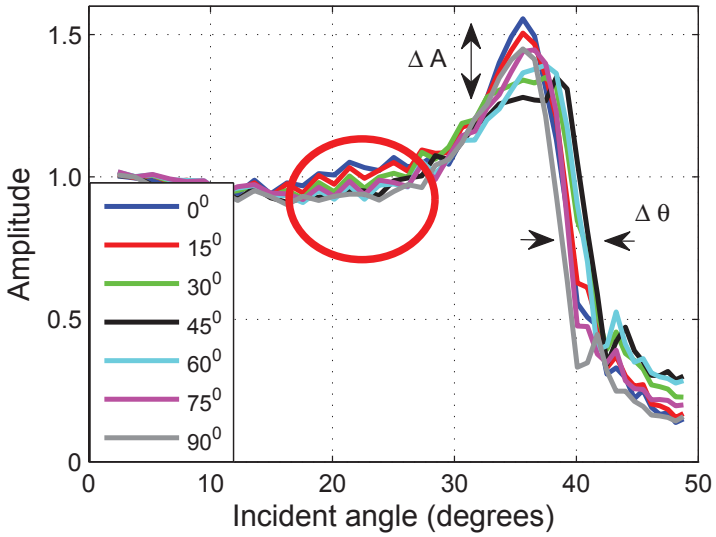

(a)

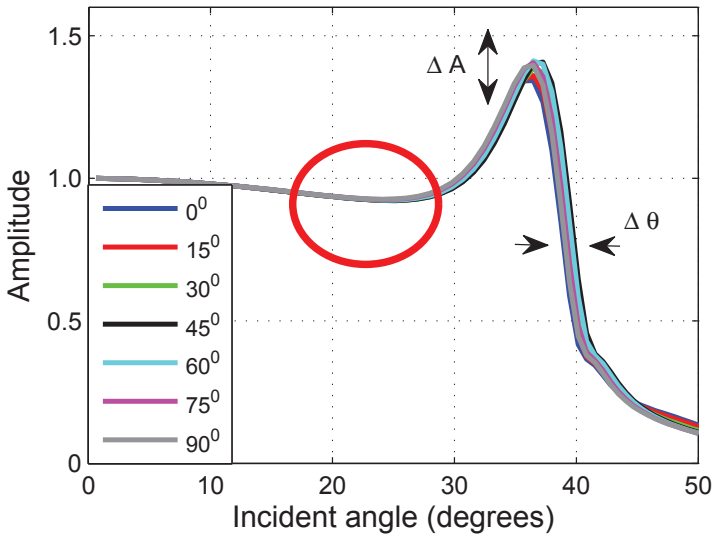

(b)

Figure 5.13: Normalized RMS curves obtained from (a) experimental and (b)synthetic data for different azimuths. RMS data are computed within 2×10^{-5} sec time window.

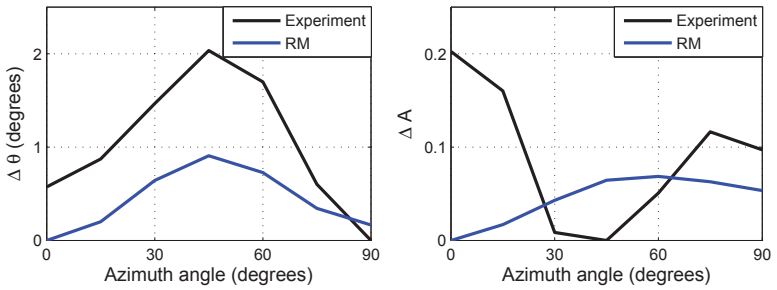

(a) (b)

Figure 5.14: Azimuthal variations in the position of the rapid amplitude changes at post-critical offsets (a) and maximal amplitude (b) of the experimental and synthetic data

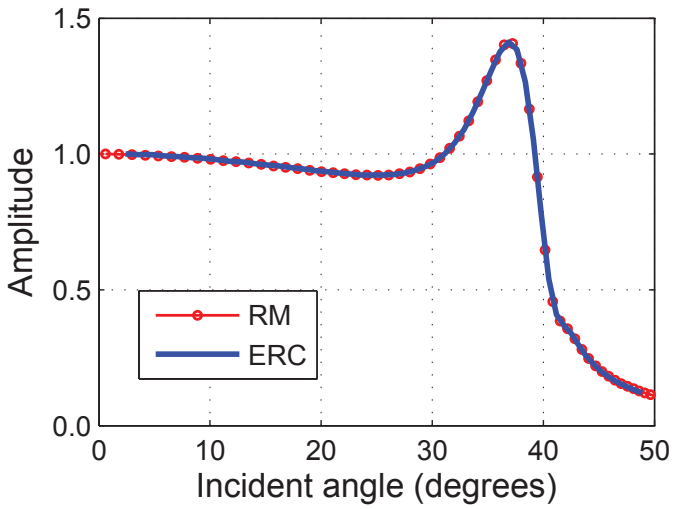

Figure 5.15: Comparison of normalized RMS curve obtained from the reflectivity modeling with ERC-based RMS curve. The azimuthal direction is 45 degrees.

the effective reflection coefficients for different frequencies with the wavelet spectrum (Skopintseva et al., 2011). Exploiting the same wavelet spectrum as in the reflectivity modeling, a perfect match between the ERC-based and the RM-based RMS curves is achieved (Figure 5.15). It allows us to exploit the ERC-based approach in the analysis of the anisotropic features at near- and post-critical offsets. The approach is more straightforward and does not require calculations of synthetic seismograms with the

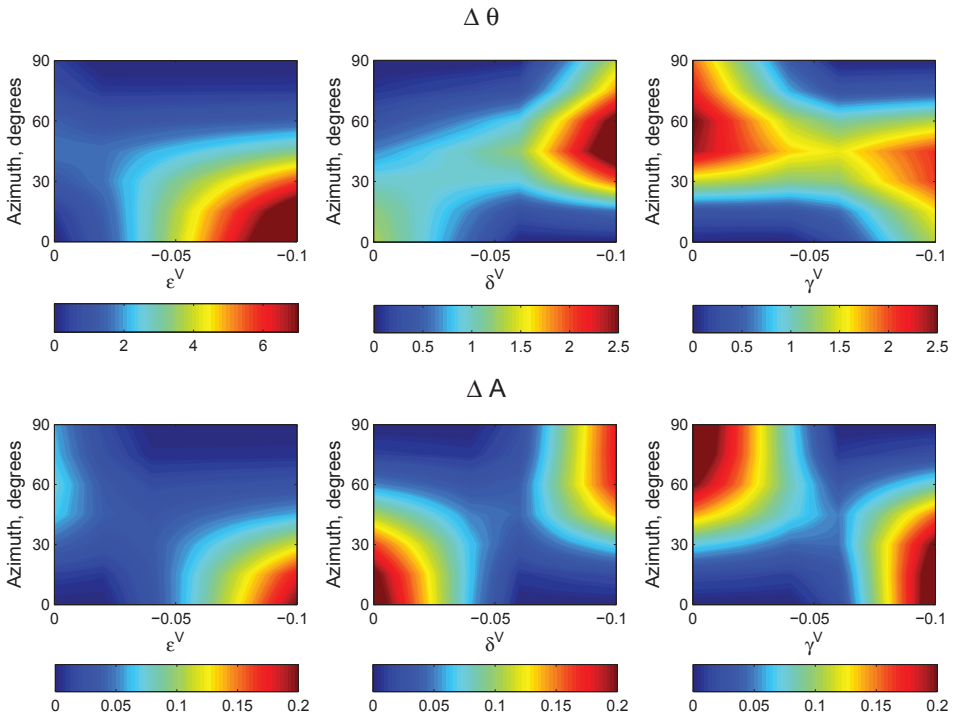

Figure 5.16: Azimuthal variations in the position of the rapid amplitude changes at post-critical offsets (a) and maximal amplitude (b) of the ERC based AVO data for different anisotropy parameters $\epsilon^{(V)}$, $\delta^{(V)}$, $\gamma^{(V)}$.

following processing.

Figure 5.16 shows azimuthal dependence of $\Delta\theta$ and ΔA for different anisotropy parameters. We observe that the shape of $\Delta\theta$ and ΔA is strongly dependent on the anisotropy parameters. We find that large values of the parameter $\gamma^{(V)}$ might result in a better fit of $\Delta\theta$. However any reasonable set of anisotropy parameters does not result in a minimal value of ΔA at azimuth 45 degrees. This observation additionally confirms that HTI model is not a best choice to explain all features in the experimental data.

5.7 Discussion

The HTI model only partly explains the frequency and azimuth behavior observed in the physical experiment. It describes the frequency dependence of the amplitudes and oscillations in the near- and post-critical domains. However, the HTI model does not predict frequency-dependent amplitudes in the pre-critical domain. We find that within the HTI model the post-critical domain might be exploited for fracture direction detection, as frequency-dependent post-critical reflections shows sufficient sensitivity to azimuth. Azimuthal dependence of frequency-dependent amplitudes in the near-critical domain seems to be weak.

Missing the periodical frequency dependence of amplitudes and phases in pre- and near-critical domains are probably associated with edge diffractions. Although reflection coefficients are not taken into account, a simple convolution modeling test qualitatevely indicates that edge diffraction effect cannot be disregarded in the data analysis. The modeling analyzes the effect of refraction from one edge point of the plexiglas. Other points of the other edges with suitable traveltimes will result in similar phenomena of frequency dependent tuning, affected the slopes of finger-shaped phenomena.

The azimuthal analysis of RMS data shows that the mismatch of the special amplitude characteristics (maximum amplitude, slope of rapid amplitude changes) in the post-critical domain between experimental and synthetic data are not related to the choice of anisotropy parameters. It shows that the HTI model does not fully explain all effects observed in the physical modeling. A discrepancy between finger shaped phenomena for isotropic model and HTI model corresponding to wave propagation in isotropic plane ($\varphi = 90^0$) indicates different influence of the points related to the Fresnel zone on the reflection at the receiver. Noticing that the wavelength is approximately 3.5 times larger than the distance between fractures in the plexiglas, the alternative model, describing reflection from a stack of layers of finite thickness relative to the wavelength has to be considered. Chapman and Liu (2003) developed a plane-wave reflection coefficients for this model and showed that fractured media is frequency and azimuthal dependent in pre-critical domain. Their approach automatically describes azimuthally dependent attenuation and dispersion effects. Extending this theory for non-plane waves might be a good quantitative tool for fracture density and fracture direction detection for any offset range and might explain azimuthal behavior of special features of amplitude characteristics (ΔA, $\Delta\theta$).

In the data analysis we do not consider the effect of the reflection from the bottom of the plexiglas. Data show that this event is well separated from the target reflection at small offsets and its amplitude is weak. However, the traveltime modeling shows that reflection from the bottom plexiglas interferes with the reflection from water/plexiglas interface in post-critical domain. Although the amplitude in post-critical domain is weak, the effect of bottom reflection might affect the amplitude oscillations.

5.8 Conclusions

Analysis of the experimental data for an interface between fluid and solid, where the underburden imitates media with vertical fracturing, reveals the complex dependency of the reflected wavefield on frequency, azimuth and offset. The periodical frequency changes of the reflection coefficients and phases at any offset range could potentially play an important role in fracture direction determination.

We use the effective reflection coefficients derived for an HTI model and the independent reflectivity modeling to verify and understand the observations made in the physical experiment. We find that the two approaches share the same amplitude dependency with frequency and azimuth. It confirms the consistency of our method and allows for exploiting the anisotropic effective reflection coefficients further in the investigation of anisotropy related effects, especially in near- and post-critical offsets. Careful analysis of the reflection coefficients in the post-critical domain for HTI media shows the potential of post-critical offsets in detecting the anisotropic behavior including the fracture direction.

The attempt to describe frequency effects of the data within the HTI model, however, was partly successful. We are able to explain the general behavior of the reflection coefficients such as the frequency dependent amplitude increase at near-critical offsets and the rapid decrease of the amplitude at post-critical offsets with frequency dependent oscillations. The strong frequency dependence at pre-critical offsets is attributed with edge diffractions overlaying the target event.

5.9 Acknowledgments

We acknowledge Mohammed Alhussain and Boris Gurevich for providing the experimental data, Statoil for financing the PhD of Lyubov Skopintseva, and KAUST for its

financial support of this work. Martin Landrø acknowledges the Norwegian Research Council for financial support and the ROSE consortium at NTNU.

5.10 Appendix A: Plane-wave reflection coefficient for liquid-solid interface

Here, we write plane-wave reflection coefficient for liquid-solid interface (See, for example, Ikelle and Amundsen (2005)). The source emitting plane wave is located in the water halfspace. Assume that the water velocity is V_{P1} and density is ρ_1. The solid media represents homogeneous isotropic halfspace with P- and S-wave velocities V_{P2} and V_{S2}, respectively, and density ρ_2. The P-wave reflection coefficient has the following form:

$$R_{P\,P} = \frac{A_1\rho_2 q_{P1} + A_2 q_{P1} q_{P2} - \rho_1 q_{P2}}{A_1\rho_2 q_{P1} + A_2 q_{P1} q_{P2} + \rho_1 q_{P2}}, \tag{A-1}$$

where

$$\begin{aligned} A_1 &= \left(1 - 2p^2 V_{S2}^2\right)^2, \\ A_2 &= 4p^2\rho_2 V_{S2}^4 q_{S2}, \end{aligned} \tag{A-2}$$

p is horizontal slowness, $q_j = \sqrt{V_j^{-2} - p^2}$, $j = P1,\ P2,\ S2$ are vertical slownesses of P- and S-waves.

5.11 Appendix B: Plane-wave reflection coefficient for water-HTI interface

Here, we introduce the derivation of the exact plane-wave reflection coefficient for the horizontal interface between water in upper halfspace and HTI media in lower halfspace, where incident P-wave propagates in upper halfspace. We associate the (x, y) - plane with the interface and let the z-axis be positive with depth. Consider (x, z)-plane as a wave propagation plane.

The wave propagation in water halfspace is associated with P-waves only. Defining the P-wave velocity as V_{P1} and horizontal slowness as p, we find the vertical slowness:

$$q_P^{(1)} = \frac{1}{V_{P1}}\sqrt{1 - V_{P1}^2 p^2}. \tag{B-1}$$

The directions of down-going and up-going wave propagation in the water are thus $\mathbf{n}_P^{d\,(1)} = \left(pV_{P1}, 0, q_P^{(1)}V_{P1}\right)$ and $\mathbf{n}_P^{u\,(1)} = \left(pV_{P1}, 0, -q_P^{(1)}V_{P1}\right)$, respectively. Here, d denotes down-going wave, u denotes up-going wave, (1) states for upper halfspace. The polarization vectors coincide with propagation vectors: $\mathbf{l}_P^{d\,(1)} = \mathbf{n}_P^{d\,(1)}$, $\mathbf{l}_P^{u\,(1)} = \mathbf{n}_P^{u\,(1)}$. The stress vector at the element of the interface in the water halfspace has only normal non-zero component: $\mathbf{t}_P^{(1)} = (0,\ 0,\ V_{P\,1}\rho_1)$.

The wave propagation in HTI halfspace is associated with quasi P-, SV-, and SH-waves (qP, qSV and qSH). Generally, the polarization of qP-wave does not coincide with the propagation direction and polarizations of qSV and qSH waves are not orthogonal to the propagation direction. Moreover, the wave propagation is azimuth-dependent.

When horizontal symmetry axis of HTI media is in the propagation plane and coincides with x-axis the stiffness tensor in Voigt notation has following form (Musgrave, 1970):

$$\mathbf{C} = \begin{pmatrix} c_{11} & c_{13} & c_{13} & 0 & 0 & 0 \\ c_{13} & c_{33} & c_{33} - 2c_{44} & 0 & 0 & 0 \\ c_{13} & c_{33} - 2c_{44} & c_{33} & 0 & 0 & 0 \\ 0 & 0 & 0 & c_{44} & 0 & 0 \\ 0 & 0 & 0 & 0 & c_{66} & 0 \\ 0 & 0 & 0 & 0 & 0 & c_{66} \end{pmatrix} \tag{B-2}$$

When horizontal symmetry axis has an angle φ in respect to the x-axis, the stiffness matrix can be written as:

$$\mathbf{C}' = \begin{pmatrix} c'_{11} & c'_{12} & c'_{13} & 0 & 0 & c'_{16} \\ c'_{12} & c'_{22} & c'_{23} & 0 & 0 & c'_{26} \\ c'_{13} & c'_{23} & c'_{33} & 0 & 0 & c'_{36} \\ 0 & 0 & 0 & c'_{44} & c'_{45} & 0 \\ 0 & 0 & 0 & c'_{45} & c'_{55} & 0 \\ c'_{16} & c'_{26} & c'_{36} & 0 & 0 & c'_{66} \end{pmatrix}, \tag{B-3}$$

where matrix components are functions of azimuth and stiffness components in old

coordinates from equation B-2:

$$\begin{aligned}
c'_{11} =& c_{11}\cos^4\varphi + 2(c_{13}+2c_{66})\cos^2\varphi\sin^2\varphi + c_{33}\sin^4\varphi,\\
c'_{22} =& c_{33}\cos^4\varphi + 2(c_{13}+2c_{66})\cos^2\varphi\sin^2\varphi + c_{11}\sin^4\varphi,\\
c'_{33} =& c_{33},\\
c'_{44} =& c_{44}\cos^2\varphi + c_{66}\sin^2\varphi,\\
c'_{55} =& c_{66}\cos^2\varphi + c_{44}\sin^2\varphi,\\
c'_{66} =& \frac{1}{8}(c_{11}-2c_{13}+4c_{66}+c_{33}-(c_{11}-2c_{13}-4c_{66}+c_{33})\cos 4\varphi),\\
c'_{16} =& \frac{1}{4}(c_{11}-c_{33}+(c_{11}-2c_{13}-4c_{66}+c_{33})\cos 2\varphi)\sin 2\varphi,\\
c'_{26} =& -\frac{1}{4}(-c_{11}+c_{33}+(c_{11}-2c_{13}-4c_{66}+c_{33})\cos 2\varphi)\sin 2\varphi,\\
c'_{36} =& (-c_{11}+c_{13}+2c_{66})\cos\varphi\sin\varphi,\\
c'_{12} =& \frac{1}{8}(c_{11}+6c_{13}-4c_{66}+c_{33}-(c_{11}-2c_{13}-4c_{66}+c_{33})\cos 4\varphi),\\
c'_{13} =& c_{13}\cos^2\varphi + (c_{11}-2c_{66})\sin^2\varphi,\\
c'_{23} =& (c_{11}-2c_{66})\cos^2\varphi + c_{13}\sin^2\varphi.
\end{aligned} \tag{B-4}$$

The vertical slowness components $q_{(2)}$ ((2) denotes lower halfspace) are obtained from the eigenvalues of Christophel equation:

$$\det\begin{vmatrix}
c'_{11}p^2 + c'_{55}\left(q^{(2)}\right)^2 - \rho_2 & c'_{16}p^2 + c'_{45}\left(q^{(2)}\right)^2 & (c'_{13}+c'_{55})\,p^2\\
c'_{16}p^2 + c'_{45}\left(q^{(2)}\right)^2 & c'_{66}p^2 + c'_{44}\left(q^{(2)}\right)^2 - \rho_2 & (c'_{36}+c'_{45})\,pq^{(2)}\\
(c'_{13}+c'_{55})\,p^2 & (c'_{36}+c'_{45})\,pq^{(2)} & c'_{55}p^2 + c'_{33}\left(q^{(2)}\right)^2 - \rho_2
\end{vmatrix} = 0 \tag{B-5}$$

and have the following form:

$$\begin{aligned}
q_P^{(2)} =& \frac{1}{2}\sqrt{K_1 - \sqrt{K_1^2 - K_2}}\\
q_{SV}^{(2)} =& \frac{1}{2}\sqrt{K_1 + \sqrt{K_1^2 - K_2}}\\
q_{SH}^{(2)} =& \sqrt{\frac{\rho_2 - \left[c_{66}\cos^2\varphi + c_{44}\sin^2\varphi\right]p^2}{c_{44}}},
\end{aligned} \tag{B-6}$$

where

$$
\begin{aligned}
K_1 =& \frac{1}{c_{66}c_{33}}\Big[2\left(c_{33}+c_{66}\right)\rho_1 \\
&+2\left(c_{13}^2 cos^2\varphi - c_{11}c_{33}cos^2\varphi\right)p^2 \\
&+4c_{66}\left(c_{13}cos^2\varphi - c_{33}\sin^2\varphi\right)p^2\Big] \\
K_2 =& \frac{4}{c_{66}c_{33}}\Big[4\rho_2^2 \\
&-4p^2\left(\rho_2 - c_{66}p^2cos^2\varphi\right)\left(c_{33}+c_{11}cos^2\varphi\right) \\
&-4p^2c_{66}\left(\rho_2 - c_{33}p^2\sin^2\varphi\right) \\
&+p^4\sin^2 2\varphi\left(-c_{13}\left(c_{13}+c_{66}\right)+c_{33}\left(c_{11}-2c_{66}\right)\right)\Big].
\end{aligned}
\tag{B-7}
$$

The phase velocities are obtained from equations:

$$
V_{j\,2} = \frac{1}{\sqrt{\left(q_j^{(2)}\right)^2 + p^2}}, \tag{B-8}
$$

where $j = qP,\ qSV,\ qSH$. It yields vectors of wave propagation directions $\mathbf{n}_j^{d\,(2)} = \left(pV_{j\,2}, 0, q_j^{(2)}V_{j\,2}\right)$.

The eigenvectors of the Christophel equation B-5 yield the polarization vectors. The analytical solution is very cumbersome and we thus do not represent its explicit form here. When the wave propagation plane does not coincide with symmetry planes of HTI media, the polarization vectors are not located within the propagation plane: $\mathbf{l}_j^{d\,(2)} = \left(l_{j\,1}^{d\,(2)},\ l_{j\,2}^{d\,(2)},\ l_{j\,3}^{d\,(2)}\right)$, $j = qP,\ qSV,\ qSH$. To choose signs of the components for polarization vectors, we exploit sign convention extended for three-dimensional case given by Schoenberg and Protazio (1992).

Stress vectors at the element of interface in HTI media have the following form:

$$
\mathbf{t}_j^{d\,(2)} = \begin{pmatrix} c'_{55}l_{j\,3}^{d\,(2)}p + c'_{55}l_{j\,1}^{d\,(2)}q_j^{(2)} + c'_{54}l_{j\,2}^{d\,(2)}q_j^{(2)} \\ c'_{54}l_{j\,3}^{d\,(2)}p + c'_{54}l_{j\,1}^{d\,(2)}q_j^{(2)} + c'_{44}l_{j\,2}^{d\,(2)}q_j^{(2)} \\ c'_{13}l_{j\,1}^{d\,(2)}p + c'_{63}l_{j\,2}^{d\,(2)}p + c'_{33}l_{j\,3}^{d\,(2)}q_j^{(2)} \end{pmatrix} \tag{B-9}
$$

Using boundary conditions at the water-HTI interface $z = 0$, which states that the normal component of the displacement and stress traction components are continuous,

we obtain the following system of equations:

$$\mathbf{b} = \mathbf{A}\mathbf{X}, \tag{B-10}$$

where

$$\mathbf{b} = \left(l^{d\,(1)}_{P\,3},\ 0,\ 0,\ V_{P\,1}\rho_1 \right)^T,$$

$$\mathbf{A} = \begin{pmatrix} -l^{u\,(1)}_{P\,3} & l^{d\,(2)}_{qP\,3} & l^{d\,(2)}_{qSV\,3} & l^{d\,(2)}_{qSH\,3} \\ 0 & t^{d\,(2)}_{qP\,1} & t^{d\,(2)}_{qSV\,1} & t^{d\,(2)}_{qSH\,1} \\ 0 & t^{d\,(2)}_{qP\,2} & t^{d\,(2)}_{qSV\,2} & t^{d\,(2)}_{qSH\,2} \\ -V_{P\,1}\rho_1 & t^{d\,(2)}_{qP\,3} & t^{d\,(2)}_{qSV\,3} & t^{d\,(2)}_{qSH\,3} \end{pmatrix}, \tag{B-11}$$

$$\mathbf{X} = \left(R_{P\,P},\ T_{P\,qP},\ T_{P\,qSV},\ T_{P\,qSH} \right)^T,$$

$R_{P\,P}$ is reflection coefficient, $T_{P\,qP}$, $T_{P\,qSV}$, $T_{P\,qSH}$ are transmission coefficients, T is the transpose sign.

Solving the system of equations B-10, we obtain plane-wave reflection coefficient for water-HTI interface. Note that incident wave generates one reflected wave and two transmitted waves with polarization within the incidence plane only if incidence plane coincides with symmetry planes of HTI media.

Chapter 6

Overburden dependent AVA inversion

Lyubov Skopintseva[1], Alexey Stovas[1]

[1] Norwegian University of Science and Technology, Trondheim, Norway

Presented at the ROSE Meeting, Trondheim, Norway, April 2008; SEG 78th Annual Meeting, Las-Vegas, USA, November 2008 and published in Geophysics in 2009.

6.1 Abstract

Amplitude-variation-with-offset (AVO) analysis is strongly dependent on interpretation of the estimated traveltime parameters. In practice, we can estimate two or three traveltime parameters that require interpretation within the families of two- or three-parameter velocity models, respectively. Increasing the number of model parameters improves the quality of overburden description and reduces errors in AVO analysis. We analyze the effect of two- and three-parameter velocity model interpretation for the overburden on AVO data and have developed error estimates in the reservoir parameters.

6.2 Introduction

Variations of seismic reflection coefficients with offset (amplitude variation with offset, or AVO)or incident angle (amplitude variation with angle, or AVA) play an important role in seismic interpretation as gas or hydrocarbon indicators (Ostrander, 1984; Swan, 1993). AVO/AVA attributes obtained by two- (Shuey, 1985) or three-term (Aki and Richards, 1980) AVO/AVA inversion are widely used in industry.

However, quality and accuracy of the inversion are affected by various factors. For example, Mora and Biondi (2000) investigate the sensitivity of AVO attributes to uncertainty in migration velocity. They consider various effects, including modeling, overburden, migration, velocity anomalies and velocity errors. Xu et al. (1993) show that an inhomogeneous overburden interpreted as homogeneous in velocity analysis causes significant errors (up to 13%) in the results in AVA inversion results.

Conventional velocity analysis assumes that all moveouts are hyperbolic and therefore only two traveltime parameters (zero-offset two-way traveltime and normal moveout velocity) can be estimated during NMO correction. Applying the Dix equation (Dix, 1955) results in two model parameters (thickness and velocity of the layer) that describe a constant velocity layer.

However, in real media the velocity distribution in the overburden is more complex. Hyperbolic velocity analysis results in wrong velocity reconstruction in the overburden that leads to incorrect raypath trajectory and offset-to-angle conversion, the source of error in AVA inversion. Moreover, errors in the raypath trajectory cause errors in the geometrical spreading correction on the amplitude data that additionally affect inversion results.

Nonhyperbolic velocity analysis that uses additional traveltime parameters called heterogeneity coefficients (Fomel and Grechka, 2001) improves velocity profile description. Practically, we can estimate only one additional traveltime parameter because of the quality of the seismic data and limited offset spread. Therefore, velocity reconstruction is limited to the family of three-parameter models (Stovas, 2008, 2009).

In this article, we investigate effects on AVA data caused by hyperbolic and nonhyperbolic velocity analysis. For simplicity, we consider a two-layer model, whose upper layer has a linear gradient in the P-wave velocity and whose lower layer is a constant-velocity reservoir. We compare two- and three-parameter power-gradient velocity model (Stovas, 2009) interpretations for this model and verify which inter-

pretation gives more accurate AVA inversion results. For illustration, we provide the results of AVA inversion and AVA attribute estimation.

6.3 Theory

Consider a vertically heterogeneous velocity model for the overburden, with the target interface represented by a horizontal reflector. From this interface, we record the reflection with traveltime $t(x)$ and amplitude function $R(x)$. To perform the AVA inversion from these data, we first need to compute the traveltime parameters from moveout $t(x)$ and then invert them for the model parameters.

The expansion of the reflection moveout squared in the Taylor series with respect to offset can be given in terms of heterogeneity coefficients (Fomel and Grechka, 2001; Taner and Koehler, 1969):

$$t^2(x) = t_0^2 \left[1 + \widetilde{x}^2 + \frac{(1 - S_2)}{4} \widetilde{x}^4 + \frac{(2S_2^2 - S_2 - S_3)}{8} \widetilde{x}^6 + \dots \right], \tag{1}$$

where $\widetilde{x} = x/\left(v_{nmo} t_0\right)$ is the normalized offset, t_0 is zero-offset two-way traveltime, v_{nmo} is the normal moveout velocity, and S_2 and S_3 are the heterogeneity coefficients of the second and third orders, respectively (Fomel and Grechka, 2001). Heterogeneity coefficients introduce a degree of heterogeneity in the media and are defined in Appendix 6.11. To compute the traveltime parameters t_0, v_{nmo}, and the heterogeneity coefficients, we need to perform the velocity analysis.

Conventional velocity analysis uses the hyperbolic approximation for reflection traveltime, a two-parameter approximation that consists of the first two terms in the series 1. For the hyperbolic velocity analysis, we assume that nonhyperbolicity related to vertical heterogeneity is negligibly small with respect to the maximum recorded offset. In this case, the heterogeneity coefficients are equal to one. We call this velocity model the constant-velocity (CV). The model parameters (thickness H and velocity v_0) can be computed easily from the traveltime parameters (t_0, v_{nmo}) using the standard Dix (Dix, 1955) inversion. Nonhyperbolic velocity analysis includes one more traveltime parameter S_2 and is based on the different nonhyperbolic traveltime approximations (shifted hyperbola, rational and generalized approximations). The shifted hyperbola approximation requires no additional information about the velocity model, whereas the rational and generalized traveltime approximation are based on the given velocity model.

In this paper, we use the power-gradient velocity model with four model parameters: layer thickness H; velocity v_0 at the top of the layer; ratio between velocities at the bottom and at the top of the layer $\gamma = v(H)/v_0$; and parameter n, which controls the curvature of velocity function (Stovas, 2009).

The power-gradient velocity model is given by

$$v^n(z) = v_0^n \left(1 + \frac{\gamma^n - 1}{H} z\right). \tag{2}$$

Note that for $n = 0$, equation 2 reduces to the $v(z) = v_0 \gamma^{z/H}$ (Stovas, 2009). To obtain the parameters for this model, four independent traveltime parameters must be estimated in the velocity analysis: t_0, v_{nmo}, S_2 and S_3. Equations for traveltime parameters are given in Appendix 6.11. In practice, the third-order heterogeneity coefficient is impractical to estimate because of seismic noise, limited offset spread and nonuniqueness of the traveltime parameters.

In the following analysis, we use the set of the velocity models defined by equation 2 with $n = -2, -1, 0, 1, 2$. Therefore, we consider the velocity models with three independent traveltime parameters: t_0, v_{nmo} and S_2. From these parameters we estimate H, γ and v_0. We also establish the relation between offset and incident angle at interface (to convert AVO data into AVA data). Then we compute the geometrical spreading factor and apply it for the recorded amplitude function. Finally, we perform the AVA inversion and show how these results depend on the chosen parameter n.

6.4 Kinematically equivalent models

Stovas (2008) introduces the family of the kinematically equivalent velocity distributions that have a limited number of equal traveltime parameters.

To invert traveltime parameters within the framework of the three-parameter model, we are free to choose any model from the family of three-parameter kinematically equivalent velocity distributions that have the same traveltime parameters t_0, v_{nmo} and S_2. Ignoring S_2 reduces to the two-parameter family of kinematically equivalent models.

The three-parameter family of velocity models is sufficient to account for all possible models ($-\infty < n < \infty$). The parameter n describes the curvature of the velocity function $v(z)$. So, for $n = 1$, the curvature of the velocity function is zero. In general,

the sign of the curvature is defined by $sign(1-n)$. The sign of the curvature in the velocity function indicates behavior of the sedimentation that can be described by the rate of sedimentation, porosity, size of grains, etc. Thus, zero curvature implies uniform changes in sedimentation behavior, positive curvature indicates small changes in sedimentation parameters at large depths with large changes at shallow depths, and negative curvature corresponds to large changes in sedimentation behavior at large depths with small changes at shallow depths. Therefore, any geologic information regarding sedimentation behavior can be useful for choosing a model.

We consider five analytical kinematically equivalent models of the three-parameter family by setting $n = -2, -1, 0, 1, 2$ in equation 2, where $n = -2, 0, 1$ correspond to well-known linear sloth velocity, exponential velocity, and linear velocity models, respectively. We also consider the constant velocity model (CV) by keeping only two traveltime parameters (this model can be obtained from equation 2 by taking the limits $n \to \pm\infty$). The two- and three-parameter kinematically equivalent models have different equations for traveltime parameter inversion (Appendix 6.11). Therefore, the same traveltime parameters t_0, v_{nmo} and S_2 result in different model parameters H, v_0 and γ, depending on the value of parameter n. The three-parameter kinematically equivalent models have different values for heterogeneity coefficients with orders larger than two. This can be illustrated by the expansion of higher order heterogeneity coefficients in terms of the second order heterogeneity coefficient (Appendix 6.11)

$$S_k = 1 + \frac{k\,(k-1)}{2}\,(S_2-1) + \frac{k\,(k-1)\,(k-2)\,(3+3k-4n)}{40}\,(S_2-1)^2 + \ldots, \quad (3)$$

where $k = 3, 4, \ldots$. The first-order coefficient in series 3 does not depend on n, but the higher-order coefficients do n; thus they are different for different models from the family of the three-parameter equivalent velocity models. Decreasing the ratio γ between the velocities at the bottom and top of the layer decreases all heterogeneity coefficients and the lessens effect of n on the higher order heterogeneity coefficients S_k, $k = 3, 4, \ldots$.

The layer thickness in the series with respect to the second-order heterogeneity coefficient is given by (combining series A-8 and A-9)

$$H = \frac{v_{nmo}t_0}{2}\left[1 - \frac{1}{8}\,(S_2-1) + \frac{3\,(9-8n)}{640}\,(S_2-1)^2 + \ldots\right]. \quad (4)$$

One can see that the main contribution comes from the first-order term. For vertically heterogeneous velocity models, $S_2 \geq 1$. So it is easy to see from equation 4 that layer thickness is less than in the case of a constant-velocity model (standard Dix equation). This follows from the inequality derived by Stovas (2009), $\gamma^{-1} \leq 2H/\,(v_{nmo}t_0) \leq 1$.

6.5 Ray tracing

To transform the data from AVO to AVA requires an offset-to-angle conversion. In a CV model, this equation is simple because of the straight rays in the medium. In the three-parameter media, the seismic rays have different curved trajectories that result in different incidence angles at zero-depth and target-depth levels. At target level $z = H$, the incident angle is defined by

$$\sin(\theta_H) = pv_H = \gamma \sin(\theta_0), \tag{5}$$

where θ_H and v_H are angle and velocity at the target level, respectively; θ_H is the incidence angle at the top of the layer. Consider the expansion of the relation between the sine of the incident angle at target level $\sin(\theta_H)$ and the normalized offset. From Appendix 6.12 we obtain

$$\sin(\theta_H) = \gamma\lambda \left[\widetilde{x} - \frac{1}{2} S_2 \widetilde{x}^3 + \frac{3}{4} \left(S_2^2 - \frac{1}{2} S_3 \right) \widetilde{x}^3 + \ldots \right], \tag{6}$$

where $\lambda = v_0/v_{nmo}$ which implies the inequality, $\gamma^{-1} \leq \lambda \leq 1$ (Stovas, 2009). The parameter λ can be expanded into the series with respect to the second-order heterogeneity coefficient (Appendix 6.11):

$$\lambda = 1 - \frac{\sqrt{3}}{2} (S_2 - 1)^{1/2} + \frac{3 - 2n}{8} (S_2 - 1) + \frac{n(1 - 3n)}{80} \sqrt{3} (S_2 - 1)^{3/2} + \ldots. \tag{7}$$

The velocity ratio γ can also be expressed as a series with respect to the second-order heterogeneity coefficient (Appendix 6.11):

$$\gamma = 1 + \sqrt{3} (S_2 - 1)^{1/2} + \frac{3}{2} (S_2 - 1) - \frac{n(5 + 3n + n^2)}{40} 3\sqrt{3} (S_2 - 1)^{3/2} + \ldots. \tag{8}$$

The series for the product $\gamma\lambda$ results in

$$\gamma\lambda = 1 + \frac{\sqrt{3}}{2} (S_2 - 1)^{1/2} + \frac{3 - 2n}{8} (S_2 - 1) - \frac{n(1 - 3n)}{80} \sqrt{3} (S_2 - 1)^{3/2} + \ldots. \tag{9}$$

Among all heterogeneity coefficients in series 6 only S_2 is the same for all models because of kinematic equivalence, whereas S_k, $k = 3, 4, \ldots$ are model dependent. This results in variable offset-to-angle relationships that impose an offset-dependent stretching factor on the AVA data.

Series 6 shows that the discrepancy between kinematically equivalent models results in different stretching factors and amplifies with increasing offset and velocity ratio γ.

6.6 Geometrical spreading

The velocity models defined in equation 2 have ray trajectories that depend on the parameter n. This affects the geometrical spreading factor. Assuming that the source and receiver are placed at the same depth, the relative geometrical spreading is (Ursin, 1990; Stovas and Ursin, 2009):

$$L(x) = \cos\theta_0 \left[\frac{1}{x}\frac{dt}{dx}\frac{d^2t}{dx^2}\right]^{-1/2} = \cos\theta_0 \left[\frac{x}{p}\frac{dx}{dp}\right]^{1/2}, \tag{10}$$

where θ_0 is the incidence angle at the top of the layer. The first and second terms in equation 10 can be expanded in a series with respect to the normalized offset (Appendix 6.12)

$$\begin{aligned} \cos^2(\theta_0) &= 1 - \lambda^2\left[\widetilde{x}^2 - S_2\widetilde{x}^4 + \frac{7S_2^2 - 3S_3}{4}\widetilde{x}^6 + \ldots\right] \\ \left[\frac{x}{p}\frac{dx}{dp}\right]^{1/2} &= v_{nmo}^2 t_0\left[1 + S_2\widetilde{x}^2 + \frac{9}{8}\left(S_3 - S_2^2\right)\widetilde{x}^4 + \ldots\right]. \end{aligned} \tag{11}$$

Note that the series 11 are valid for arbitrary vertically heterogeneous medium. The series show that geometrical spreading depends on the higher-order heterogeneity coefficients and λ. The three-parameter kinematically equivalent models have different λ and S_k, $k = 3, 4, \ldots$. The discrepancy in geometrical spreading among these models is more pronounced for large offset. Being applied in true-amplitude AVO-oriented processing, the geometrical spreading factor imposes an offset-dependent scaling on the data.

6.7 Numerical examples

To illustrate the theory, we consider a two-layer model, whose overburden has the P-wave velocity distribution given in equation 2 for $n = 1$ (linear velocity model) and whose reservoir is a constant velocity layer with properties: $V_{P2} = 2850\, m/s$, $V_{S2} = 1600\, m/s$ and $\rho_2 = 2100\, kg/m^3$. Parameters of the overburden are: $v_0 = V_{P1}(0) = 1800\, m/s$, $\gamma = 1.5$, $H = 1000\, m$, $V_{S1}(H) = 1380\, m/s$ and $\rho_1 = 1800\, kg/m^3$. We consider PP reflections only. The distribution of S-wave velocity and density in the overburden can be arbitrary because they do not affect on P-wave propagation - only their contrast at the target level is important for AVO inversion.

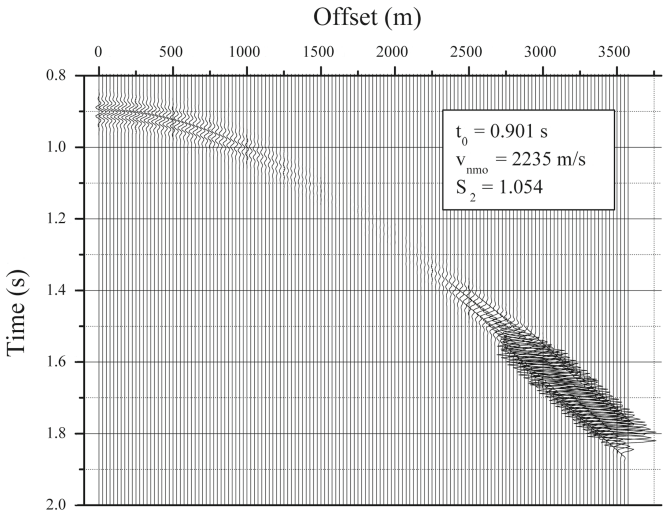

Figure 6.1: Synthetic seismogram. Estimated traveltime parameters are shown in the box.

The synthetic seismogram for this model is computed using the ray tracing for an offset range from 0 to $3500\,m$ (Figure 6.1). Assume that three traveltime parameters are estimated accurately in the velocity analysis with the values $t_0 = 0.901\,s$, $v_{nmo} = 2235\,m/s$ and $S_2 = 1.054$. Figure 6.2 shows the real part of the reflection amplitude $R\,(x)$. Reflection amplitude changes polarity between $1500 - 2100\,m$, and critical reflection is at the offset of $2900\,m$.

Velocity interpretation is performed for the five three-parameter models and one two-parameter CV model mentioned above. We analyze different P-wave velocity models in the overburden, assuming that S-wave velocity and density distributions are the same in all cases. The model parameters are computed from the inverting traveltime parameters (equation A-6) for the given value of n. To perform the inversion for the two-parameter CV model, we ignore the value of heterogeneity coefficient S_2 and use the standard Dix equations. Figure 6.3 shows kinematically equivalent velocity distributions computed in the inversion. The three-parameter velocity models ($n = -2, -1, 0, 1, 2$) are close to the ideal model ($n = 1$), but the parameters for the CV model have the largest deviation. The error in depth estimation is largest for the CV model ($\Delta H = 6.9\,m$); the three-parameter velocity models result in an error of less than 0.5 m (Figure 6.4).

Figure 6.5 shows the true-amplitude correction factor computed from geometrical

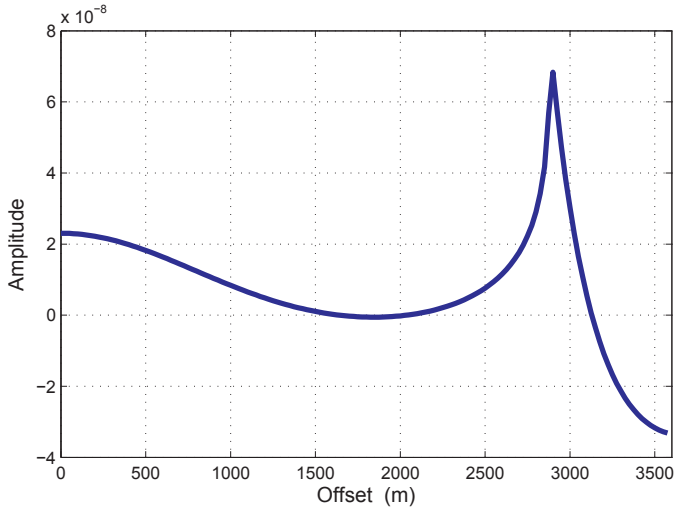

Figure 6.2: AVO response obtained from the seismogram in Figure 6.1

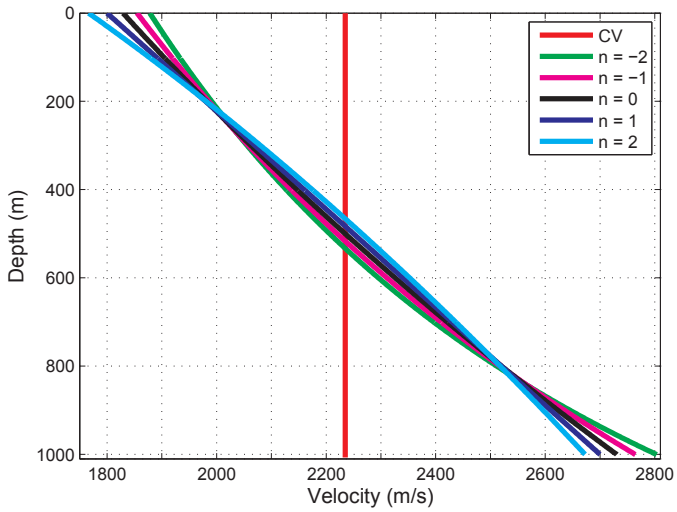

Figure 6.3: Kinematically equivalent overburden velocity models computed by inverting the traveltime parameters. The red line corresponds to the CV model (the value for heterogeneity coefficient is ignored).Lines in other colors correspond to three-parameter velocity models.

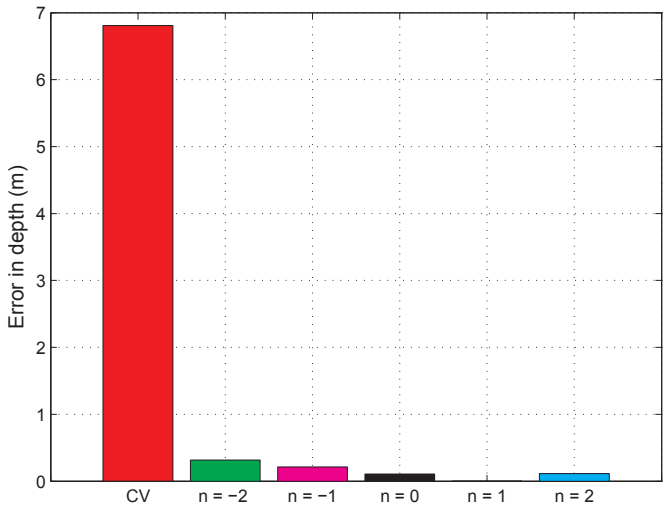

Figure 6.4: Errors in estimation of the depth for different velocity models.

spreading. The correction factor is the ratio of geometrical spreading calculated for the interpreted velocity model compared to the true model ($n = 1$). When the velocity interpretation is close to the true model, the correction factor is equal to one. The influence of this factor is very small for three-parameter models at near offset and increases at large offsets, where the reflected wave becomes a diving wave. At this offset, the caustic singularity appears and creates a region, where geometrical spreading becomes infinite. Because the position of the caustic singularity is model dependent, its influence on geometrical spreading is also model dependent. For the two-parameter velocity distribution, the deviation of the correction factor dramatically increases with offset. A similar trend in the deviation from the exact velocity model is observed in the offset-angle plot (Figure 6.6).

Figure 6.7 shows model-dependent true-amplitude AVA curves computed from the AVO response obtained from the seismogram (Figure 6.1). Two different effects are evident: the scaling effect from geometrical spreading correction and the stretching effect from offset/incident angle conversion. These effects are most significant for CV models and are observed for all incident angles. Analysis of Figures 6.5- 6.7 shows that stretching effect for the three-parameter model is evident for all angles, whereas scaling effect mostly takes place at large incident angles where post-critical reflection is generated. Therefore, the three-parameter velocity models are very similar for the pre-critical range of incident angles.

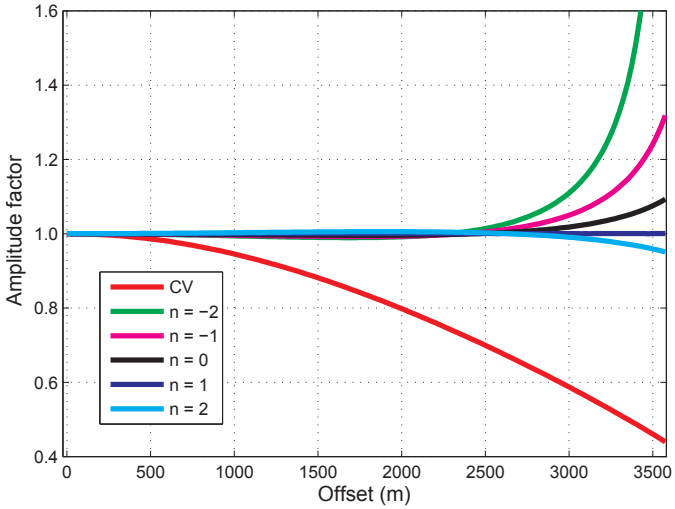

Figure 6.5: Errors in relative geometrical spreading for different velocity models normalized with the velocity model($n = 1$).

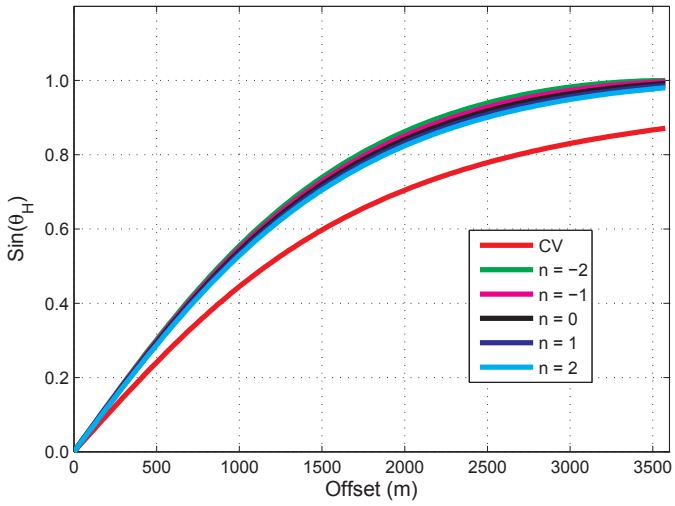

Figure 6.6: Model-dependent offset-to-angle conversion.

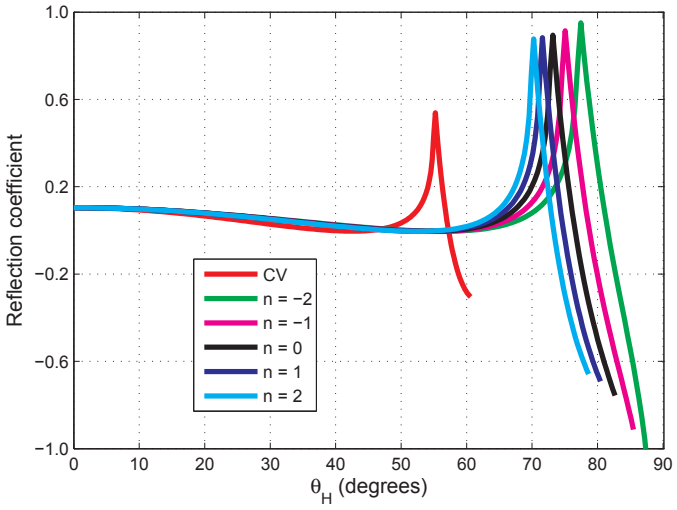

Figure 6.7: Model-dependent true-amplitude AVA curves computed from the original AVO response (Figure 6.2) using different velocity models. Note the effect of stretching and scaling factors.

6.8 AVA inversion

To quantify the errors imposed by velocity misinterpretation (the wrong choice of velocity model), we solve the AVA inverse problem. Only the parameters of the target layer are estimated. We assume that the velocities in the overburden are computed from the kinematic interpretation described above, and the density for the overburden is known.

We consider two inversion methods: the least-squares method, where the AVA attributes are computed, and the nonlinear Nelder-Mead method (Himmelblau, 1972), with estimation of the medium parameters. The first method is widely used in the industry for conventional AVA inversion where only small incidence angles are involved; the second method is free of these restrictions. We use model-dependent true-amplitude AVA curves shown in Figure 6.7 as input data in the inversion.

The least-squares method is based on the approximation of the reflection coefficient (Aki and Richards, 1980):

$$R(\theta_H) \approx R(0) + G \sin^2(\theta_H) + K \sin^4(\theta_H), \tag{12}$$

where $R(0)$, G, K denote the intercept, gradient and curvature of the reflection

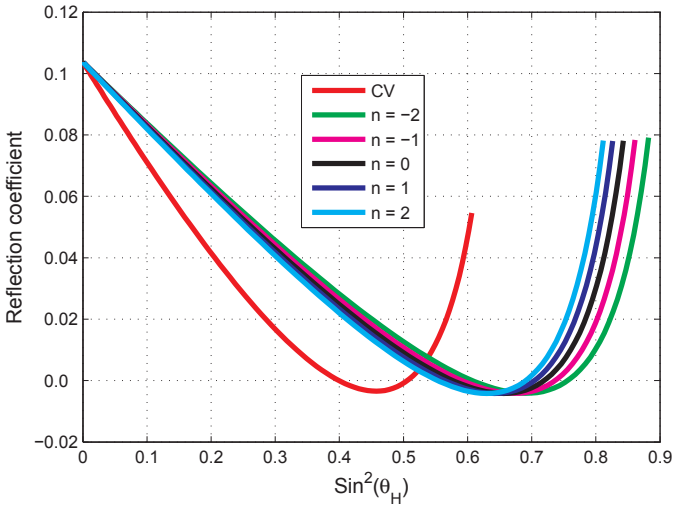

Figure 6.8: Pre-critical true-amplitude AVA dependences from Figure 6.7 plotted versus sine squared of the incident angle.

coefficient and where θ_H is the angle of incidence. This approximation is valid up to 50 degrees in incident angle, so we limited the source-to-receiver distance up to 2500 m to guarantee only pre-critical reflections.

Figure 6.8 shows the true-amplitude AVA dependences plotted against $\sin^2(\theta_H)$. Stretching and scaling are observed; however, the stretching effect is more evident than the scaling effect. The attributes defined in equation 12 differ, depending on the velocity model; however, intercept $R(0)$ is very close to the true intercept for all considered curves. The shape of the AVA-dependent curves indicates that using the CV model will produce the largest errors in G and K. The errors in AVO-attributes are plotted in Figure 6.9. As expected, the largest errors are obtained for the CV model. Note that the errors in attributes increase with their order, regardless of the velocity model. Intercept estimates are most accurate, gradient has medium accuracy, and curvature has the largest error. It is easy to see that all curves have practically the same AVO intercept, whereas the AVO gradient and AVO curvature are different for the different velocity models. The results from the three-parameter interpretation are more accurate than the two-parameter one. Error values have some symmetry relative to the true model ($n = 1$). The closer velocity interpretation is to the true model, the more accurate solution obtained.

Optimization with Nelder-Mead method does not require any approximations of the

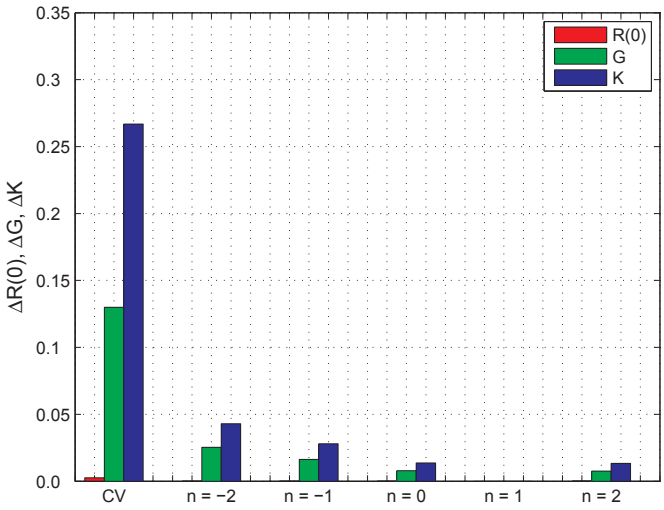

Figure 6.9: Errors in AVO attributes (intercept, gradient and curvature) for different velocity models.

reflection coefficient and uses exact Zoeppritz equation. We performed inversion for two offset ranges: pre-critical (up to $2500m$) and an extended range that includes post-critical reflections (up to $3575\,m$). We used the real part of the reflection coefficient for the first case and the magnitude of the reflection coefficient for the latter.

Figure 6.10a shows the relative errors in the reservoir parameters computed from pre-critical incident angles only. In general, errors gradually increase with parameter deviation from the true model. The most inaccurate estimates in reservoir parameters are obtained for the CV case, and they are three times larger than for the three-parameter velocity models. Among reservoir parameters, P-wave velocity estimates have the best accuracy for all considered models, whereas S-wave velocity estimates have small errors only for the three-parameter models. The largest error from the applying the CV model (the least accurate case) is in reservoir density, which is about 12%. The largest error from the application of three-parameter models is in S-wave velocity (about 3%) for the model with $n = -2$.

Figure 6.10b shows the relative error in reservoir-parameter estimates from AVA inversion; post-critical incident angles are included. We observe a similar trend in parameter estimation for different classes of the velocity models. The most inaccurate estimates are obtained for the two-parameter model, whereas estimates for the three-parameter models become more precise closer to the true model. Comparison

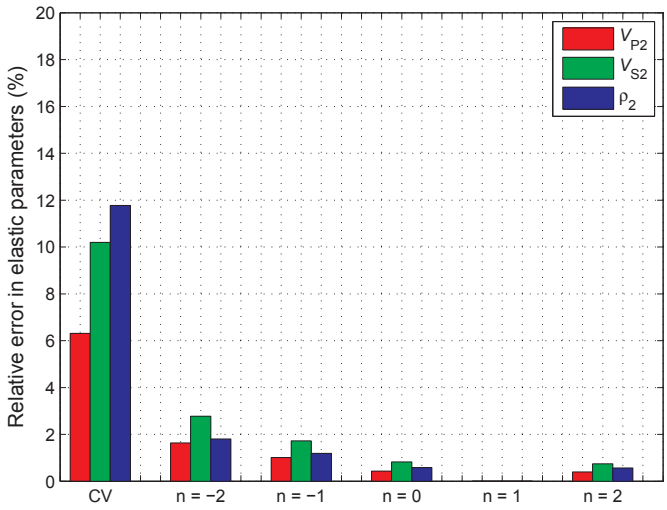

(a)

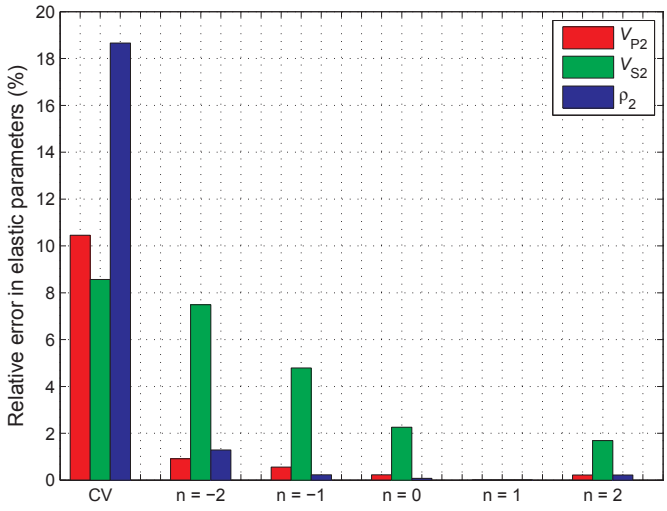

(b)

Figure 6.10: Relative errors in reservoir parameter estimates from AVA inversion, where (a) only pre-critical angles and (b) both pre-critical and post-critical angles are included.

with the results for pre-critical reflections (Figure 6.10a) shows that including post-critical reflections increases errors in S-wave velocity estimation but improves P-wave velocity and density estimates. This is because distortions from velocity analysis at

the post-critical region are more significant than at pre-critical offsets. When we use only the PP reflection coefficient, we obtain very good estimates for P-wave velocities but less precise estimates for S-wave velocity. Different behavior in accuracy among reservoir parameters for two- and three-parameter models in Figures 6.10b and 6.10a is probably because scaling and stretching effects have the largest influence on AVA dependences for the two-parameter case, making these results more unstable.

6.9 Conclusions

Wrong velocity interpretation of estimated traveltime parameters has two major effects on amplitude data: stretching from offset-to-angle conversion and scaling from geometrical spreading correction. Results show that these effects are significant for the two-parameter velocity interpretation even for small offsets, whereas they decrease significantly for three-parameter velocity interpretation and distort mostly amplitudes at far offsets. However, the family of three-parameter velocity models describes a variety of velocity distributions. Geologic information might be useful for estimating the parameter n and could improve quality of the inversion.

AVA inversion for attributes showed that intercept estimates are not affected by the choice of the velocity model, whereas accuracy of gradient and curvature significantly improves for three-parameter models. AVA inversion for reservoir parameters at pre-critical offsets gives three times better estimates of parameters for three-parameter velocity models than for CV model. Including post-critical offsets improves P-wave velocity and density estimates but impairs S-wave velocity accuracy for three-parameter models; estimates for CV are unstable.

Investigations have been made under the assumption that traveltime parameters are precisely estimated. Therefore, the presence of additional errors in the AVA inversion caused by uncertainties in traveltime-parameters estimation requires further analysis. We expect that three-parameter velocity models will produce better estimates of the reservoir parameters than the two-parameter model.

6.10 Acknowledgments

We acknowledge StatoilHydro and the ROSE project for financial support.

6.11 Appendix A: The power-gradient velocity model

The parametric form of the time-offset relationship for the vertically heterogeneous velocity model $v(z)$, $z \in [0, H]$ can be written as the parametric equations:

$$\begin{aligned} x(p) &= 2\int_0^H \frac{pv(z)\,dz}{\sqrt{1-p^2v^2(z)}} \\ t(p) &= 2\int_0^H \frac{dz}{v(z)\sqrt{1-p^2v^2(z)}}, \end{aligned} \tag{A-1}$$

where p is the ray parameter or horizontal slowness. Substituting the power-gradient velocity model from the equation 2 into the offset-traveltime equations A-1 results in the analytic expressions given by the hypergeometric functions (Stovas, 2009):

$$\begin{aligned} x(p) = \frac{2pv_0Hn}{(\gamma^n-1)(n+1)}\Bigg[&\gamma^{n+1}{}_2F_1\left(\frac{n+1}{2},\frac{1}{2},\frac{n+3}{2},p^2v_0^2\gamma^2\right) - \\ &-{}_2F_1\left(\frac{n+1}{2},\frac{1}{2},\frac{n+3}{2},p^2v_0^2\right)\Bigg] \\ t(p) = \frac{2Hn}{(\gamma^n-1)(n-1)v_0}\Bigg[&\gamma^{n-1}{}_2F_1\left(\frac{n-1}{2},\frac{1}{2},\frac{n+1}{2},p^2v_0^2\gamma^2\right) - \\ &-{}_2F_1\left(\frac{n-1}{2},\frac{1}{2},\frac{n+1}{2},p^2v_0^2\right)\Bigg] \end{aligned} \tag{A-2}$$

where ${}_2F_1(a,b,c,x)$ is the hypergeometric function. Equations A-2 can be expanded into Taylor series in terms of horizontal slowness

$$\begin{aligned} x(p) = \frac{2pv_0Hn(\gamma^{n+1}-1)}{(\gamma^n-1)(n+1)}\Bigg[&1+\frac{1}{2}p^2v_0^2\frac{n+1}{n+3}\frac{(\gamma^{n+3}-1)}{(\gamma^{n+1}-1)}+\frac{3}{8}p^4v_0^4\frac{n+1}{n+5}\frac{(\gamma^{n+5}-1)}{(\gamma^{n+1}-1)}+ \\ &+\ldots+\frac{1\cdot3\cdot\ldots\cdot(2k-1)}{k!2^k}p^{2k}v_0^{2k}\frac{n+1}{n+1+2k}\frac{\left(\gamma^{2k+1}-1\right)}{(\gamma^{n+1}-1)}+\ldots\Bigg] \\ t(p) = \frac{2Hn(\gamma^{n-1}-1)}{(\gamma^n-1)(n-1)v_0}\Bigg[&1+\frac{1}{2}p^2v_0^2\frac{n-1}{n+3}\frac{(\gamma^{n+1}-1)}{(\gamma^{n-1}-1)}+\frac{3}{8}p^4v_0^4\frac{n-1}{n+5}\frac{(\gamma^{n+3}-1)}{(\gamma^{n-1}-1)}+ \\ &+\ldots+\frac{1\cdot3\cdot\ldots\cdot(2k-1)}{k!2^k}p^{2k}v_0^{2k}\frac{n-1}{n-1+2k}\frac{\left(\gamma^{2k-1}-1\right)}{(\gamma^{n-1}-1)}+\ldots\Bigg] \end{aligned} \tag{A-3}$$

To compute the traveltime parameters in vertically heterogeneous media $v(z)$, $z \in [0, H]$, we need to define the velocity moments (Fomel and Grechka, 2001):

$$I_m = \int_0^H v^m(z)\, dz,\ m = -1, 1, 3. \tag{A-4}$$

Then the traveltime parameters can be expressed by combinations of the velocity moments

$$\begin{aligned} t_0 &= 2I_{-1}, \\ v_{nmo}^2 &= \frac{I_1}{I_{-1}}, \\ S_2 &= \frac{I_3 I_{-1}}{I_1^2}, \\ S_3 &= \frac{I_5 I_{-1}^2}{I_1^3}, \\ &\dots, \\ S_k &= \frac{I_{2k-1} I_{-1}^{k-1}}{I_1^k}. \end{aligned} \tag{A-5}$$

In a homogeneous medium, $t_0 = 2H/v_0$, $v_{nmo} = v_0$ and all heterogeneity coefficients are equal to one, i.e. $S_k = 1,\ k = 2, 3 \dots$. The expressions for the traveltime parameters in terms of the model parameters can be obtained by substituting equation 2 into equations A-4 and A-5. Explicitly, the traveltime parameters have the following form (Stovas, 2009).

$$\begin{aligned} t_0 &= \frac{2H}{v_0} \frac{n}{(n-1)} \frac{\gamma^{n-1} - 1}{\gamma^n - 1}, \\ v_{nmo}^2 &= v_0^2 \frac{(n-1)}{(n+1)} \frac{\gamma^{n+1} - 1}{\gamma^{n-1} - 1}, \\ S_2 &= \frac{(n+1)^2}{(n+3)(n-1)} \frac{(\gamma^{n+3} - 1)(\gamma^{n-1} - 1)}{(\gamma^{n+1} - 1)^2}, \\ S_3 &= \frac{(n+1)^3}{(n+5)(n-1)^2} \frac{(\gamma^{n+5} - 1)(\gamma^{n-1} - 1)^2}{(\gamma^{n+1} - 1)^3}, \\ &\dots, \\ S_k &= \frac{(n+1)^k}{(n-1+2k)(n-1)^{k-1}} \frac{\left(\gamma^{n-1+2k} - 1\right)(\gamma^{n-1} - 1)^{k-1}}{(\gamma^{n+1} - 1)^k}. \end{aligned} \tag{A-6}$$

Note that $\lim_{m \to 0} \frac{\gamma^m - 1}{m} = \ln \gamma$.

By substituting equations A-6 into equations A-3, we obtain the parametric moveout

expression in terms of traveltime parameters:

$$\begin{aligned} x(p) &= pt_0 v_{nmo}^2 \left[1 + \sum_{m=2}^{\infty} q_m S_m (pv_{nmo})^{2m-2}\right], \\ t(p) &= t_0 \left[1 + \sum_{m=2}^{\infty} q_m S_{m-1} (pv_{nmo})^{2m-2}\right], \end{aligned} \tag{A-7}$$

where $q_m = \frac{1\cdot 3\cdot \ldots \cdot (2m-3)}{2\cdot 4\cdot \ldots \cdot (2m-2)}$, $m = 2, 3 \ldots$ and $S_1 = 1$. Expanding the traveltime parameters from equation A-6 in the Taylor series at $\gamma = 1$, we obtain

$$\begin{aligned} t_0 &= \frac{2H}{v_0}\left[1 - \frac{1}{2}(\gamma-1) - \frac{1}{12}(\gamma-5)(\gamma-1)^2 + \frac{1}{8}(\gamma-3)(\gamma-1)^3 + \ldots\right], \\ v_{nmo}^2 &= v_0^2\left[1 - (\gamma-1) + \frac{1}{6}n(\gamma-1)^2 + 0 + \ldots\right], \\ S_2 &= 1 + \frac{1}{3}(\gamma-1)^2 + \frac{1}{3}(\gamma-1)^3 + \frac{1}{60}\left(n^2+2n-20\right)(\gamma-1)^4 + \ldots, \\ S_3 &= 1 + (\gamma-1)^2 + (\gamma-1)^3 + \frac{1}{60}\left(3n^2+10n-72\right)(\gamma-1)^4 + \ldots, \\ &\ldots, \\ S_k &= 1 + \frac{1}{6}k(k-1)(\gamma-1)^2 + \frac{1}{6}k(k-1)(\gamma-1)^3 + \\ &\quad + \frac{1}{360}k(k-1)\left(54 + 3k^2 + 2n - 3n^2 - 3k - 4kn\right)(\gamma-1)^4 + \ldots. \end{aligned} \tag{A-8}$$

We consider three-parameter kinematically equivalent models, with the traveltime parameters t_0, v_{nmo} and S_2 the same but S_k, $k = 3, 4, \ldots$ different; so it is important to express the higher-order heterogeneous coefficients through the heterogeneous coefficient of the second-order S_2. Then we can analyze the influence of n. Inverting the series for the second-order heterogeneous coefficient from equation A-8, we obtain the series for the velocity contrast γ as follows:

$$\gamma = 1 + \sqrt{3}(S_2-1)^{1/2} + \frac{3}{2}(S_2-1) + \frac{5+3n+n^2}{40}3\sqrt{3}(S_2-1)^{3/2} + \ldots. \tag{A-9}$$

Note that n appears in the third-order coefficient of the series. Using equation A-9, we can express the higher-order heterogeneous coefficients from equation A-8 in terms of the second-order coefficient (see equation 3). Substituting the series A-9 into the second expression in equation A-8 results in the series for parameter $\lambda = v_0/v_{nmo}$ (see equation 7).

6.12 Appendix B: Series for the relative geometrical spreading

Let us introduce the normalized offset as a function of slowness

$$\widetilde{x}\left(p\right)=\frac{x\left(p\right)}{v_{nmo}t_0}. \tag{B-1}$$

Substituting the expression for offset from equation A-7 into equation B-1 and performing the inversion of the series, we obtain the series for slowness in terms of normalized offset

$$p\left(\widetilde{x}\right)=\frac{1}{v_{nmo}}\left[\widetilde{x}-q_2S_2\widetilde{x}^3+\left(3\left(q_2S_2\right)^2-q_3S_3\right)\widetilde{x}^5+\ldots\right]. \tag{B-2}$$

Substituting equation B-2 into the equation 11 for the radiation pattern results in

$$\cos\left(\theta_0\right)=\sqrt{1-\left(pv_0\right)^2}=\sqrt{1-\lambda^2\left[\widetilde{x}^2-S_2\widetilde{x}^4+\frac{7S_2^2-3S_3}{4}\widetilde{x}^6+\ldots\right]}, \tag{B-3}$$

where $\lambda=v_0/v_{nmo}$. Expansion of equation B-3 into Taylor series gives

$$\begin{aligned}\cos\left(\theta_0\right)=&1-\frac{1}{2}\lambda^2\widetilde{x}^2-\frac{\lambda^4-4S_2\lambda^2}{8}\widetilde{x}^4-\\&-\frac{14S_2^2\lambda^2-6S_3\lambda^2-4\lambda^4S_2+\lambda^6}{16}\widetilde{x}^6-\ldots,\end{aligned} \tag{B-4}$$

Substituting equation B-2 into the relation for the incident angle from equation 5 at the target level results in

$$\begin{aligned}\sin\left(\theta_H\right)=&pv\left(H\right)=\frac{\sin\left(\theta_0\right)}{v_0}v\left(H\right)=\\=&\gamma\lambda\left[\widetilde{x}-\frac{1}{2}S_2\widetilde{x}^3+\frac{3}{4}\left(S_2^2-\frac{1}{2}S_3\right)\widetilde{x}^5+\ldots\right]\end{aligned} \tag{B-5}$$

The second term in equation 11 for the relative geometrical spreading can be written similarly. By using the expression for the offset from equation A-3, expanding the second term into the Taylor series, and substituting the equation B-2, we obtain

$$\begin{aligned}\left[\frac{x}{p}\frac{dx}{dp}\right]^{1/2}=&v_{nmo}^2t_0\left[1+S_2p^2v_{nmo}^2+\frac{1}{8}\left(9S_3-S_2^2\right)p^4v_{nmo}^4+\ldots\right]=\\=&v_{nmo}^2t_0\left[1+S_2\widetilde{x}^2+\frac{9}{8}\left(S_3-S_2^2\right)\widetilde{x}^4+\ldots\right].\end{aligned} \tag{B-6}$$

Chapter 7

Concluding remarks

The reflections in the post-critical domain are associated with amplitude increase, phase shifts, head wave interference and frequency effects, which bring additional information about the media parameters. This thesis is focused on exploring the benefits of exploiting reflections around and beyond the critical offsets in AVO studies for isotropic and HTI models. The entire study is carried out for one interface between two elastic halfspaces. The formulation of a long offset AVO problem is based on the theory of effective reflection coefficients (Ayzenberg et al., 2007, 2009) since it provides an adequate description of reflection amplitudes around and beyond the critical angle, which captures interference between the reflected and head wave.

The reflection coefficients have different sensitivities to the changes in model parameters prior to and beyond the critical angle, which provides a potential for joint inversion. For isotropic media post-critical reflections are most sensitive to the P-wave velocities. They also have a better sensitivity to densities than to S-wave velocity of underburden. For azimuthally-anisotropic media, post-critical reflections are additionally more sensitive to anisotropy parameter $\epsilon^{(V)}$ and symmetry direction, while pre-critical reflections shows better sensitivity to anisotropy parameters $\delta^{(V)}$ and $\gamma^{(V)}$, and P- and S-wave velocities.

Effective reflection coefficients inherit frequency, wavefront curvature and interface curvature information combined in additional argument $k_P r^*$. This argument results in the appearance of amplitude characteristic, such as the amplitude maximum, representative for the post-critical domain. The analysis of the amplitude maximum position with azimuth can be a useful tool for symmetry axis detection in fractured

media or interface shape detection in media with curved interfaces. A mismatch of the amplitude maximum position with the critical offset, controlled by the $k_P r^*$, however, does not allow straightforward estimation of P-wave velocities or anisotropy parameters.

Representation of AVO data can be done in time and in frequency domains. AVO data obtained in a time domain contain information about all frequencies of the wavelet and might be more robust to the irregular noise. AVO data obtained in the frequency domain can be used for analysing the frequency dependencies of the data. Such analysis might be useful to highlight regular noise, which is difficult to analyse in a time domain. Additionally, the azimuthal changes of frequency dependent amplitude in a post-critical domain can be employed for fracture direction identification.

Two AVO inversion approaches based on effective reflection coefficients and AVO data representation in time and frequency domains are developed. The inversion of long offset AVO data provides sufficient improvement in parameter estimates compared with the inversion of reflections in pre-critical offsets. The dependence of an effective reflection coefficient on the additional argument $k_P r^*$ allows recovery of five medium parameters instead of four as in the case of plane-wave reflection coefficients.

This thesis represents mainly theoretical studies. The results can be used as a motivation for further development in theoretical and practical aspects.

The important issue is the development of approximations of reflection coefficients valid around and beyond the critical angle. The first attempt is made recently by Alulaiw and Gurevich (2011), where they derived a weak-contrast approximation, valid beyond the critical angle. Considering the growing interest of industry to the strong contrast reservoirs, alternative approximations have to be found.

It is interesting to explore the possibility of exploiting the argument $k_P r^*$. The equivalence of the argument $k_P r^*$ to the product of the frequency and reflection traveltime ωt for plane interfaces is way of combining reflection traveltime and amplitude information in the joint inversion. An explicit relation between the amplitude maximum and critical offset as a function of the argument $k_P r^*$ should simplify an estimation of P-wave velocities and anisotropy parameters $\epsilon^{(V)}$ and $\delta^{(V)}$.

An application of long-offset AVO analysis and inversion to the real data is associated with many challenges in data processing and theoretical aspects. Interference of reflections from different layers and influence of regular noise, such as water-column noise in a post-critical domain requires extending the one-interface AVO approach to

the multi-layered model and developing appropriate filters. The important issue in AVO pre-processing is the data imaging. The existing imaging techniques are not valid in post-critical domain. Post-critical reflections, therefore, are often muted in the standard data pre-processing. The application of long-offset AVO techniques thus requires an advanced imaging technique.

Although the reflections around and beyond the critical angle are associated with a large amount of obstacles in processing and a lack of theoretical framework, the author believes that exploiting the post-critical reflections in AVO analysis and inversion might be a useful tool in reservoir characterization.

Appendix A

Potential improvements in reservoir monitoring using permanent seismic receiver arrays

Martin Landrø[1], Lyubov Skopintseva[1]

[1] Norwegian University of Science and Technology, Trondheim, Norway

Presented at the 70th EAGE Conference & Exhibition, Rome, Italy, June 2008; Published in the Leading Edge in December 2008

A.1 Abstract

Although interest in permanent instrumentation for monitoring hydrocarbon fields is increasing, we have not seen a boom in this technologyÚespecially for massive seismic monitoring. Only a few examples have followed the first implementation at Valhall Field offshore Norway in 2003. BP has acquired 11 surveys using a network of seafloor cables that covers 70% of the entire field since that installation, and the quality of these 4D data is excellent. So why is the adoption of the permanent seismic acquisition system so slow? A commonly accepted explanation is the difficulties and uncertainties associated with the cost-benefit analysis for new fields. The smaller a field, the less the benefit compared to the up-front cost to establish a permanent receiver array. Another explanation is that repeated conventional streamer surveys are often regarded as sufficient (e.g., Norne Field). Therefore, geophysicists are often confronted by the question: Is the improvement gained from the permanent array sufficient to risk high up-front costs compared to the conventional technology that often is sufficient? Several additional benefits can be obtained from a permanent seismic array, and some will be discussed in this paper, although this is not an attempt to cover all of them. For instance, the extra information obtained from passive seismic in a 4D mode is not yet fully explored. The main objective of this paper is to draw attention to some possibilities offered by permanent instrumentation that have not been extensively discussed previously. In 4D seismic analysis, we are always seeking the optimal, clean 4D signal, and we think that permanent receivers offer a multiplicity of possibilities to enhance this signal.

A.2 Increased shot-time interval

A 2008 paper by Landrø shows that the signal-to-noise ratio increases as the time between successive shots is increased. Figure 1 shows how the signal-to-noise ratio varies as a function of shot-time interval for a calibrated synthetic model. An increase in the shot-time interval from 10 to 15 s corresponds to an increase in the SNR from 12.5 to 18.8. It should be noted that SNR in this case is defined in a strictly narrow manner: The noise is considered to be only that generated by the decaying signal from the previous shot; all other noise sources are neglected. Th is means that if, for instance, the weather noise is above the noise generated by the previous shot after, say, 13 s of recording time, the full benefit of the increased shot-time interval

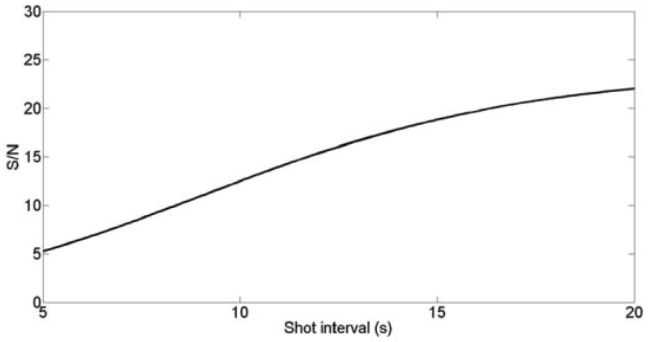

Figure A.1: Signal-to-noise ratio (considering only the noise from the previous shot as the noise contribution) as a function of shot-time interval.

will not be gained. Therefore, the curve in Figure A.1 should be used with care. In practice, other noise sources have to be considered, and the combined study of all noise sources should be done prior to choosing a different shot-time interval. However, the main purpose of this section is to stress that for highly repeatable 4D seismic data, it might be beneficial to increase the shot-time interval because for permanent receiver arrays, the extra cost of increasing the shot-time interval is far less than for a conventional streamer survey. Figure A.2 shows that the SNR generated by the previous shot can be increased by increasing the source strength. For 4D purposes, we will therefore argue that the source should be of significant strength to ensure that the SNR is defined by other noise sources rather than the signal generated by previous shots. It is interesting to note that these suggestions seem to contradict some ideas presented in the July 2008 issue of TLE, where simultaneous sources are cited for improving acquisition time and the illumination for seismic imaging. However, the increased shot-time interval and source strength suggested here are meant to improve 4D signal analysis, not necessarily for improved imaging of the reservoir. Accurate imaging of the reservoir is always an important part of a 4D study and, for permanent monitoring, it might be possible to acquire complementary repeated surveys, where imaging (by using several sources and wide azimuths) is the focus for some surveys and repeatability is the focus of other surveys.

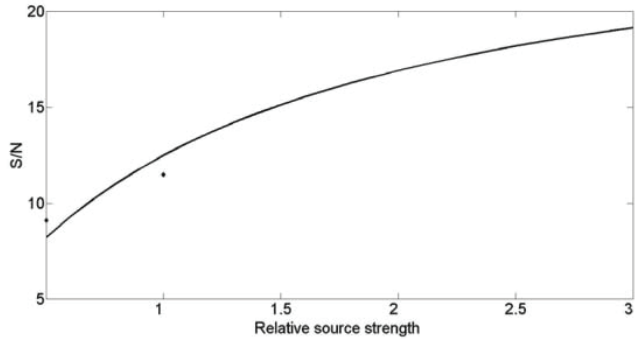

Figure A.2: Signal-to-noise ratio versus source strength (using the same calibrated model as in Figure A.1). The diamonds show measured data from Haltenbanken, offshore Norway.

A.3 Dense shooting close to injectors

Close to injectors it might be of interest to monitor fluid or pressure changes during a relatively short time interval (e.g., weeks or maybe 1-2 months). In such cases a semipermanent acquisition pattern might be used. Deploying nodes close to the injector well (or instrumenting the well itself by permanent sensors), and shooting several surveys over the area might achieve a nice way of monitoring the early stages of the flow. Figure A.3 shows an example from Gullfaks Field (using conventional-streamer data) where the flow of gas turns out to be more complex that initially expected. The 4D seismic data reveal that the gas migration path from the injector well (A-42) is southwest and that a local structural high (at tip of the first red arrow) fills up with gas and spills over so that the gas migrates northeast and reaches the producer (A-9H). In this case, gas breakthrough in the producer was observed some months after injection started. Approximately 470 million cubic meters of gas were injected. The major advantage of a semipermanent (or permanent) array in such a case would be to determine the major directions of gas flow and to estimate the velocity of the fluid front. Another challenge is to determine how much oil the gas has pushed toward the producer, and we think that multiple, ultrafrequent seismic acquisition close to the injector well will be of significant value for such detailed 4D analysis.

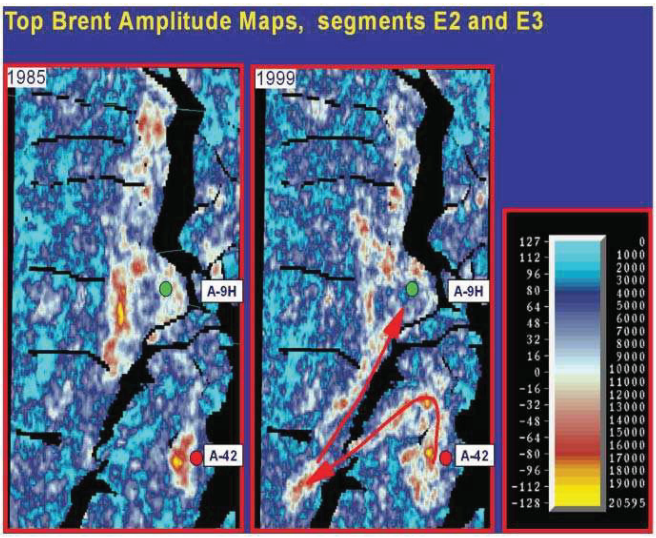

Figure A.3: Interpreted pathway for gas injection in well A-42 at Gullfaks. Gas breakthrough in well A-9H was observed after some months of injection (courtesy of StatoilHydro).

A.4 Ultrafrequent acquisition

Ultrafrequent 4D seismic acquisition (Skopintseva and Landrø, 2008) is particularly interesting for a field equipped with permanent receivers. Normally, 4D analysis includes 2-3 monitor surveys that are compared to the base data. One major limitation of conventional time-lapse seismic analysis is to detect changes from thin sections within a reservoir unit (Amundsen and Landrø, 2007). By ultrafrequent acquisition we mean typically several hundreds of repeated surveys. The purpose of this ultrafrequent sampling in time is two-fold: to monitor short term-reservoir changes (as discussed in the previous section) and to improve the 4D detectability by exploiting the multiplicity of the 4D data in an efficient way. Ultrafrequent 4D acquisition is most likely to be applied in permanent installations, when the cost of extra shooting is low. Here we use zero-off set data as a simplistic example. For land seismic monitoring, Meunier et al. (2001) showed that it is indeed possible to detect minor time-lapse changes using permanent sources and receivers and ultrafrequent surveys. For marine 4D seismic data, ultrafrequent 4D acquisition will face some additional challenges (such as temperature variations in the water layer, tidal effects, and repeatability issues of the source array). We use a horizontally layered model with

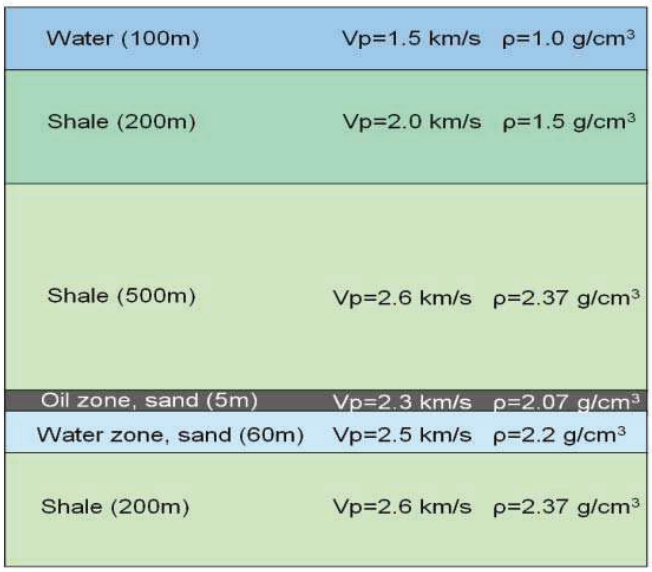

Figure A.4: 1D model, with a thin oil zone overlaying a thicker water zone, used to test ultrafrequent 4D acquisition.

layer parameters as indicated in Figure A.4. Note that the target zone is an oil layer with a thickness of 5 m. Figure A.5 (far left) shows two events and the difference trace where the monitor event corresponds to fully water-saturated zone properties in the oil zone (100% sweep efficiency). For the next three traces, we have added 10% random noise to the data. One can see that this amount of random noise distorts the 4D difference signal significantly within the target zone. Since the random noise introduces high-frequency noise outside the normal bandwidth of the seismic data, a band-pass filter was applied (next three traces in Figure A.5). There is a significant difference between the 'correct' 4D difference (trace number 3 in Figure A.5) and the corresponding difference after adding noise and bandpass filtering (trace 9 in Figure A.5). However, if we exploit the increased signal-to-noise ratio gained from the ultrafrequent acquisition (i.e., by stacking), the 4D signal (trace 12 in Figure A.5) is close to the desired 4D anomaly (trace 3). We assume that the acoustic properties in the oil zone gradually change toward water-zone properties by 0.01% every day, and we do a survey every day. Finally we have 680 seismic simulated measurements. For instance, the relative P-wave velocity and density increase from 0 on day 1 to 6.8% on day 680. To increase the SNR, we stack traces in a sliding window (width of 80 traces). Figure A.6 illustrates how the 4D difference signal improves as more and

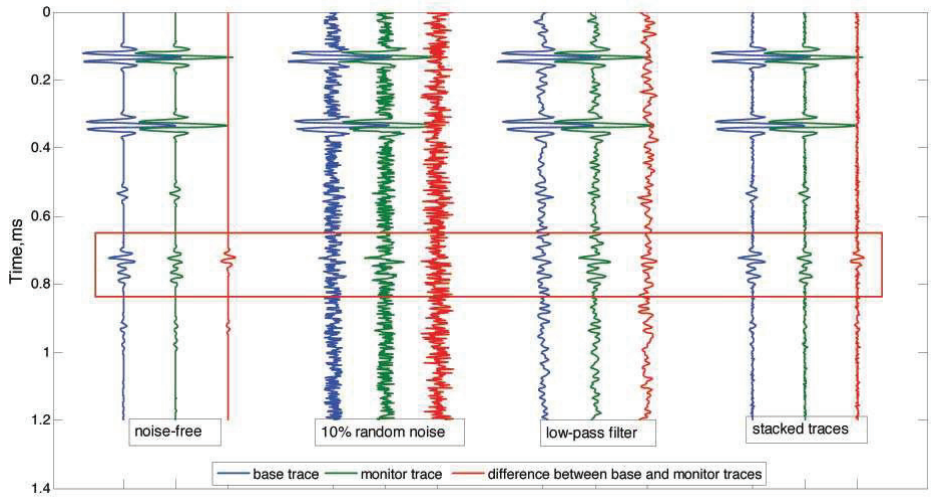

Figure A.5: Synthetic 1D modeling: noise-free data (far left), with 10% random noise using two surveys only (left), after applying a band-pass filter (right), and, finally, the ultrafrequent version (far right)

more surveys are stacked and calendar time elapses. The technique described above eliminates the effect of random noise. However, in reality, other factors also have significant distortion effects on the difference signal- seasonal temperature changes in the water layer (leading to velocity changes), tidal variations, source signature variations, sea surface roughness changes, and changing weather noise. We have simulated seasonal water velocity changes as described by Hatchell et al. (2007). Such changes introduce severe systematic errors in the estimated 4D differences. However, we find that it is possible to correct for these systematic changes in water velocity by using a crosscorrelation technique for the seabed reflection. The crosscorrelation technique is used to estimate the 4D time shift caused by the water velocity change and, hence, the 4D data can be corrected accordingly. Simulations show that we can detect 2% property changes in reservoir zone certainly when 10% random noise is added. We are currently working on a more comprehensive paper on this issue, where the systematic noise types listed above will be discussed in more detail.

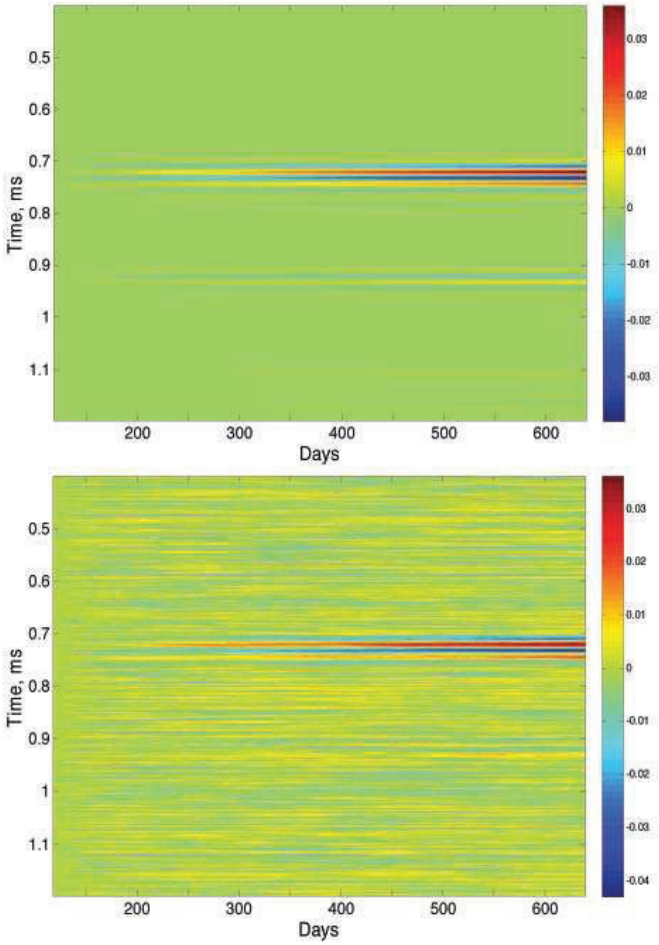

Figure A.6: 4D difference sections using ultrafrequent stacking (sliding window of 80 traces) as a function of calendar time: noise-free data (top) and 10% random noise (bottom).

A.5 Calibration by varying the source strength

At SEG's 2008 Annual Meeting, Landrø (Landrø, 2008) presented a new method for calibrating the 4D signal by varying the source strength in a controlled manner for the repeat survey. We think that this method is well suited for permanent receiver arrays, since the source boat is easier to control and adjust for such a set-up (the source vessel does not worry about towing streamers). The steps in this method are:

- For a selected 2D line (or sailing line in a 3D survey), gradually reduce the source strength from 100% to say 50% at the end of the line.
- Process the test line and the original (base line) 2D line in the same way as the planned 4D seismic data will be processed.
- Subtract the two processed lines and try to establish a threshold for how big the amplitude change within the reservoir (or below) needs to be in order to be detectable.

This can then be used both as a feasibility study and (probably more important) as a calibration and guide for which 4D anomalies that can be trusted and which anomalies that are more likely to be below the detection threshold. As an example, we have analyzed an inline (taken from the 3D seismic cube at Gullfaks) and assumed that, for the test line, the source strength is gradually decreased from 100% at the beginning of the line to 50% at the end. In this example we have added random noise to the data (SNR = 5) in order to include the nonrepeatable noise (Figure A.7). In a second example, the difference section between the 1996 and 1985 data from Gullfaks was used to simulate the nonrepeatable noise, and the result using this (more realistic) noise level is shown as the bottom section in Figure A.7. The typical NRMS (normalized RMS difference) is between 60 and 70% for the Gullfaks 4D data. More recent 4D surveys (Osdal et al., 2006) show much lower nrms values, around 20-30%. Therefore the example shown in Figure A.7 (bottom) represents a relatively high nonrepeatable noise level. It is also interesting to notice that the shallow part of the difference section in Figure A.7 (bottom) shows high-amplitude levels for low scaling (upper left of this section). This is typical and is due to the fact that such sections are less repeatable for shallow data. Furthermore, we observe that the reservoir-related amplitude anomalies are visible (red arrows) when the source strength is reduced by approximately 20%, an indication that amplitude changes for the Gullfaks 4D data (using 1985 and 1996 data sets) above 20Ű30% should be detectable at reservoir level. However, for the shallower horizon at approximately 1 s (black arrow in the

bottom section), we observe that an amplitude effect of close to 40% is needed. For a field equipped with permanent sensors and a dedicated source vessel, it should be possible to use this calibration method for various locations in the field to determine the amount of amplitude changes needed to be above the 4D detection threshold. The expected amplitude change caused by a fluid or pressure change might be computed by conventional rock physics. The huge advantage compared to more traditional 4D feasibility studies is that this calibration method includes the 4D background noise, since the calibration is done directly at the field. A possible extension of this method is to do the calibration procedure for various weather conditions and test how robust the expected 4D signal is to various levels of weather noise. Also, other noise types can be tested in a similar manner, for instance interference noise from other seismic acquisitions or ship traffic. In the simulations shown in the previous section, it is assumed that the source strength can be varied so that a linear trend can be achieved along a 2D line. Th is will not be possible in practice, since various source positions will be assigned to the same common midpoint position. Nevertheless, this smearing effect should not complicate the interpretation of the processed data too much. Near-offset stacks will have less of this smearing effect and probably give more precise information for the proposed calibration. The source strength can be varied gradually in several ways. One is to gradually reduce the firing pressure for all air guns in the source array. There are some concerns associated by this method, since for instance the bubble time period will change as the firing pressure of the air gun is decreased. Another way to change the source strength is to build arrays that are composed of several identical subarrays, and then drop subarrays one by one as the acquisition proceeds. GI-gun arrays offer a third alternative, since such arrays can be composed of several, identical air guns. Since each air gun takes care of its own bubble, there is no need for clustering or using various gun volumes to attenuate the unwanted bubble signal that is common for air guns. As an example, an air-gun array consisting of 24 GI guns can be gradually scaled by dropping out single guns during a survey, obtaining a smooth decrease in the source strength. For land surveys using dynamite or other explosive sources, it should be straightforward to adjust the source strength. For land vibrators (hydraulic), the most obvious way is to change the hydraulic force. In arctic areas (with snow or ice cover), it is common to use explosives as sources, so in such areas it should also be straightforward to vary the source strength systematically along a 2D line.

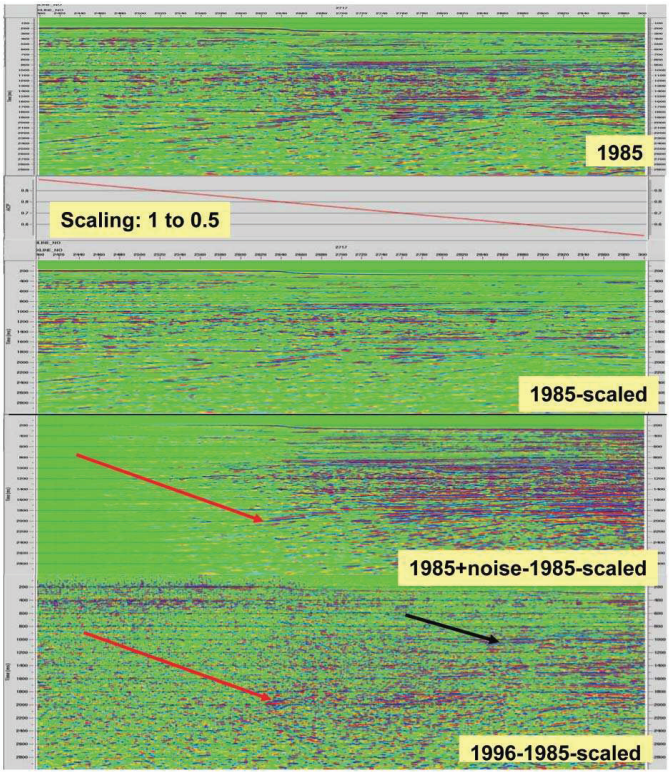

Figure A.7: Simulating the effect of varying the source strength for 4D calibration. (top to bottom) Inline from the Gullfaks Field (1985); after gradual scaling (from 1.0 to 0.5 at the end); difference between the original line and the scaled line; the scaled 1985 data subtracted from the 1996 data. Prior to the subtraction of the third profile, random noise (SNR = 5) was added to the base line data; this was not done when the scaled 1985 data were subtracted from the 1996 data. Observe that the differences at reservoir level (red arrows) become apparent for approximately 20% reduction in the source strength for the two bottom sections (which are scaled twice as much as the two top sections). Horizontal distance is 7.5 km, and time interval for all sections is 0Ű3 s.

A.6 Continuous monitoring of background noise

A permanent receiver array may be used to monitor the background noise on the field continuously. The various noise sources as discussed above can vary considerably with production time. An example is shown in Figure A.8 where the RMS level of three sets of noise records is compared. All records contain 120 traces with 7 s of data, and the RMS level is the average for all traces. The weather conditions for the three data sets are listed in Table A.1. All data were recorded, with the low-cut filter in, by M/V Bernier in 1988 offshore Norway (Haltenbanken area) as a part of a research project focusing on various types of noise and their impact on seismic data.

Table A.1: Weather conditions for three data sets

Data set	Swell	Wind	Sea state
58-62	1 m	No	0.5
63-67	1-2 m	16 kts	4
68-72	0.5 m	17 kts	3

Note that there is apparently no correlation between the sea state (or the wind strength) and the average RMS level. In fact, the data set with calmest sea and wind conditions (records 58-62) has a significantly higher rms level (around 3 microbar) than the two other data sets (around 1.5 microbar). As an example on how such continuous noise monitoring might be used, let us assume that the dashed line in Figure A.8 represents a possible 4D signal strength of 2 microbar caused by injection of gas. In 4D analysis, we often observe that new seismic events are created by gas injection. One such example from the well-known CO_2 injection at Sleipner Field offshore Norway is shown in Figure A.9, where we clearly see a new seismic event (enhanced by blue on the 2001 data). The interpretation is that the injected CO_2 is trapped below a very thin shale layer which is below seismic resolution and therefore not visible on the 1994 data set. However, after injection of CO_2, the contrast between the CO_2 layer and the surrounding sand and shale is significant and, therefore, a new strong seismic event appears below the thin shale. In such cases, the question is not to observe a change at a given interface (which is the classic 4D anomaly) but rather to detect a new event at a depth with a weak (or even without) a seismic signal on the base survey. For the hypothetical example displayed in Figure A.8, we observe that the first noise records (58-62) are well above the 4D detection threshold of 2 microbar, and the conclusion might therefore be that 4D is not possible with this background

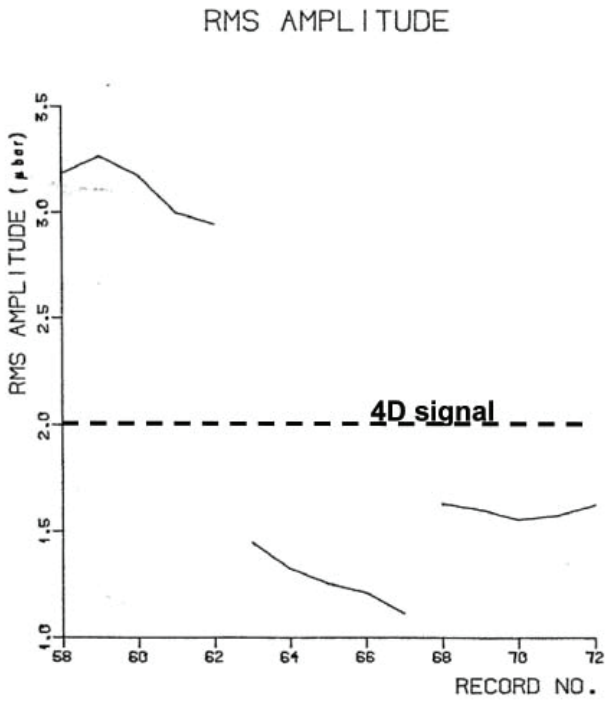

Figure A.8: The RMS amplitude of noise records from conventional streamer data. Records 58-62, 63-67, and 68-72, acquired during three different time periods, show considerable difference in RMS level. Data were acquired by M/V Bernier in 1988 off shore Norway, and consisted of 120 channels and 7 s recording time.

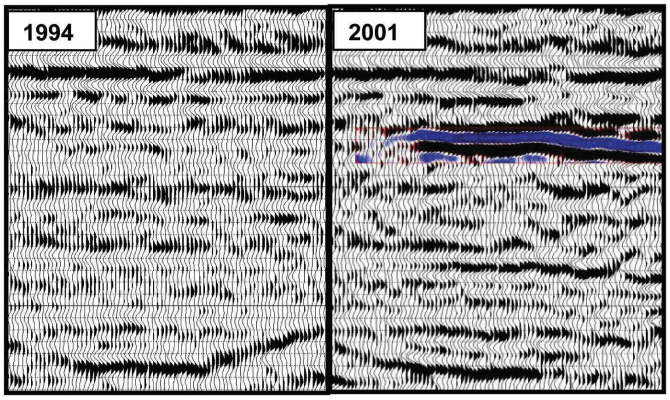

Figure A.9: Example of a new 4D event. Injected CO_2 is trapped below a thin shale layer (not visible on the 1994 pre-injection data to the left) and appears as a strong reflection in 2001 (blue on the post-injection data to the right).

noise level. For a permanent receiver system (as for a conventional streamer), it is possible to exploit the multichannel layout to detect other features of the noise by, for instance, f-k analysis. For the present example, the f-k analysis (FigureA.10) reveals that the noise source is directive with an apparent velocity of approximately 5500 m/s and, hence, it is possible to attenuate the noise by applying a simple fan filter in the f-k domain. The huge advantage for a permanent receiver system is, however, that it is cheap to record the background noise level, and to use the observed changes in the background noise level directly to enhance the 4D signal. One example might be the one described above (apply directional filters), and another might be to delay the seismic acquisition until the noise source moves away or simply attenuates (weather noise, rig noise, or ship traffic).

A.7 Source stability

With the present repeatability of 4D seismic data (between 10-40% measured in normalized rms error), the stability of the seismic source (assumed on the order of 5-10%) is not a major bottleneck. However, and especially for fields equipped with permanent sensors, one might expect in the future that source stability will become more critical. If this is the case, it is interesting to note that stacking two shot gathers might improve the 4D repeatability significantly. A zero-off set VSP study of Troll Field (Andorsen and Landrø, 2000) found that the NRMS error decreases from 16 to

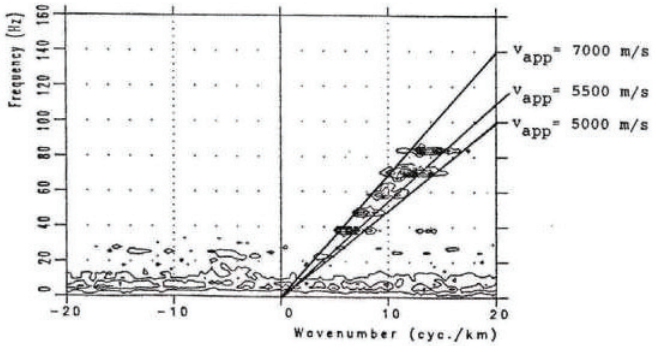

Figure A.10: The f-k contour plot of noise records 58-62 (shown in FigureA.8), which clearly indicates that a major part of the noise is directional with an average apparent velocity of 5500 m/s. This noise can be easily attenuated by a fan filter.

6% by simply stacking two succeeding shots (Figure A.11). It should be noted that this is for a VSP experiment, where the source array used has significantly less gun volume than a conventional air-gun array. The source stability increases as the array increases (less influenced by small variations in each gun), and therefore one must expect less improvement for a normally sized air-gun array. Normal streamer data also have higher fold, so some of the expected gain from stacking in the shot domain will be reduced when we try to employ the results of this VSP experiment on a field equipped with permanent receiver arrays. However, if it is established that the source stability is a critical issue for 4D monitoring of the field, it might be worth considering if one should acquire two base surveys and two repeats to build a 'super-repeatable' 4D data set. As a result of the increased use of 4D seismic, the focus on each element of the seismic acquisition chain has led to improved source stability. Therefore we might expect that the source arrays being used in future surveys at fields with permanent receivers are highly repeatable.

A.8 Discussion and conclusions

Fields equipped with permanent seismic receivers can use more sophisticated monitoring and normally more expensive methods than conventional monitoring. For instance, a single shooting vessel is much easier and cheaper to operate than a 3D marine seismic vessel towing many long cables. The most obvious advantage with

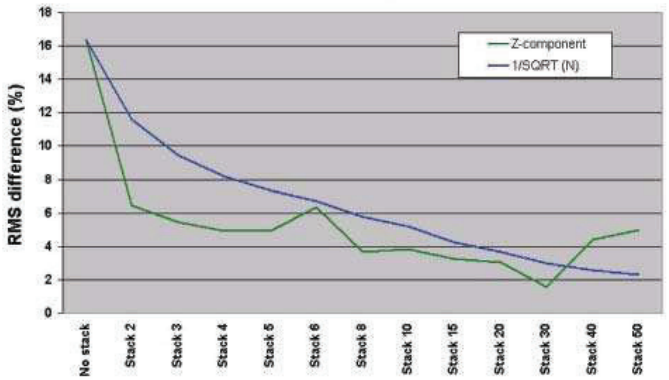

Figure A.11: Stacking of successive shot gathers for a zero-offset VSP experiment. No stacking to the left and stacking of up to 50 shots on the right (green line). For comparison, the standard $1/\sqrt{N}$ is shown by the blue line. (From Andorsen and Landrø (2000))

permanent receivers is that the positioning issue is resolved for the receiver side, and all attention related to repeating the position is focused on the source side. For such an instrumented hydrocarbon field, it is possible to acquire ultrafrequent seismic surveys, either close to a desired location or for a limited period. For instance, if a survey is acquired every day for a period of some weeks, the multiplicity in such a data set can enhance the 4D signal as well as detect rapid changes in the flow or pressure properties in a certain area. The most critical challenges for such a method are to reduce or attenuate the effect of varying sea-water temperature, changes in weather-related noise, or environmental noise that is varying with calendar time. The source strength is an important factor in all seismic surveys. There are two obvious ways to reduce the influence of the previous shot on seismic data: increase the shot-time interval or increase the source strength. For an instrumented oil field, both options are possible and realistic. It is proposed that varying the source strength in a controlled manner for a repeated 2D line or a small area of the field can directly quantify how big an amplitude change is needed to be detected by 4D seismic data. If this calibration technique is done for different types of background noise (such as weather noise, rig noise, ship traffic, interference noise), it will be very useful for the analysis of the time-lapse data. It should be possible to use this technique to guide the interpretation and distinguish between real and false anomalies in a more precise manner. Permanent seismic arrays can monitor the background noise level continuously, and this knowledge can be used to attenuate the background noise or optimize the timing

for the repeated seismic surveys (avoid time periods with high background noise level on the field). The challenge for the geophysicist is to handle enormous amounts of data in an efficient way.

A.9 Acknowledgments

The authors acknowledge StatoilHydro for financial support of the PhD study of Lyubov Skopintseva. Martin Landrø acknowledges the Norwegian Research Council for financial support to the ROSE (Rock Seismic) project at NTNU. We thank StatoilHydro and its Gullfaks partner Petoro for permission to use and present their data. PGS is acknowledged for permission to use data from the seismic noise project acquired by SERES in 1988. Th ese data were acquired by M/V Bernier in JulyŰ́August 1988 and analyzed by M. Landrø, R. Haugen, A. Sodal, E. Nielsen, and S. Vaage in 1989. Finally, we thank the Center for Integrated Operations in the Petroleum Industry at NTNU for support.

Bibliography

Aizenberg, A., M. Ayzenberg, H. B. Helle, and J. Pajchel, 2005, Reflection and transmission of acoustic wavefields at a curved interface of two inhomogeneous media: Continuum Dynamics, Acoustics of Inhomogeneous Media, **123**, 73–79.

Aki, K. and P. Richards, 1980, Quantitative seismology: Theory and methods. vol[]1: W.H. Freeman & Co.

———, 2002, Quantitative Seismology (2nd edition): University Science Books.

Al-Dajani, A. and T. Alkhalifah, 2000, Reflection moveout inversion for horizontal transverse isotropy: Accuracy, limitation, and acquisition: Geophysics, **65**, 222–231.

Alhussain, M., 2007, Spherical wave AVO response of isotropic and anisotropic media: laboratory experiment versus numerical simulations.: Master's thesis, Curtin University of Technology.

Alhussain, M., B. Gurevich, and M. Urosevic, 2008, Experimental verification of spherical-wave effect on the AVO response and implications for three-term inversion: Geophysics, **73**, C7–C12.

Alkhalifah, T. and I. Tsvankin, 1995, Velocity analysis for transversely isotropic media: Geophysics, **60**, 1550–1566.

Alulaiw, B. H. and B. Gurevich, 2011, Analytical wavefront curvature correction for spherical wave avo: 73rd EAGE Conference&Exhibition, Extended Abstracts, P314.

Amundsen, L. and M. Landrø, 2007, 4D seismic - status and future challenges, part II: GeoExpro, **4**, 54–58.

Andorsen, K. and M. Landrø, 2000, Source signature variations versus repeatability - a study based on a zero-offset vsp experiment: Journal of Seismic Exploration, **9**, 61–71.

Arntsen, B., E. Tantserev, and L. Amundsen, 2010, True-amplitude cross-correlation shot-profile imaging condition: SEG Technical Program Expanded Abstracts, **29**, 3273–3277.

Avseth, P., T. Mukerji, G. Mavko, and J. A. Tyssekvam, 2001, Rock physics and AVO analysis for lithofacies and pore fluid prediction in a North Sea oil field: The Leading Edge, **20**, 429–434.

Ayzenberg, M., I. Tsvankin, A. Aizenberg, and B. Ursin, 2009, Effective reflection coefficients for curved interfaces in transversely isotropic media: Geophysics, **74**, WB33–WB53.

Ayzenberg, M. A., A. M. Aizenberg, H. B. Helle, K. D. Klem-Musatov, J. Pajchel, and B. Ursin, 2007, Three-dimensional diffraction modeling of singly scattered acoustic wavefields based on the combination of surface integral propagators and transmission operators: Geophysics, **72**, SM19–SM34.

Bluman, G. W. and S. Kumei, 1989, Symmetries and differential equations: Springer-Verlag, New York.

Brekhovskikh, L. M., 1960, Waves in layered media: Academic Press, New-York.

Carcione, J., 2007, Wave fields in real media: Wave propagation in anisotropic, anelastic, porous and electromagnetic media: Elsevier Ltd.

Červený, V., 1961, The amplitude curves of reflected harmonic waves around the critical point: Stud. geophys. geod, **5**, 319–351.

———, 2001, Seismic Ray Theory: Cambridge University Press.

Červený, V., F. Hron, and B. Novak, 1964, Reflection coefficients of plane waves of PP-type for weak interfaces: Geofys. Sbor, **11**, 79–142.

Červený, V., J. Langer, and I. Pšenčik, 1974, Computation of Geometric Spreading of Seismic Body Waves in Laterally Inhomogeneous Media with Curved Interfaces: Geophys. J. R. astr. Soc., **38**, 9–19.

Červený, V. and R. Ravindra, 1971, Theory of Seismic Head Waves: Univ. of Toronto Press, Toronto.

Chapman, M. and E. Liu, 2003, The frequency dependent azimuthal AVO response of fractured rock: SEG Expanded Abstracts, **22**, 105–108.

De Santo, J. A., 1983, Scattering of scalar waves from a rough interface using a single integral equation: Wave Motion, **5**, 125–135.

Dix, C. H., 1955, Seismic velocities from surface measurements: Geophysics, **20**, 68–86.

Downton, J. E. and C. Ursenbach, 2006, Linearized amplitude variation with offset (AVO) inversion with supercritical angles: Geophysics, **71**, E49–E55.

Favretto-Cristini, N., P. Cristini, and E. de Bazelaire, 2009, What is a seismic reflector like?: Geophysics, **74**, T13–T23.

Fomel, S. and V. Grechka, 2001, Nonhyperbolic reflection moveout of P waves. An overview and comparison of reasons: Colorado School of Mines Report, CWP–372.

Gray, F. D., G. Roberts, and K. J. Head, 2002, Recent advances in determination of fracture strike and crack density from P-wave seismic data: The Leading Edge, **21**, 280–285.

Grechka, V., I. Tsvankin, and J. K. Cohen, 1999, Generalized Dix equation and analytic treatment of normal-moveout velocity for anisotropic media: Geophysical Prospecting, **47**, 117–148.

Grechka, V., I. Vasconcelos, and M. Kachanov, 2006, The influence of crack shape on the effective elasticity of fractured rocks: Geophysics, **71**, D153–D160.

Haase, A. B., 2004, Spherical wave AVO modeling of converted waves in isotropic media: SEG Technical Program Expanded Abstracts, **23**, 263–266.

Hall, S. and J. M. Kendall, 2003, Fracture characterization at Valhall: Application of P-wave amplitude variation with offset and azimuth AVOA analysis to a 3-D ocean-bottom data set: Geophysics, **68**, 1150–1160.

Hansteen, F., P. B. Wills, K. Hornman, and L. Jing, 2011, Refraction monitoring shows promise in Heavy Oil Field: E & P.

Hatchell, P., P. B. Wills, and M. Landrø, 2007, Analysis of guided waves recorded on permanent ocean bottom cables: 69th EAGE Conference & Exhibition, Extended Abstracts, P–063.

Himmelblau, D. M., 1972, Applied Nonlinear Programming: Mc Graw-Hill Book Company.

Hubral, P., 1979, A wavefront curvature approach to computing ray amplitudes in inhomogeneous media with curved interfaces: Studia Geoph. et Geod., **23**, 131–137.

———, 2002, A wavefront curvature approach to computing ray amplitudes in inhomogeneous media with curved interfaces: Studia Geoph. et Geod., **Special issue**, 13–19.

Ikelle, L. T. and L. Amundsen, 2005, Introduction to petroleum seismology: Society of Exploration Geophysics.

Jin, S. and D. Yin, 2008, Computational high frequency waves through curved interfaces via the Liouville equation and geometric theory of diffraction: Journal of Computational Physics, **227**, 6106 – 6139.

Kennett, B. L. N., 1984, Reflection operator methods for elastic waves: Wave Motion, **6**, 407–429.

Kennett, B. N., 1983, Seismic wave propagation in stratified media: Cambridge University Press,Cambridge.

Klem-Musatov, K., A. M. Aizenberg, J. Pajchel, and H. B. Helle, 2008, Edge and tip diffractions: Theory and applications in seismic prospecting: Society of Exploration Geophysics.

Klem-Musatov, K. D., A. M. Aizenberg, H. B. Helle, and J. Pajchel, 2004, Reflection and transmission at curvilinear interface in terms of surface integrals: Wave Motion, **39**, 77–92.

Korn, G. A. and T. M. Korn, 1968, Mathematical Handbook for Scientists and Engineers: Definitions, Theorems, and Formulas for Reference and Review: New York: McGraw-Hill.

Kurt, H., 2007, Join inversion of AVA data for elastic parameters by bootstrapping: Computer&Geosciences, **33**, 367–382.

Landrø, M., 2006, Future challenges and unexplored methods for 4D seismic analysis: CSEG RECORDER, **Special edition**, 128–135.

———, 2008, Source strength variations and 4D seismic: SEG Technical Program Expanded Abstracts, **27**, 2742–2746.

Landrø, M. and I. Tsvankin, 2007, Seismic critical-angle reflectometry: A method to characterize azimuthal anisotropy?: Geophysics, **72**, D41–D50.

Lavaud, B., N. Kabir, and G. Chavent, 1999, Pushing AVO inversion beyond linearized approximation: Journal of Seismic Exploration, **8**, 279–302.

Lynn, H. B., D. Campagna, K. M. Simon, and W. E. Beckham, 1999, Relationship of P-wave seismic attributes, azimuthal anisotropy, and commercial gas pay in 3-D P-wave multiazimuth data, Rulison Field, Piceance Basin, Colorado: Geophysics, **64**, 1293–1311.

Mehdi Zadeh, H., 2011, Long-offset time-lapse seismic and monitoring of unconventional reservoirs: PhD thesis, NTNU.

Mehdi Zadeh, H., M. Landrø, and O. I. Barkved, 2011, Long-offset time-lapse seismic: Tested on the Valhall LoFS data: Geophysics, **76**, O1–O13.

Meunier, J., F. Huguet, and P. Meynier, 2001, Reservoir monitoring using permanent sources and vertical receiver antennae: The Cere-la-Ronde case study: The Leading Edge, **20**, 622–629.

Mora, C. and B. Biondi, 2000, Estimation of AVO attributes sensitivity to velocity uncertainty using forward modeling: Technical report, a progress report: Stanford University, SEP-103.

Muerdter, D. and D. Ratcliff, 2001, Understanding subsalt illumination through ray-trace modeling, Part 1: Simple 2-D salt models: The Leading Edge, **20**, 578–594.

Musgrave, M. J. P., 1970, Crystal Acoustics: Holde-Day, San-Francissco, California.

Ortiz-Osornio, M. and D. R. Schmitt, 2011, Physical modelling of the reflectivity and transmissivity of anisotropic materials: 72nd EAGE Conference&Exhibition, Extended Abstracts, D027.

Osdal, B., O. Husby, H. A. Aronsen, N. Chen, and T. Alsos, 2006, Mapping the fluid

front and pressure buildup using 4D data on Norne Field: The Leading Edge, **25**, 1134–1141.

Ostrander, W. J., 1984, Plane-wave reflection coefficients for gas sands at nonnormal angles of incidence: Geophysics, **49**, 1637–1648.

Petrashen, 1957, Materials for the quantative study of dynamic of seismic waves., volume **1**: Leningrad University.

Riedel, M. and F. Theilen, 2001, AVO investigations of shallow marine sediments: Geophysical Prospecting, **49**, 198–212.

Rüger, A., 2001, Reflection Coefficients and Azimuthal AVO Analysis in Anisotropic Media: Society of Exploration Geophysics.

Schoenberg, M. and J. Protazio, 1992, 'Zoeppritz' rationalized and generalized to anisotropy: Journal of Seismic exploration, **1**, 125–144.

Shuey, R. T., 1985, A simplification of the Zoeppritz equations: Geophysics, **104**, 609–614.

Skopintseva, L., A. M. Ayzenberg, M. A. Aizenberg, M. Landrø, and T. V. Nefedkina, 2010, Applicability of AVO inversion based on effective reflection coefficients to long-offset data from curved interfaces: 72nd EAGE Conference&Exhibition, Extended Abstracts, A030.

Skopintseva, L., M. Ayzenberg, M. Landrø, T. V. Nefedkina, and M. A. Aizenberg, 2011, Long-offset AVO inversion of PP reflections from plane interface using effective reflection coefficients: Geophysics (Accepted).

Skopintseva, L. and M. Landrø, 2008, High-frequent 4D-surveys for identification of subtle reservoir property changes: 70th EAGE Conference&Exhibition, Extended Abstracts, P232.

Skopintseva, L. V., M. A. Ayzenberg, M. Landrø, T. V. Nefedkina, and A. M. Aizenberg, 2008, AVO inversion of long-offset synthetic PP data based on effective reflection coefficients: 70th EAGE Conference & Exhibition, Extended Abstracts, 609–614.

———, 2009, Testing the performance of the AVO inversion based on effective reflection coefficients on long-offset synthetic PP-data: 71th EAGE Conference&Exhibition, Extended Abstracts, S022.

Skopintseva, L. V., T. V. Nefedkina, M. A. Ayzenberg, and A. M. Aizenberg, 2007, An approach to the AVO-inversion problem based on the effective reflection coefficients: 69th EAGE Conference & Exhibition, Extended Abstracts, P354.

Stovas, A., 2008, Kinematically equivalent velocity distributions: Geophysics, **73**, VE369–VE375.

———, 2009, Power-gradient velocity model: Geophysics, **74**, 13–33.

Stovas, A. and B. Ursin, 2009, Improved geometric-spreading approximation in layered transversely isotropic medium: Geophysics, **74**, 85–95.

Swan, H. W., 1993, Offset dependent reflectivity - Theory and practice of AVO analysis, chapter Properties of direct AVO hydrocarbon indicators, 78–92. Society of Exploration Geophysics.

Taner, M. T. and F. Koehler, 1969, Velocity spectra—digital computer derivation applications of velocity functions: Geophysics, **34**, 859–881.

Thomsen, L., 1986, Weak elastic anisotropy: Geophysics, **51**, 1954–1966.

———, 1990, Poisson was not a geophysicist: The Leading Edge, **9**, 27–29.

Tod, S., B. Taylor, R. Johnston, and T. Allen, 2007, Fracture prediction from wide-azimuth land seismic data in SE Algeria: The Leading Edge, **26**, 1154–1160.

Ursenbach, C. P., A. B. Haase, and J. E. Downton, 2007, An efficient method for AVO modeling of reflected spherical waves: Journal of Seismic Exploration, **16**, 561.

Ursin, B., 1990, Offset-dependent geometrical spreading in a layered medium: Geophysics, **55**, 492–496.

Van der Baan, M. and D. Smit, 2006, Amplitude analysis of isotropic P-wave reflections: Geophysics, **71**, C93–C103.

Wright, J., 1986, Reflection coefficients at pore-fluid contactes as a function of offset: Geophysics, **51**, 1858–1860.

Xu, X. and I. Tsvankin, 2007, A case study of azimuthal AVO analysis with anisotropic spreading correction: The Leading Edge, **26**, 1552–1561.

Xu, Y., G. H. F. Gardner, and J. A. McDonald, 1993, Some effects of velocity variation on AVO and its interpretation: Geophysics, **58**, 1297–1300.

Zoeppritz, K., 1919, Erdbebenwellen, On the reflection and penetration of seismic waves through unstable layers: Göttinger Nachrichten, **1**, 66–84.